NASA TECHNICAL MEMORANDUM

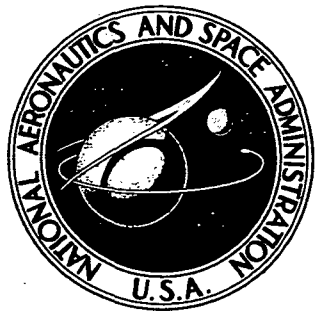



NASA TM X-2724

NASA TM X-2724



# EFFECT OF NOZZLE LATERAL SPACING, ENGINE INTERFAIRING SHAPE, AND ANGLE OF ATTACK ON THE PERFORMANCE OF A TWIN-JET AFTERBODY MODEL WITH CONE PLUG NOZZLES

*by Bobby L. Berrier*

*Langley Research Center*
*Hampton, Va. 23665*

NATIONAL AERONAUTICS AND SPACE ADMINISTRATION • WASHINGTON, D. C. • AUGUST 1973

| 1. Report No. | 2. Government Accession No. | 3. Recipient's Catalog No. |
|---|---|---|
| NASA TM X-2724 | | |

| 4. Title and Subtitle | 5. Report Date |
|---|---|
| EFFECT OF NOZZLE LATERAL SPACING, ENGINE INTERFAIRING SHAPE, AND ANGLE OF ATTACK ON THE PERFORMANCE OF A TWIN-JET AFTERBODY MODEL WITH CONE PLUG NOZZLES | August 1973 |
| | 6. Performing Organization Code |
| 7. Author(s) | 8. Performing Organization Report No. |
| Bobby L. Berrier | L-8690 |
| | 10. Work Unit No. |
| 9. Performing Organization Name and Address | 501-24-06-01 |
| NASA Langley Research Center<br>Hampton, Va. 23665 | 11. Contract or Grant No. |
| | 13. Type of Report and Period Covered |
| 12. Sponsoring Agency Name and Address | Technical Memorandum |
| National Aeronautics and Space Administration<br>Washington, D.C. 20546 | 14. Sponsoring Agency Code |

15. Supplementary Notes

16. Abstract

Twin-jet afterbody models were investigated by using two balances to measure separately the thrust minus total axial force and the afterbody drag at Mach numbers from 0 to 1.3. Angle of attack was varied from $-2^{\circ}$ to $8.5^{\circ}$. Translating shroud cone plug nozzles were tested at dry-power and maximum-afterburning-power settings with a high-pressure air system used to provide jet total-pressure ratios up to 9.0. Two nozzle lateral spacings were studied by using afterbodies with several interfairing shapes. The close- and wide-spaced afterbodies had identical cross-sectional area distributions when similar interfairings were installed on each. The results show that the highest overall performance was obtained with the close-spaced afterbody and basic interfairings. Increasing angle of attack decreased performance for all configurations and conditions investigated.

| 17. Key Words (Suggested by Author(s)) | 18. Distribution Statement |
|---|---|
| Twin-engine installation<br>Cone plug nozzles<br>Nozzle lateral spacing<br>Angle of attack | Unclassified – Unlimited |

| 19. Security Classif. (of this report) | 20. Security Classif. (of this page) | 21. No. of Pages | 22. Price* |
|---|---|---|---|
| Unclassified | Unclassified | 142 | $3.00 |

*For sale by the National Technical Information Service, Springfield, Virginia 22151

# EFFECT OF NOZZLE LATERAL SPACING, ENGINE INTERFAIRING SHAPE, AND ANGLE OF ATTACK ON THE PERFORMANCE OF A TWIN-JET AFTERBODY MODEL WITH CONE PLUG NOZZLES

By Bobby L. Berrier
Langley Research Center

## SUMMARY

An investigation has been conducted to determine the effect of nozzle lateral spacing, engine interfairing shape, and angle of attack on the performance of twin-engine afterbody configurations with translating shroud cone plug nozzles at Mach numbers from 0 to 1.3. Angle of attack was varied from $-2^{\circ}$ to $8.5^{\circ}$. A high-pressure air system was used to provide jet total-pressure ratios up to 9.0. Two nozzle lateral spacings (ratio of distance between nozzle center lines to maximum nozzle diameter equal to 1.12 and 1.61) were studied by using afterbodies with several interfairing shapes. The close- and wide-spaced afterbodies had identical cross-sectional area distributions when similar interfairings were installed on each.

The results of the investigation indicate that the overall performance term, thrust-minus-total-axial-force ratio, was highest for the close-spaced afterbody and basic interfairings. Increasing angle of attack decreased performance for all configurations and conditions investigated.

## INTRODUCTION

Recent experiences with multiengine airplanes have indicated that due consideration of the engine-nozzle installation is mandatory during the early design process in order to avoid a severe detrimental impact on mission performance of the flight article. Recent investigations have shown that nozzle performance is very sensitive to afterbody installation effects (refs. 1 to 5) and, similarly, that afterbody drag is very sensitive to nozzle installation effects (refs. 2, 4, 5, and 6). Because of the complex nature of the flow field in the nozzle-afterbody region, particularly for engines buried in the aft fuselage, and a lack of accurate theoretical methods for use in this local region, the design engineer must rely heavily on trends obtained from experimental data.

As part of a continuing program on engine-airframe integration, the Langley Research Center is evaluating the performance of twin-jet afterbody models utilizing

various nozzle types. References 7, 8, and 9 report the results of investigations on twin-jet afterbodies utilizing convergent, convergent-divergent, and cone plug nozzles, respectively. These investigations were made at an angle of attack of $0^{\circ}$. The present investigation shows the effects on performance of nozzle lateral spacing, engine interfairing shape, and angle of attack for translating shroud cone plug nozzles. The nozzle configurations and several of the afterbody-interfairing configurations used in the present investigation are identical to those reported in reference 9, the only difference being the support system which allows variation of angle of attack in the present investigation. Close- and wide-spaced afterbodies were tested with several alternate engine interfairing shapes. Both afterbodies, with corresponding engine interfairings, had identical cross-sectional area distributions.

Data from reference 9 indicate that interfairing base regions in proximity to the nozzle exits are aspirated by the nozzle exhaust flow and significantly increased afterbody drag, particularly for the close-spaced afterbody. The present paper presents results on interfairing configurations identical to those of reference 9 and on a similar interfairing configuration with the base region moved forward away from the exhaust flow.

Previous investigations have shown that plug-nozzle internal performance is detrimentally affected by external flow because of overexpansion of the exhaust flow (refs. 10 and 11). Nonoptimum expansion of the exhaust flow occurs because the outer boundary of the exhaust flow at the nozzle exit must adjust, not to free-stream static pressure, but usually to some lower static pressure on the nozzle-boattail surface and base. Reference 11 suggests that this external-flow effect may be minimized by reducing the nozzle base area. The present investigation presents results from a modified dry-power nozzle on which all base area was removed.

The investigation was conducted in the Langley 16-foot transonic tunnel at Mach numbers from 0 to 1.3 with nozzle throat areas corresponding to dry power (minimum throat area) and maximum afterburning power (maximum throat area). Jet total-pressure ratio was varied from approximately 1.0 (jet off) to 9.0. Angle of attack was generally varied from $-2^{\circ}$ to $8.5^{\circ}$ with the jets off. Jet-on data were obtained at a nominal angle of attack of $0^{\circ}$ for all Mach numbers investigated and also at a nominal angle of attack of $6^{\circ}$ at Mach numbers of 0.8 and 0.9.

## SYMBOLS

$A$ cross-sectional area, $m^2$

$A_{e,ext}$ nozzle exit area for fully expanded flow of one nozzle (fig. 6), $m^2$

$A_{e,int}$ nozzle exit area at shroud exit of one nozzle (fig. 6), $m^2$

$A_{eng}$ engine-tailpipe maximum cross-sectional area, $m^2$

$A_{max}$ maximum cross-sectional area of afterbody, $m^2$

$A_{seal}$ cross-sectional area enclosed by seal strip, $m^2$

$A_t$ throat area of one nozzle, $m^2$

$C_{D,a}$ drag coefficient of afterbody including force on nozzle-clearance annuli, $\frac{D_a}{q_\infty A_{max}}$

$C_{p,a}$ afterbody pressure coefficient, $\frac{p_a - p_\infty}{q_\infty}$

$D_a$ afterbody drag including drag on nozzle-clearance annuli, N

$d_{eng}$ diameter of engine tailpipe at maximum cross section, m

$d_{plug}$ maximum diameter of plug, m

$F_A$ total axial force (afterbody axial force plus nozzle-shroud axial force), positive downstream, $F_{A,a} + F_{A,n}$, N

$F_{A,a}$ afterbody axial force including axial force on nozzle-clearance annuli, N

$F_{A,bal}$ axial force measured by afterbody drag balance, positive downstream, N

$F_{A,n}$ nozzle-shroud axial force, N

$F_i$ ideal thrust for complete isentropic expansion of jet flow, $\dot{m}_j\sqrt{\frac{2\gamma}{\gamma - 1}RT_{t,j}\left[1 - \left(\frac{p_\infty}{p_{t,j}}\right)^{\frac{\gamma-1}{\gamma}}\right]}$, N

$F_j$ nozzle thrust, positive upstream, N

$\left(F_j - F_A\right)_{bal}$ jet thrust minus total axial force measured by thrust-minus-drag balance, positive upstream, N

| | |
|---|---|
| $F_{N,a}$ | afterbody normal force, positive up, N |
| H | afterbody height at maximum cross section (fig. 3), m |
| $h_1,h_2$ | height of afterbody interfairings (fig. 3), m |
| $l$ | length of model measured from model nose to dry-power shroud exit, m |
| $l_a$ | afterbody length measured from seal station (fig. 1), m |
| $l_p$ | plug length measured from nozzle throat (fig. 5), m |
| M | free-stream Mach number |
| $\dot{m}_j$ | measured mass-flow rate, kg/s |
| $p_a$ | afterbody static pressure, $N/m^2$ |
| $p_{ex}$ | external static pressure at seal station, $N/m^2$ |
| $p_i$ | internal static pressure, $N/m^2$ |
| $p_{plug}$ | plug static pressure, $N/m^2$ |
| $p_{t,j}$ | jet total pressure, $N/m^2$ |
| $p_\infty$ | free-stream static pressure, $N/m^2$ |
| $q_\infty$ | free-stream dynamic pressure, $N/m^2$ |
| R | gas constant ($\gamma$ = 1.4), 287.3 $\frac{N\text{-}m}{kg\text{-}K}$ |
| r | radius of engine nacelle (fig. 3), m |
| s | spacing distance between engine-nozzle center lines (fig. 3), m |
| $T_{t,j}$ | jet stagnation temperature, K |

| | |
|---|---|
| $x$ | axial distance from model nose, positive downstream, m |
| $x_p$ | axial distance from nozzle throat location on plug surface, positive downstream, m |
| $y$ | horizontal distance perpendicular to model center line, m |
| $y_1, y_2$ | afterbody interfairing y-dimensions, m |
| $z$ | vertical distance perpendicular to model center line, m |
| $z_1, z_2$ | afterbody interfairing z-dimensions, m |
| $\alpha$ | nominal angle of attack, positive nose up, deg |
| $\gamma$ | ratio of specific heats |

A bar over a symbol denotes an average condition.

## APPARATUS AND METHODS

### Wind Tunnel

The experimental investigation was conducted in the Langley 16-foot transonic tunnel which is a single-return, atmospheric tunnel with a slotted, octagonal test section and continuous air exchange. The tunnel has a continuously variable speed range from $M = 0.20$ to $M = 1.30$.

### Model and Support System

A sketch of the twin-jet afterbody model with dry-power nozzles installed is presented in figure 1 and a photograph of the model installed in the tunnel is shown in figure 2. The model is supported in the tunnel by a sting-supported strut (see fig. 2). The strut attaches to the model forebody and starts at the model nose as shown in figure 1. In the region near the model, the strut design is similar to the strut used for the investigation reported in reference 9. Appendix A presents a comparison of the data obtained on identical configurations utilizing these two different support systems.

The term "afterbody," as used in this paper, is the metric portion of the model (that portion of the model on which forces and moments are measured), not including the

nozzles, and starts at the model metric break or seal station (station 83.82). The seal station is indicated in the sketch of figure 1 and can be seen in the photograph shown in figure 2. A teflon strip inserted into grooves machined into the metric afterbody and nonmetric forebody was used as a seal to prevent internal flow in the model. The afterbody was attached to a drag balance which was attached in tandem to a thrust-minus-nozzle-drag balance. An annular clearance gap between the afterbody and nozzles was required to prevent fouling of the afterbody drag balance. This balance arrangement is discussed in more detail in reference 8.

To insure a turbulent boundary layer over the afterbody, a 0.38-cm-wide transition strip of No. 100 carborundum grit was fixed 5.72 cm from the model nose. The twin-engine simulator utilized a high-pressure air system, described in reference 8, to simulate the exhaust flow of a twin-jet configuration.

Two basic afterbody configurations, one close spaced and one wide spaced, in conjunction with several alternate engine interfairings were used in this investigation. Figure 3 presents sketches and geometry details of the afterbody and interfairing configurations. Two lateral spacings between engine-nozzle center lines ($s/d_{eng} = 1.12$ for close-spaced afterbody, $s/d_{eng} = 1.61$ for wide-spaced afterbody) were selected for the basic afterbodies. The close spacing was determined by the minimum practical clearance between parallel tailpipes, and the wide spacing was limited to the confines of the maximum model width. The basic afterbodies had engine interfairings which ended ahead of the nozzle at $x/l = 0.962$ and had no base. The alternate interfairings which attached directly to the afterbodies had reduced closure angles but ended with a base. The geometry of the two alternate interfairings investigated with each basic afterbody was identical with the exception of base location. The alternate 2 interfairing (so denoted to remain consistent with reference 9 which reported results at $\alpha = 0^{o}$) had a base at the dry-power nozzle exit (station $x/l = 1.0$); the short alternate 2 interfairing had a base at station $x/l = 0.962$. The basic afterbodies had identical longitudinal distributions of cross-sectional area, as shown in figure 4. Addition of the alternate interfairings to the basic afterbodies also results in identical cross-sectional area distributions. The area distribution of the basic afterbodies shown in figure 4, between $x/l = 0.62$ and $x/l = 0.97$, was calculated by a computer program for axisymmetric bodies adapted from reference 12 and is representative of a minimum wave-drag body at $M = 1.000001$ with the restraint of a given forebody geometry, afterbody length, base area, and an infinite cylindrical-base streamtube. Afterbody configurations with alternate interfairings represent a deviation from the theoretically obtained area distribution.

One additional interfairing was investigated on the wide-spaced afterbody. This interfairing extended downstream of the dry-power exits and was used to simulate engines

installed next to a fuselage wall. Appendix B presents pressure distributions obtained utilizing this configuration.

Sketches presenting the geometry of the cone plug nozzles are given in figure 5 and important geometric parameters are given in figure 6. Two power settings were investigated, one representing dry power and one representing maximum afterburner (abbreviated max A/B) power. The dry-power nozzles were investigated with and without shroud bases and had shroud boattail angles of $7^{\circ}$ and $9.1^{\circ}$, respectively. The nozzles were designed for use with air as a fluid medium ($\gamma = 1.4$). The ratio of max A/B power throat area to dry-power throat area was 2.5. Photographs of several afterbody-interfairing-nozzle configurations are shown in figure 7.

## Instrumentation

External static-pressure orifices were located on the afterbodies and interfairings at the locations indicated in figure 3. External static-pressure orifice locations on the nozzle plugs are shown in figure 5. Internal pressures were measured in the afterbody cavity at six internal orifice locations. The average external-seal static pressure was obtained from eight external orifices located on both sides of the seal gap between the forebody and afterbody. Four equal area-weighted total pressures and the stagnation temperature of the jet flow were measured in each tailpipe at locations indicated in figure 1.

Forces and moments on the metric portions of the model were measured by strain-gage balances. A three-component main balance was used to measure nozzle thrust minus afterbody and nozzle drag, and a five-component balance was used to measure afterbody forces and moments. An electronic turbine flowmeter was used to obtain the air mass-flow rate to the nozzles.

All data for both the model and wind-tunnel facility were recorded simultaneously on magnetic tape. Approximately 10 frames of data were taken over a time period of about 10 seconds for each data point; average values were used for computations.

## Tests

Data were obtained in the Langley 16-foot transonic tunnel at static conditions ($M = 0$) and at Mach numbers from 0.5 to 1.3. Reynolds number based on model length (134.71 cm) varied from approximately $1.23 \times 10^7$ at $M = 0.5$ to $1.66 \times 10^7$ at $M = 1.2$. The ratio of jet total pressure to free-stream static pressure was varied from approximately 1.0 (jet off) to about 9.0, depending on Mach number. Angle of attack was generally varied from $-2^{\circ}$ to $8.5^{\circ}$ with the jets off. Jet-on data were obtained at a nominal angle of attack of $0^{\circ}$ at all Mach numbers investigated and also at a nominal angle of attack of $6^{\circ}$ at $M = 0.8$ and 0.9.

## Data Reduction

The recorded data were used to compute standard force and pressure coefficients. The external-seal and internal pressure forces on the afterbodies were obtained by multiplying the difference between the average pressure (external-seal or internal) and free-stream static pressure by the affected projected area normal to the model axis.

Nozzle thrust minus total axial force (afterbody and nozzle axial force) was obtained directly by the thrust-minus-drag balance (see fig. 1). This performance term was computed as follows:

$$F_j - F_A = \left(F_j - F_A\right)_{bal} + \left(\bar{p}_{ex} - p_\infty\right)\left(A_{max} - A_{seal}\right) + \left(\bar{p}_i - p_\infty\right)A_{seal} \tag{1}$$

The forces sensed by the balance and included in the term $\left(F_j - F_A\right)_{bal}$ are nozzle thrust, external and internal axial forces on the nozzle shroud and plug, and afterbody external and internal axial forces transferred to the thrust-minus-drag balance through the tandem-mounted drag balance.

Afterbody drag was obtained directly from the tandem-mounted drag balance (see fig. 1) and computed from the following equations:

$$F_{A,a} = F_{A,bal} - \left(\bar{p}_{ex} - p_\infty\right)\left(A_{max} - A_{seal}\right) - \left(\bar{p}_i - p_\infty\right)\left(A_{seal} - 2A_{eng}\right) \tag{2}$$

$$D_a = F_{A,a} \cos \alpha + F_{N,a} \sin \alpha \tag{3}$$

Included in the afterbody-axial-force balance term $F_{A,bal}$ are external and internal axial forces on the afterbody shell (including base areas of afterbody and alternate interfairings). Included in the afterbody axial force $F_{A,a}$, but not felt by the balance term $F_{A,bal}$, is a pressure area term to account for the annuli between the afterbody and nozzles.

Thrust-minus-nozzle-axial-force performance is obtained by combining the two balance measurements as follows:

$$\begin{aligned} F_j - F_{A,n} &= \left(F_j - F_A\right) + F_{A,a} \\ &= \left(F_j - F_A\right)_{bal} + F_{A,bal} + \left(\bar{p}_i - p_\infty\right)\left(2A_{eng}\right) \end{aligned} \tag{4}$$

At static conditions (M = 0), this equation yields nozzle internal performance since nozzle (shroud) axial force is approximately zero with no external flow. However, at

Mach numbers other than zero, equation (4) includes nozzle-boattail axial force and external-flow effects on nozzle internal performance (effect of external flow on plug pressures).

## DISCUSSION

### Pressure Distributions

Afterbody pressures.- Typical pressure distributions on the engine interfairing (model center line) are shown in figures 8 and 9 for the dry-power and max A/B power nozzles, respectively. Data are shown for various jet total-pressure ratios at $M = 0.8$ and 1.2 for each configuration investigated. Additional interfairing pressure distributions for the basic and alternate 2 interfairing configurations are presented in reference 9. At $M = 0.8$, jet operation generally increased (in a positive direction) the interfairing pressure coefficients near the end of the afterbody for the basic interfairing configurations with dry-power nozzles installed and for all afterbody-interfairing configurations with max A/B power nozzles installed. The effect of jet operation on the pressure distributions of the alternate interfairing configurations with dry-power nozzles installed was mixed. Jet-interference effects were negligible at $M = 1.2$ except for the basic interfairing configurations, on which the interfairing pressures aft of station $x/l = 0.90$ were increased by jet operation. Small jet-interference effects were indicated at the most forward pressure orifice location (station $x/l = 0.717$) for several configurations at $M = 0.8$.

Figures 10, 11, and 12 present the effects of interfairing shape and nozzle power setting, angle of attack, and dry-power nozzle-shroud base area, respectively, on engine-interfairing pressure distributions. The effect of lateral spacing on interfairing pressures has been previously reported in reference 9.

The effect of interfairing shape on interfairing pressures, shown in figure 10 at total-pressure ratios typical of air-breathing engines, was found to be dependent on Mach number, nozzle lateral spacing, and nozzle power setting. Similar results were reported in reference 9.

Figure 11 presents the effects of varying angle of attack on the top-row interfairing pressure distributions with the jets off. For the close-spaced afterbody, increasing angle of attack generally increased the top-row interfairing pressure coefficients. One exception is shown at $x/l = 0.952$ for the basic interfairing configuration with dry-power nozzles installed (see fig. 11(a)). Unfortunately, this orifice was not good on the remaining close-spaced afterbody configurations, and thus it is not known what occurs for these configurations. Similarly, for the wide-spaced afterbody, increasing angle of attack

tended to slightly increase the pressures measured at the forward orifice locations; however, mixed results were obtained near the rear of the afterbody. Comparison of the pressure distributions obtained on the close-spaced and wide-spaced afterbodies shows that interfairing pressures on the wide-spaced afterbody were not so sensitive to varying angle of attack as on the close-spaced afterbody. An unusual trend with increasing angle of attack, probably associated with a boundary-layer instability, was observed at $M = 0.8$ for the wide-spaced afterbody, short alternate 2 interfairing configuration (see fig. 11(d)). With the dry-power nozzles installed, the pressure coefficients near the rear of the engine interfairing have two obvious levels; one level of pressure coefficient was obtained at $\alpha = -1.99^{\circ}$ and $0^{\circ}$ and a second, lower level was obtained at values of angle of attack greater than $0^{\circ}$. By comparing the interfairing pressure distributions at $M = 0.5$, 0.8, and 0.9 (see figs. 11(c), 11(d), and 11(e)), it can be seen that the pressure distributions obtained at $M = 0.8$, $\alpha = -1.99^{\circ}$ and $0^{\circ}$ are similar to those obtained at $M = 0.9$ whereas the pressure distributions obtained at $M = 0.8$, $\alpha > 0^{\circ}$ are similar to those obtained at $M = 0.5$. Since a rather large base is located immediately downstream ($x/l = 0.962$) of these pressure measurements, it might be expected that the jet-off afterbody drag could be affected with varying angle of attack and Mach number for this configuration. With the max A/B power nozzles installed, the pressure coefficients near the rear of the afterbody generally have the same level with the exception of $\alpha = 7.98^{\circ}$, which has a lower level.

The effect of the dry-power nozzle-shroud base area on the interfairing pressure coefficients is shown in figure 12. Shroud base area had little or no effect on the interfairing pressures except at the extreme rear of the interfairing where slightly higher pressures were measured with the modified dry-power nozzle (base removed).

It should be pointed out that although the previous results and discussion are indicative of various effects on the interfairing pressures, they do not necessarily indicate what happens to the pressures on the rest of the afterbody or to the base pressures on the alternate interfairings. Thus, afterbody drag may or may not have the trend expected when based on interfairing pressures.

Plug pressures.- The effects of angle of attack and dry-power nozzle-shroud base area on the nozzle-plug static-pressure distributions are shown in figures 13 and 14, respectively. Typical plug static-pressure distributions at several Mach numbers and jet total-pressure ratios for most configurations of this investigation have been reported previously in reference 9 and are not shown here. The pressure distributions shown in figures 13 and 14 are given in the form of a ratio of plug static pressure to jet total pressure $p_{plug}/p_{t,j}$; for convenience, values of $p_{\infty}/p_{t,j}$, which indicate whether the plug static pressures are greater or less than free-stream static pressure (i.e.,

$p_{plug}/p_{t,j} > p_\infty/p_{t,j}$ indicates $p_{plug} > p_\infty$, and vice versa), are shown as solid symbols. The geometric nozzle throat (minimum area) is located at plug station $x_p/l_p = 0$.

Angle of attack had no effect on the max A/B plug static-pressure distributions and only a small effect on the dry plug static-pressure distributions. This might be expected since the plug surface is shielded by the exhaust flow to a greater extent for the max A/B power nozzles than for the dry-power nozzles. Dry-power nozzle-shroud base area had little effect on the plug static-pressure distributions (see fig. 14).

## Performance Characteristics

Effect of angle of attack on jet-off afterbody drag.- Figure 15 presents the effect of angle of attack on jet-off afterbody drag coefficient. Data are shown for each configuration tested at Mach numbers of 0.5, 0.8, 0.9, and 1.2. Afterbody drag coefficient increased with increasing angle of attack for all configurations and Mach numbers investigated. A large, almost discontinuous, increase in afterbody drag coefficient is shown between $\alpha = 0^\circ$ and $\alpha = 2^\circ$ at $M = 0.8$ for the wide-spaced afterbody, short alternate 2 interfairing, dry-power nozzle configuration (see fig. 15(f)). These data, obtained from balance readings, are consistent with the interfairing-static-pressure-distribution data which were discussed previously (see fig. 11(d)) and are probably a result of a boundary-layer instability which appears to be tripped by varying angle of attack. A similar increase and, then, a decrease in afterbody drag coefficient is shown between $\alpha = 6^\circ$ and $\alpha = 8.4^\circ$ at $M = 0.8$ for the same configuration with max A/B power nozzles installed. In addition, by comparing the data at $M = 0.8$, $\alpha = 6^\circ$ obtained before (plain symbol) and after (flagged symbol) a jet total-pressure-ratio sweep, it can be seen that the boundary layer appears to be attached before the jet sweep but separated after the jet was turned off. Figure 16 presents the top interfairing static-pressure distributions for the two points just discussed. Although the difference in pressure levels shown in figure 16 is insufficient to account for the total drag shift shown in figure 15(f), these data do show that the interfairing pressure levels are shifted as indicated by the drag data.

With increasing Mach number, afterbody drag coefficient generally tends to increase or remain fairly constant, depending on configuration. One exception to this trend is again evident for the wide-spaced afterbody, short alternate 2 interfairing configuration and is again probably a result of a boundary-layer instability.

Effect of jet total-pressure ratio on afterbody drag.- Figures 17 to 20 present the variation of afterbody drag coefficient with jet total-pressure ratio for all test configurations and Mach numbers. Initial operation of the jet below choked conditions $\left(p_{t,j}/p_\infty < 1.89\right)$ generally reduced afterbody drag, particularly with the max A/B power

nozzles installed. After the initial effect of turning on the jet flow, afterbody drag generally tended to level out or increase slightly until some value of $p_{t,j}/p_\infty$ between 2.0 and 5.0 (depending on configuration) was reached; increasing $p_{t,j}/p_\infty$ above this value generally reduced afterbody drag. Noticeable exceptions to this trend were the alternate interfairing configurations with dry-power nozzles installed, particularly for the close-spaced afterbody. See figure 17(a), for example. For these configurations, initial jet operation caused an increase in afterbody drag, probably as a result of the jet-exhaust-flow pumping action on the large interfairing bases. Similar results were reported in reference 9 on the alternate 2 interfairing configurations. The short alternate 2 interfairing configurations were included in this investigation in order to determine the effect of moving the interfairing base upstream of the dry-power nozzle exits in an attempt to reduce the detrimental effect of the jet-exhaust-flow pumping action. In actuality, the data show that the reverse effect generally occurred (i.e., the detrimental jet-pumping effect was increased) and that the short alternate 2 interfairing configuration is not a viable solution to the detrimental jet-pumping effect. The highest jet-on afterbody drag, except for the close-spaced afterbody with dry-power nozzles installed where the highest drag was obtained with the alternate 2 interfairing, was generally obtained on the short alternate 2 interfairing configurations whereas the lowest jet-on afterbody drag was generally obtained on the basic interfairing configurations.

Static ($M = 0$) nozzle performance.- The variation of thrust-minus-nozzle-axial-force ratio with jet total-pressure ratio at $M = 0$ is shown in figure 21. Since these data were obtained at $M = 0$ and $\alpha = 0^\circ$, nozzle-shroud drag (axial force) should be essentially zero except for any jet-pumping effects which should be negligible. Hence, these data are a close approximation of static nozzle internal performance or gross thrust $F_j/F_i$. These data were faired with curves identical to those used in reference 9 for the same nozzle designs and indicate excellent agreement between these investigations for static nozzle internal performance.

Thrust-minus-nozzle-axial-force performance.- Figures 22 and 23 present the variation of thrust-minus-nozzle-axial-force ratio with jet total-pressure ratio for each configuration at nominal angles of attack of $0^\circ$ and $6^\circ$, respectively. Thrust minus nozzle axial force includes the gross nozzle thrust, the effect of an external stream and any interference effects on nozzle internal performance, and external nozzle axial force. Although the effect of an external stream on nozzle internal performance is negligible (for unseparated nozzle flow) for convergent and convergent-divergent nozzles like those presented in references 7 and 8, reference 10 indicates that this effect can be significant for cone plug nozzles.

For the dry-power nozzle configurations, large variations in thrust minus nozzle axial force were obtained with varying Mach number. These variations are attributable

to varying nozzle axial force and changes in nozzle internal performance. It should be noted that the basic interfairing configurations had higher thrust-minus-nozzle-axial-force performance at subsonic speeds than was obtained statically (M = 0). At low jet total-pressure ratios and at Mach numbers of 0.8 and 0.9, values greater than 1.0 were obtained and indicate negative nozzle axial force (thrust) and/or favorable external stream effects on nozzle internal performance. Similar results were reported in reference 9 on identical configurations mounted on a different support system. At M = 1.2, thrust minus nozzle axial force was significantly lower than obtained at subsonic speeds because of increased nozzle drag and/or detrimental effects of the external stream on nozzle internal performance.

The thrust-minus-nozzle-axial-force performance of the max A/B power nozzle configurations was relatively insensitive to changes in Mach number at subsonic speeds. The max A/B nozzle axial force should be very small and vary little with Mach number since the translating shroud was cylindrical in shape. Similarly, since the max A/B cone plug was collapsed and had little projected area when compared with the dry-power cone plug, the effect of Mach number on internal performance should be small.

Thrust-minus-total-axial-force performance.- The variation of thrust-minus-total-axial-force ratio with jet total-pressure ratio is presented in figures 24 and 25 for each configuration at nominal angles of attack of $0^{\circ}$ and $6^{\circ}$, respectively. Thrust minus total axial force is the configuration overall performance term and includes installed nozzle thrust, nozzle external axial force, and afterbody external axial force.

Thrust minus total axial force decreased with increasing Mach number, primarily because afterbody axial force increased with increasing Mach number. The effect of angle of attack on thrust minus nozzle axial force can be determined by comparing data from figures 22 and 23 and on thrust minus total axial force by comparing data from figures 24 and 25. However, the effect of angle of attack on performance is shown directly on a summary plot (fig. 29) and is discussed separately in a later section.

## Performance Characteristics at Typical Jet Total-Pressure Ratios for a Turbofan Engine

Turbofan-jet total-pressure-ratio schedule.- To simplify data analysis, data have been cross plotted at selected jet total-pressure ratios. Figure 26 presents the variation of a typical (maximum dry power) schedule of turbofan-engine total-pressure ratio with Mach number, which was used for comparison purposes in this investigation. Although any trends and conclusions arrived at by using this particular schedule of $p_{t,j}/p_{\infty}$ as a function of M would generally be true for other schedules not too greatly different, the absolute levels of data plotted in the following cross plots would vary slightly.

Effect of nozzle power setting and alternate interfairings.- Figure 27 presents the variation of afterbody drag coefficient, thrust-minus-nozzle-axial-force ratio, and thrust-minus-total-axial-force ratio with Mach number at the scheduled values of $p_{t,j}/p_\infty$ from figure 26. The effect of the alternate interfairings is shown directly, whereas an examination of the left and right sides of each plot gives a comparison of the dry-power and max A/B power nozzles.

Installation of the alternate interfairings, alternate 2 and short alternate 2, to the basic afterbodies generally increased $C_{D,a}$, decreased $(F_j - F_{A,n})/F_i$, and decreased $(F_j - F_A)/F_i$. The effect of the alternate interfairings on the performance of the dry-power nozzle configurations was significant but was generally small for the max A/B power nozzle configurations. The detrimental effects of the short alternate 2 interfairing were always larger than for the alternate 2 interfairing, with exception of the close-spaced afterbody, dry-power nozzle configuration.

Comparison of the left and right sides of each figure indicates that changing the nozzle power setting from dry power to max A/B power generally decreases $C_{D,a}$ and increases $(F_j - F_A)/F_i$, particularly for $M > 0.5$. Several reasons for this performance gain can be given. First, the max A/B power nozzles are designed for operation at higher $p_{t,j}/p_\infty$ than the dry-power nozzles such that nozzle internal performance increases with increasing Mach number. Second, since the max A/B power nozzles are cylindrical in shape, nozzle pressure drag is essentially zero. Third, a strong compression at the afterbody-nozzle juncture tends to increase the afterbody pressures and thus decreases afterbody drag (see fig. 10).

Comparison of all configurations shown in figure 27 shows that the highest overall performance was always obtained with the close-spaced afterbody, basic interfairing configuration.

Effect of nozzle lateral spacing.- The variation of $C_{D,a}$, $(F_j - F_{A,n})/F_i$, and $(F_j - F_A)/F_i$ with nozzle lateral spacing is shown in figure 28. This figure is a cross plot of data at the scheduled jet total-pressure ratio for each Mach number. Each line shown in this figure is faired through two data points and, hence, the variation of data with spacing ratio may not be linear as shown.

Overall performance $(F_j - F_A)/F_i$ decreased with increased nozzle lateral spacing for all configurations and test conditions investigated with exception of the alternate 2 interfairing configuration with dry-power nozzles installed. Overall performance of this configuration increased with increased nozzle lateral spacing, probably resulting from reduced jet exhaust pumping on the interfairing base. Similar results were reported in reference 9 for this configuration.

The largest effect of nozzle lateral spacing on performance occurred on the short alternate 2 interfairing configuration with dry-power nozzles installed. A significant reduction in performance of this configuration occurred with increased nozzle lateral spacing, primarily because of a large increase in afterbody drag.

Effect of angle of attack.- The variation of $C_{D,a}$, $(F_j - F_{A,n})/F_i$, and $(F_j - F_A)/F_i$ with angle of attack at scheduled $p_{t,j}/p_\infty$ at each Mach number is shown in figure 29 in the form of a bar chart. Each set of two bars represents a distinct configuration; the first bar of each set presents data at a nominal angle of attack of $0^\circ$, and the second bar of each set presents data at a nominal angle of attack of $6^\circ$. The effect of alternate interfairings and nozzle power settings on performance can also be readily determined from this figure but are not discussed here since they have been presented previously at $\alpha = 0^\circ$. However, it can be noted from figure 29 that the trends did not change appreciably at $\alpha = 6^\circ$ and thus appear to be reasonably independent of angle of attack.

Increasing angle of attack increased $C_{D,a}$ and decreased overall performance $(F_j - F_A)/F_i$ for all configurations and conditions tested. Angle of attack had only a small effect on $(F_j - F_{A,n})/F_i$. The detrimental effect of increased angle of attack on performance was generally larger for the dry-power nozzle configurations (as much as 3 percent of $F_i$) than for the max A/B power nozzle configurations (generally less than 1 percent of $F_i$).

Effect of dry-power nozzle-shroud base area.- Figure 30 presents the effect of shroud base area on $C_{D,a}$, $(F_j - F_{A,n})/F_i$, and $(F_j - F_A)/F_i$ as a function of Mach number. Data were obtained for the wide-spaced afterbody, basic interfairing configuration at $\alpha = 0^\circ$ only. Although a slight decrease in overall performance $(F_j - F_A)/F_i$ is shown for the dry-power nozzle with shroud base removed, the effect is generally small (less than 1 percent of $F_i$). This result is consistent with the nozzle-plug static-pressure distributions presented in figure 14.

## CONCLUSIONS

An investigation of the effect of nozzle lateral spacing, engine interfairing shape, and angle of attack on the drag and performance of twin-jet afterbodies utilizing two nozzle power settings of translating shroud cone plug nozzles was conducted at Mach numbers of 0 and 0.5 to 1.3. The jet total-pressure ratio was varied from jet off to approximately 9.0, depending on Mach number and nozzle power setting. Two lateral spacings of the nozzle exits were tested with two afterbodies having identical normal cross-sectional area distributions when either the basic or alternate interfairings were installed.

At scheduled jet total-pressure ratios assumed for a turbofan engine, the following results are indicated:

1. Increased nozzle lateral spacing generally decreased the overall performance parameter (thrust minus total axial force) regardless of Mach number, angle of attack, or nozzle power setting. One exception was noted with the basic-length alternate interfairing and dry-power nozzles installed; increased nozzle lateral spacing increased overall performance.

2. Installation of alternate interfairings (one of basic length and one reduced in length) with large flat bases increased afterbody drag coefficient and decreased overall performance at all test conditions, especially for the dry-power nozzle configurations.

3. Increasing angle of attack increased afterbody drag coefficient and decreased overall performance for all configurations and conditions tested.

4. Removing the dry-power nozzle-shroud base area had little effect on performance (less than 1 percent of ideal thrust).

5. The highest overall performance was obtained with the close-spaced afterbody with basic interfairing (no base).

Langley Research Center,
National Aeronautics and Space Administration,
Hampton, Va., April 9, 1973.

## APPENDIX A

## COMPARISON OF DATA OBTAINED ON TWIN-JET AFTERBODY MODELS UTILIZING TWO DIFFERENT SUPPORT SYSTEMS

The pressure and force data presented in this report were obtained from models supported in the wind tunnel by a sting-mounted-strut support system which allowed variation in angle of attack. Several configurations, identical to those reported herein, were also tested previously (see ref. 9) and were supported in the wind tunnel by a fixed $(\alpha = 0^{\circ})$ floor-mounted-strut support system. Figure 31 presents sketches showing the geometry of these two different model support systems. This appendix presents a comparison of pressure and force data, at $\alpha = 0^{\circ}$, obtained on identical configurations but utilizing different model support systems.

### Pressure Data

Figure 32 presents the static-pressure distributions on the afterbody top center line for several different configurations mounted on the support systems shown in figure 31. The effect of the support system on the afterbody (top) pressure coefficients was generally small. The sting-mounted strut generally tended to produce slightly higher pressure coefficients on the model afterbody than the floor-mounted strut. The effect of the support system on the afterbody bottom center-line pressure coefficients is shown in figure 33 at two $x/l$ stations as a function of Mach number. The afterbodies had only two static-pressure orifices on the bottom surface and they were located at $x/l$ stations of 0.717 and 0.849. The effect of the support system was more pronounced on the afterbody bottom-surface pressure coefficients than was observed on the top surface (see fig. 32). This might be expected since the bottom-surface orifices are washed by the strut wake. The highest afterbody pressure coefficients (bottom center line) were obtained on models utilizing the sting-supported-strut support system. The effect of the support system on afterbody pressure coefficients was greater at station $x/l = 0.717$ than at station $x/l = 0.849$, probably as a result of the proximity to the strut for station $x/l = 0.717$.

### Performance Characteristics

The variation of $C_{D,a}$, $(F_j - F_{A,n})/F_i$, and $(F_j - F_A)/F_i$ with Mach number is presented in figure 34 for several configurations mounted on two different support systems at $\alpha = 0^{\circ}$. These data are shown for the scheduled values of $p_{t,j}/p_{\infty}$ presented previously in figure 26. The effect of the two support systems on $C_{D,a}$, $(F_j - F_{A,n})/F_i$,

and $(F_j - F_A)/F_i$ was generally small, particularly for the max A/B power nozzle configurations. The largest difference in the overall performance term $(F_j - F_A)/F_i$ was observed for the close-spaced afterbody, alternate 2 interfairing, dry-power nozzle configuration at $M = 0.5$ and was equal to 2.5 percent of the ideal thrust. The sting-mounted-strut support system generally produced lower afterbody drag, lower thrust-minus-nozzle-axial-force (drag) ratio, and lower thrust-minus-total-axial-force (drag) ratio than the floor-mounted-strut support system.

In summary, the differences in pressure and force measurements obtained on models utilizing the two different support systems shown in figure 31 are generally small, and the trends of both sets of data are similar. Thus, although small differences exist in the absolute pressure and force measurements shown in this report and in reference 9, the trends and conclusions presented appear to be unaffected by the support system.

## APPENDIX B

## EFFECT OF CONE-PLUG-NOZZLE EXHAUST FLOW ON A SIMULATED FUSELAGE SIDE

An additional configuration was tested during the present investigation to determine the effect of plug-nozzle exhaust flow on the static-pressure distributions of a fuselage surface located adjacent to a cone plug nozzle. Similarly, this configuration was used to study the effect of an adjacent fuselage surface on the nozzle-plug static-pressure distributions. The configuration consisted of a long, slab-sided interfairing mounted on the wide-spaced afterbody and utilized the modified dry-power nozzles (base removed). Figure 35 presents a sketch of the simulated fuselage configuration showing important dimensions and orifice locations, and photographs of the configuration mounted in the wind tunnel are shown in figure 36. (Location of the static-pressure orifices on the cone-plug surface was shown in fig. 5(a).) Because of the added restraints from additional pressure tubing, force data were not obtained on this configuration; and because of the additional loads, angle of attack was limited to $0^{\circ}$.

### Fuselage Static-Pressure Distributions

The longitudinal static-pressure distributions on the simulated fuselage are shown in figure 37 for several values of Mach number and jet total-pressure ratio. As might be expected for surfaces adjacent to nozzle exhaust flow, jet-interference effects (difference between jet off and jet on) were significant; the smallest jet-interference effects were obtained on the fuselage top surface (row 1) for $p_{t,j}/p_{\infty} < 6.0$. The pressures on the fuselage fairing ahead of the nozzle exits (row 2) generally recovered to positive values of pressure coefficient at subsonic Mach numbers. The pressure coefficients on the slab side of the simulated fuselage (rows 3 to 5) show large variations with jet total-pressure ratio and longitudinal location. These large variations are probably a result of the series of expansions and compressions going on inside the exhaust-flow core and also of the local three-dimensional channel-flow characteristics between the exhaust-flow plume and the fuselage side.

### Isobaric Contours

Figure 38 presents isobaric contours on the simulated fuselage side for several different jet total-pressure ratios at Mach numbers of 0.5 and 1.2. These contours were obtained by a linear interpolation between pressure orifices and were machine plotted. It should be noted the symbols shown in this figure do not represent static-pressure orifice locations (see fig. 35) but are machine-calculated intercept points of constant

pressure coefficient on rows 1, 3, 4, and 5. Examination of this figure gives some insight into the effect of increasing jet total-pressure ratio on the fuselage static pressures. For example, at $M = 0.5$, the high pressure region (solid symbols) centered at $x/l = 1.048$ for $p_{t,j}/p_\infty = 1.40$ tends to move downstream and grow larger with increasing jet total-pressure ratio; also, a second high pressure region forms downstream of the first at the higher values of $p_{t,j}/p_\infty$. At $M = 1.2$, a high pressure region forms near the end of the plug and tends to intensify with increasing $p_{t,j}/p_\infty$. Also, at $M = 1.2$, a severe change in the flow pattern occurs between $p_{t,j}/p_\infty = 2.93$ and $p_{t,j}/p_\infty = 5.02$. Unfortunately, additional jet total-pressure ratios in this range were not obtained.

## Plug Static-Pressure Distributions

The effect of the simulated fuselage on the modified dry-power (base removed) nozzle-plug static-pressure distributions is shown in figure 39 for several Mach numbers and jet total-pressure ratios. The plain symbols show data with the simulated fuselage off and the flagged symbols show data with the simulated fuselage on. The left-hand side of each plot shows data from the left plug (orifices on top) and the right-hand side shows data on the right plug (orifices on inside surface toward simulated fuselage). As can be noted from this figure, the adjacent fuselage did affect the plug static-pressure distributions; the magnitude of this effect was generally small at $M = 0.5$ and tended to increase with increasing Mach number. As might be expected from the proximity of the orifice locations to the fuselage side, the static pressures on the inside surface of the plug (right plug) were affected by the adjacent fuselage more than the static pressures on the top surface of the plug (left plug). It should be noted that at $M = 1.2$, the adjacent fuselage caused a severe overexpansion of the exhaust flow on the plug surface (right plug, $p_{t,j}/p_\infty \leq 5.03$); this result is similar to that discussed in references 10 and 11. Although force measurements were not made on this configuration, it can be inferred from the plug static-pressure measurements shown that an adjacent fuselage surface would have a significant impact on plug-nozzle internal performance.

## REFERENCES


1. Schmeer, James W.; Lauer, Rodney F., Jr.; and Berrier, Bobby L.: Performance of Blow-in-Door Ejector Nozzles Installed on a Twin-Jet Variable-Wing-Sweep Fighter Airplane Model. NASA TM X-1383, 1967.

2. Mercer, Charles E.; and Berrier, Bobby L.: Effect of Afterbody Shape, Nozzle Type, and Engine Lateral Spacing on the Installed Performance of a Twin-Jet Afterbody Model. NASA TM X-1855, 1969.

3. Berrier, Bobby L.; and Maiden, Donald L.: Effect of Nozzle-Exhaust Flow on the Longitudinal Aerodynamic Characteristics of a Fixed-Wing, Twin-Jet Fighter Airplane Model. NASA TM X-2389, 1971.

4. Runckel, Jack F.: Jet-Exit and Airframe Interference Studies on Twin-Engine-Fuselage Aircraft Installations. NASA TM X-1274, 1966.

5. Corson, Blake W., Jr.; and Runckel, Jack F.: Exploratory Studies of Aircraft Afterbody and Exhaust-Nozzle Interaction. NASA TM X-1925, 1969.

6. Lee, Edwin E., Jr.; and Runckel, Jack F.: Performance of Closely Spaced Twin-Jet Afterbodies With Different Inboard-Outboard Fairing and Nozzle Shapes. NASA TM X-2329, 1971.

7. Maiden, Donald L.; and Runckel, Jack F.: Effect of Nozzle Lateral Spacing on Afterbody Drag and Performance of Twin-Jet Afterbody Models With Convergent Nozzles at Mach Numbers up to 2.2. NASA TM X-2099, 1970.

8. Pendergraft, Odis C., Jr.; and Schmeer, James W.: Effect of Nozzle Lateral Spacing on Afterbody Drag and Performance of Twin-Jet Afterbody Models With Convergent-Divergent Nozzles at Mach Numbers up to 2.2. NASA TM X-2601, 1972.

9. Berrier, Bobby L.: Effect of Nozzle Lateral Spacing on Afterbody Drag and Performance of Twin-Jet Afterbody Models With Cone Plug Nozzles at Mach Numbers up to 2.20. NASA TM X-2632, 1972.

10. Berrier, Bobby L.: Effect of Plug and Shroud Geometry Variables on Plug-Nozzle Performance at Transonic Speeds. NASA TN D-5098, 1969.

11. Rabone, George R.: Low-Angle Plug Nozzle Performance Characteristics. AIAA Paper No. 66-664, June 1966.

12. Harris, Roy V., Jr.: An Analysis and Correlation of Aircraft Wave Drag. NASA TM X-947, 1964.

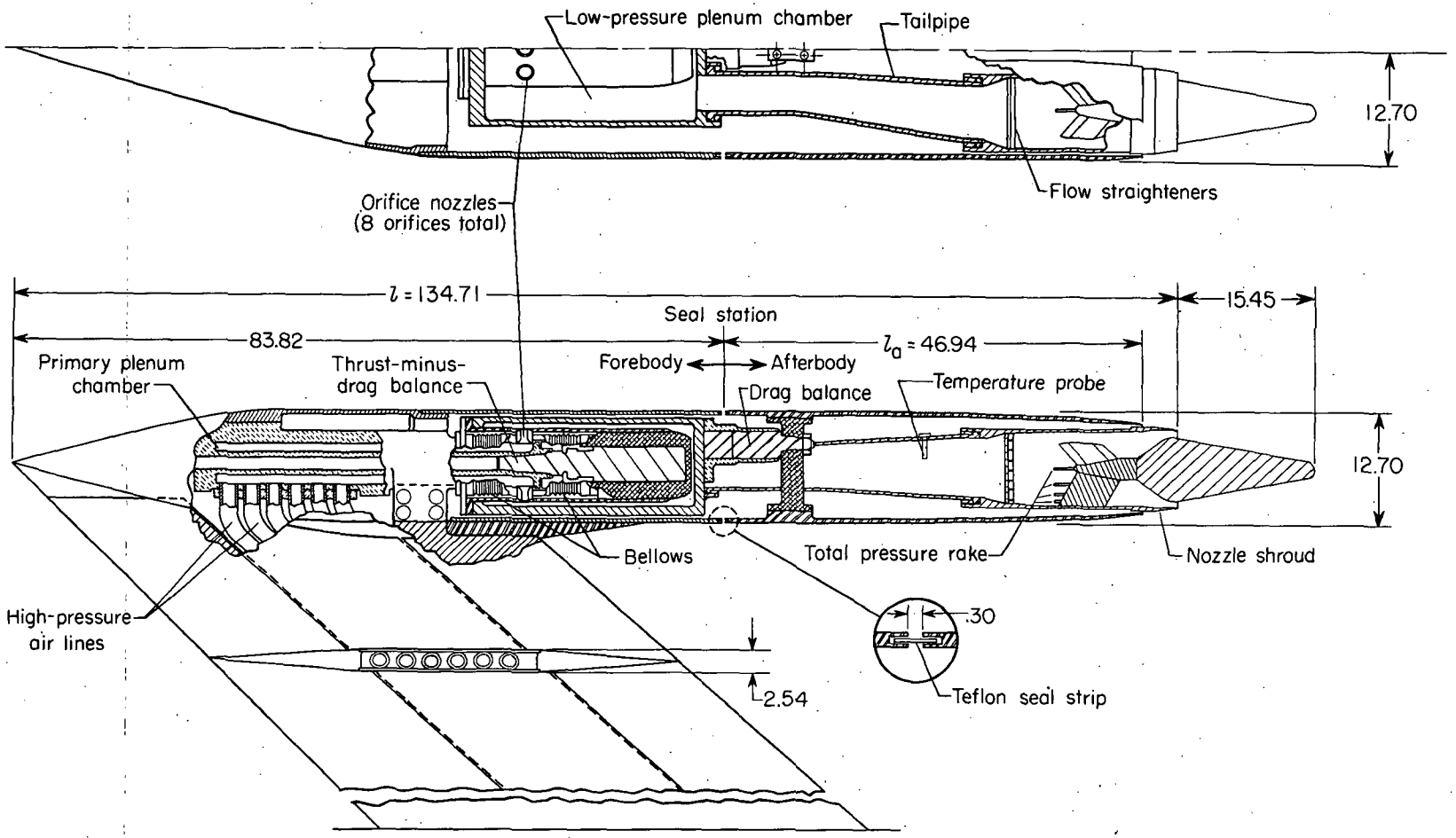


Figure 1.- Sketch of air-powered twin-jet model with dry-power plug nozzles installed. All dimensions are in centimeters.

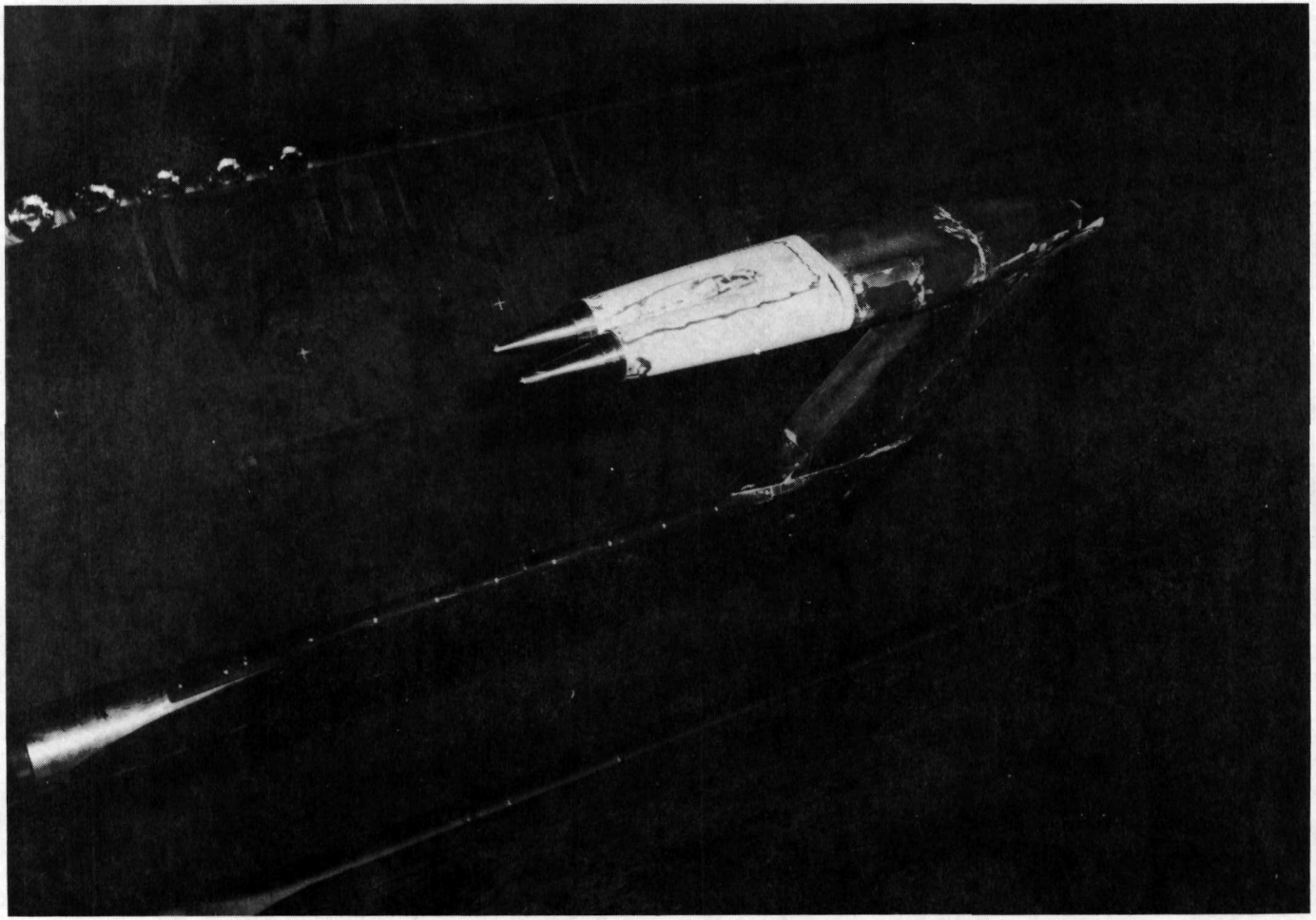

L-72-3847

Figure 2.- Photograph of twin-jet model mounted in the Langley 16-foot transonic tunnel.

| Afterbody geometry | | | | | Orifice location | |
|---|---|---|---|---|---|---|
| x/l | s/2H | r/H | $h_1/H$ | $h_2/H$ | Top | Bottom |
| 0.623 | 1.000 | 1.000 | 1.000 | 1.000 | | |
| .679 | .988 | .988 | .976 | .988 | | |
| .717 | .972 | .972 | .944 | .972 | X | X |
| .754 | .960 | .952 | .884 | .952 | | |
| .792 | .948 | .926 | .830 | .926 | X | |
| .849 | .930 | .880 | .720 | .880 | X | X |
| .877 | | | | | X | |
| .886 | .896 | .852 | .630 | .852 | | |
| .896 | | | | | X | |
| .915 | | | | | X | |
| .924 | .860 | .820 | .460 | .820 | | |
| .933 | | | | | X | |
| .952 | | | | | X | |
| .962 | .822 | .778 | 0 | .778 | | |
| .971 | .820 | .760 | —— | .760 | | |
| .999 | —— | —— | —— | .684 | | |

Note: Values of h/H for the short alternate 2 interfairing are identical to those for the alternate 2 interfairing up to $x/l = 0.962$ where the short alternate 2 interfairing ends with a flat base.

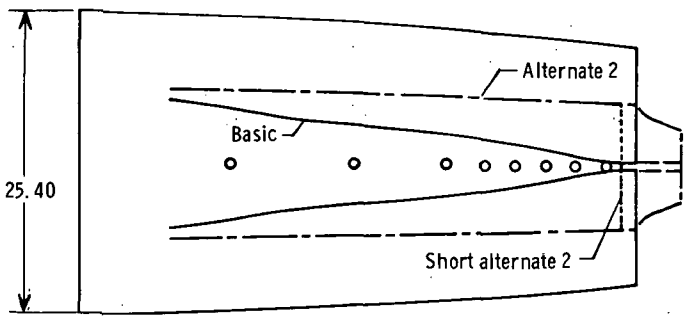


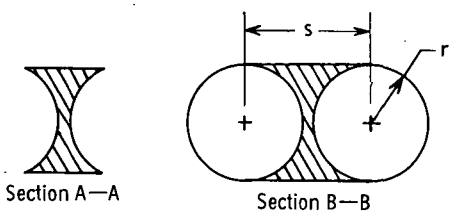


Cross sections show alternate interfairings only

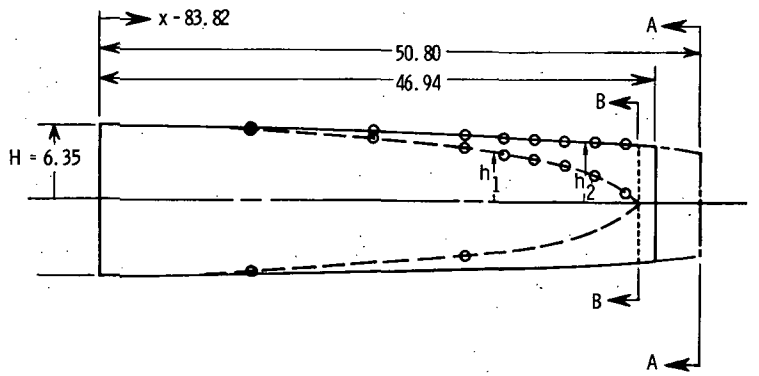


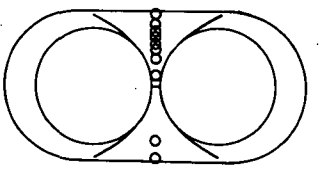

Note: Alternate interfairings have orifices on top only.

(a) Close-spaced afterbody.

Figure 3.- Sketch of afterbodies and alternate interfairings showing important dimensions and orifice locations. All dimensions are in centimeters.

| Afterbody geometry | | | | | Orifice location | |
|---|---|---|---|---|---|---|
| x/l | s/2H | r/H | $h_1/H$ | $h_2/H$ | Top | Bottom |
| 0.623 | 1.000 | 1.000 | 1.000 | 1.000 | | |
| .679 | 1.012 | .988 | .944 | .960 | | |
| .717 | 1.028 | .972 | .860 | .908 | X | X |
| .754 | 1.048 | .952 | .740 | .834 | | |
| .792 | 1.074 | .926 | .634 | .768 | X | |
| .849 | 1.120 | .880 | .416 | .646 | X | X |
| .877 | | | | | X | |
| .886 | 1.148 | .852 | .256 | .544 | | |
| .896 | | | | | X | |
| .915 | | | | | X | |
| .924 | 1.180 | .820 | .106 | .444 | | |
| .933 | | | | | X | |
| .952 | | | | | X | |
| .962 | 1.182 | .778 | 0 | .380 | | |
| .971 | 1.180 | .760 | —— | .380 | | |
| .999 | —— | —— | —— | .362 | | |

Note: Values of h/H for the short alternate 2 interfairing are identical to those for the alternate 2 interfairing up to x/l = 0.962 where the short alternate 2 interfairing ends with a flat base.

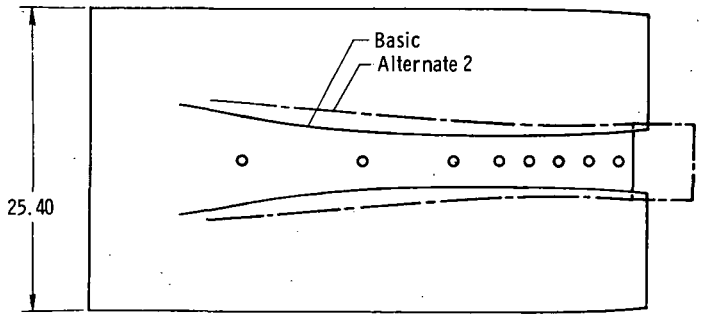


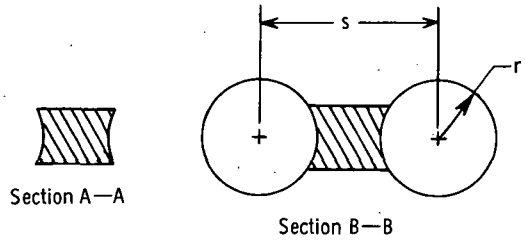


Cross sections show alternate interfairings only

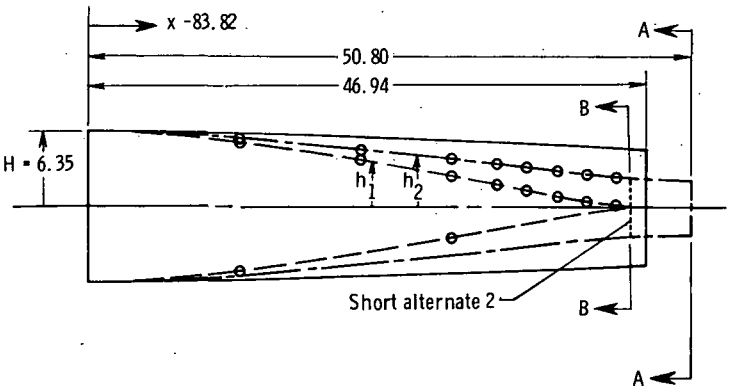


Note: Alternate interfairings have orifices on top only.

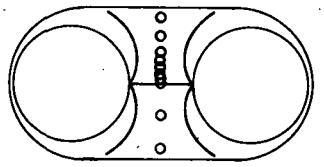

(b) Wide-spaced afterbody.

Figure 3.- Concluded.

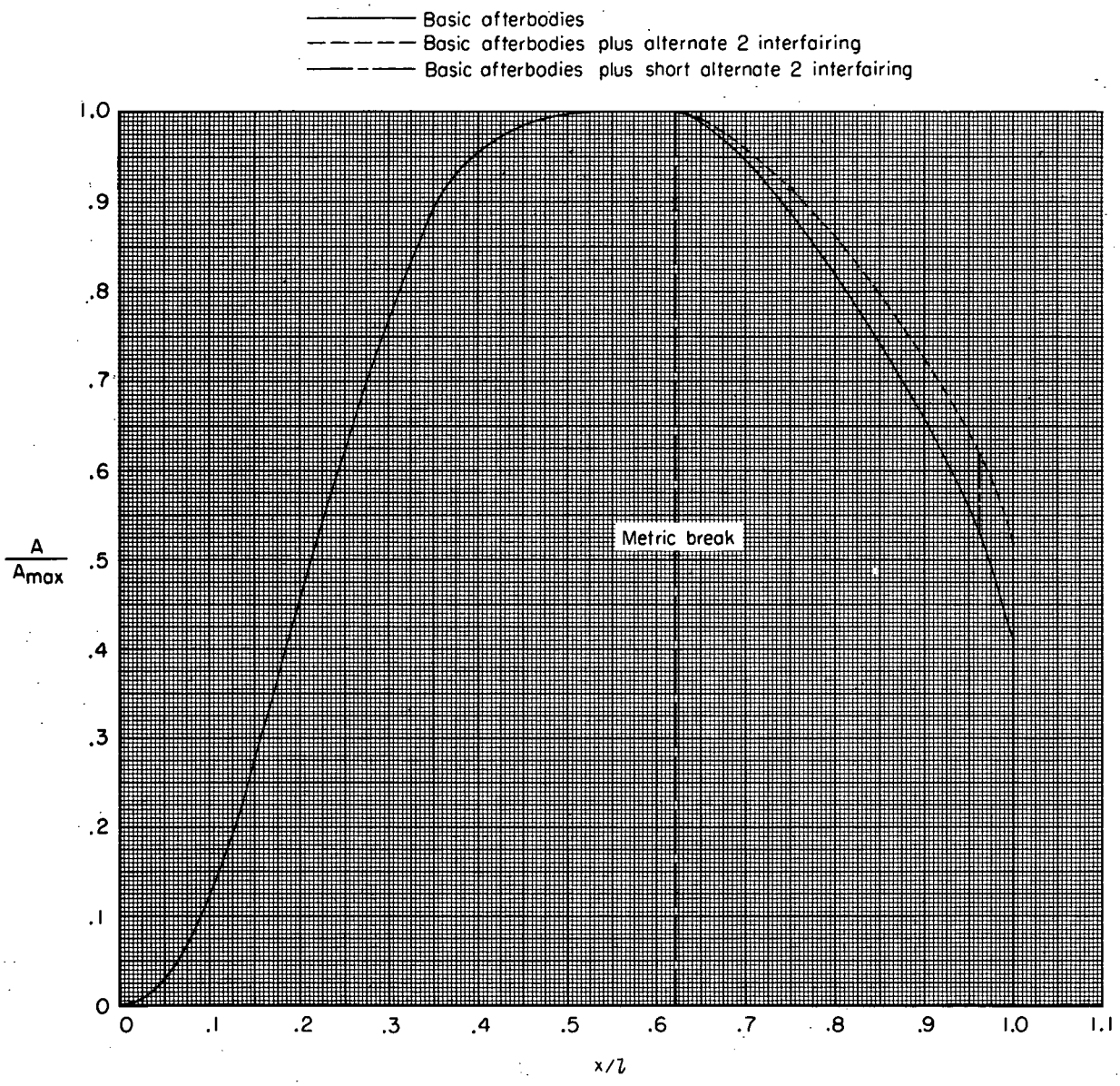


Figure 4.- Area distributions of twin-jet afterbody configurations with dry-power nozzles. Boattail angle of $7^{o}$; $A_{max} = 287.90\ cm^2$.

| Orifice locations | | | |
|---|---|---|---|
| $x_p/l_p$ | Row 1 | Row 2 | Row 3 |
| -0.025 | | X | |
| 0 | X | X | X |
| .082 | X | X | |
| .164 | X | X | |
| .327 | X | X | X |
| .409 | | X | |
| .491 | X | X | |
| .572 | | X | |
| .654 | X | | X |
| .736 | | X | |
| .818 | X | | |
| .899 | | X | |
| .970 | | X | |
| 1.000 | X | X | X |

Note: Rows 1 and 3 are on left-hand plug looking upstream.
Row 2 is on right-hand plug looking upstream.

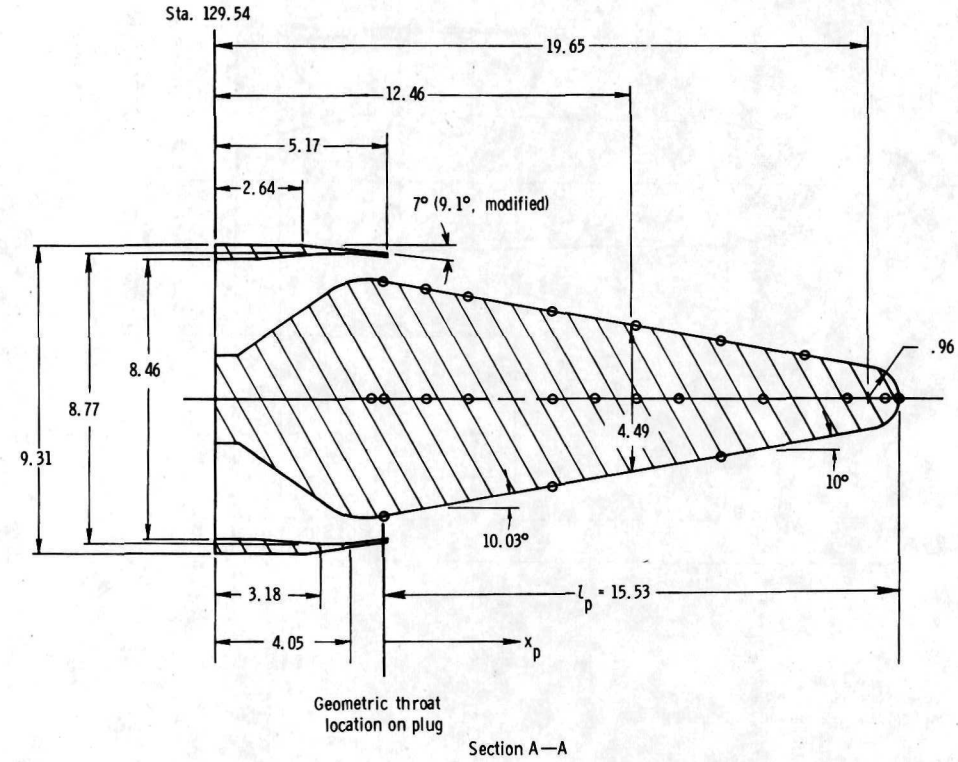


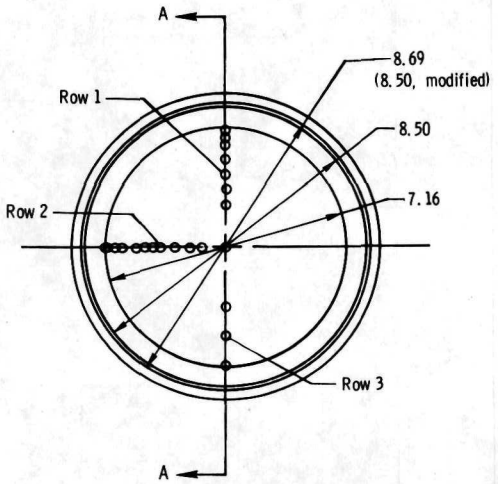


(a) Dry-power nozzles.

Figure 5.- Sketch of nozzle configurations showing important dimensions and orifice locations. All dimensions are in centimeters.

| Orifice locations | | | |
|---|---|---|---|
| $x_p/l_p$ | Row 1 | Row 2 | Row 3 |
| -0.040 | | X | |
| 0 | X | X | X |
| .089 | X | X | |
| .170 | X | X | |
| .332 | X | X | X |
| .413 | | X | |
| .495 | X | X | |
| .576 | | X | |
| .657 | X | | X |
| .738 | | X | |
| .819 | X | | |
| .901 | | X | |
| .966 | | X | |
| 1.000 | X | X | X |

Note: Rows 1 and 3 are on left-hand plug looking upstream.
Row 2 is on right-hand plug looking upstream.

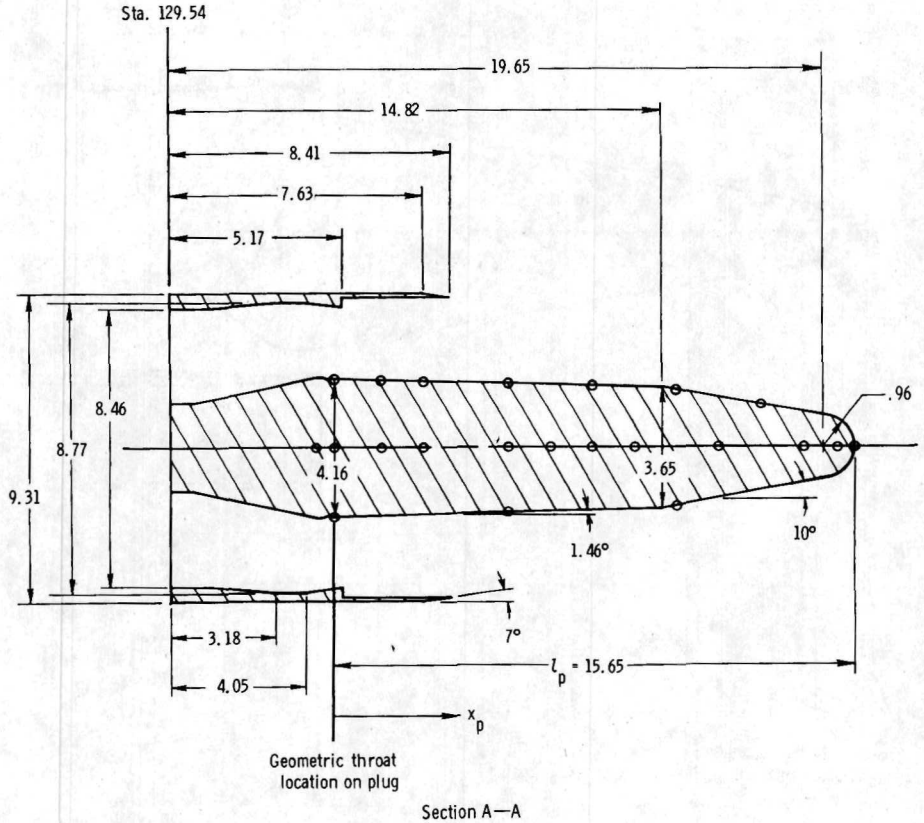


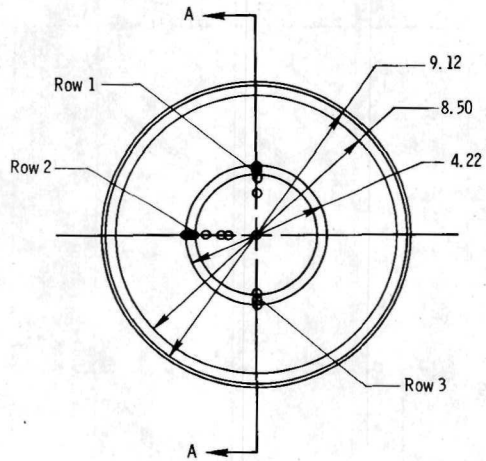


(b) Max A/B power nozzles.

Figure 5.- Concluded.

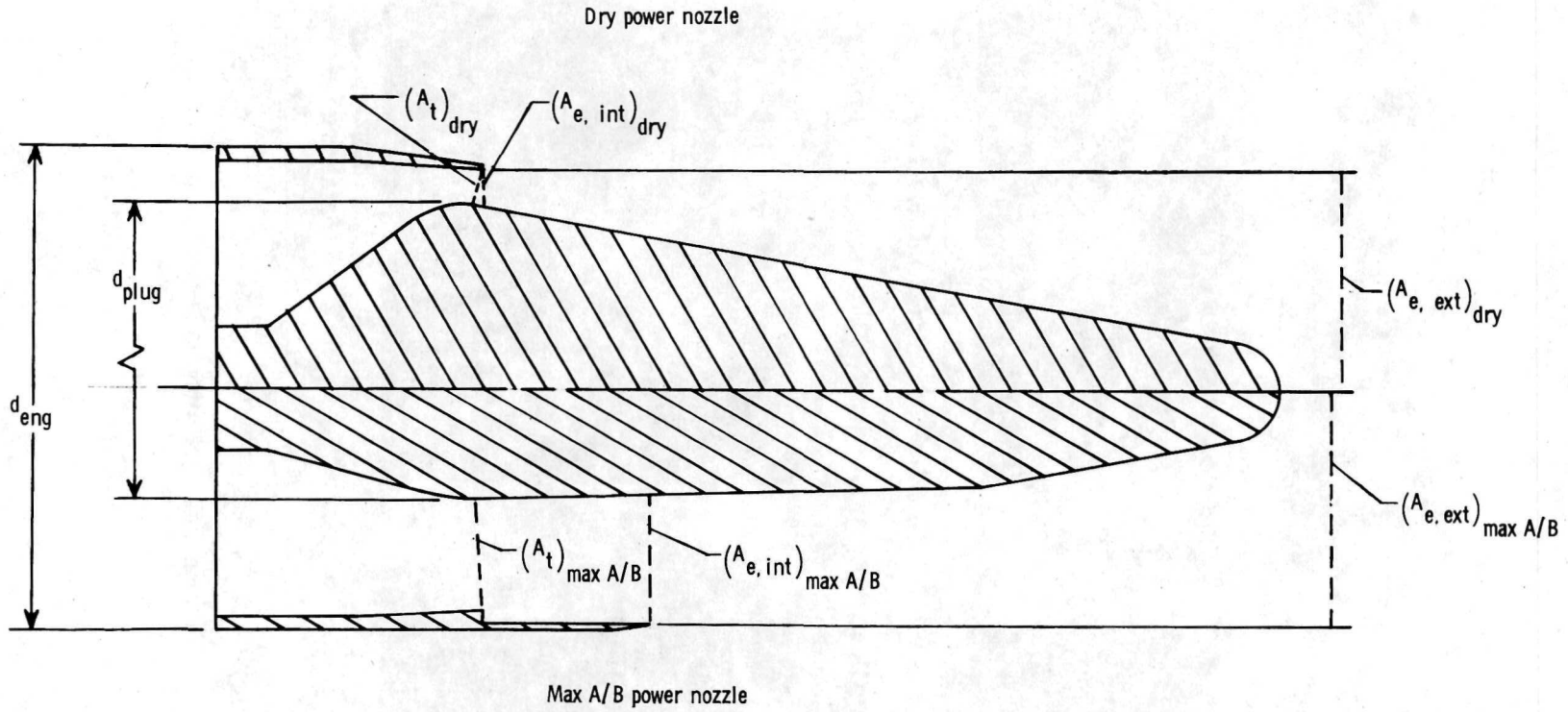


| Geometric parameters | | | | | |
|---|---|---|---|---|---|
| Nozzle power setting | $A_t$, $cm^2$ | $d_{plug}/d_{eng}$ | $A_t/A_{eng}$ | $A_{e,\ int}/A_t$ | $A_{e,\ ext}/A_t$ |
| Dry | 17.277 | 0.769 | 0.254 | 1.016 | 3.283 |
| Max A/B | 43.200 | .453 | .635 | 1.217 | 1.511 |

Figure 6.- Important geometric parameters of nozzle configurations.

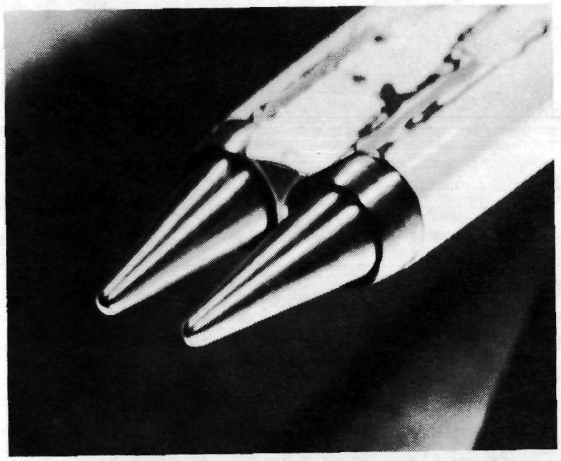

Dry power nozzles, alternate 2 interfairing

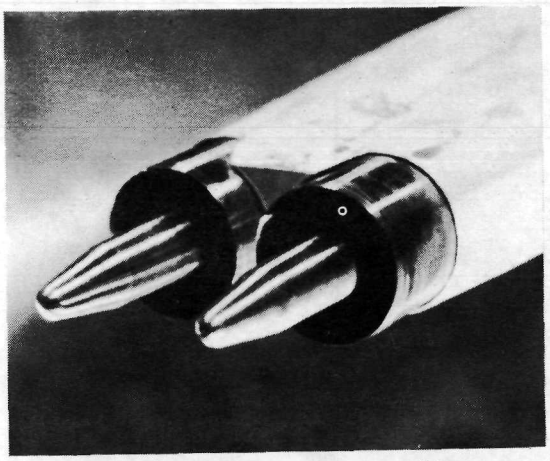

Max A/B power nozzles, alternate 2 interfairing

(a) Close-spaced afterbody.

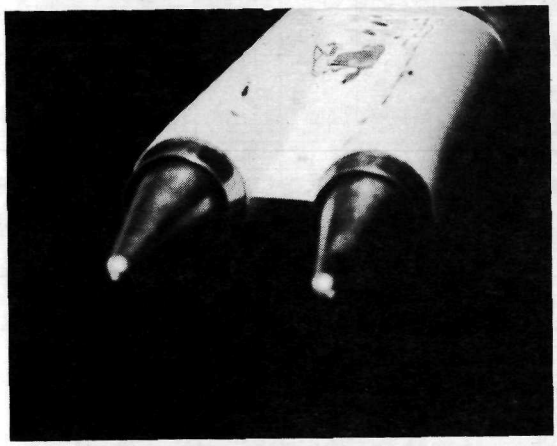

Dry power nozzles, basic interfairing

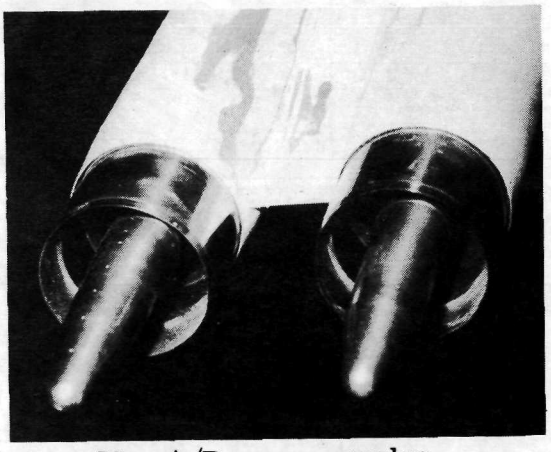

Max A/B power nozzles, basic interfairing

L-73-3031

(b) Wide-spaced afterbody.

Figure 7.- Photographs of several twin-jet afterbody configurations.

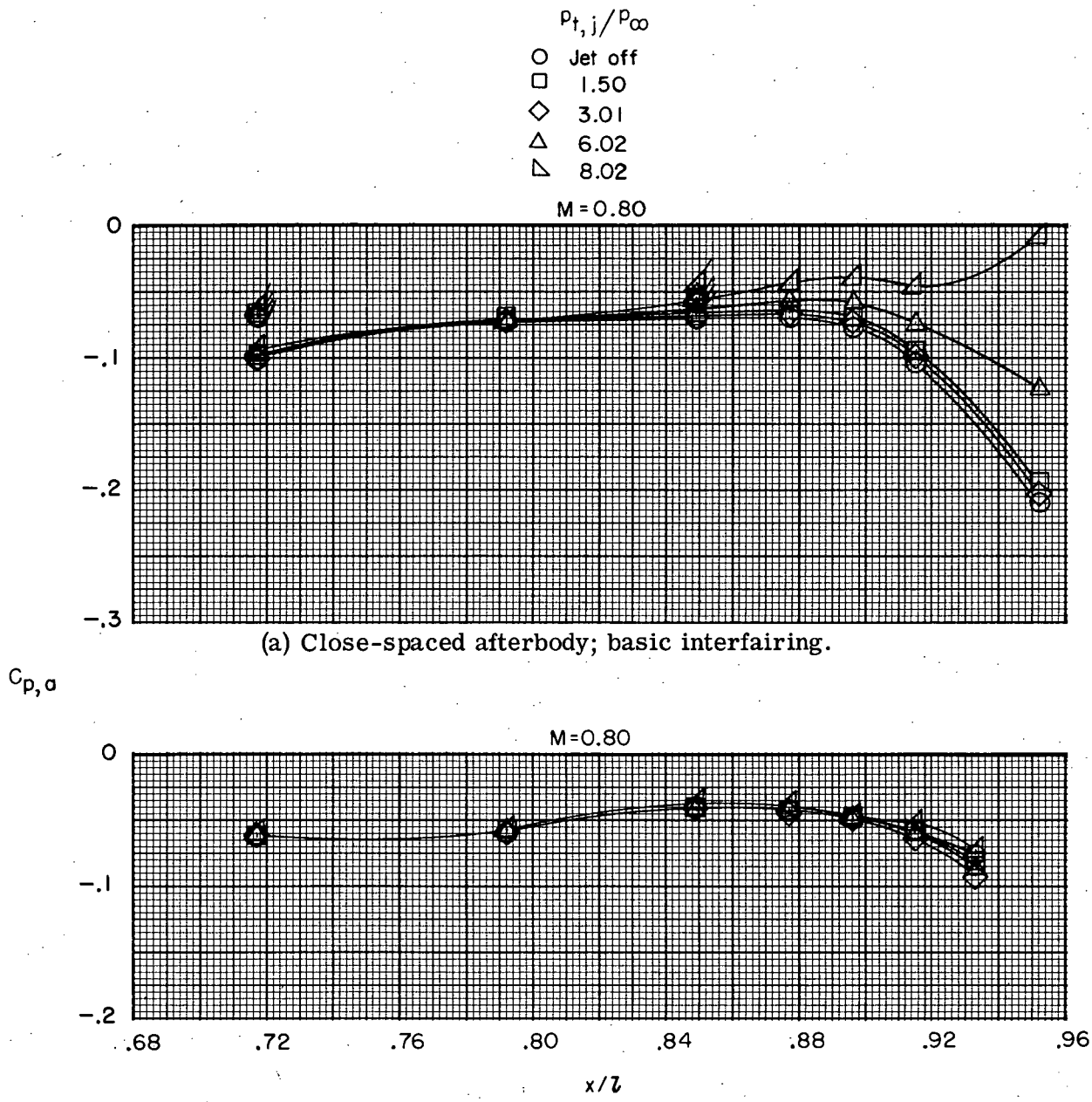


(a) Close-spaced afterbody; basic interfairing.

(b) Close-spaced afterbody; alternate 2 interfairing.

Figure 8.- Typical longitudinal pressure distributions at several jet total-pressure ratios. Dry-power nozzles; $\alpha = 0^{\circ}$; symbols with flags indicate bottom row.

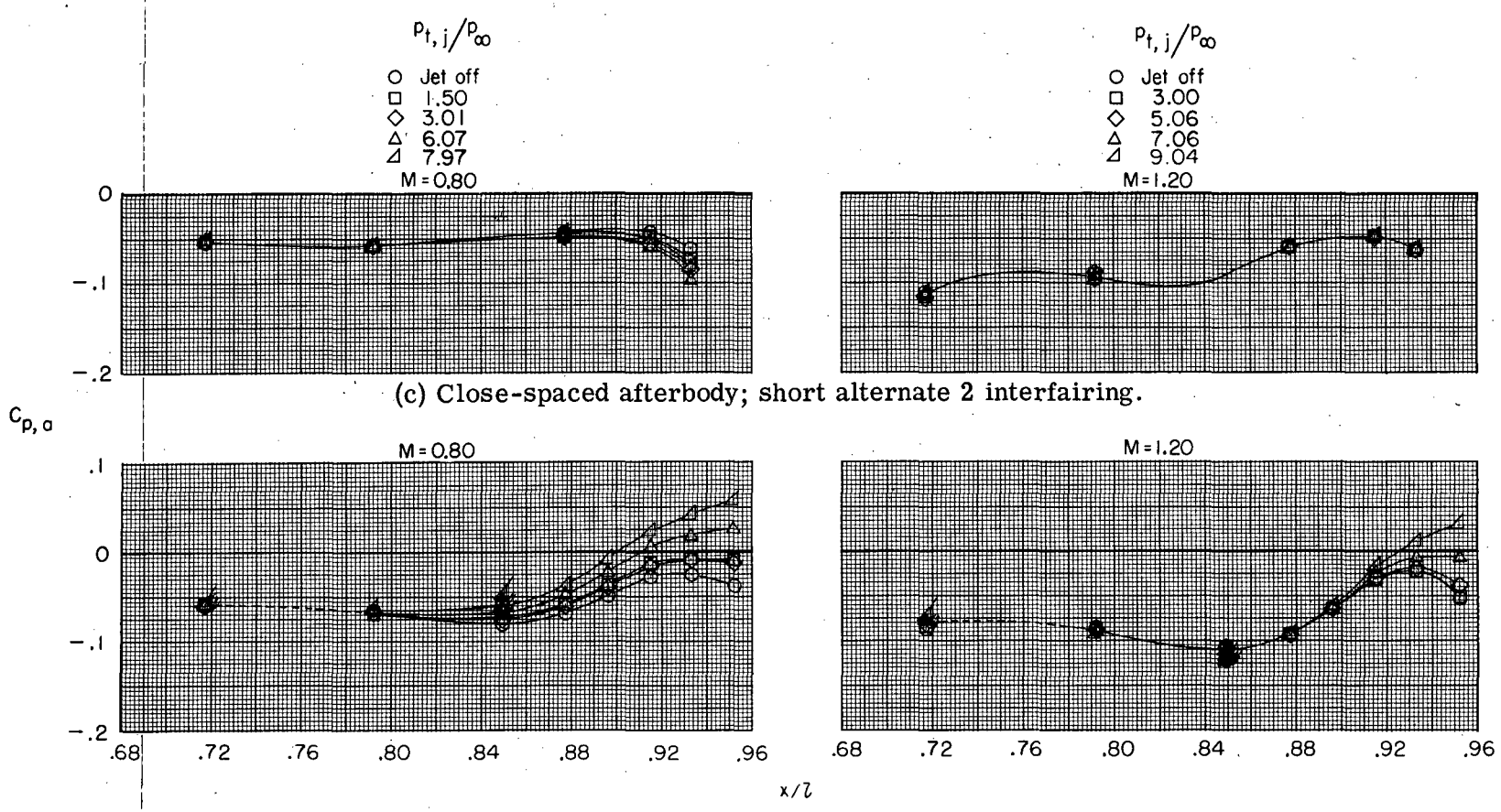


(c) Close-spaced afterbody; short alternate 2 interfairing.

(d) Wide-spaced afterbody; basic interfairing.

Figure 8.- Continued.

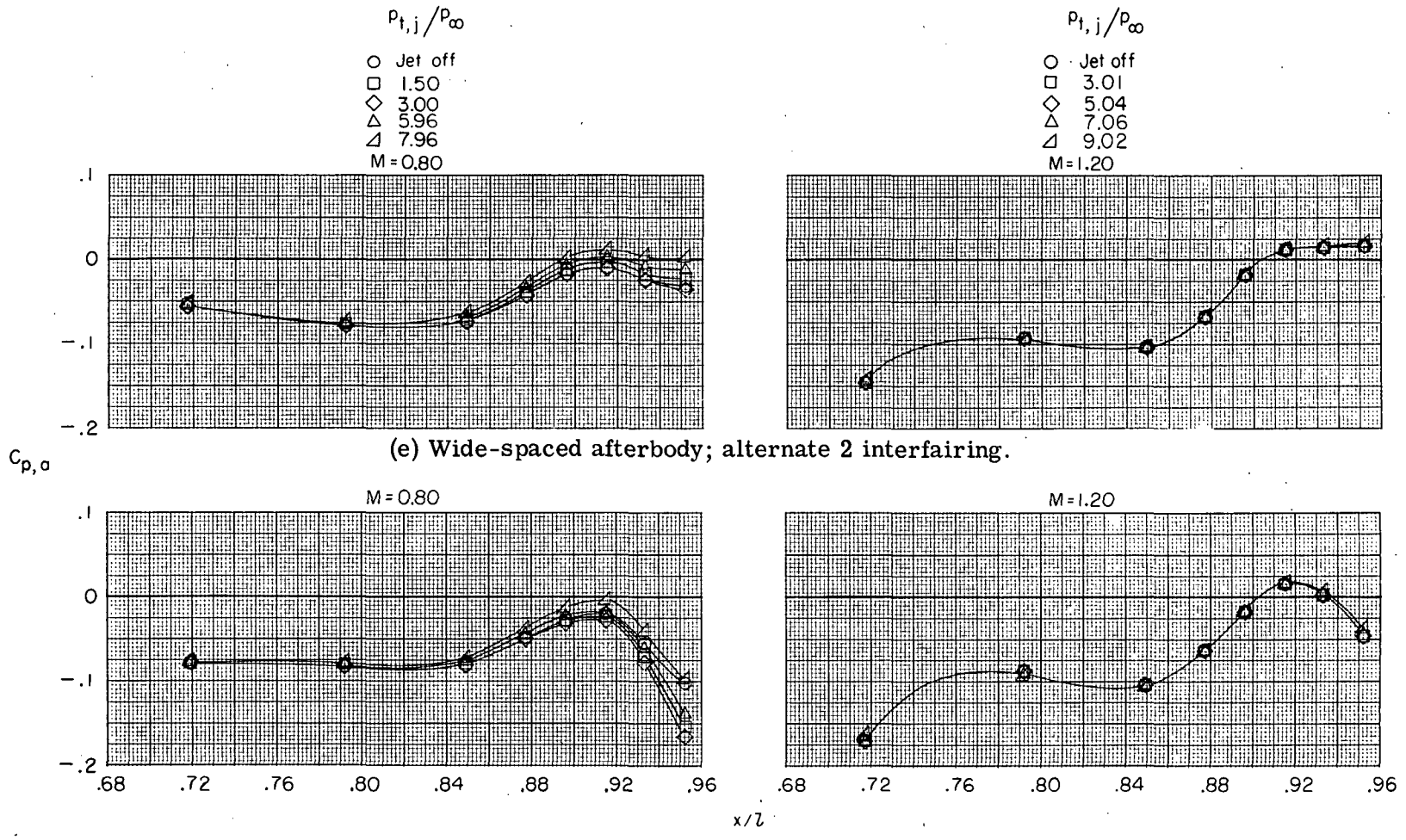


(e) Wide-spaced afterbody; alternate 2 interfairing.

(f) Wide-spaced afterbody; short alternate 2 interfairing.

Figure 8.- Concluded.

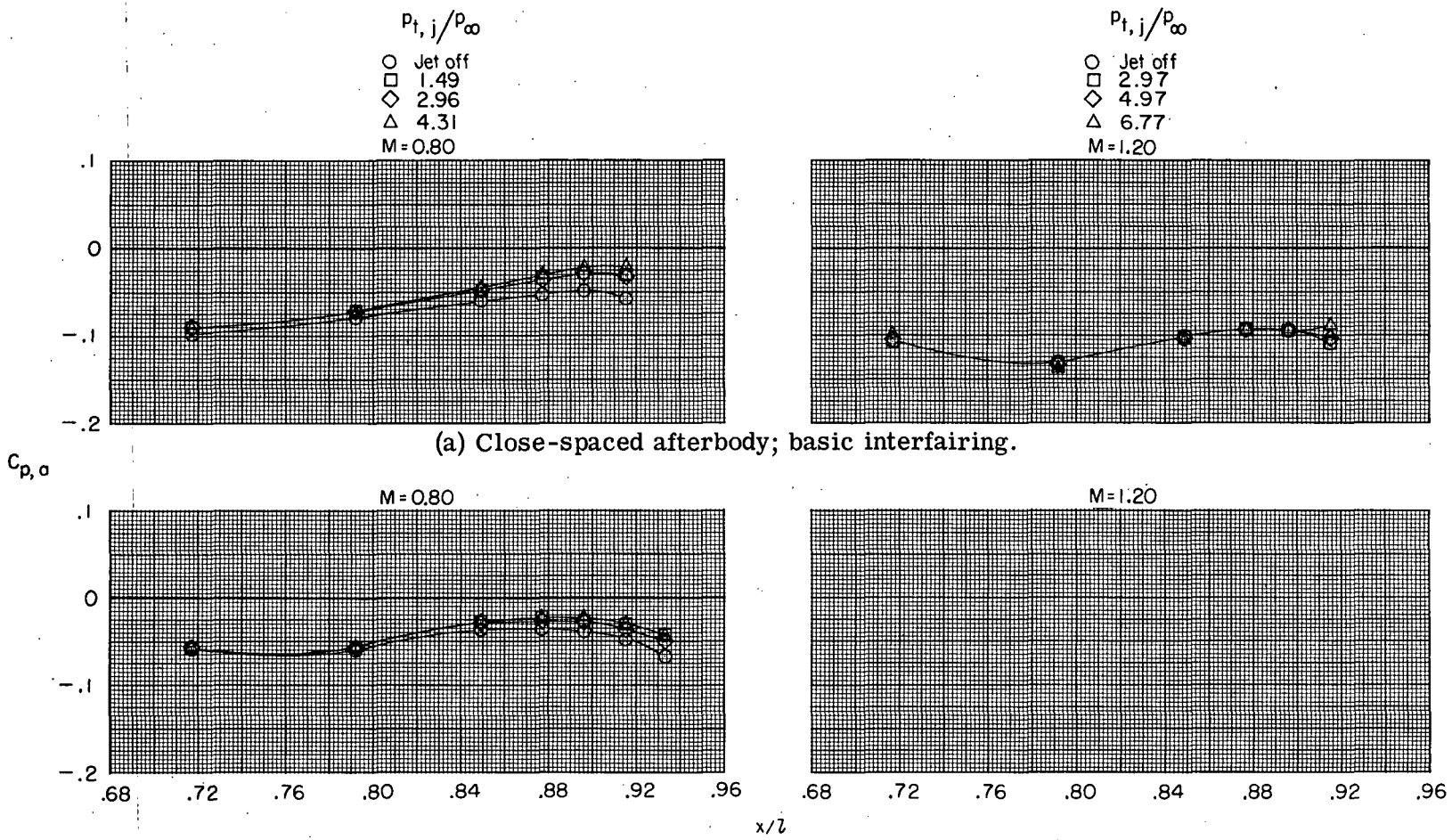


(a) Close-spaced afterbody; basic interfairing.

(b) Close-spaced afterbody; alternate 2 interfairing.

Figure 9.- Typical longitudinal pressure distributions at several jet total-pressure ratios. Max A/B power nozzles; $\alpha = 0^{o}$; symbols with flags indicate bottom row.

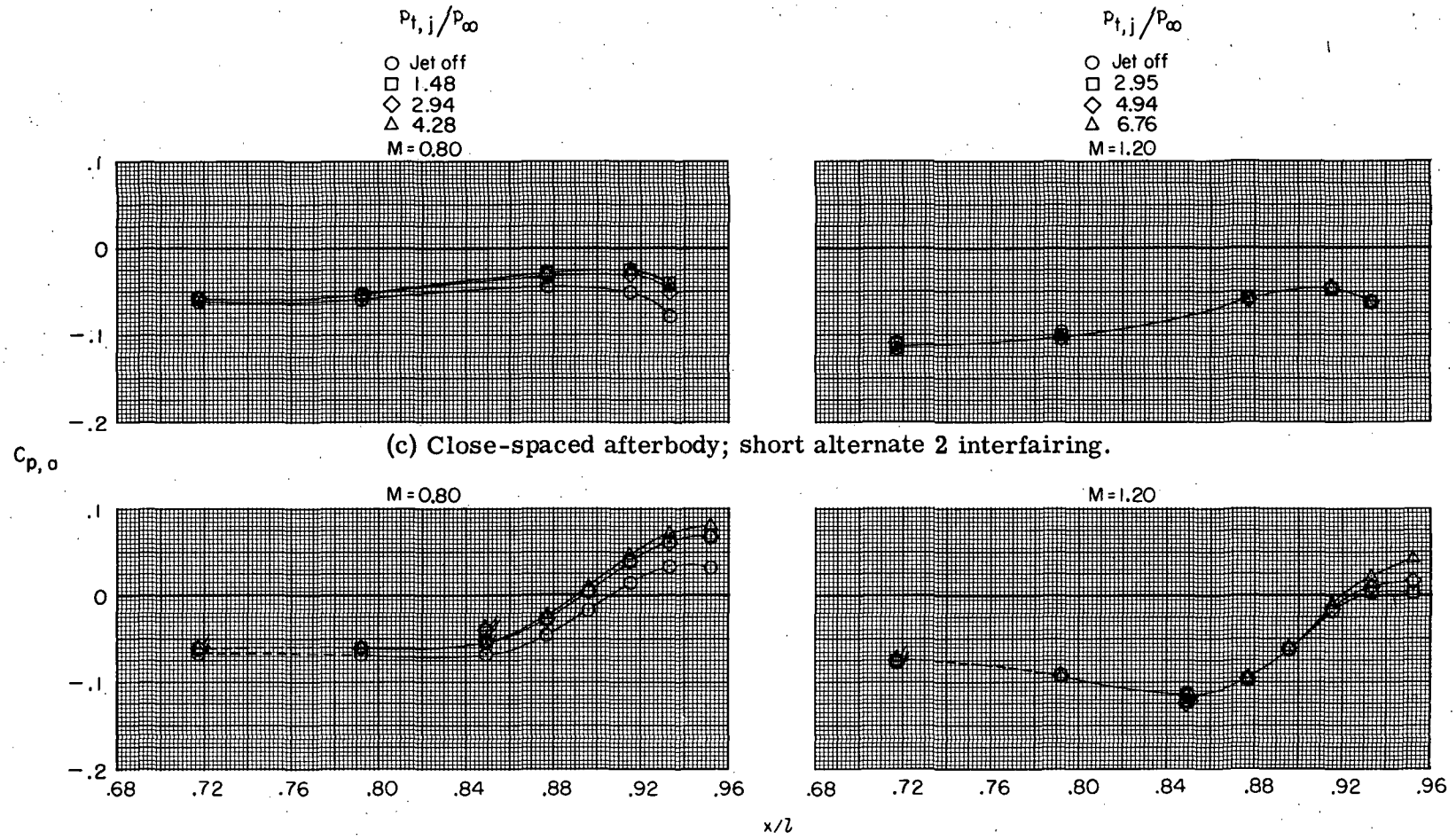


(c) Close-spaced afterbody; short alternate 2 interfairing.

(d) Wide-spaced afterbody; basic interfairing.

Figure 9.- Continued.

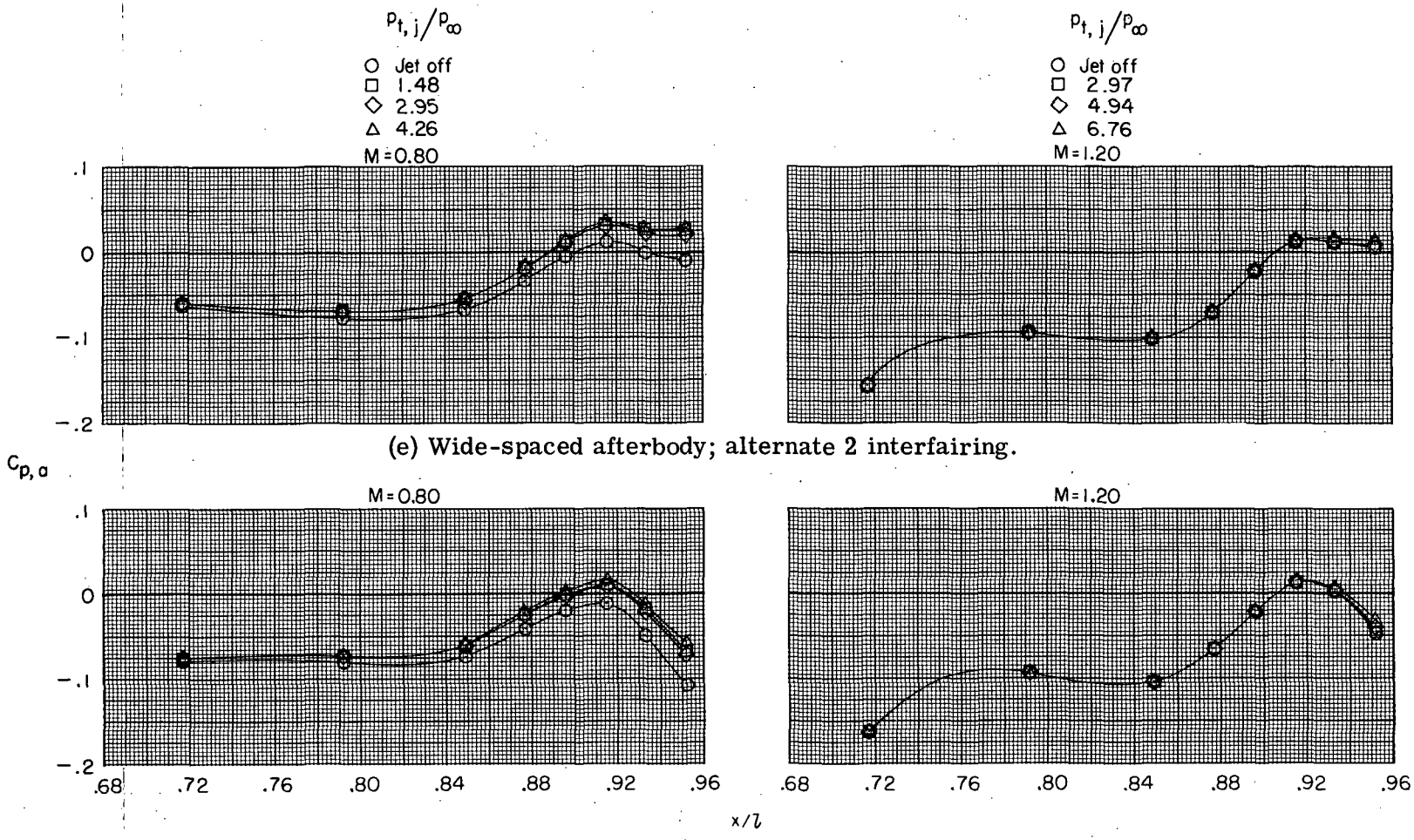


(e) Wide-spaced afterbody; alternate 2 interfairing.

(f) Wide-spaced afterbody; short alternate 2 interfairing.

Figure 9.- Concluded.

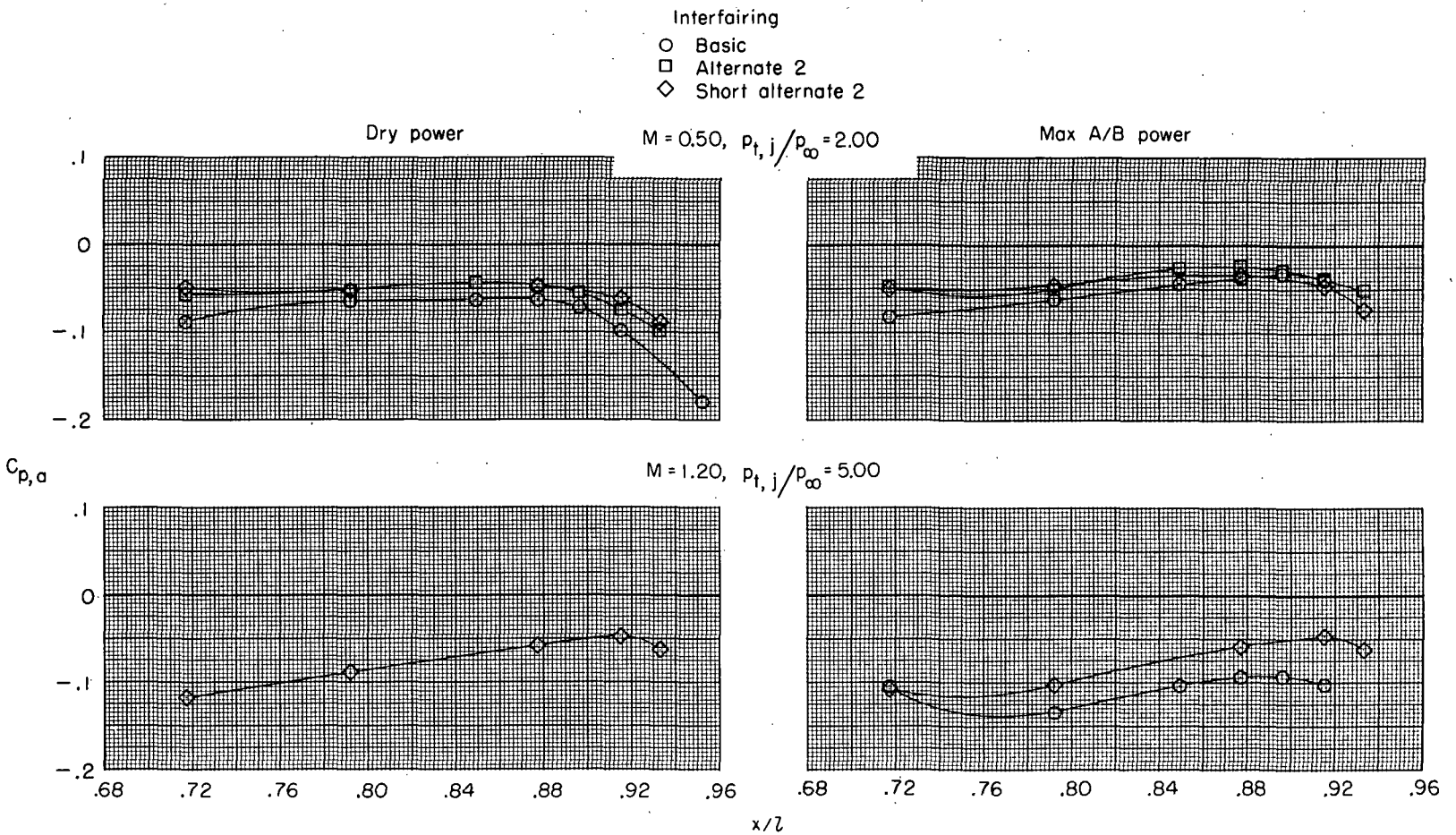


(a) Close-spaced afterbody.

Figure 10.- Effect of engine interfairing and nozzle power setting on interfairing pressure distributions. $\alpha = 0^{o}$.

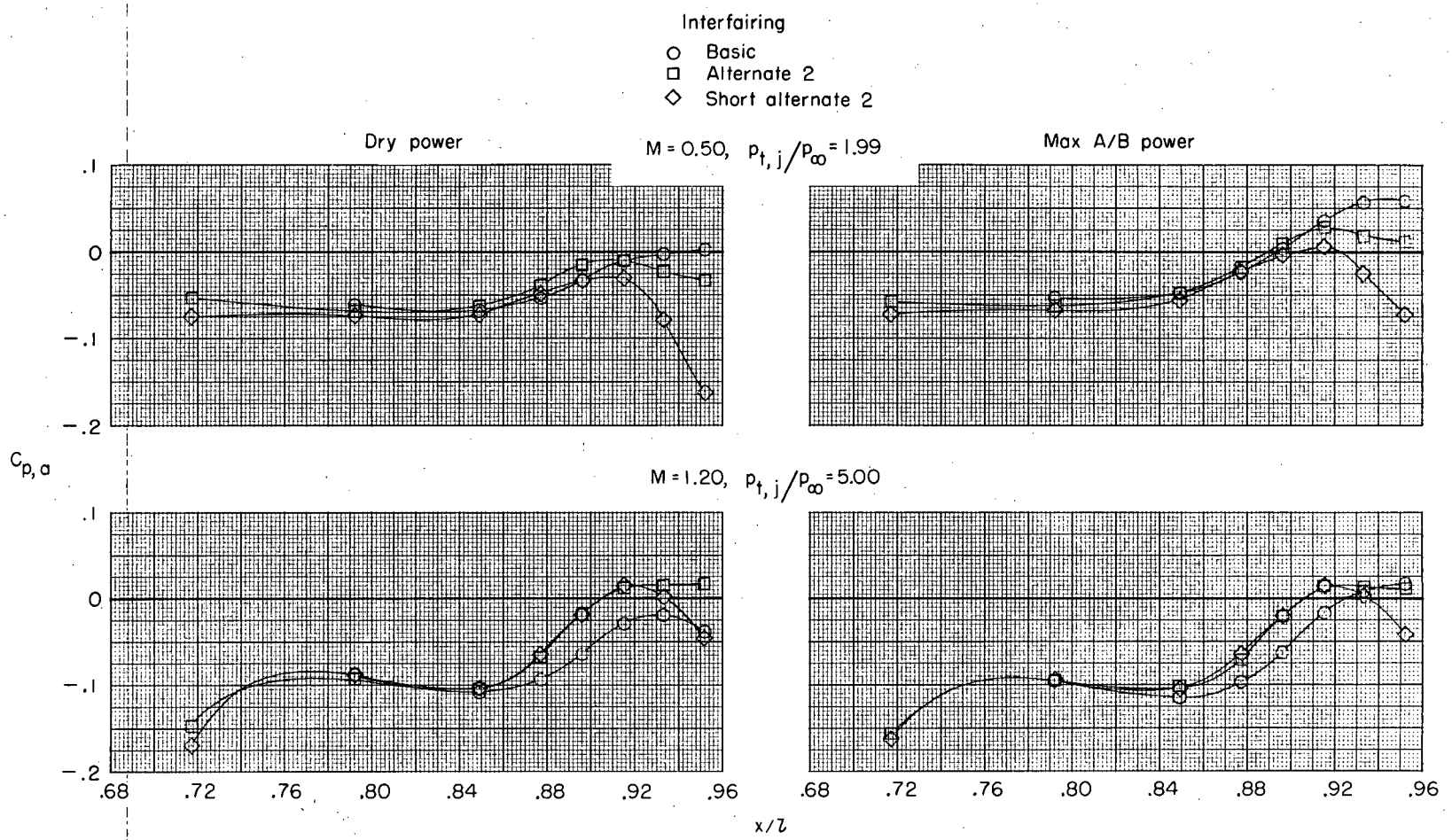


(b) Wide-spaced afterbody.

Figure 10.- Concluded.

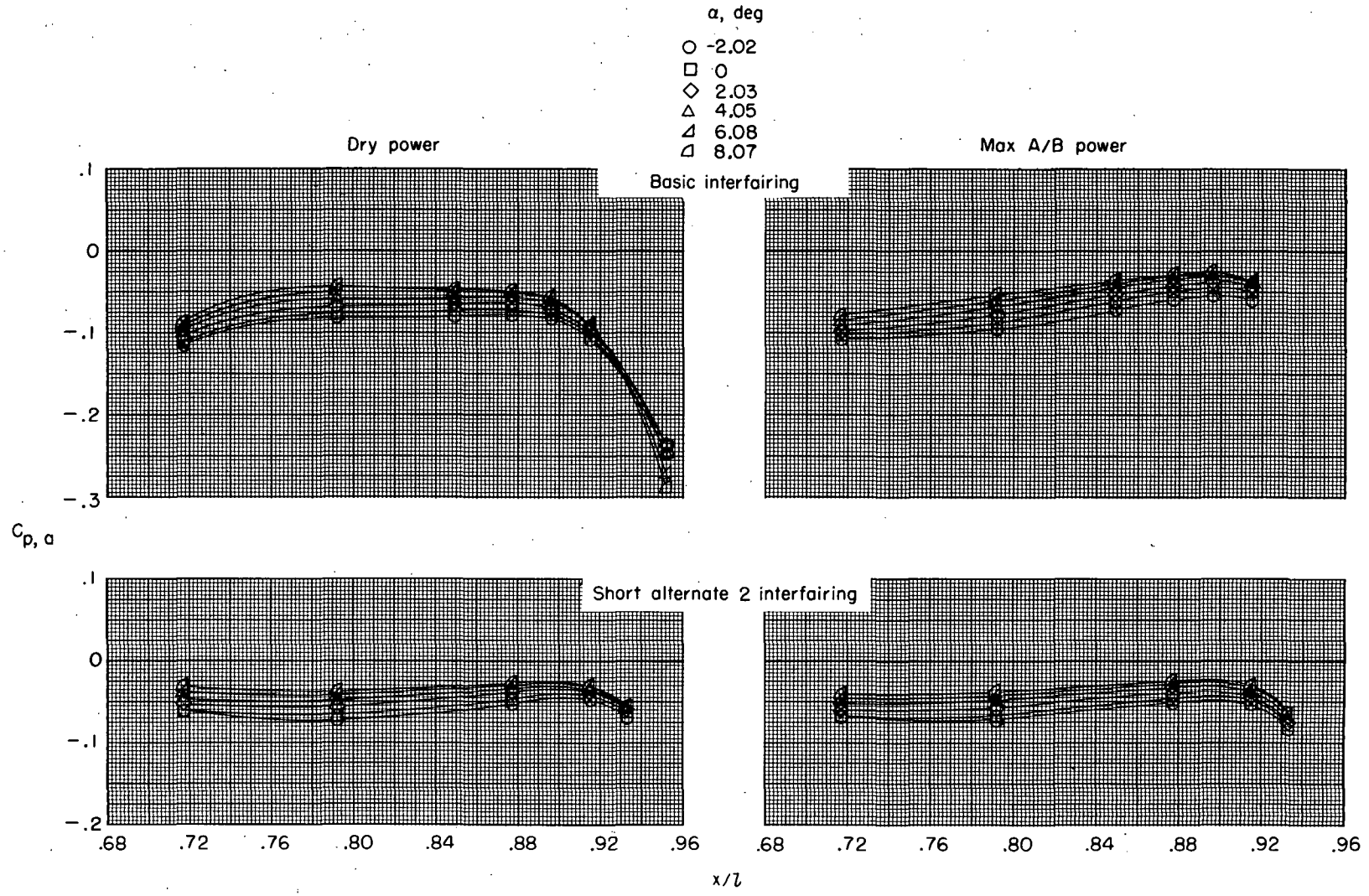


(a) Close-spaced afterbody; M = 0.90.

Figure 11.- Effect of angle of attack on afterbody top-row interfairing pressure distributions. Jet off.

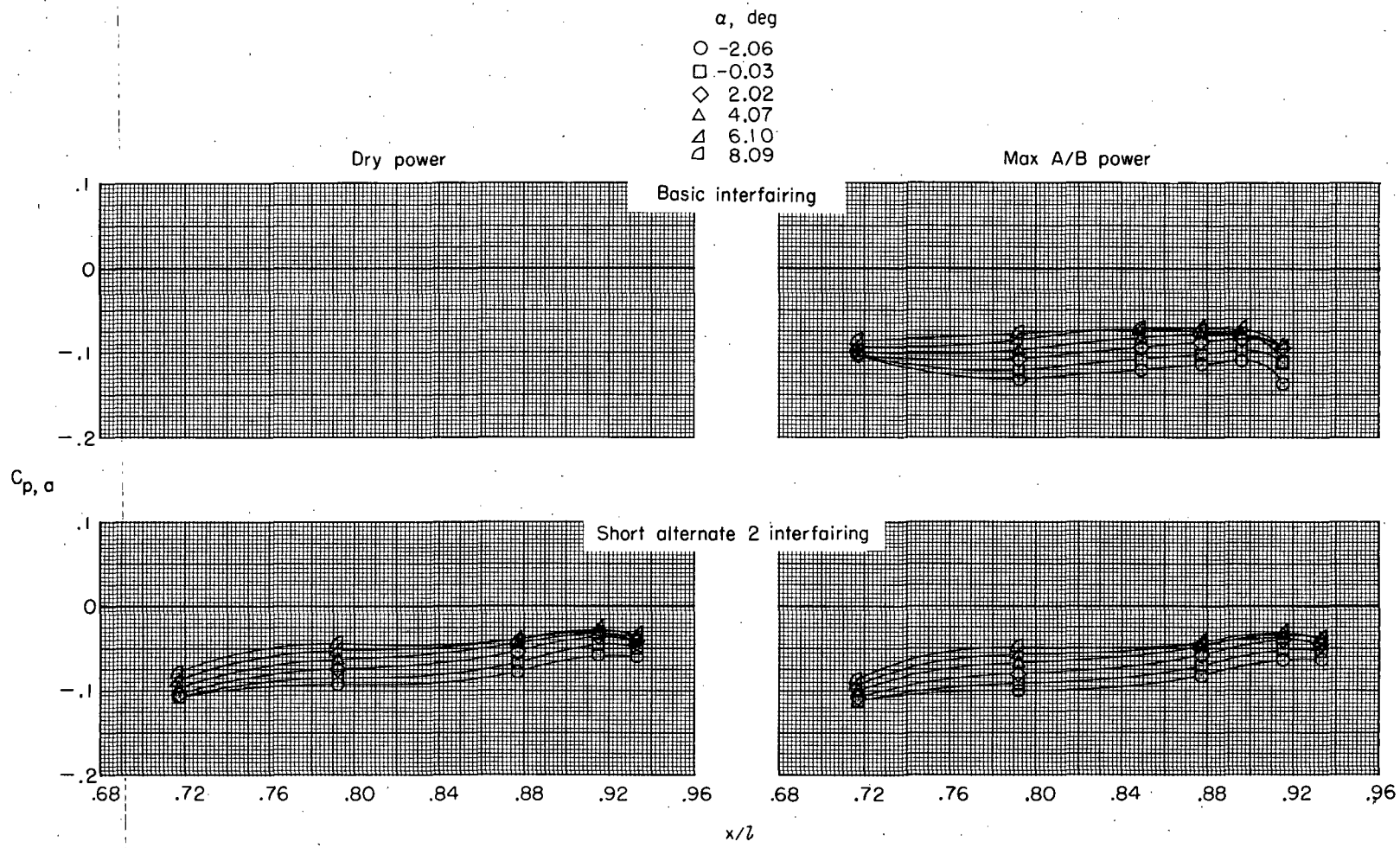


(b) Close-spaced afterbody; M = 1.30.

Figure 11.- Continued.

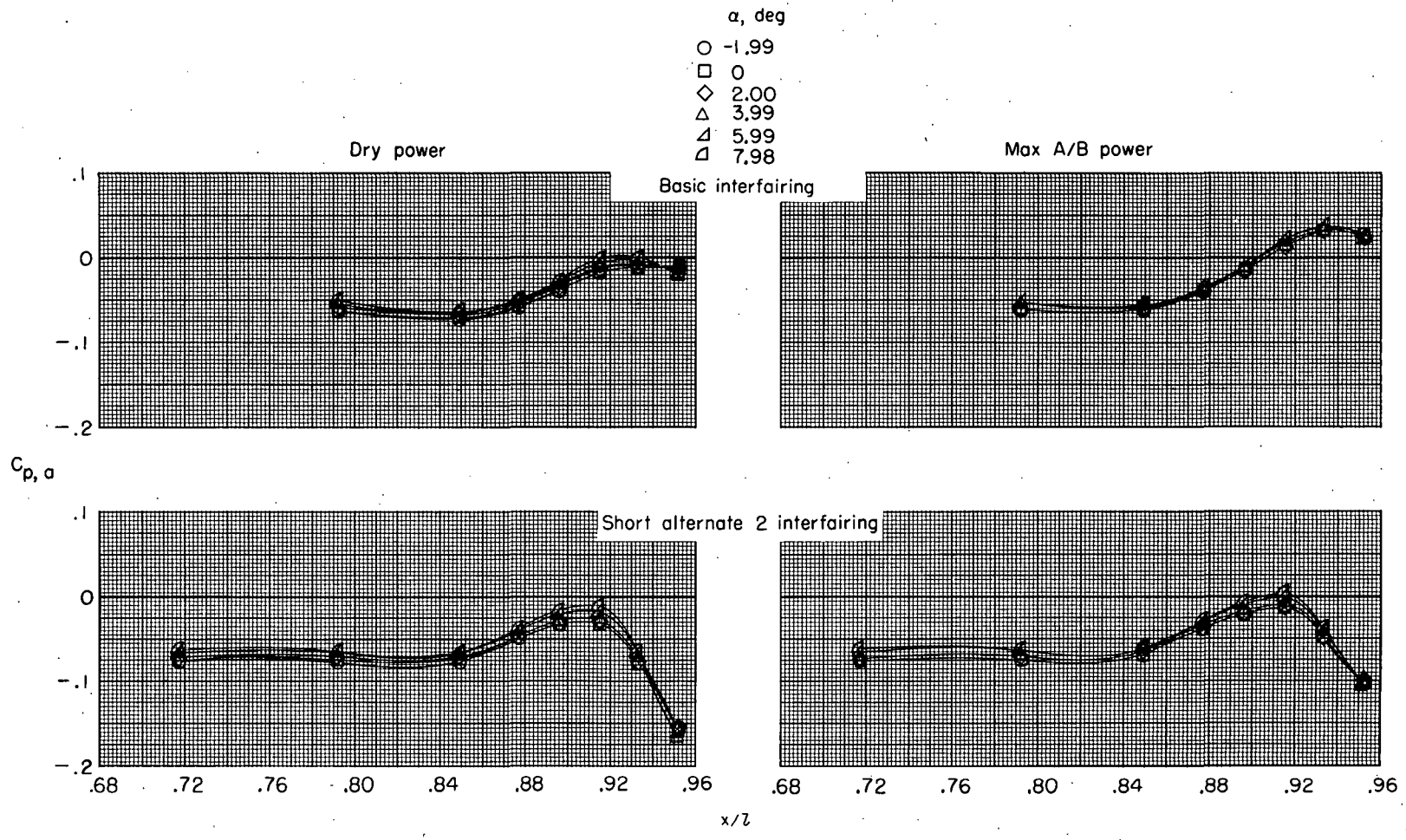


(c) Wide-spaced afterbody; M = 0.50.

Figure 11.- Continued.

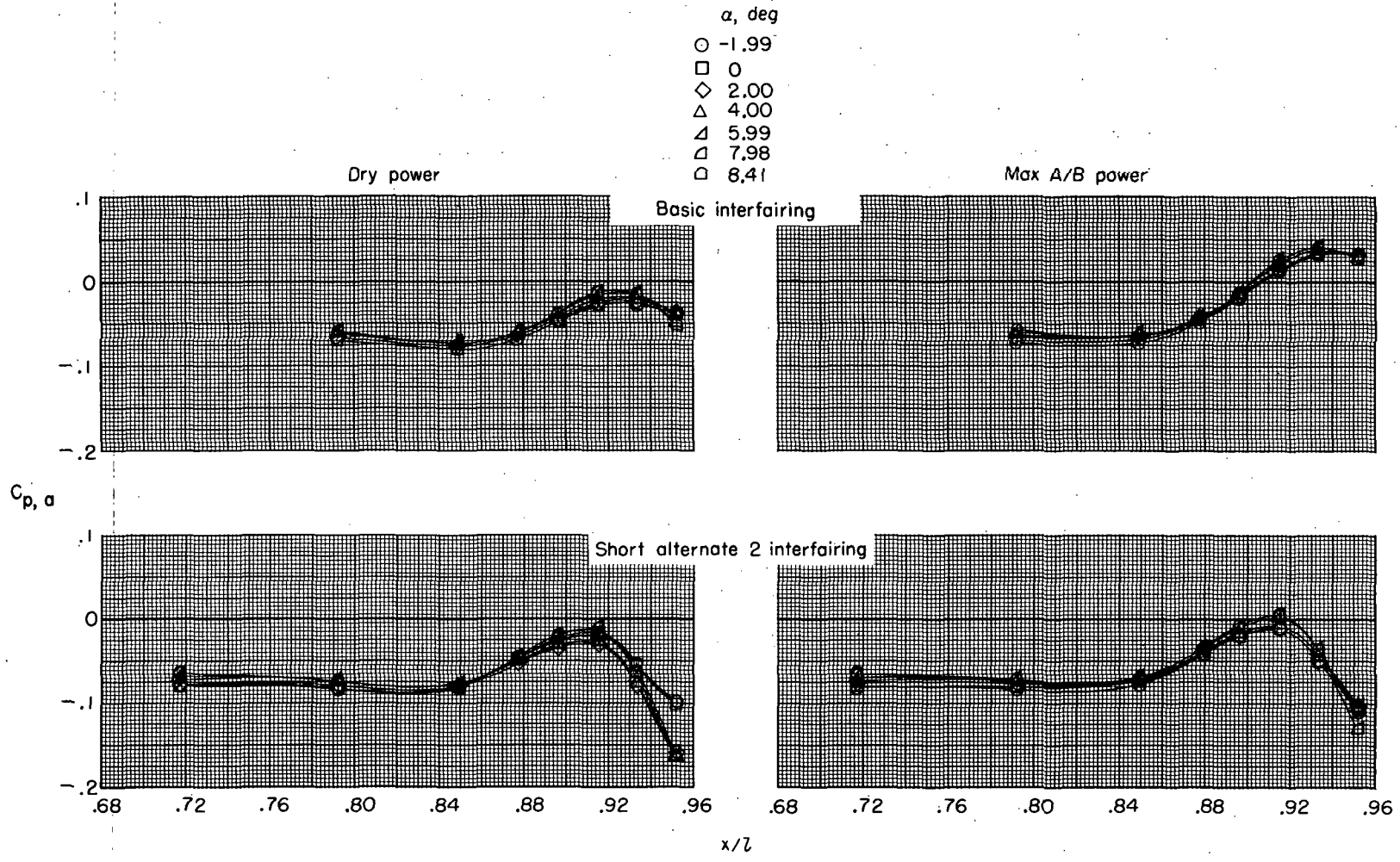


(d) Wide-spaced afterbody; M = 0.80.

Figure 11.- Continued.

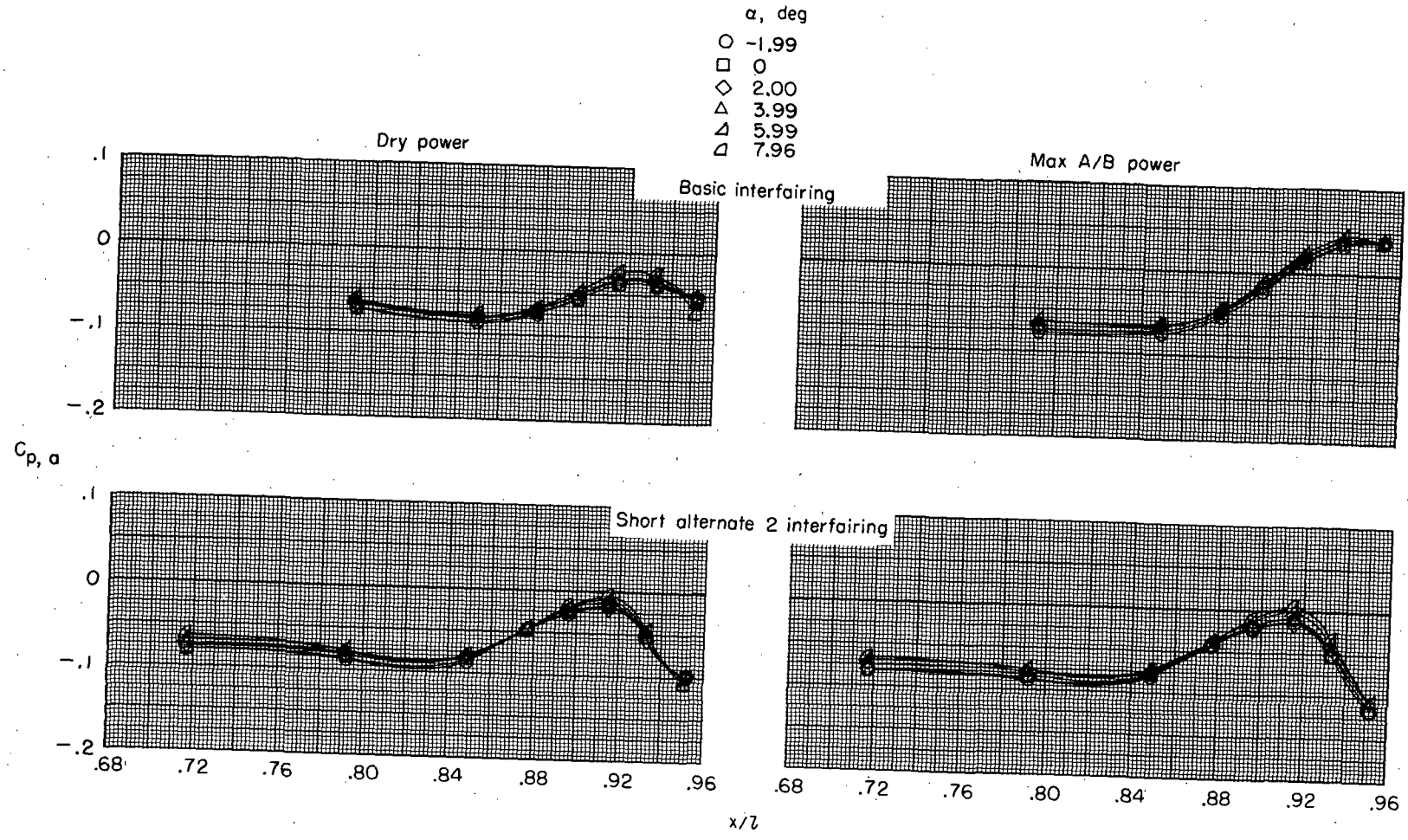


(e) Wide-spaced afterbody; M = 0.90.

Figure 11.- Continued.

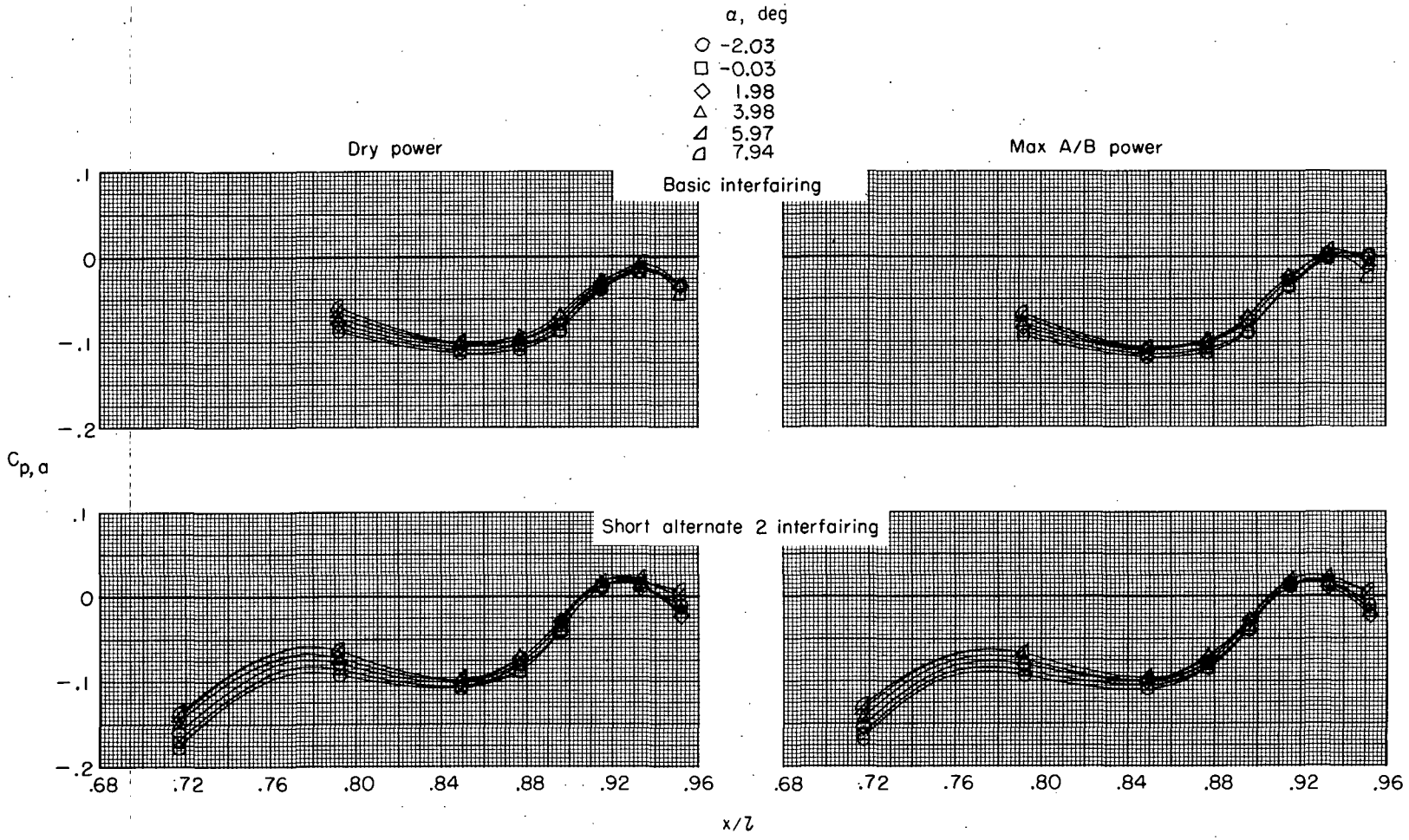


(f) Wide-spaced afterbody; M = 1.30.

Figure 11.- Concluded.

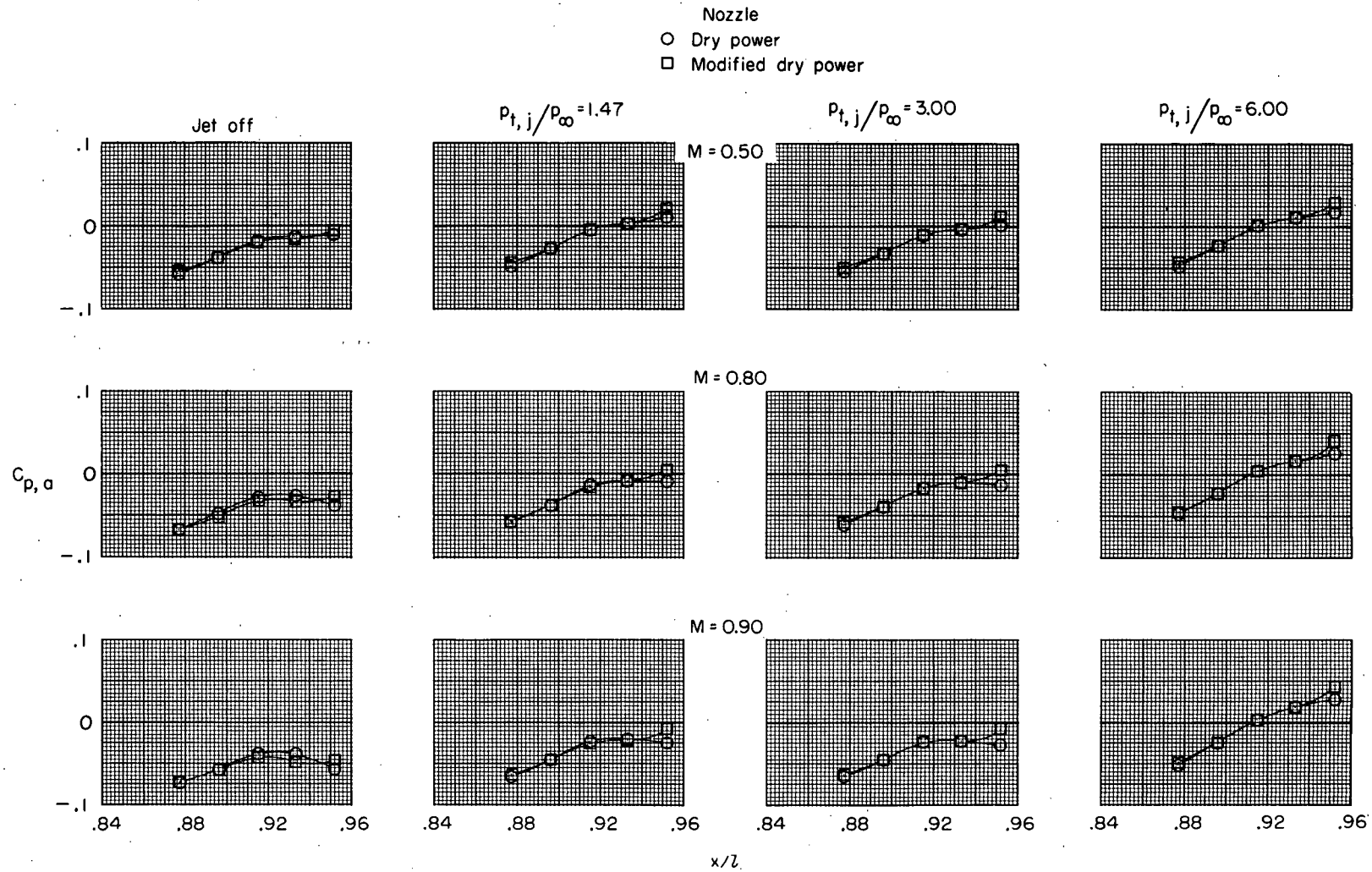


Figure 12.- Effect of dry-power nozzle-shroud base area on interfairing pressure distributions. Wide-spaced afterbody; basic interfairing; $\alpha = 0^{o}$.

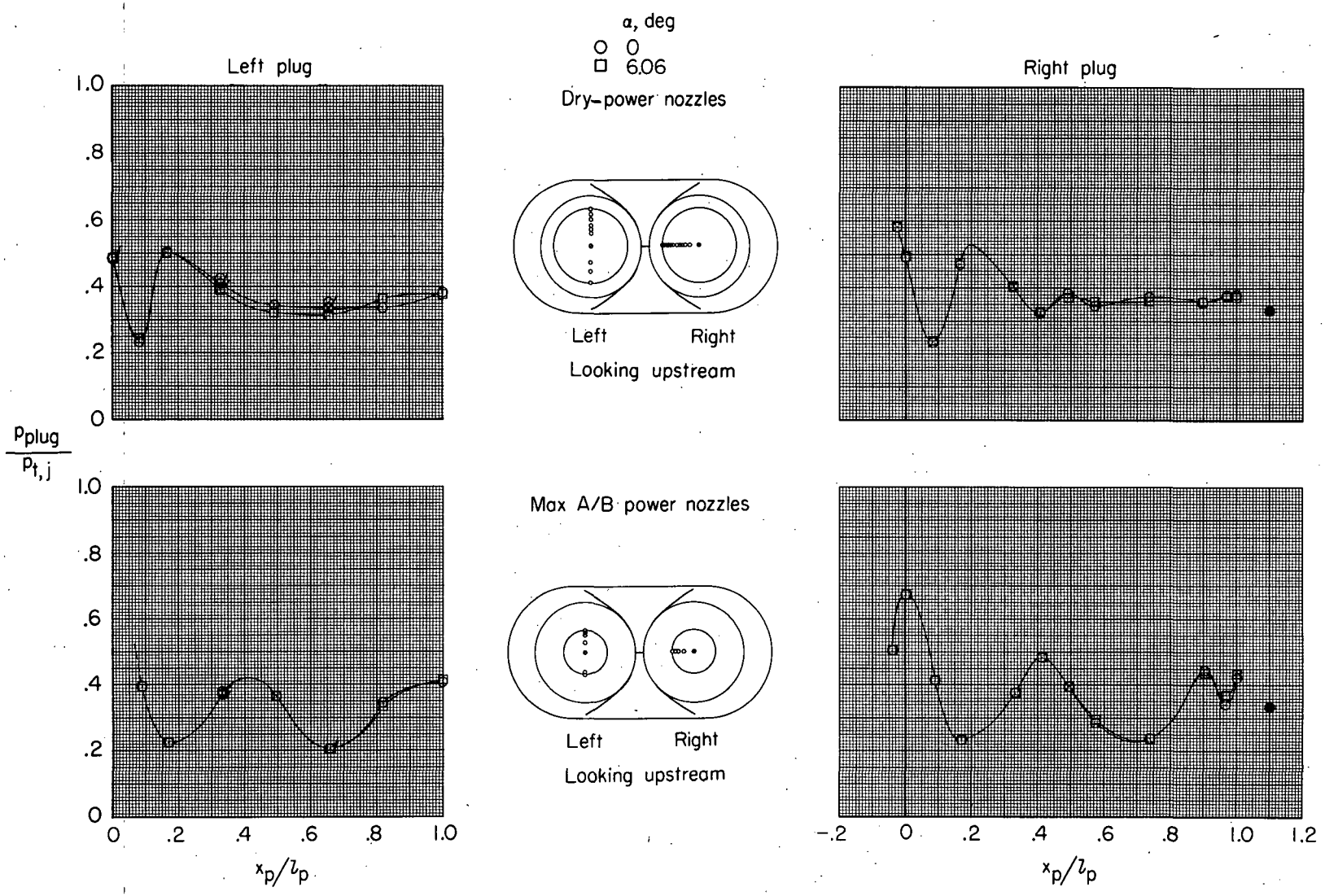


(a) Close-spaced afterbody.

Figure 13.- Effect of angle of attack on plug static-pressure distributions for two nozzle power settings. Basic interfairing; $M = 0.80$; $p_{t,j}/p_\infty = 2.98$; symbols with flags indicate bottom-row orifices; solid symbols indicate values of $p_\infty/p_{t,j}$.

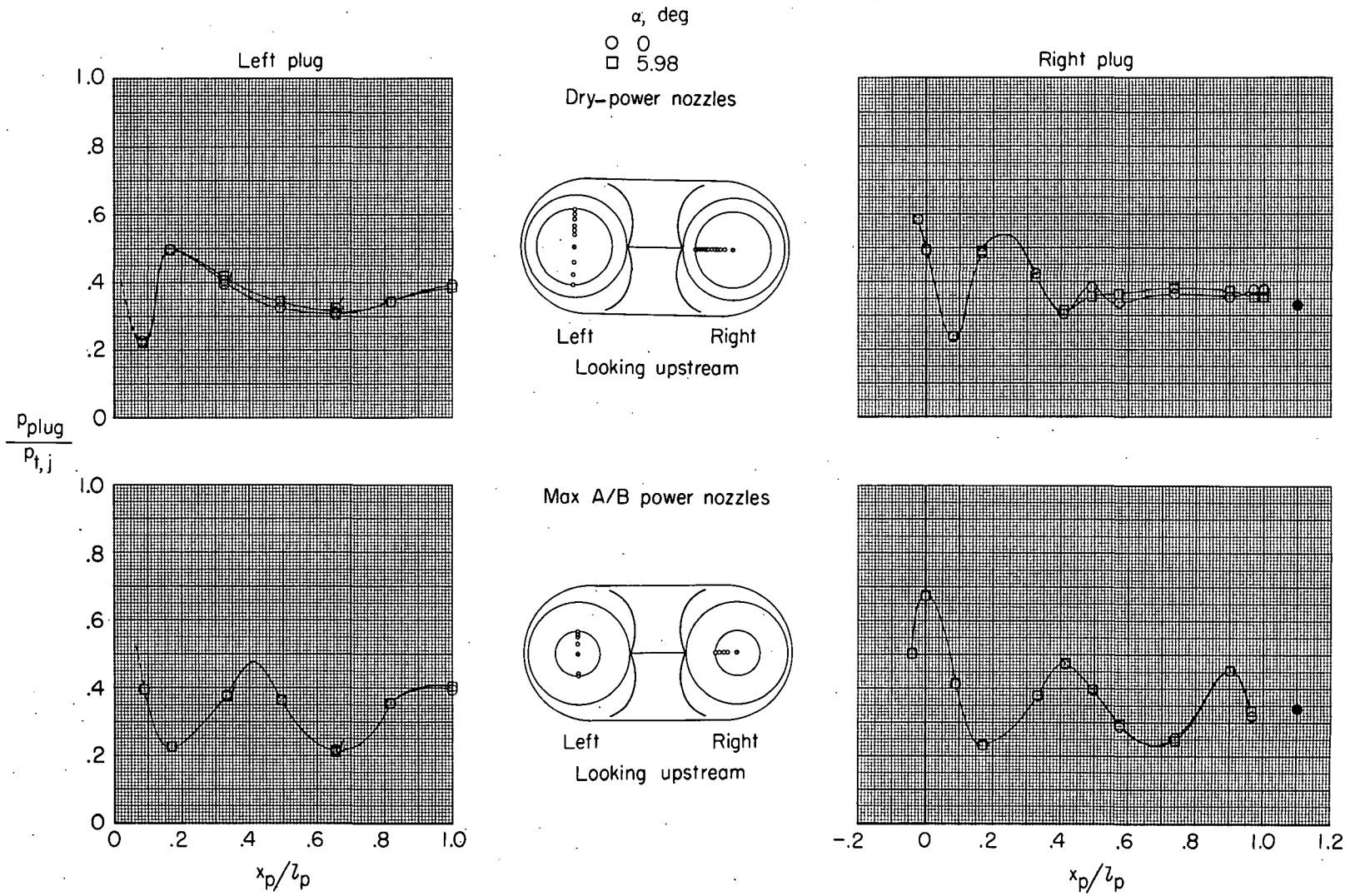


(b) Wide-spaced afterbody.

Figure 13.- Concluded.

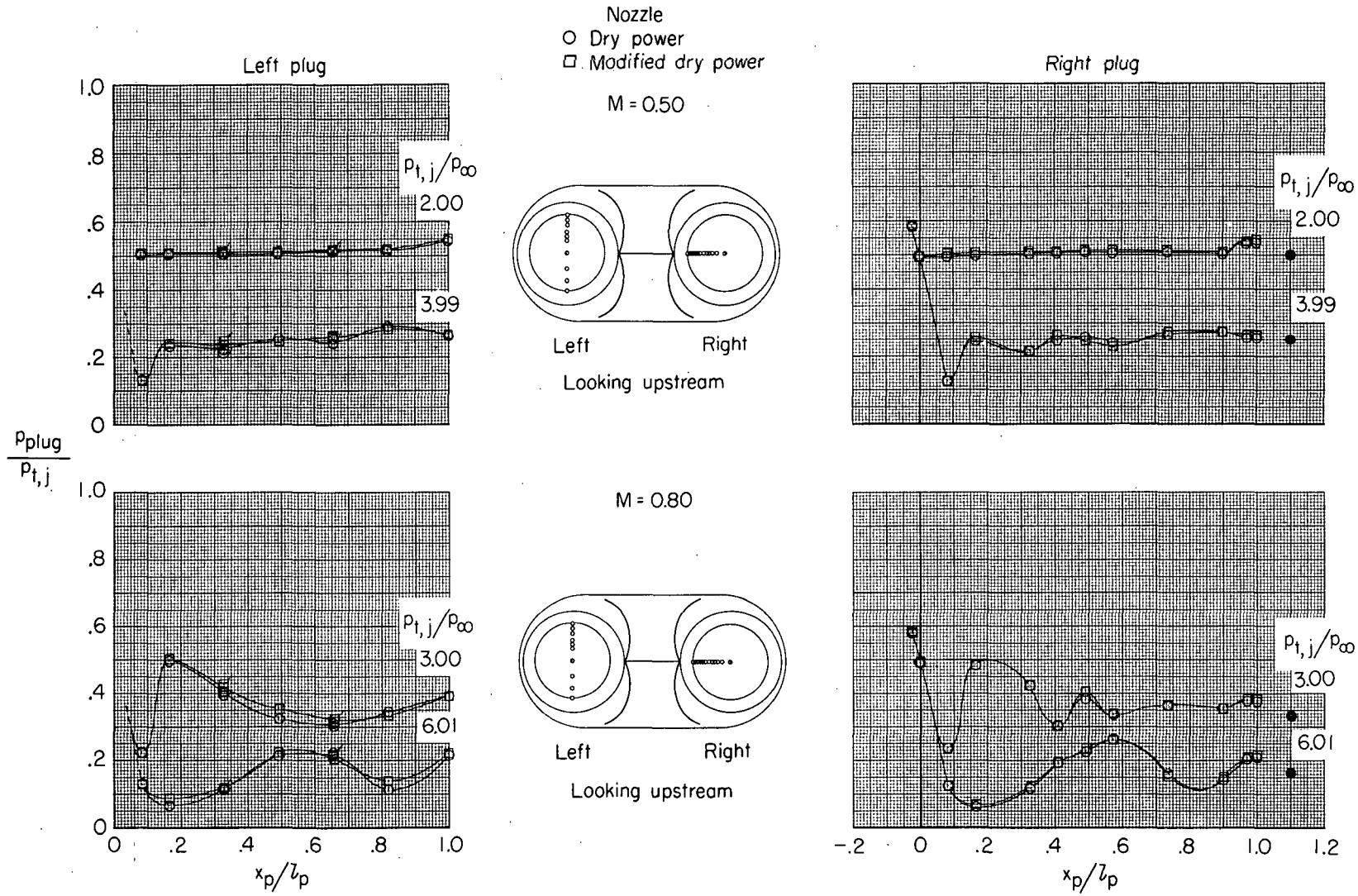


(a) M = 0.50 and 0.80.

Figure 14.- Effect of shroud base area on the dry-power plug static-pressure distributions at several Mach numbers. Wide-spaced afterbody with basic interfairing; $\alpha = 0^o$; symbols with flags indicate bottom-row orifices; solid symbols indicate values of $p_\infty/p_{t,j}$.

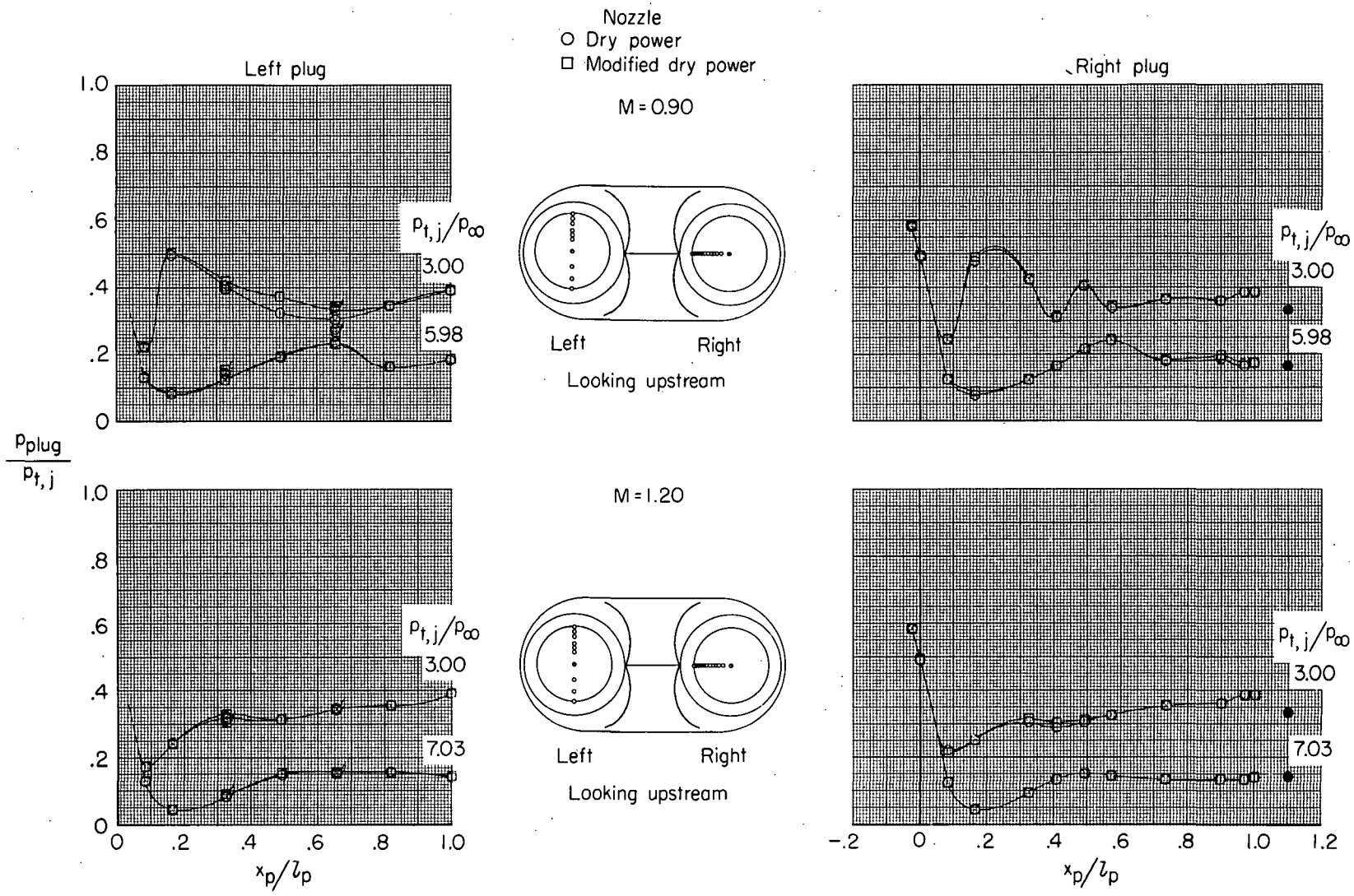


(b) M = 0.90 and 1.20.

Figure 14.- Concluded.

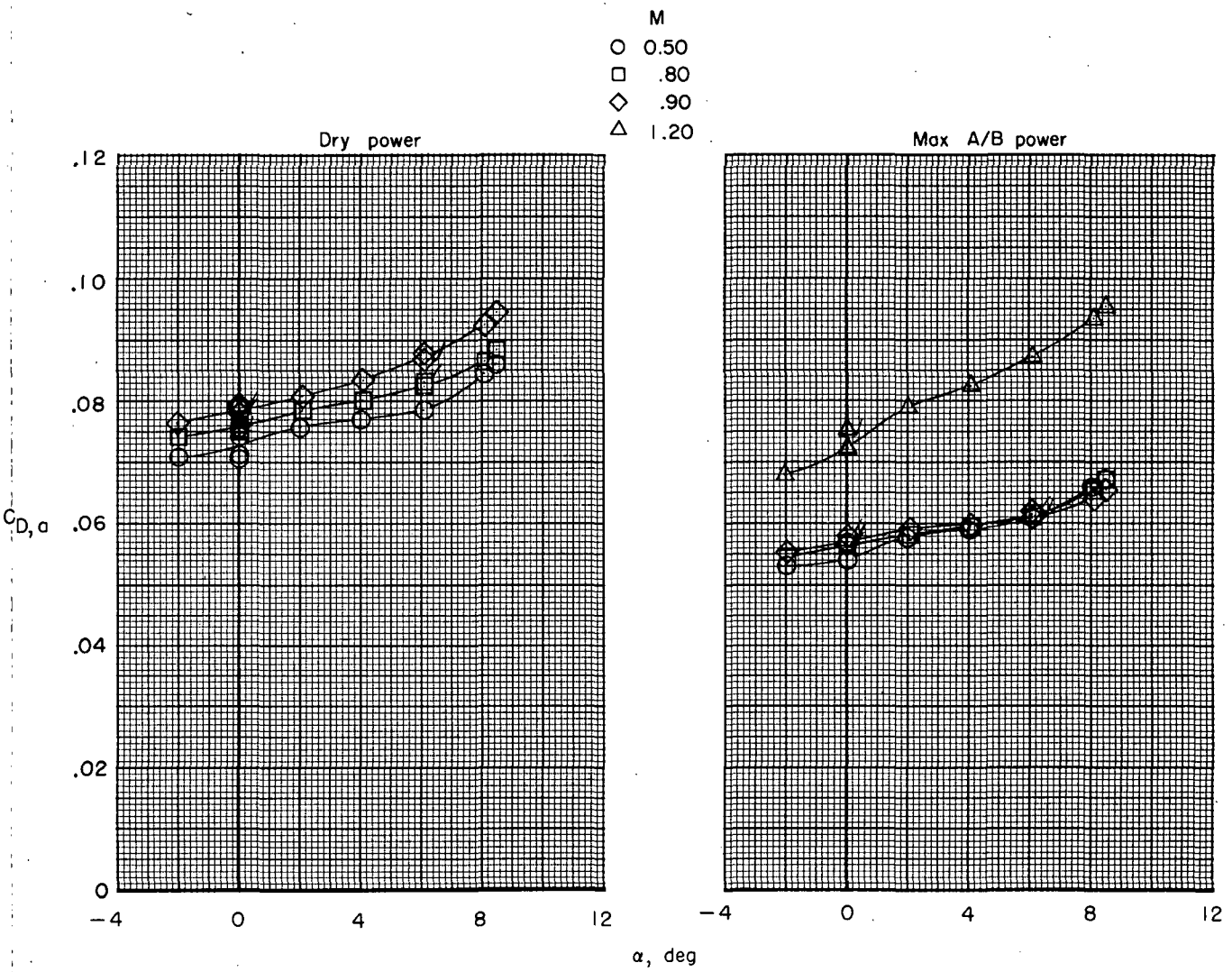


(a) Close-spaced afterbody; basic interfairing.

Figure 15.- Effect of angle of attack on afterbody drag coefficient. Jet off; symbols with flags indicate points taken immediately after a jet total-pressure-ratio sweep.

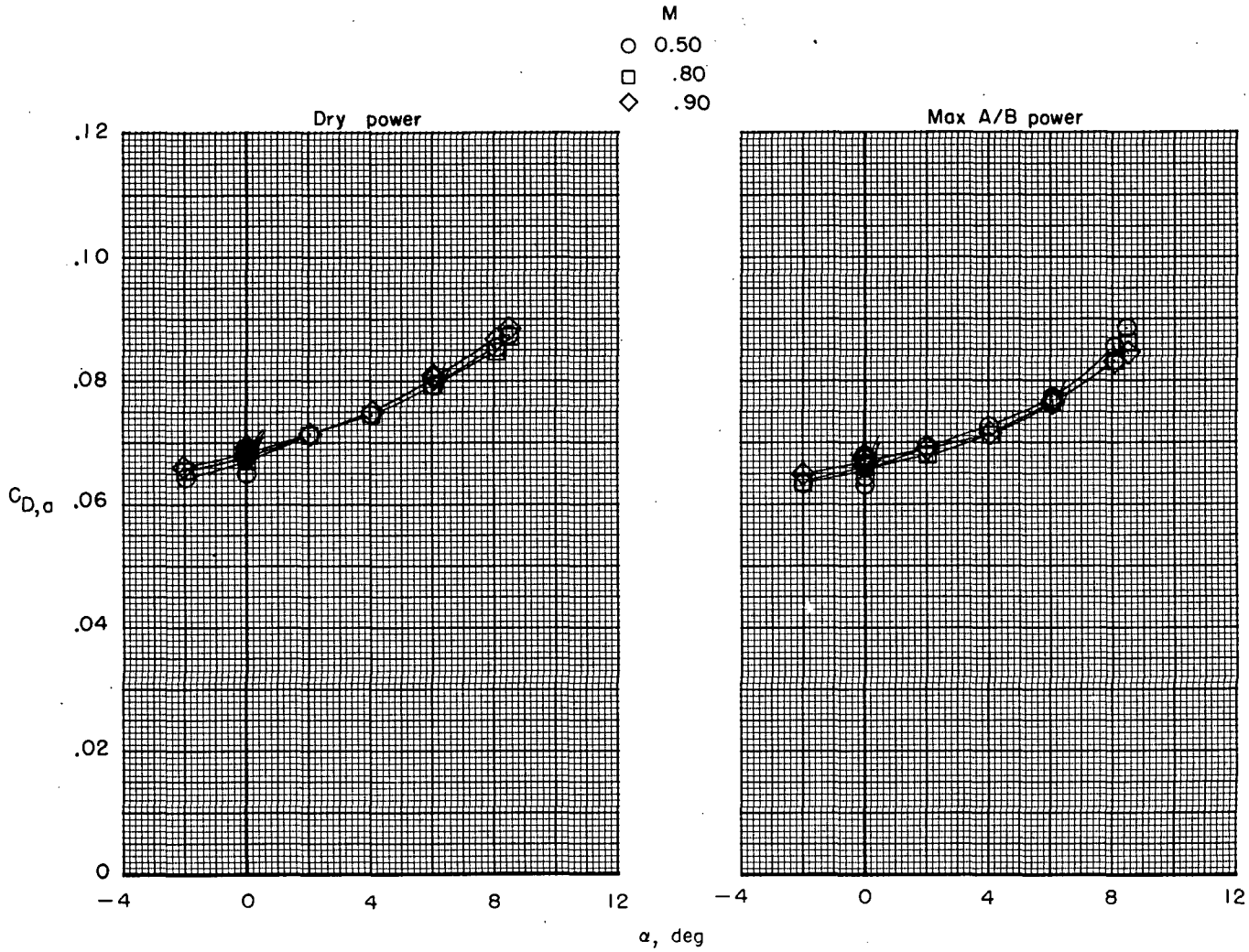


(b) Close-spaced afterbody; alternate 2 interfairing.

Figure 15.- Continued.

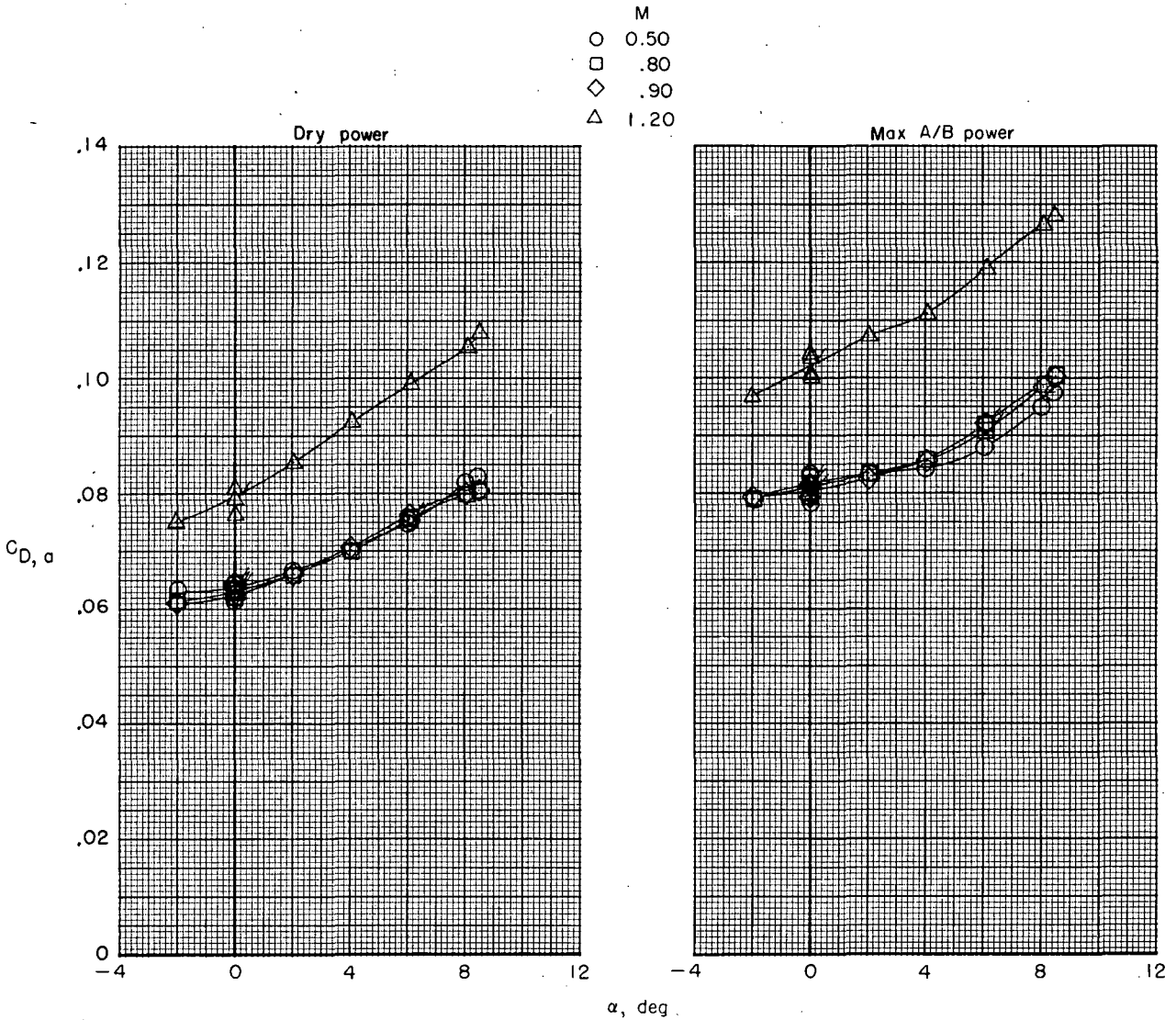


(c) Close-spaced afterbody; short alternate 2 interfairing.

Figure 15.- Continued.

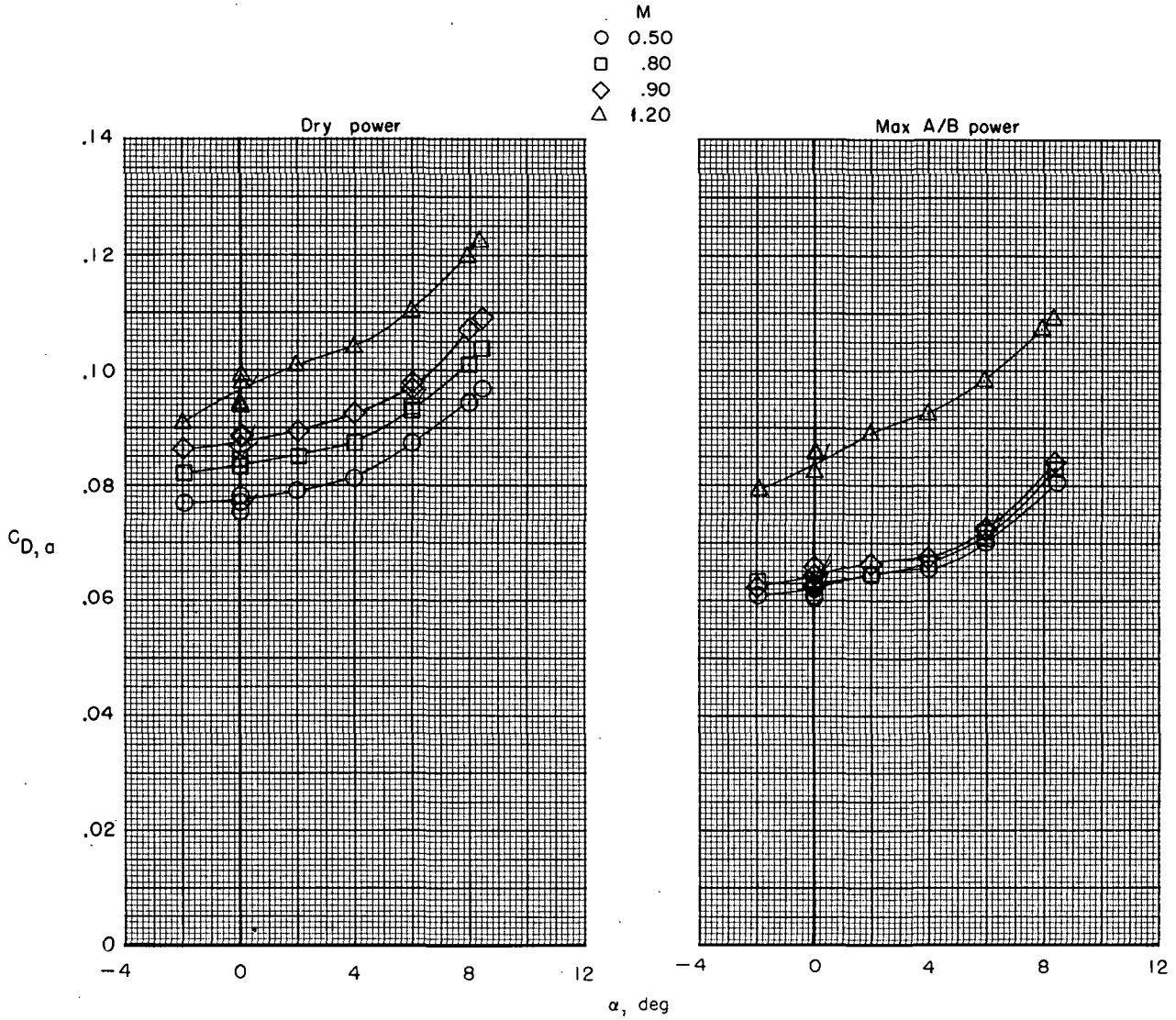


(d) Wide-spaced afterbody; basic interfairing.

Figure 15.- Continued.

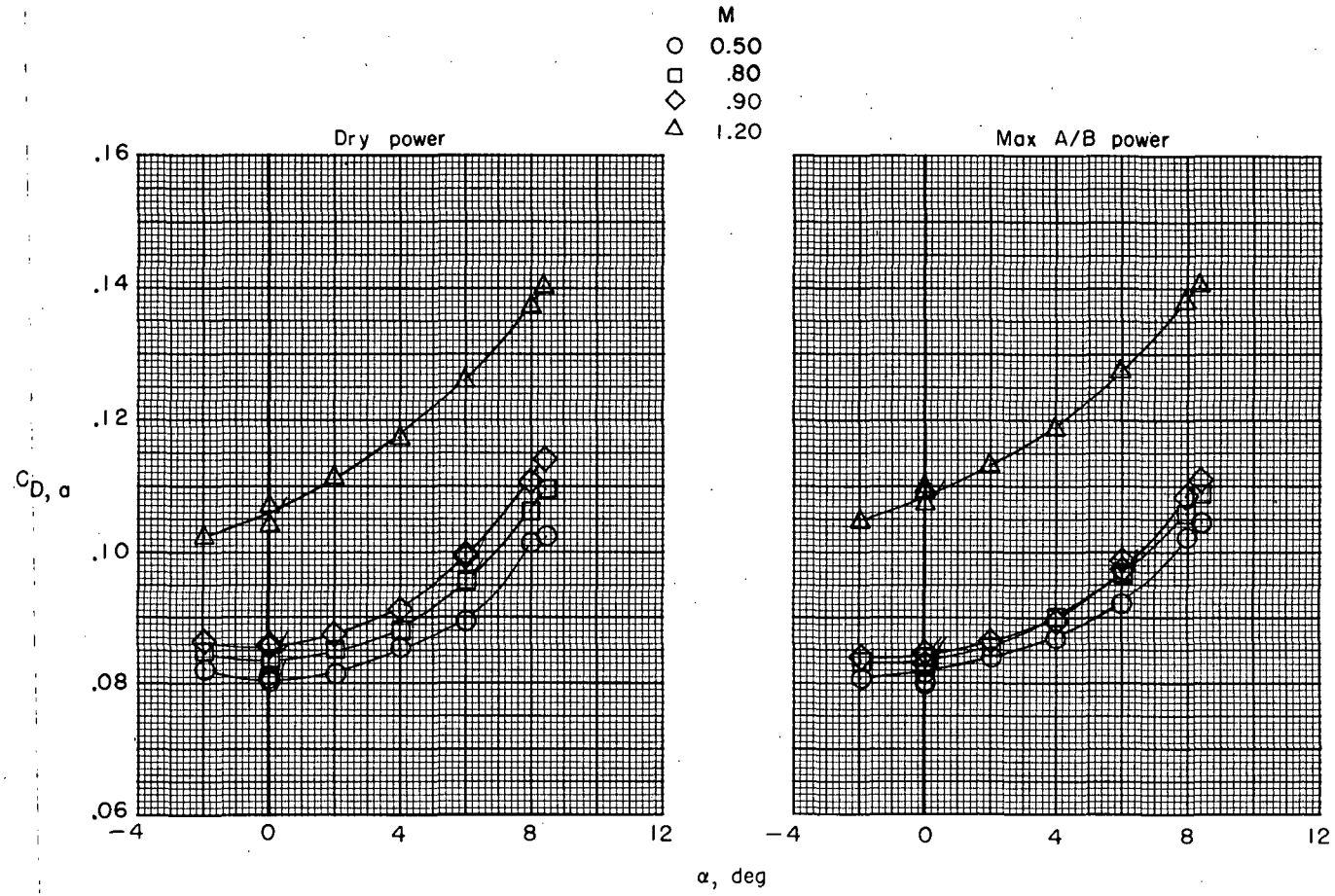


(e) Wide-spaced afterbody; alternate 2 interfairing.

Figure 15.- Continued.

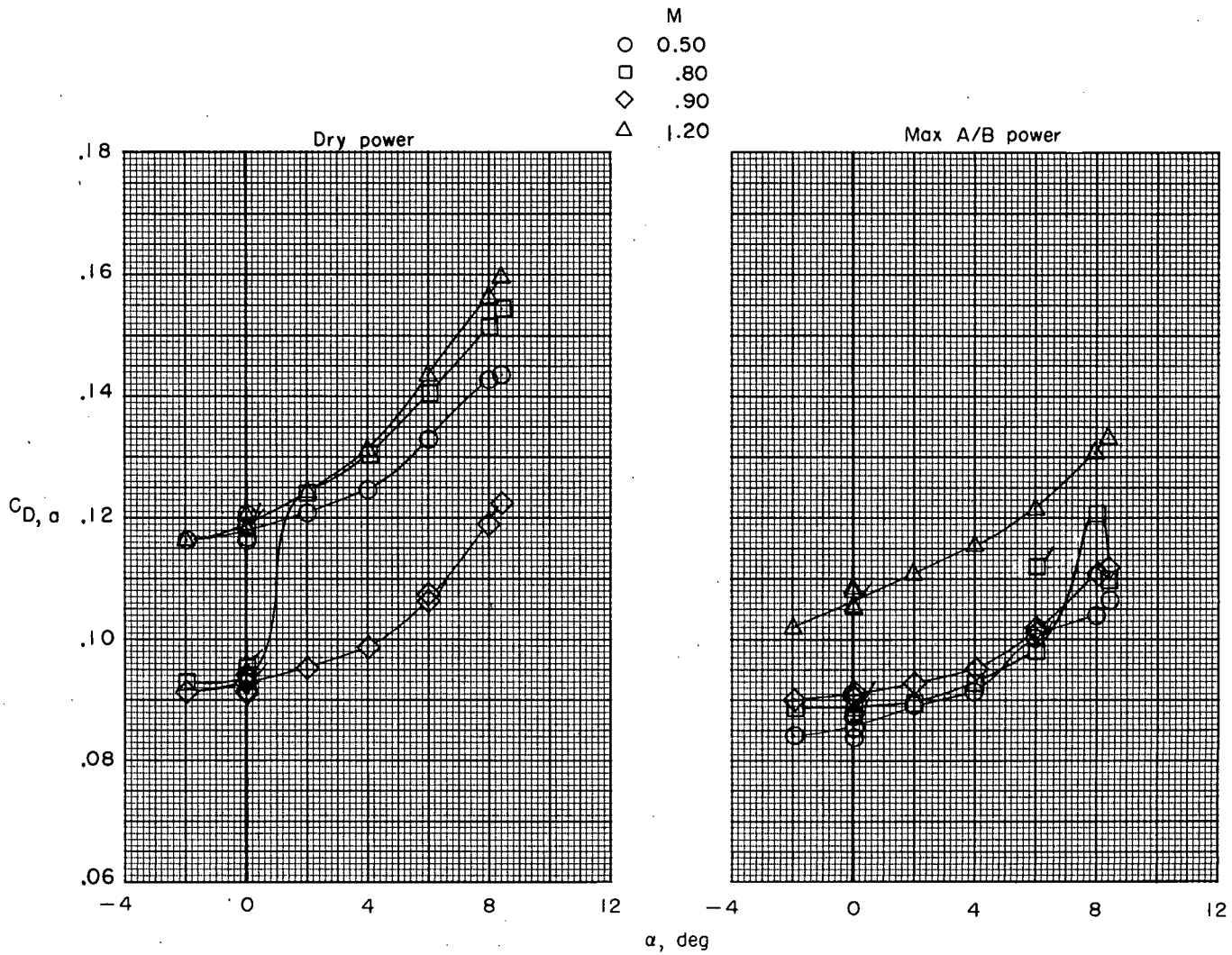


(f) Wide-spaced afterbody; short alternate 2 interfairing.

Figure 15.- Concluded.

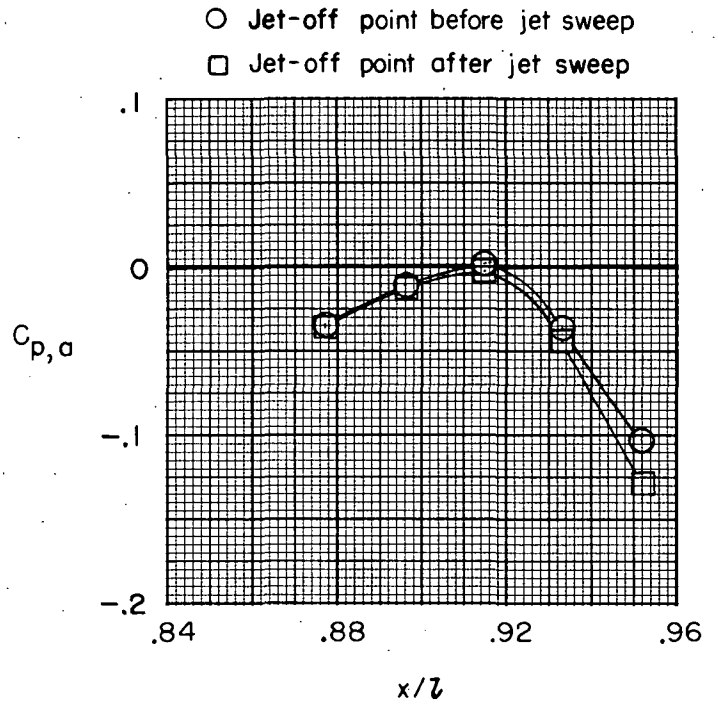


Figure 16.- Comparison of jet-off pressure distributions before and after jet sweep. Wide-spaced afterbody; short alternate 2 interfairing; max A/B power nozzles; M = 0.80; $\alpha = 6.00^{o}$.

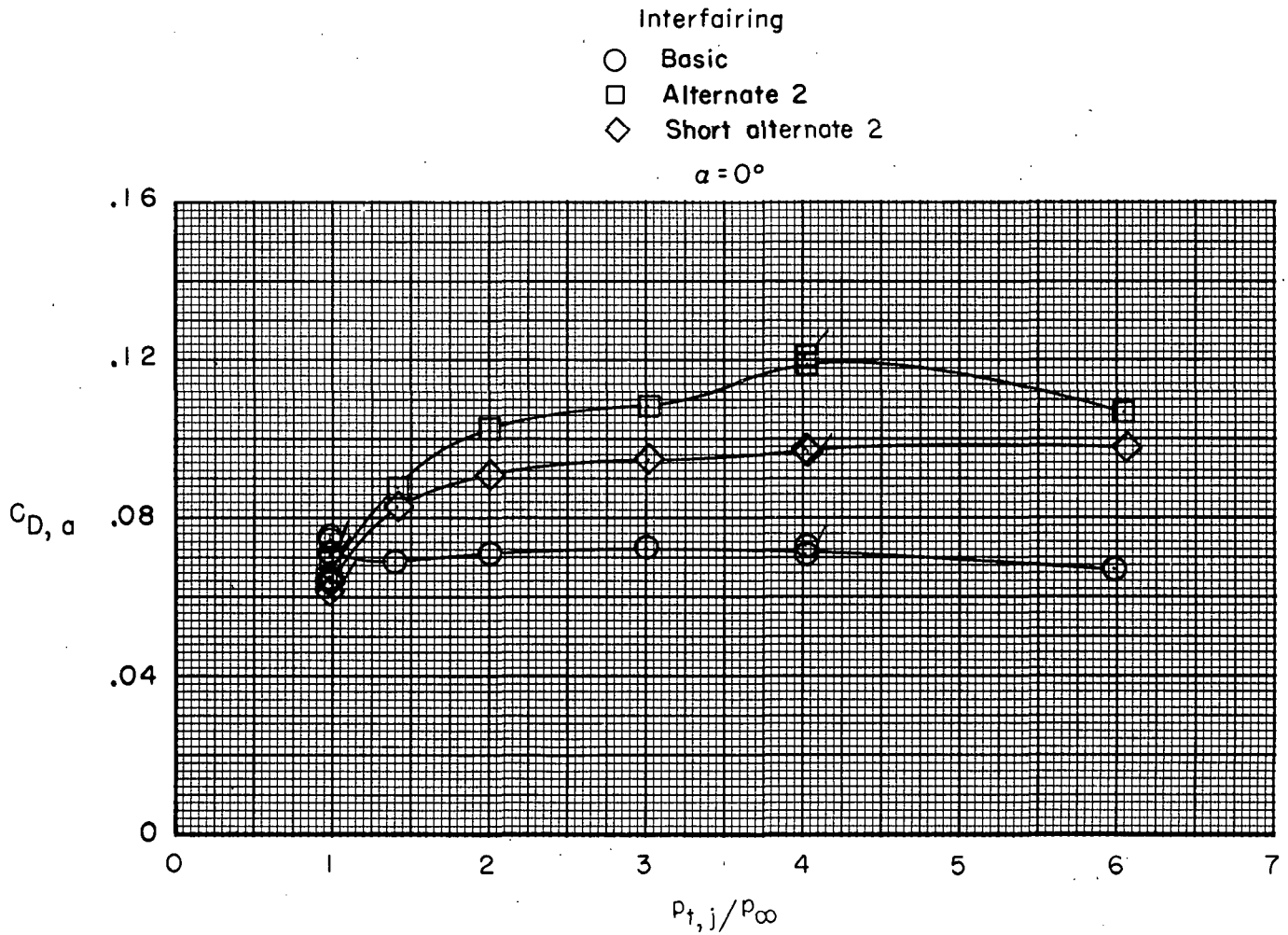


(a) M = 0.50.

Figure 17.- Variation of afterbody drag coefficient with jet total-pressure ratio. Close-spaced afterbody; dry-power nozzle; symbols with flags indicate decreasing jet total-pressure ratio.

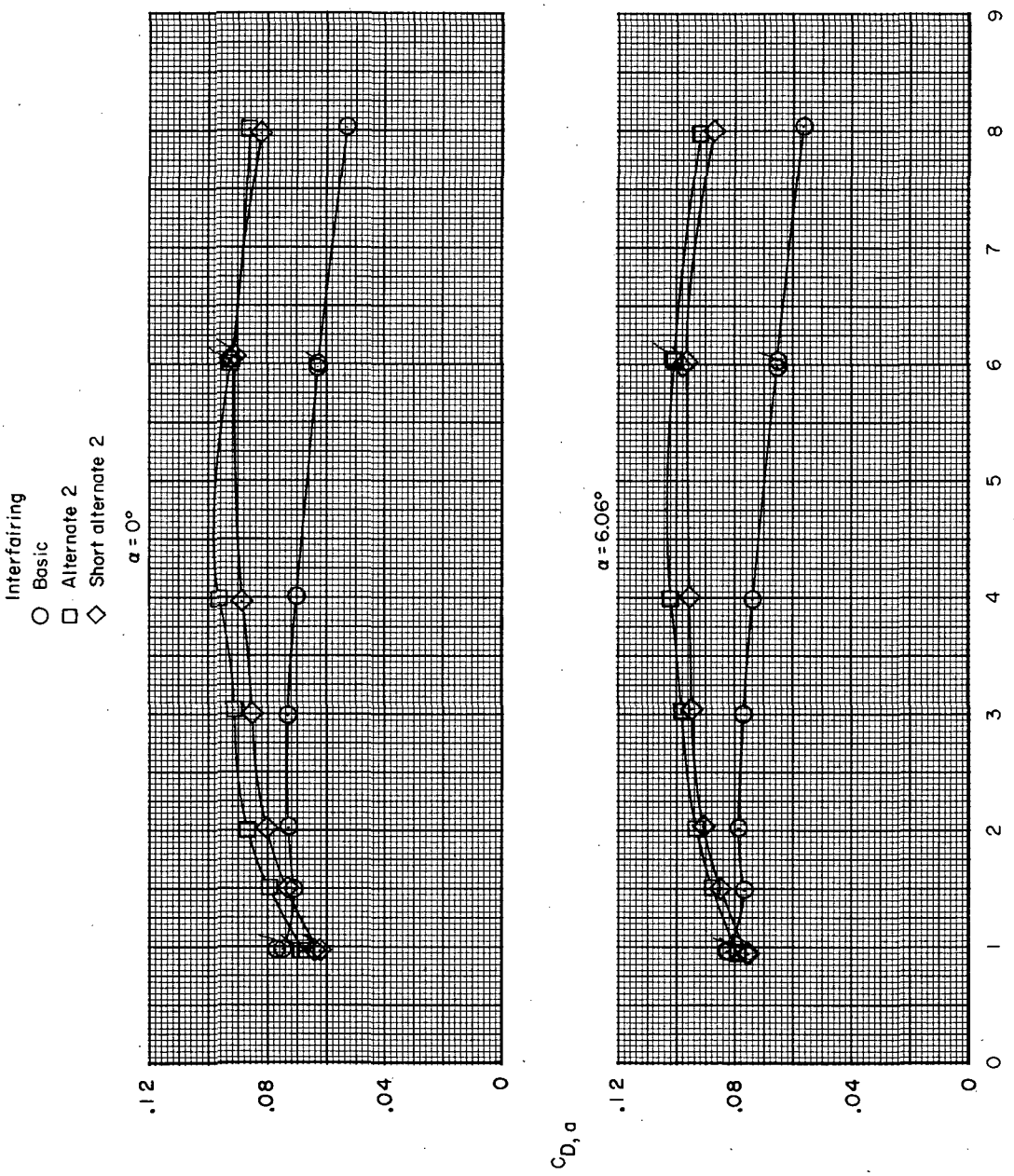


(b) M = 0.80.

Figure 17.- Continued.

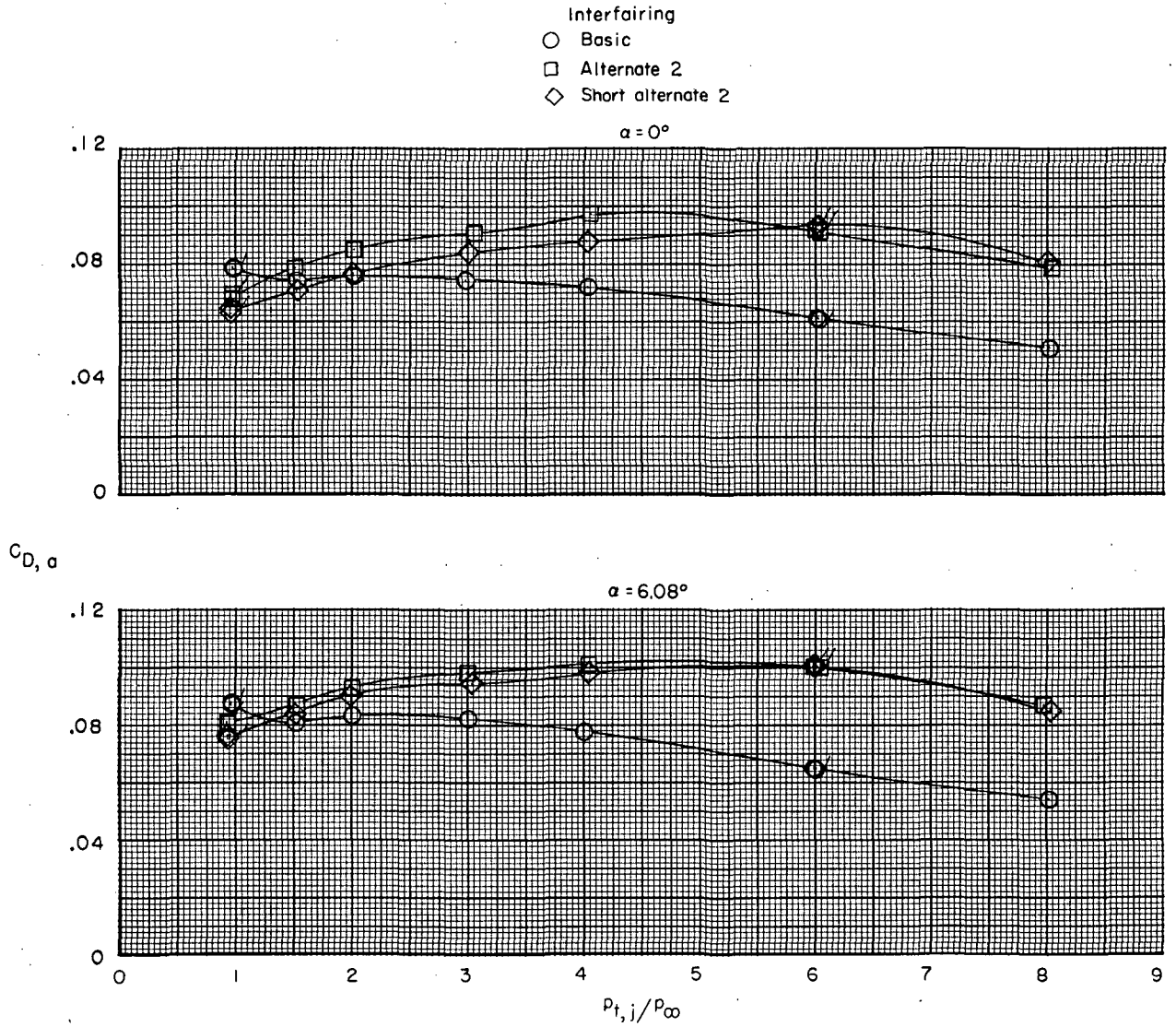


(c) M = 0.90.

Figure 17.- Continued.

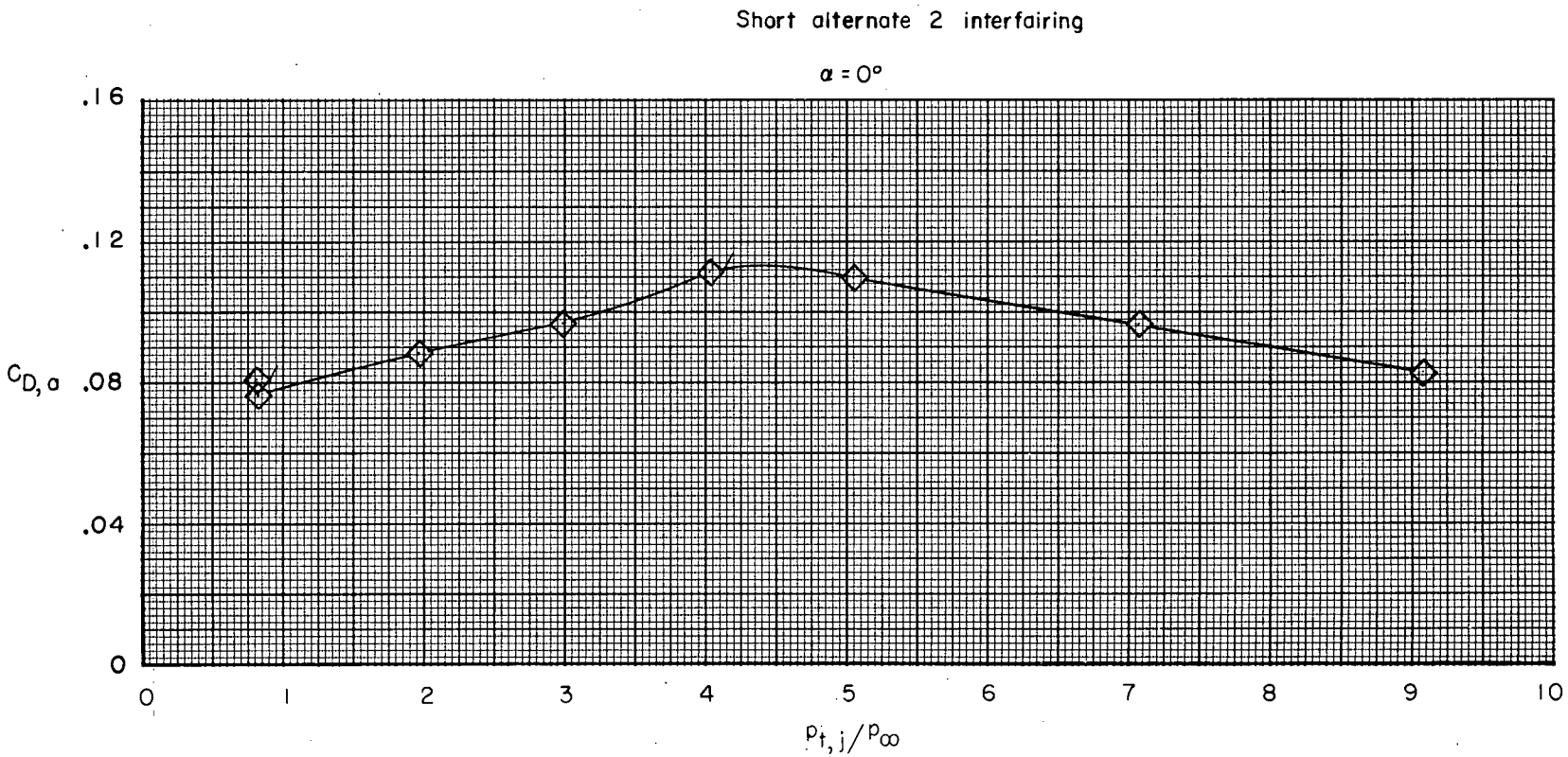


(d) M = 1.20.

Figure 17.- Concluded.

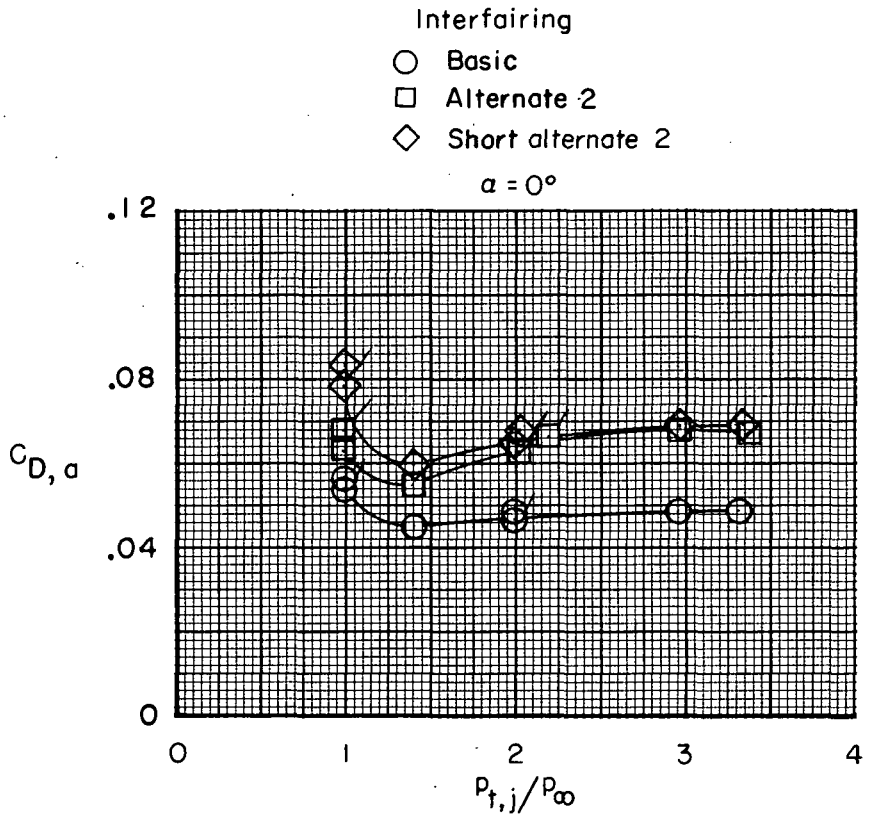


(a) M = 0.50.

Figure 18.- Variation of afterbody drag coefficient with jet total-pressure ratio. Close-spaced afterbody, max A/B power nozzles; symbols with flags indicate decreasing jet total-pressure ratio.

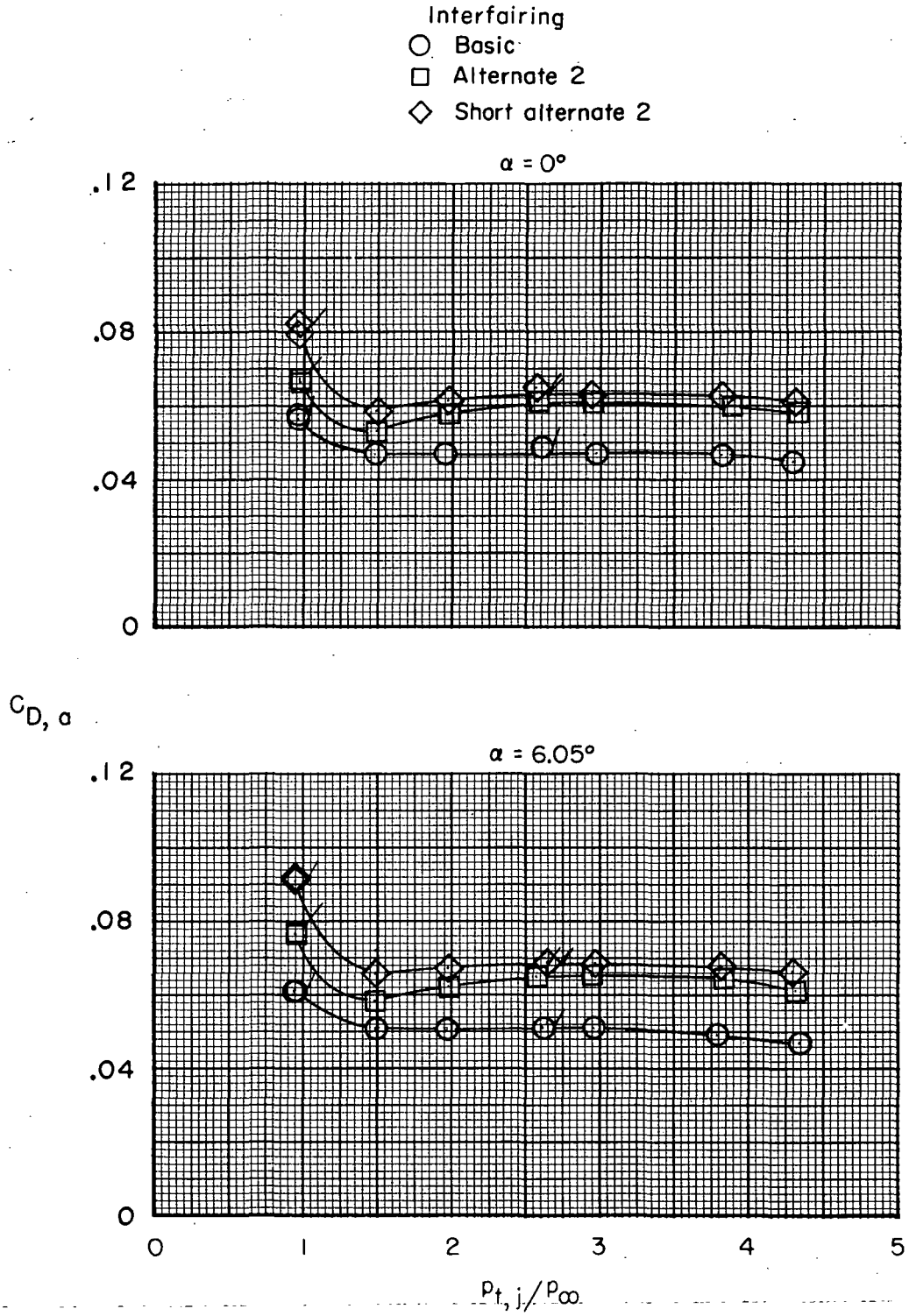


(b) M = 0.80.

Figure 18.- Continued.

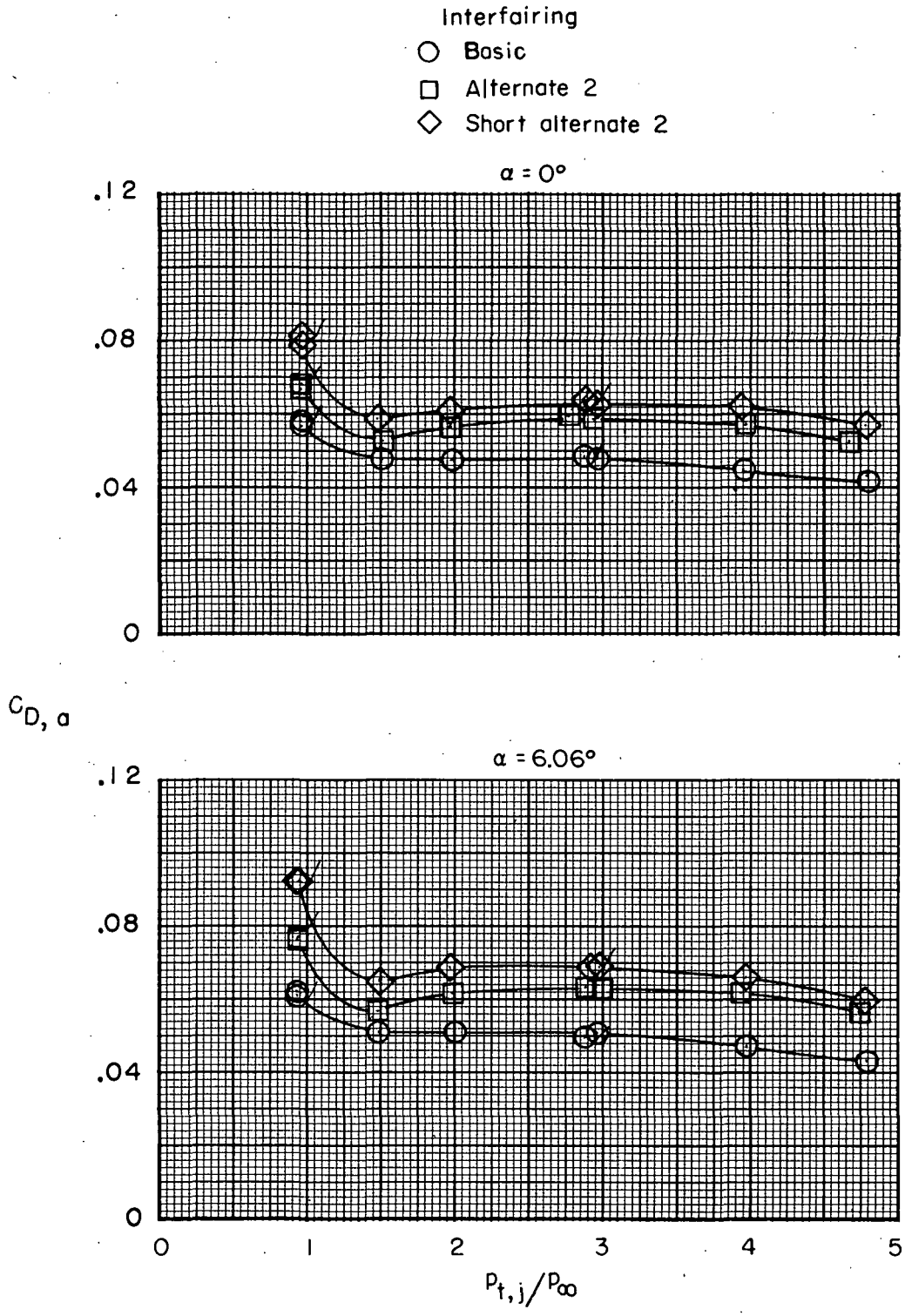


(c) M = 0.90.

Figure 18.- Continued.

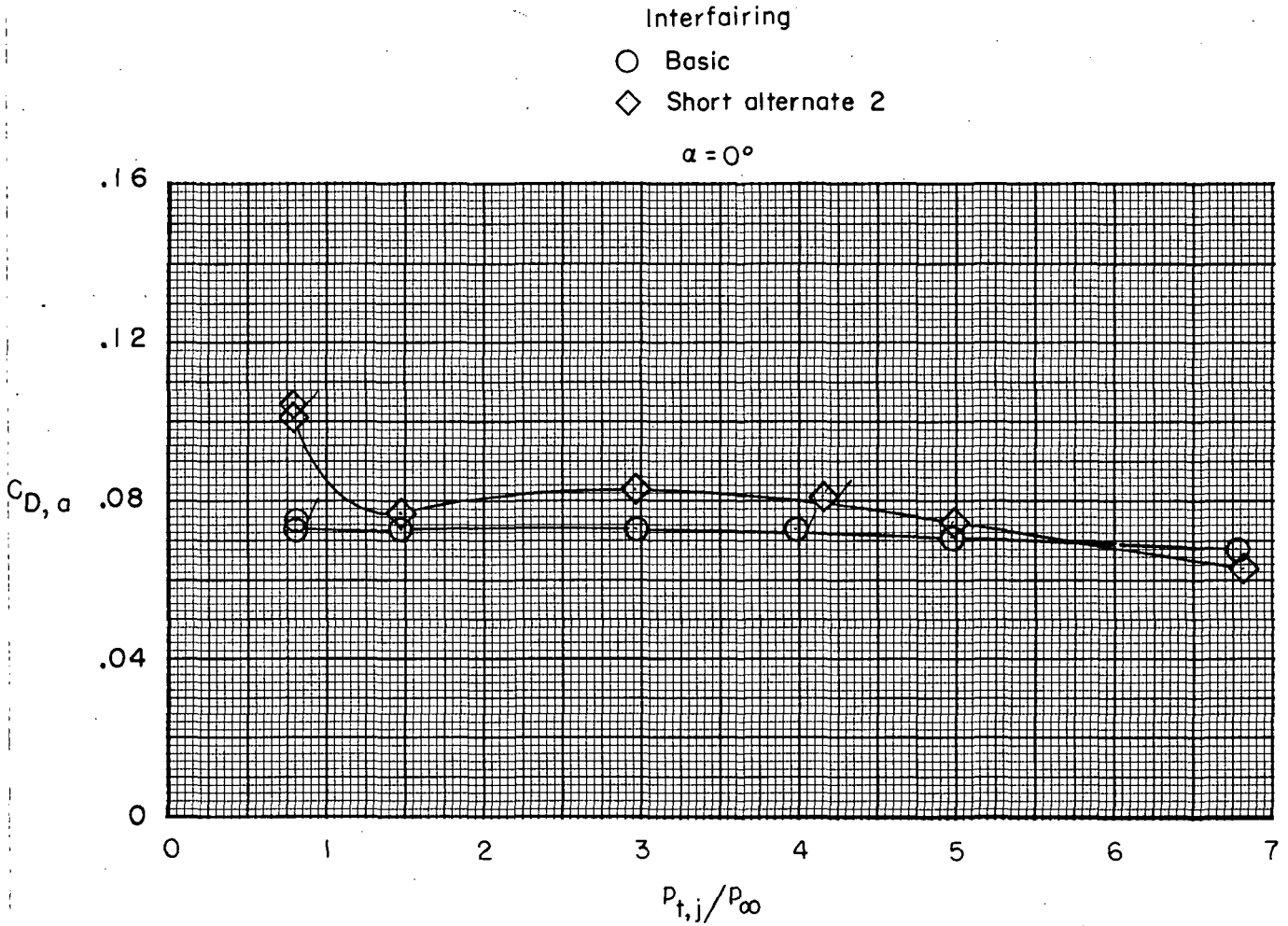


(d) M = 1.20.

Figure 18.- Concluded.

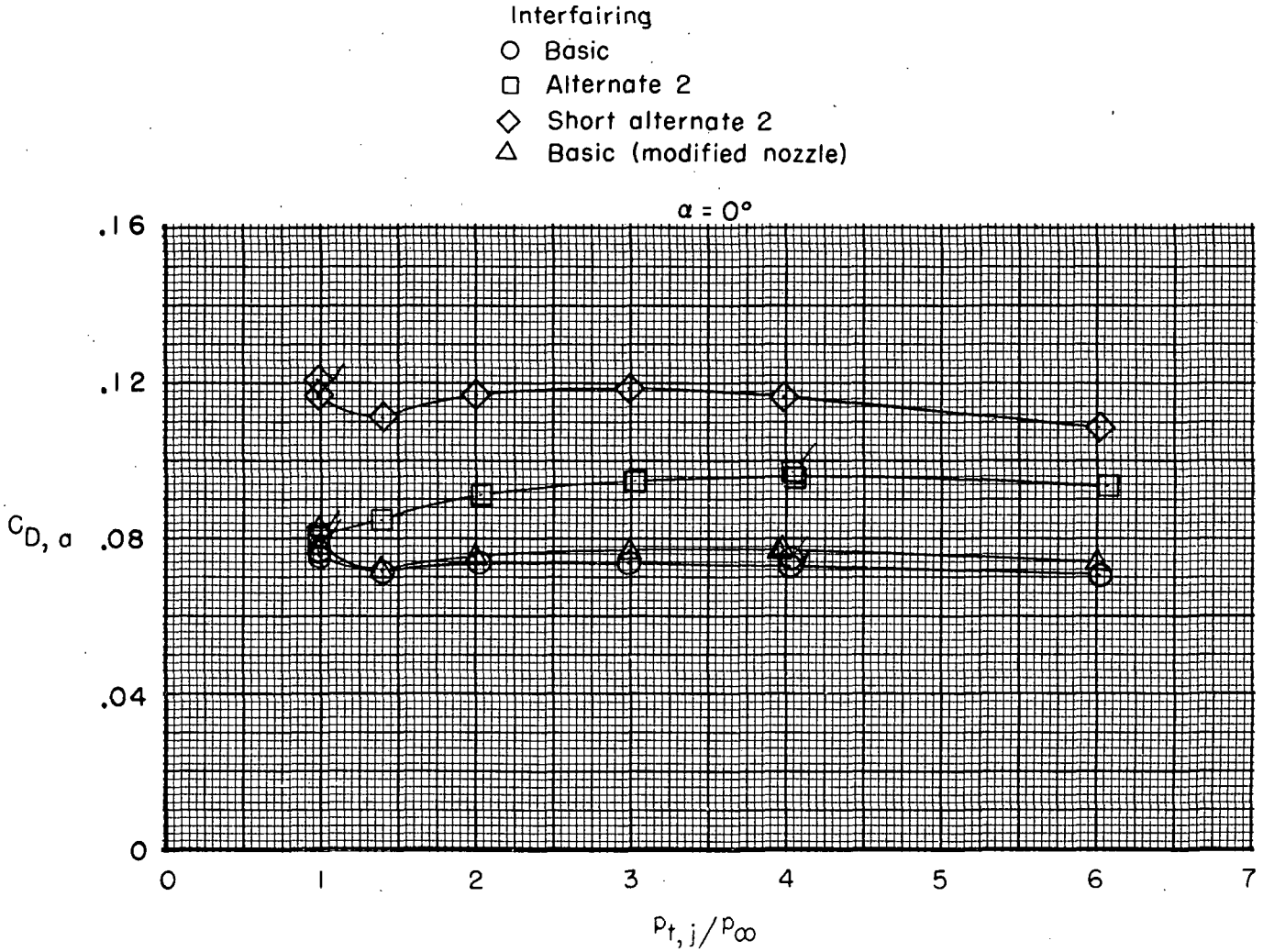


(a) M = 0.50.

Figure 19.- Variation of afterbody drag coefficient with jet total-pressure ratio. Wide-spaced afterbody; dry-power nozzles; symbols with flags indicate decreasing jet total-pressure ratio.

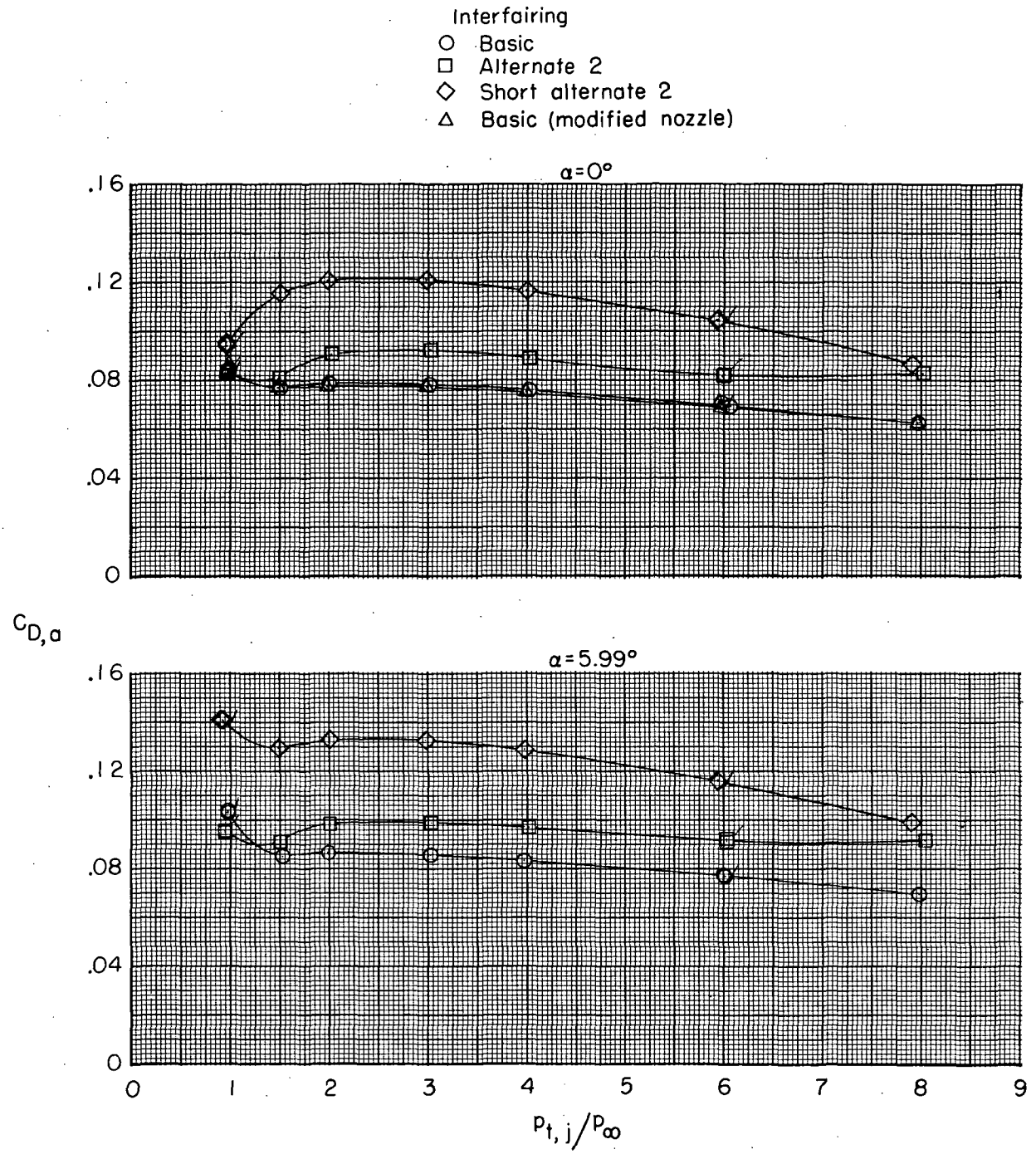


(b) M = 0.80.

Figure 19.- Continued.

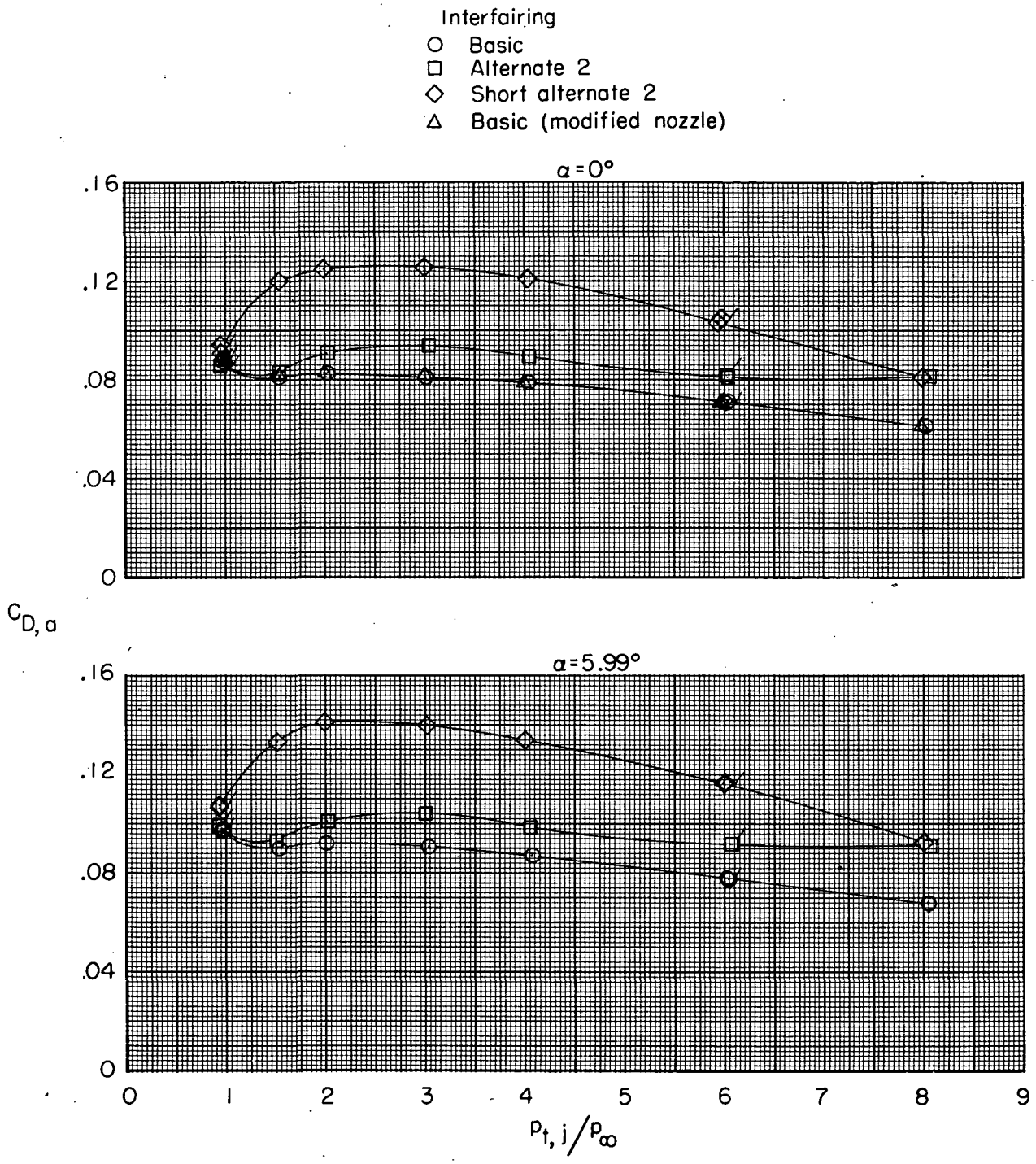


(c) M = 0.90.

Figure 19.- Continued.

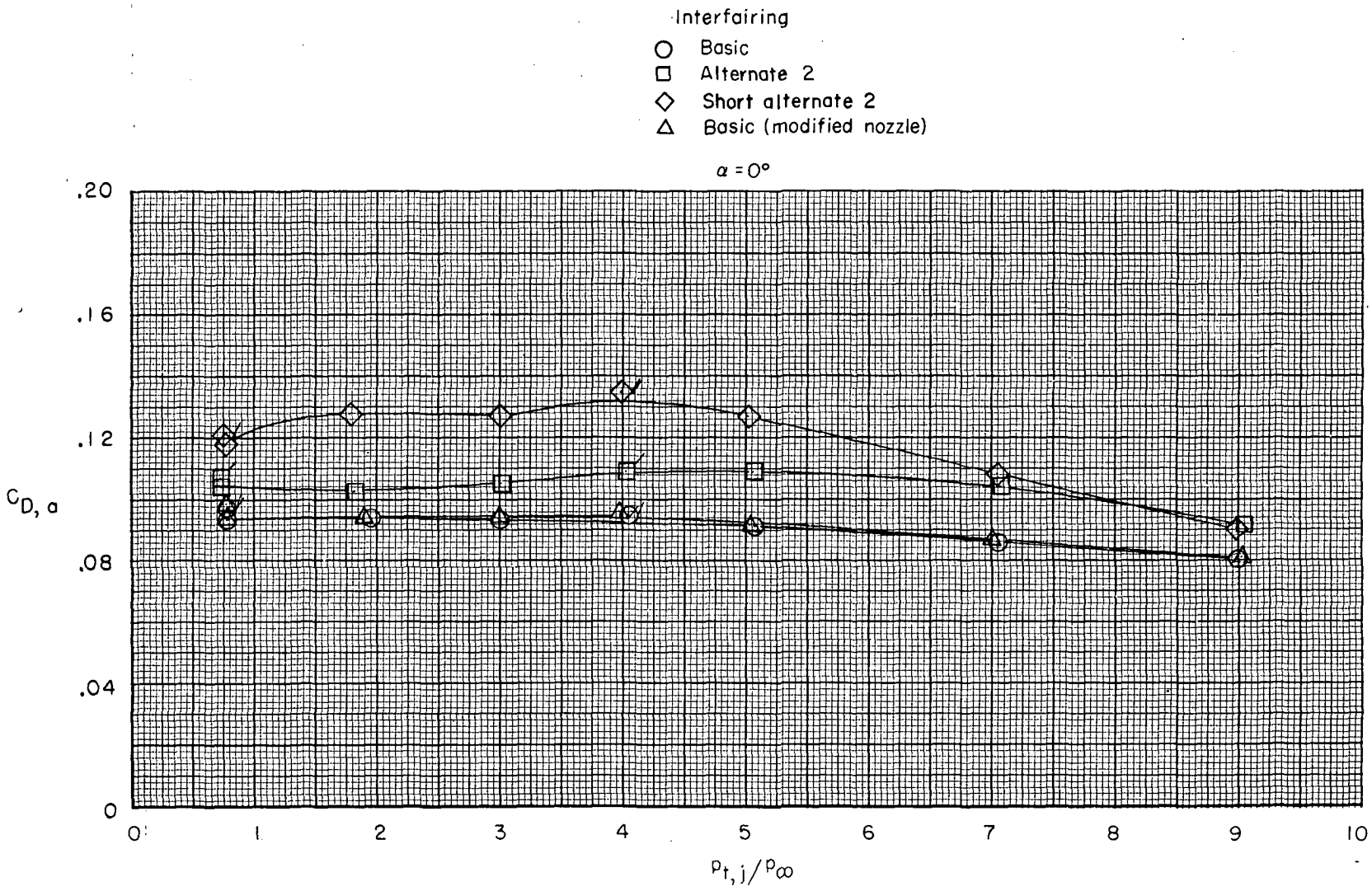


(d) M = 1.20.

Figure 19.- Concluded.

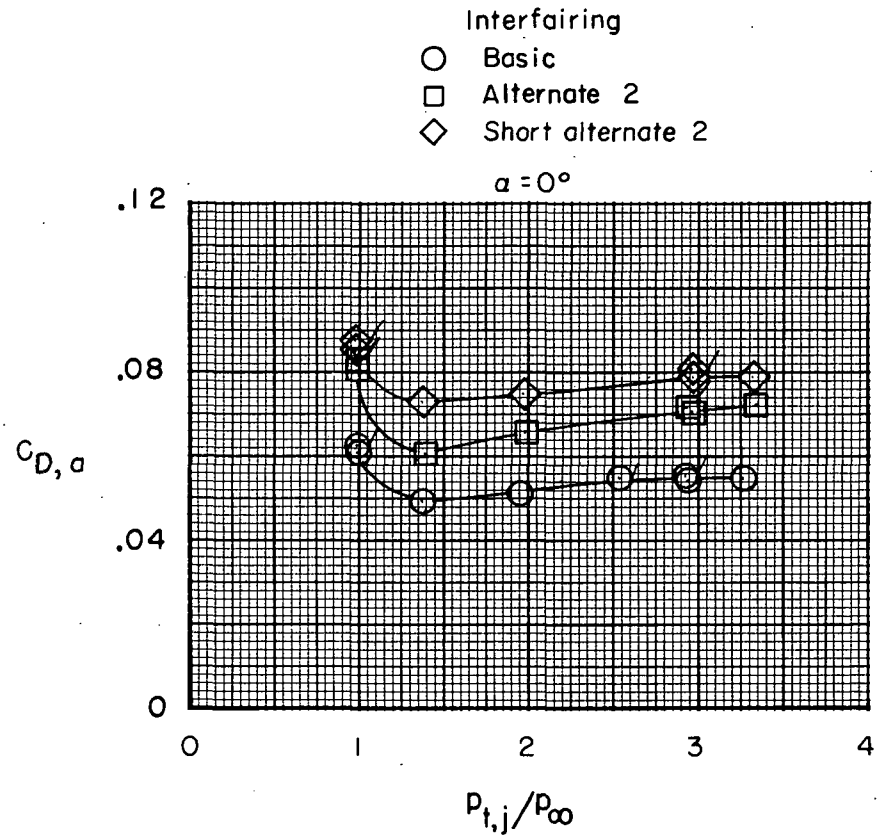


(a) M = 0.50.

Figure 20.- Variation of afterbody drag coefficient with jet total-pressure ratio. Wide-spaced afterbody; max A/B power nozzles; symbols with flags indicate decreasing values of jet total-pressure ratio.

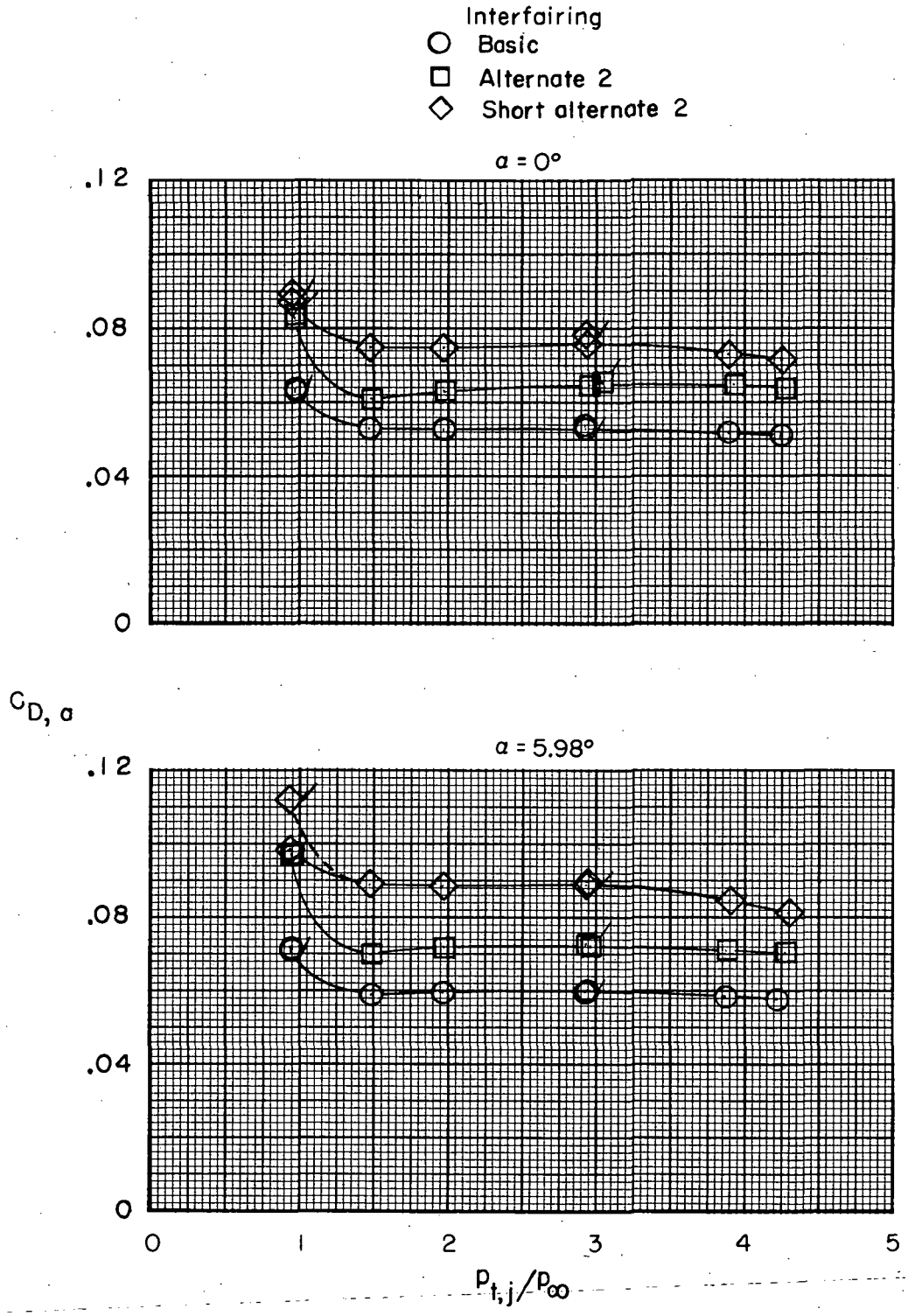


(b) M = 0.80.

Figure 20.- Continued.

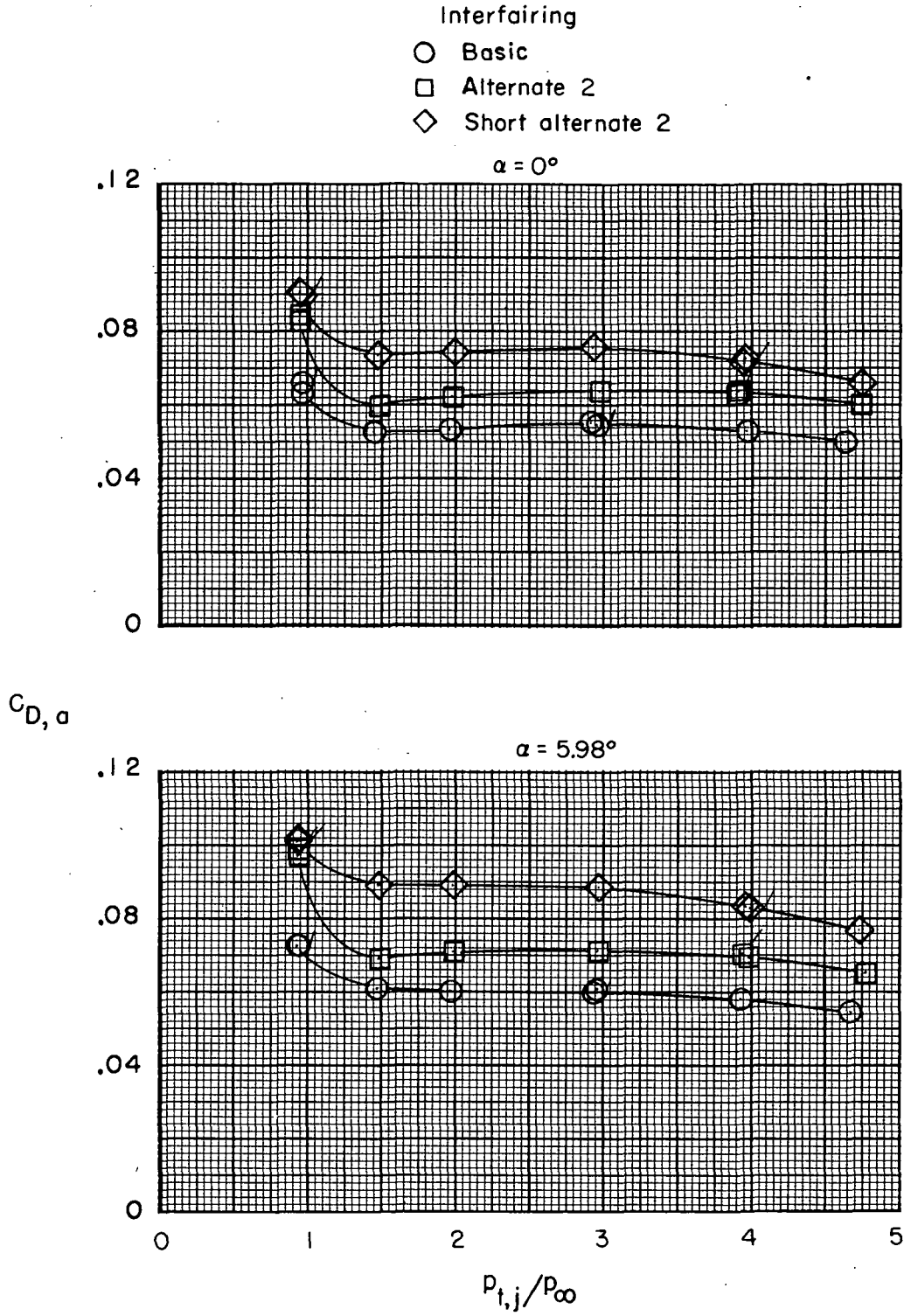


(c) M = 0.90.

Figure 20.- Continued.

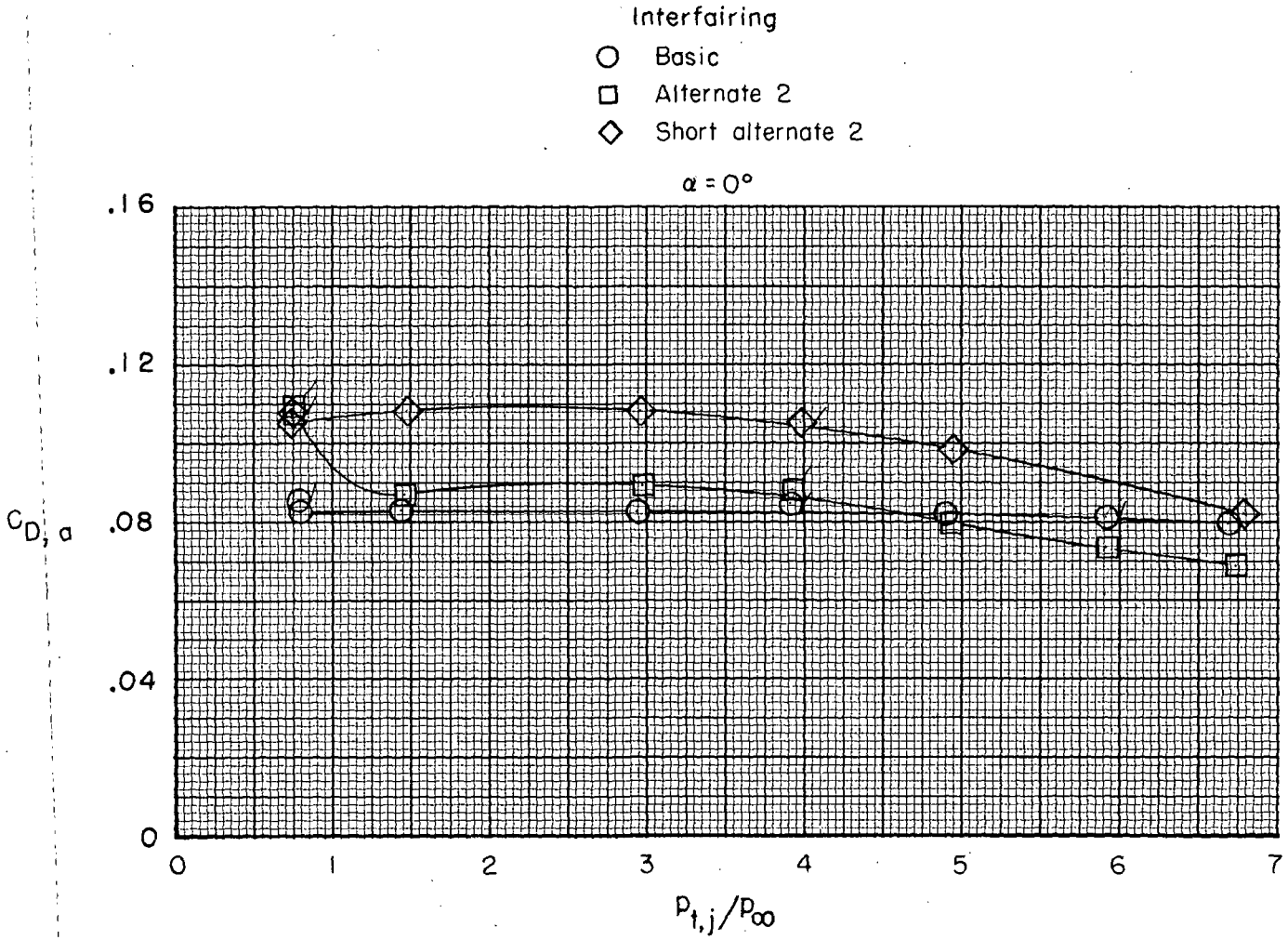


(d) M = 1.20.

Figure 20.- Concluded.

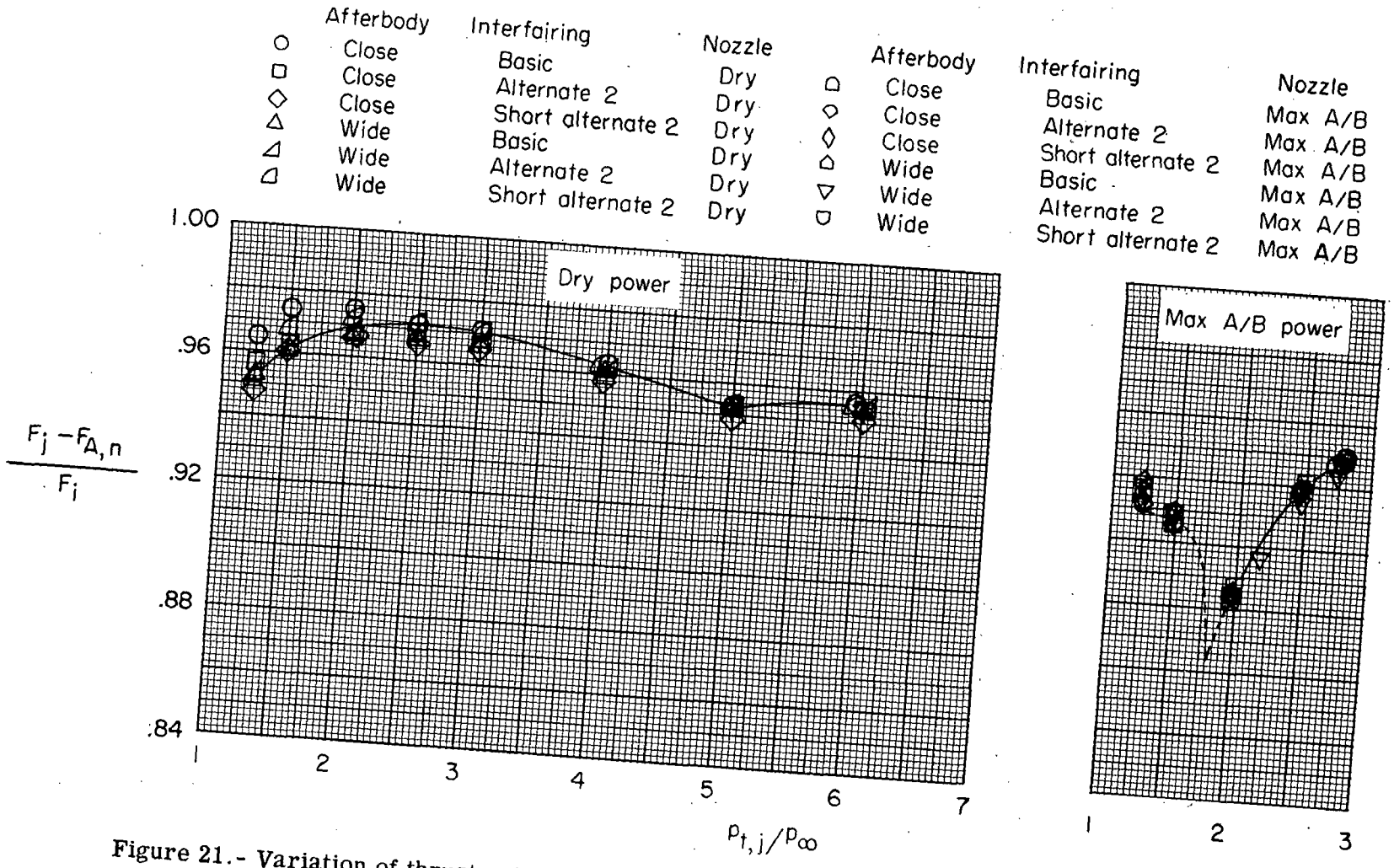


Figure 21.- Variation of thrust-minus-nozzle-axial-force ratio with jet total-pressure ratio at $M = 0$ and $\alpha = 0^o$.

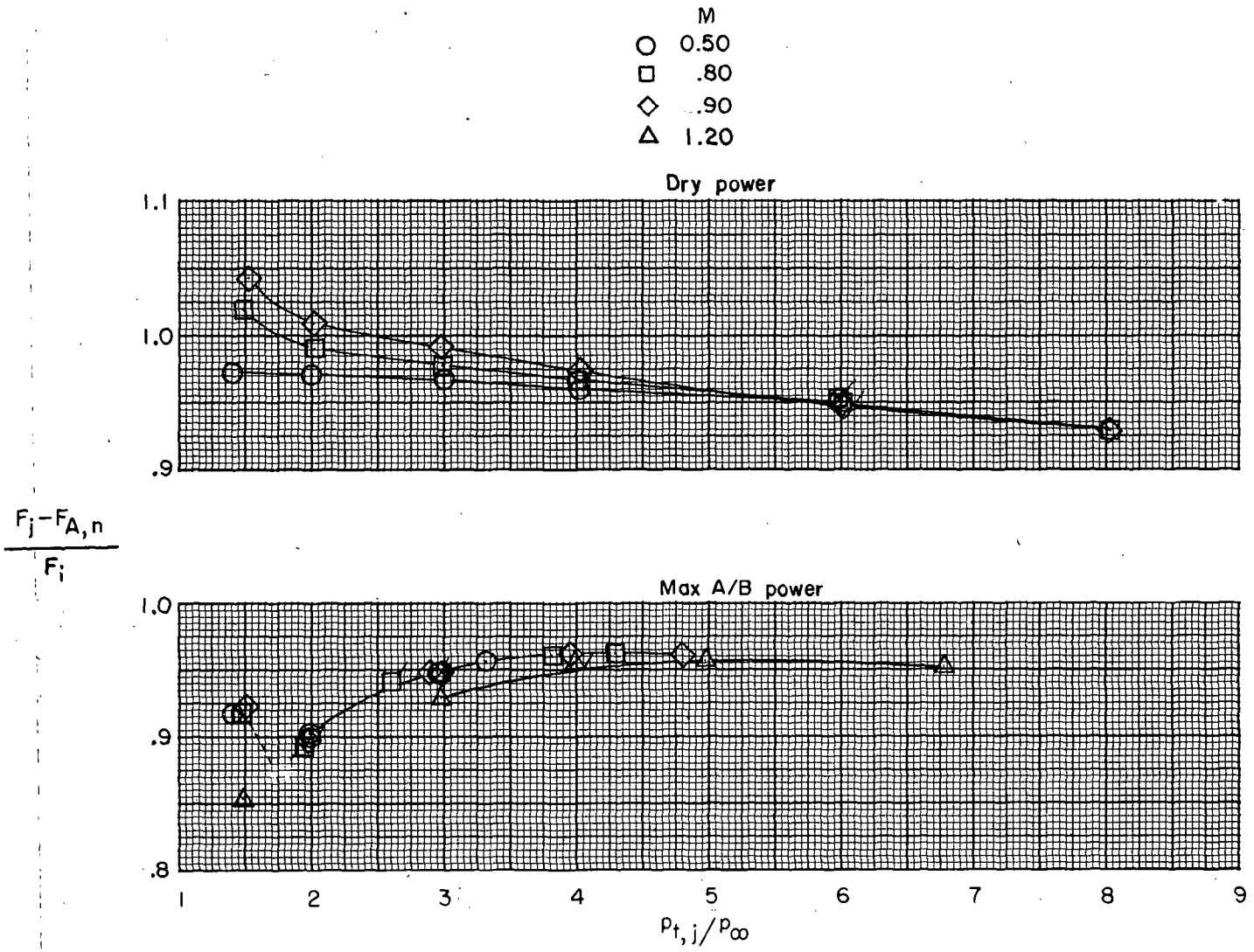


(a) Close-spaced afterbody; basic interfairing.

Figure 22.- Variation of thrust-minus-nozzle-axial-force ratio with jet total-pressure ratio for two nozzle power settings. Symbols with flags indicate decreasing jet total-pressure ratio; $\alpha = 0^o$.

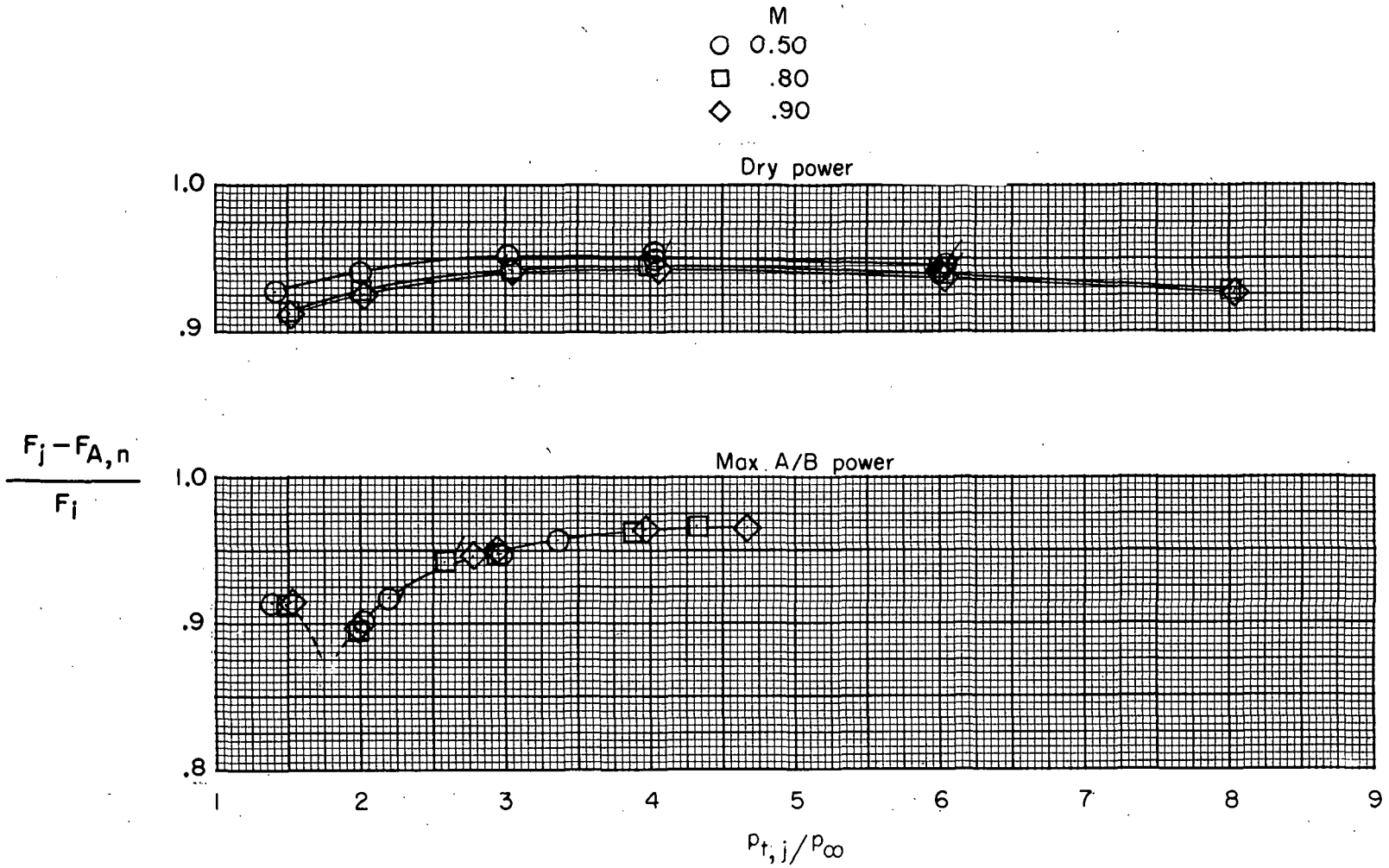


(b) Close-spaced afterbody; alternate 2 interfairing.

Figure 22.- Continued.

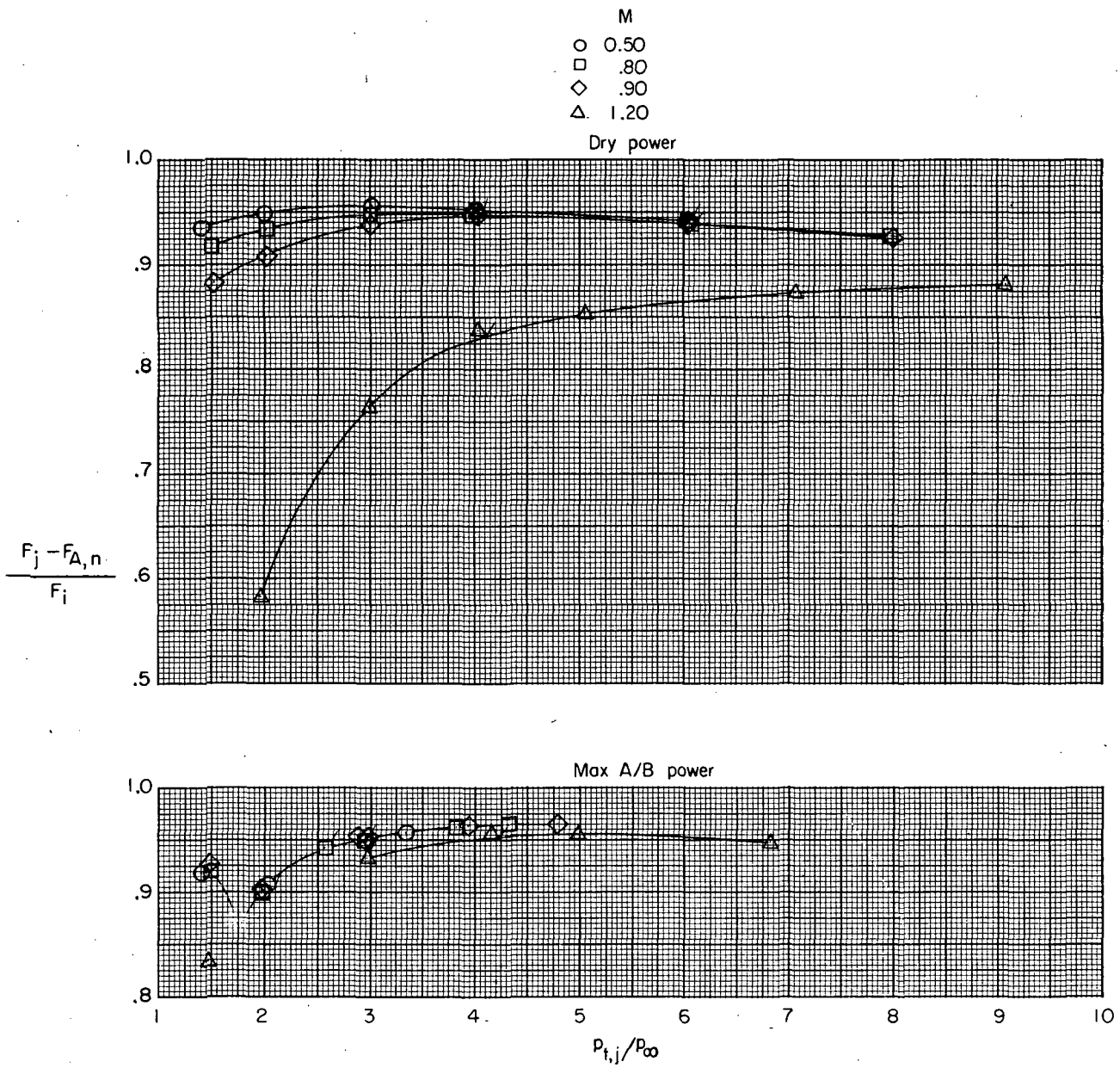


(c) Close-spaced afterbody; short alternate 2 interfairing.

Figure 22.- Continued.

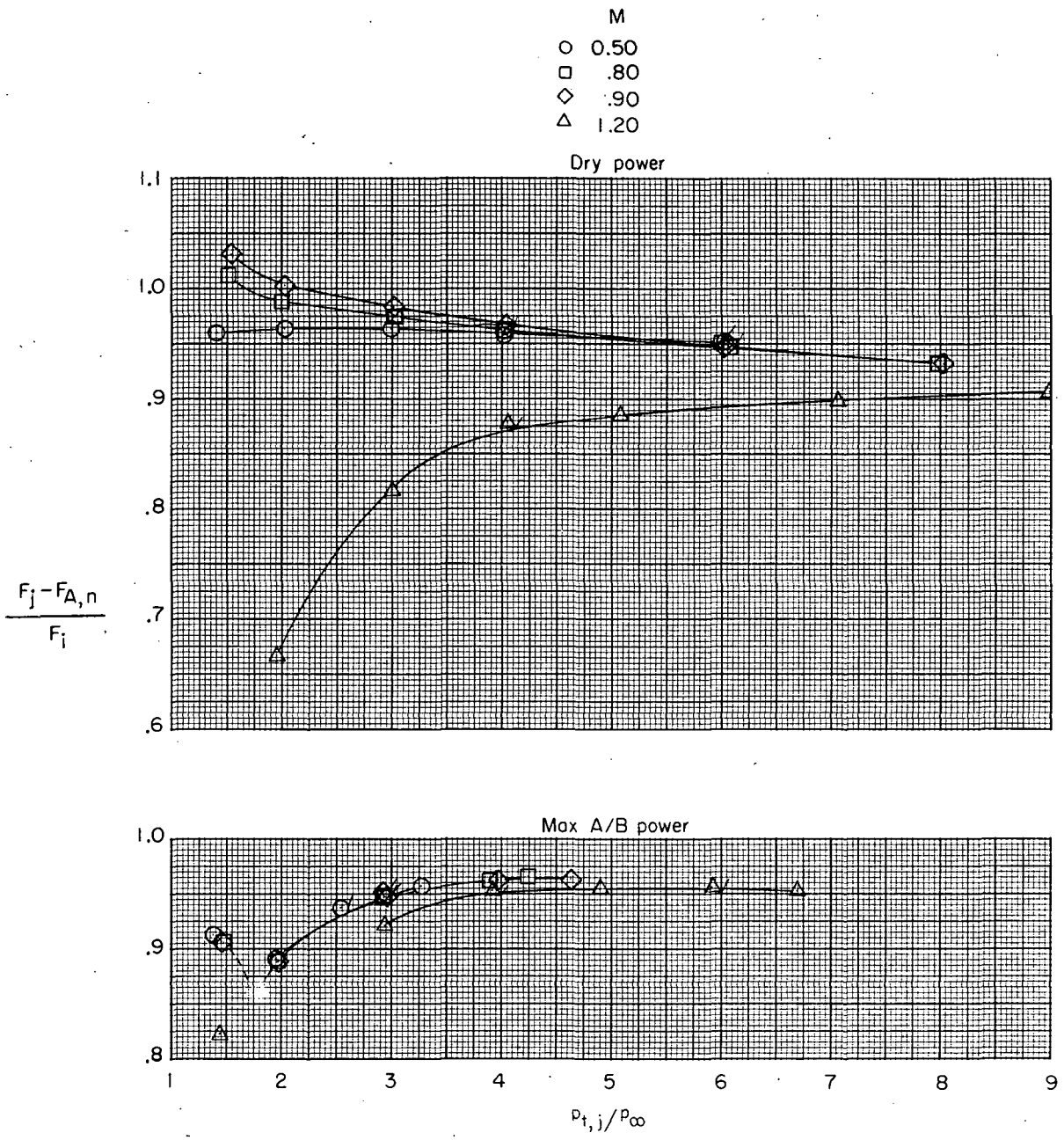


(d) Wide-spaced afterbody; basic interfairing.

Figure 22.- Continued.

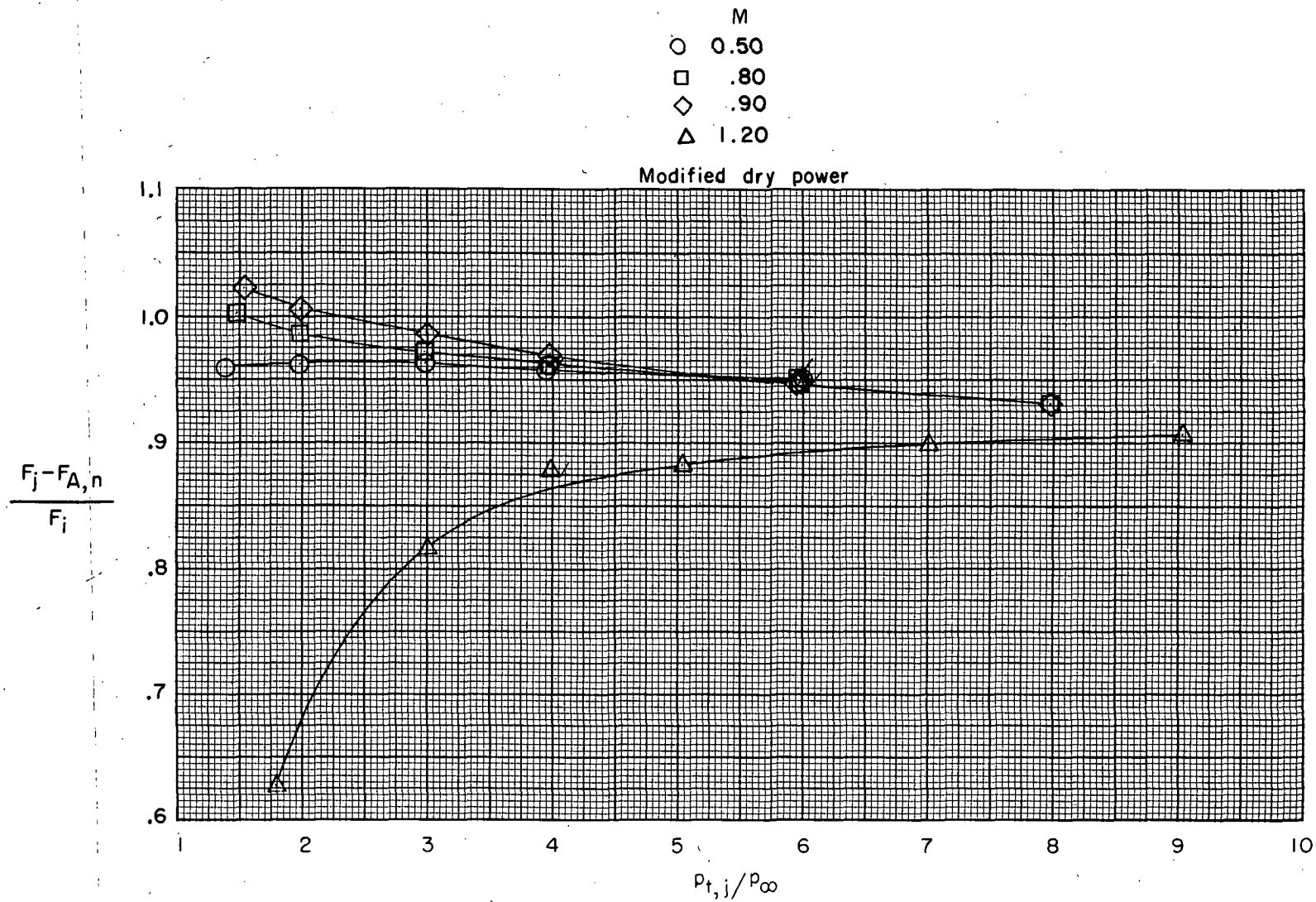


(d) Concluded.

Figure 22.- Continued.

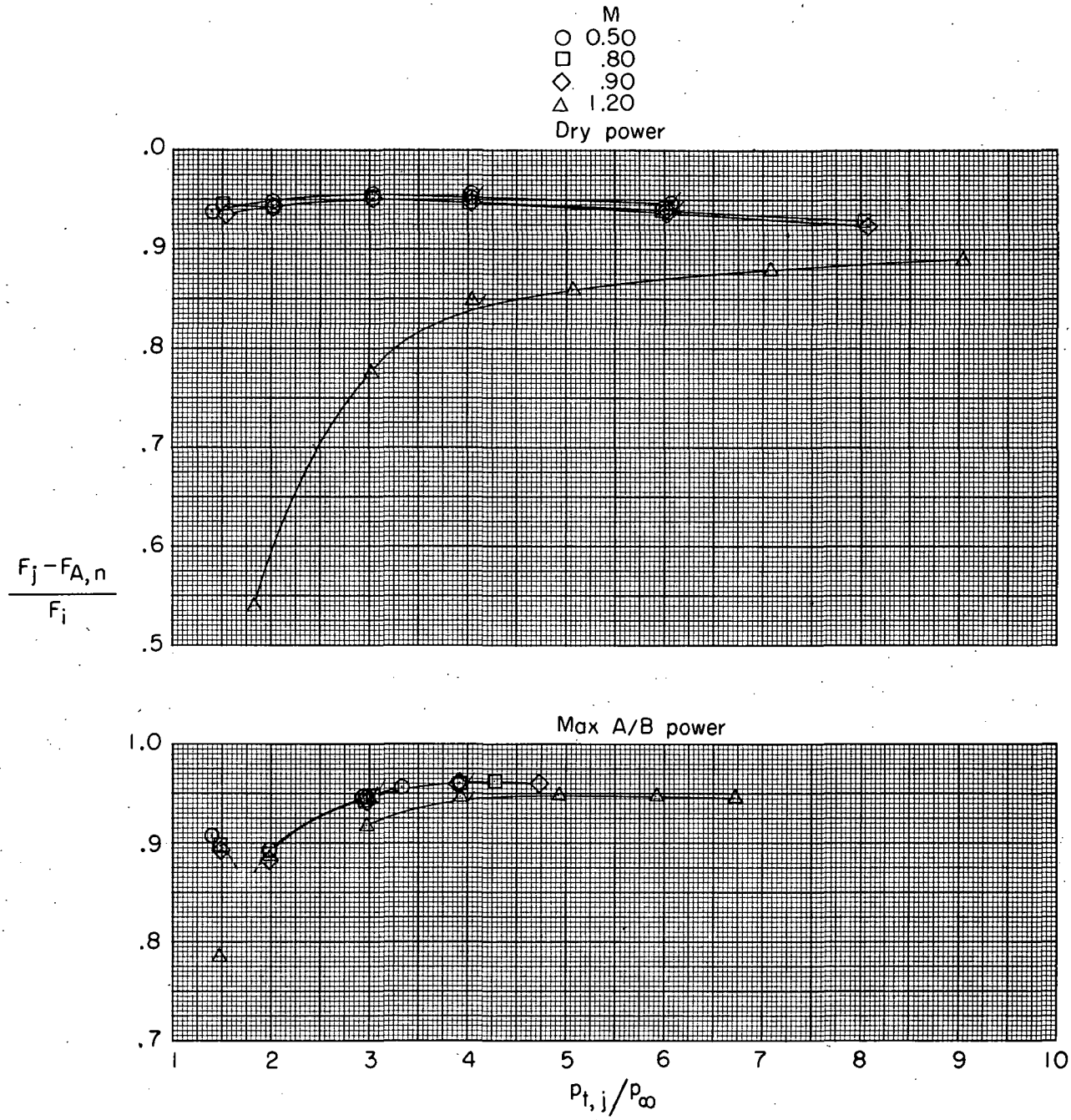


(e) Wide-spaced afterbody; alternate 2 interfairing.

Figure 22.- Continued.

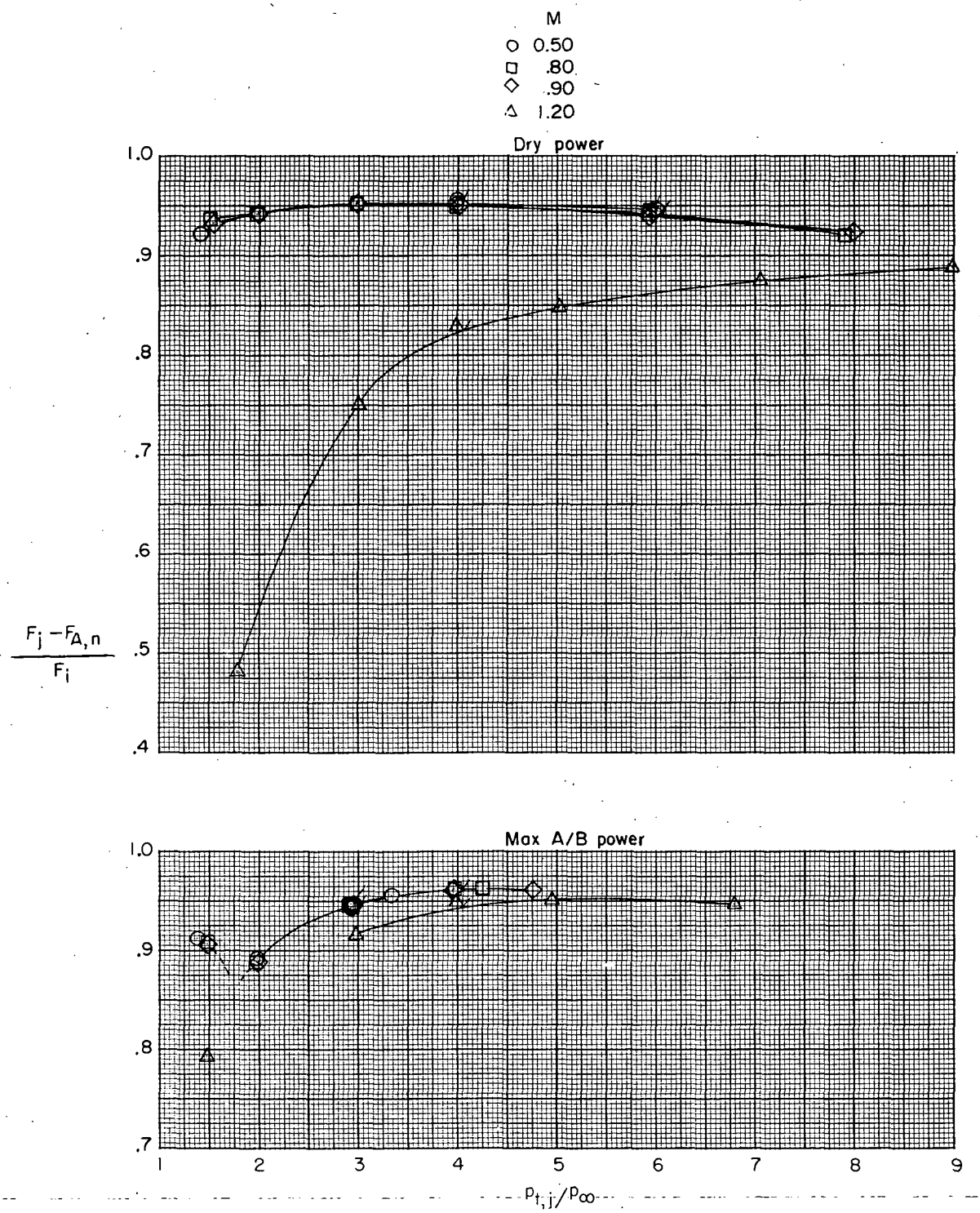


(f) Wide-spaced afterbody; short alternate 2 interfairing.

Figure 22.- Concluded.

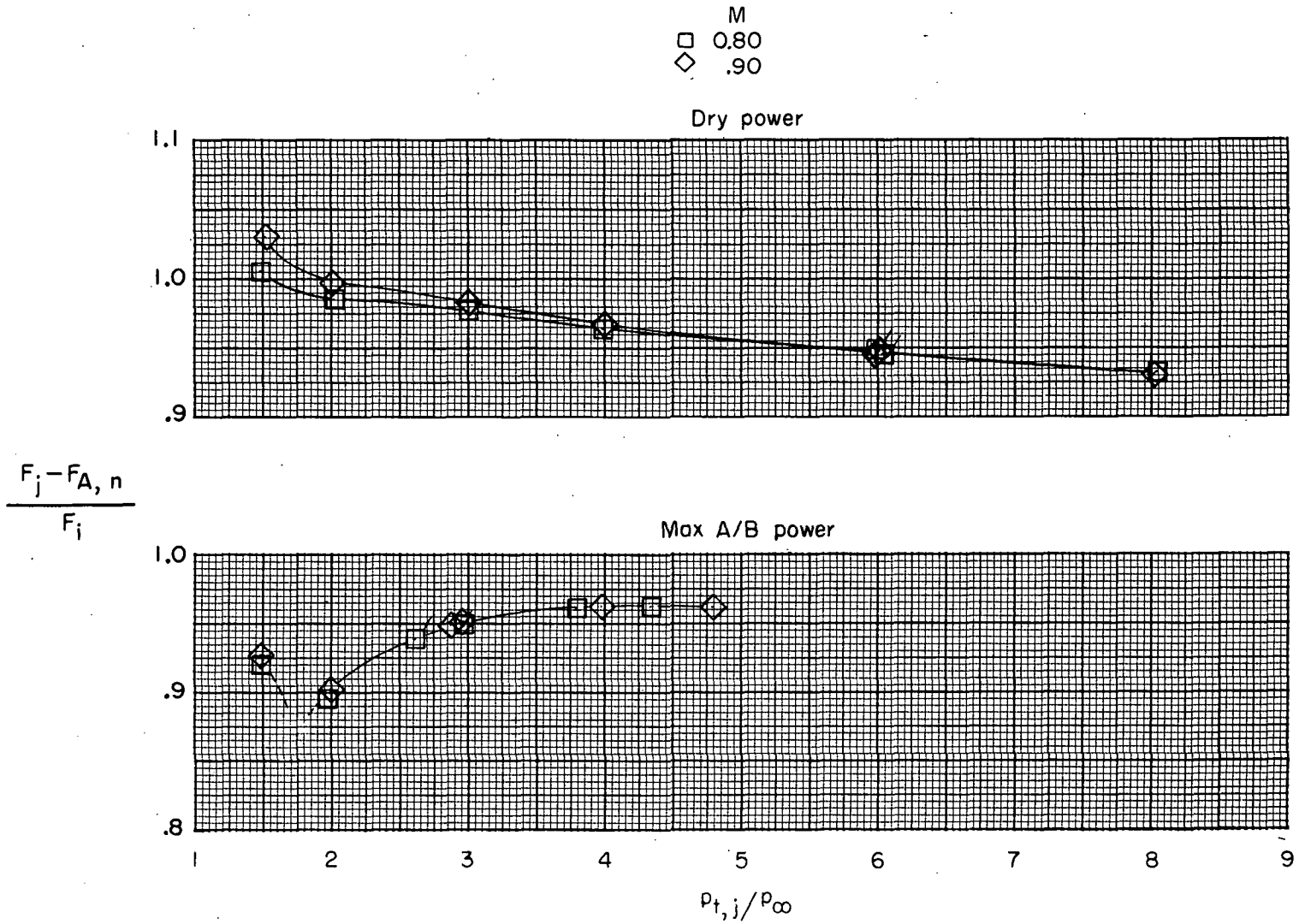


(a) Close-spaced afterbody; basic interfairing.

Figure 23.- Variation of thrust-minus-nozzle-axial-force ratio with jet total-pressure ratio at two nozzle power settings. Symbols with flags indicate decreasing jet total-pressure ratio; nominal $\alpha = 6^{o}$.

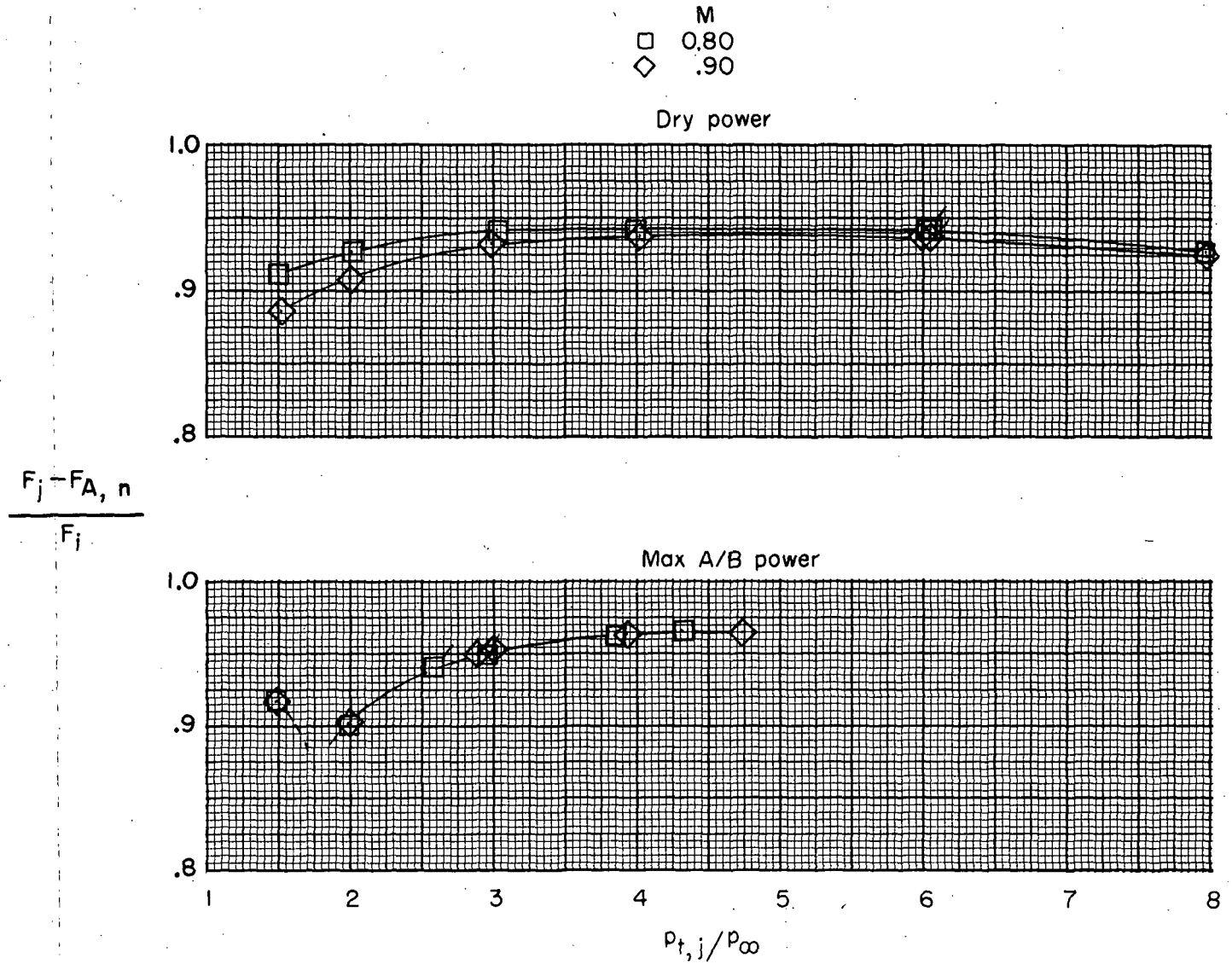


(b) Close-spaced afterbody; alternate 2 interfairing.

Figure 23.- Continued.

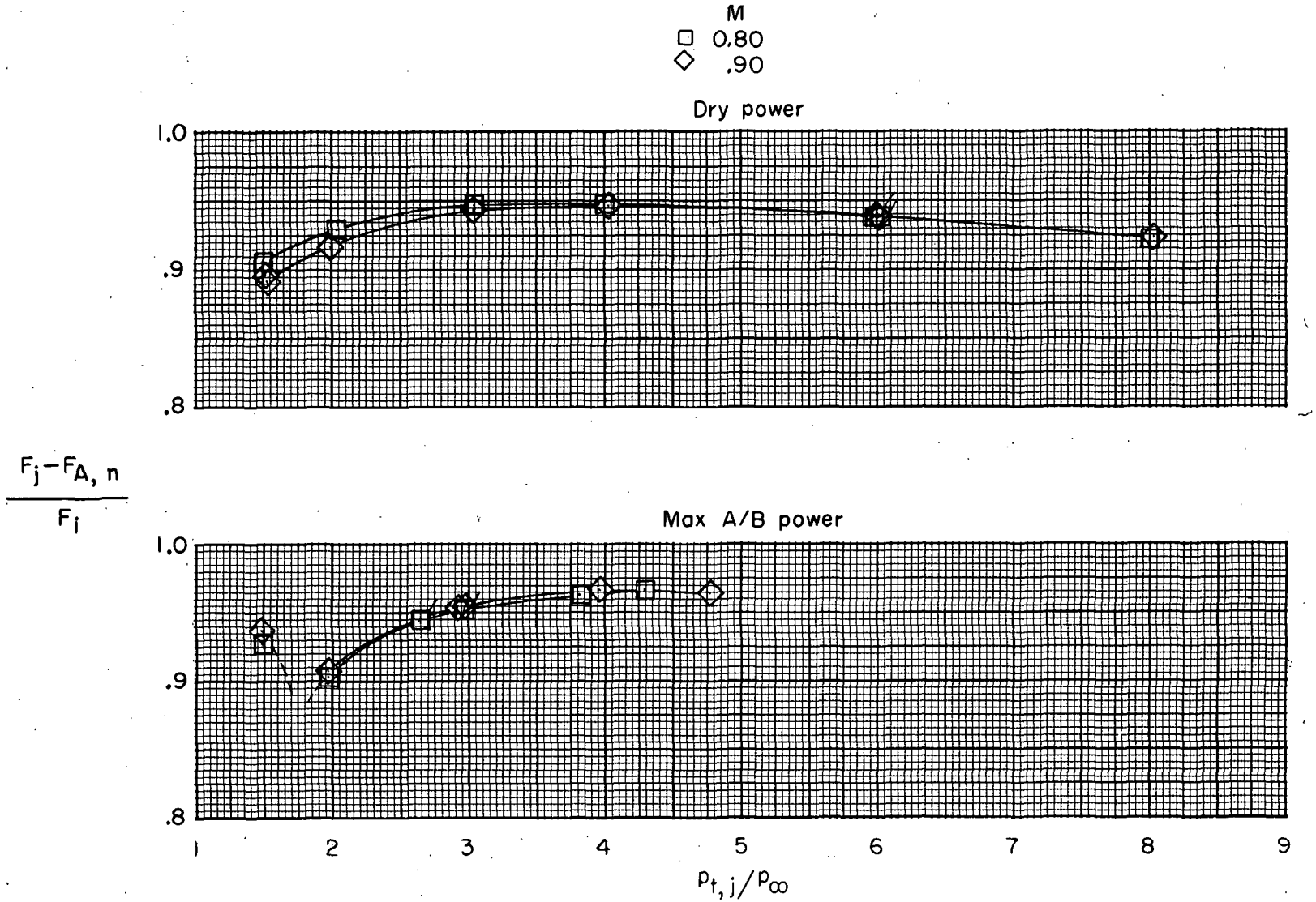


(c) Close-spaced afterbody; short alternate 2 interfairing.

Figure 23.- Continued.

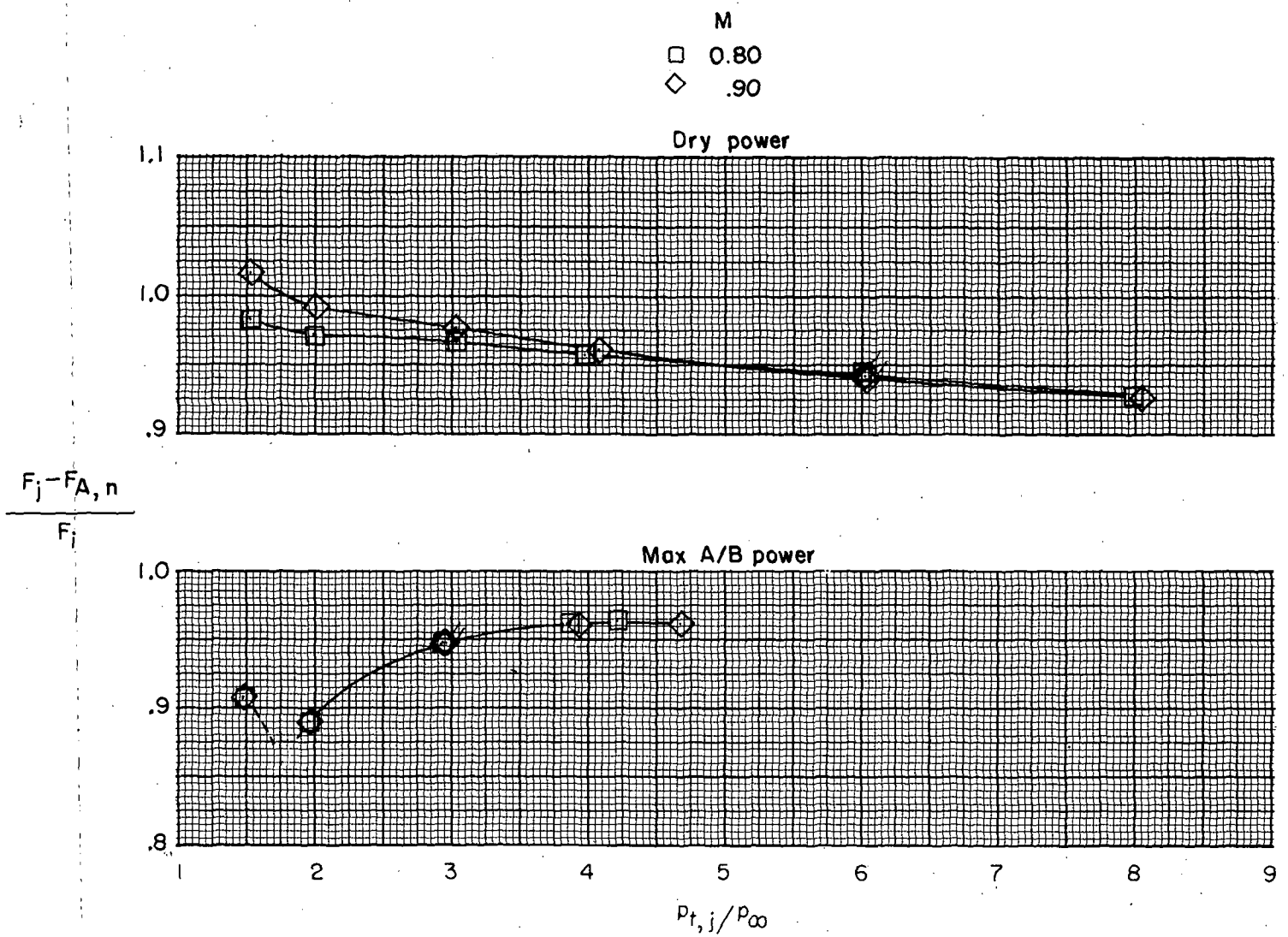


(d) Wide-spaced afterbody; basic interfairing.

Figure 23.- Continued.

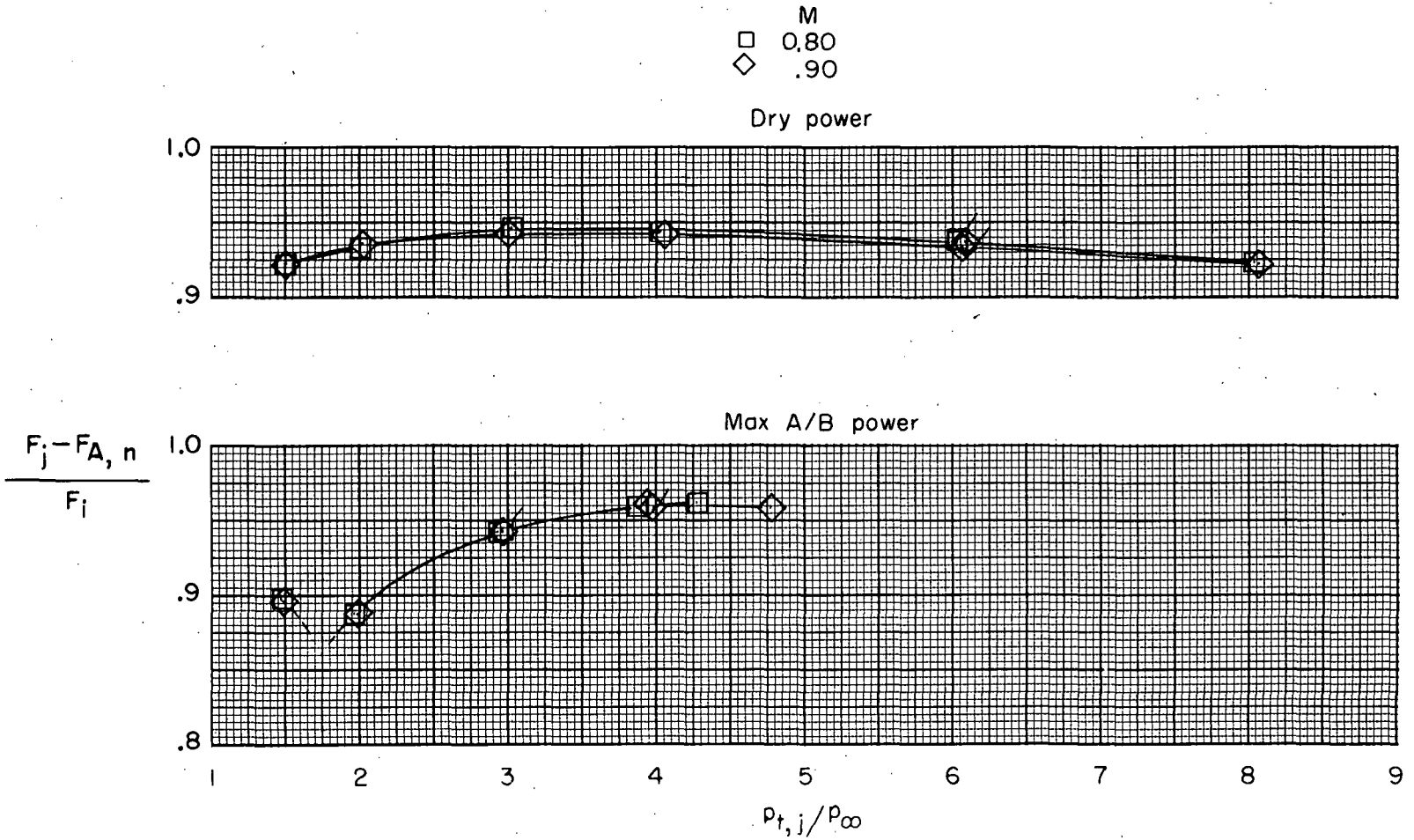


(e) Wide-spaced afterbody; alternate 2 interfairing.

Figure 23.- Continued.

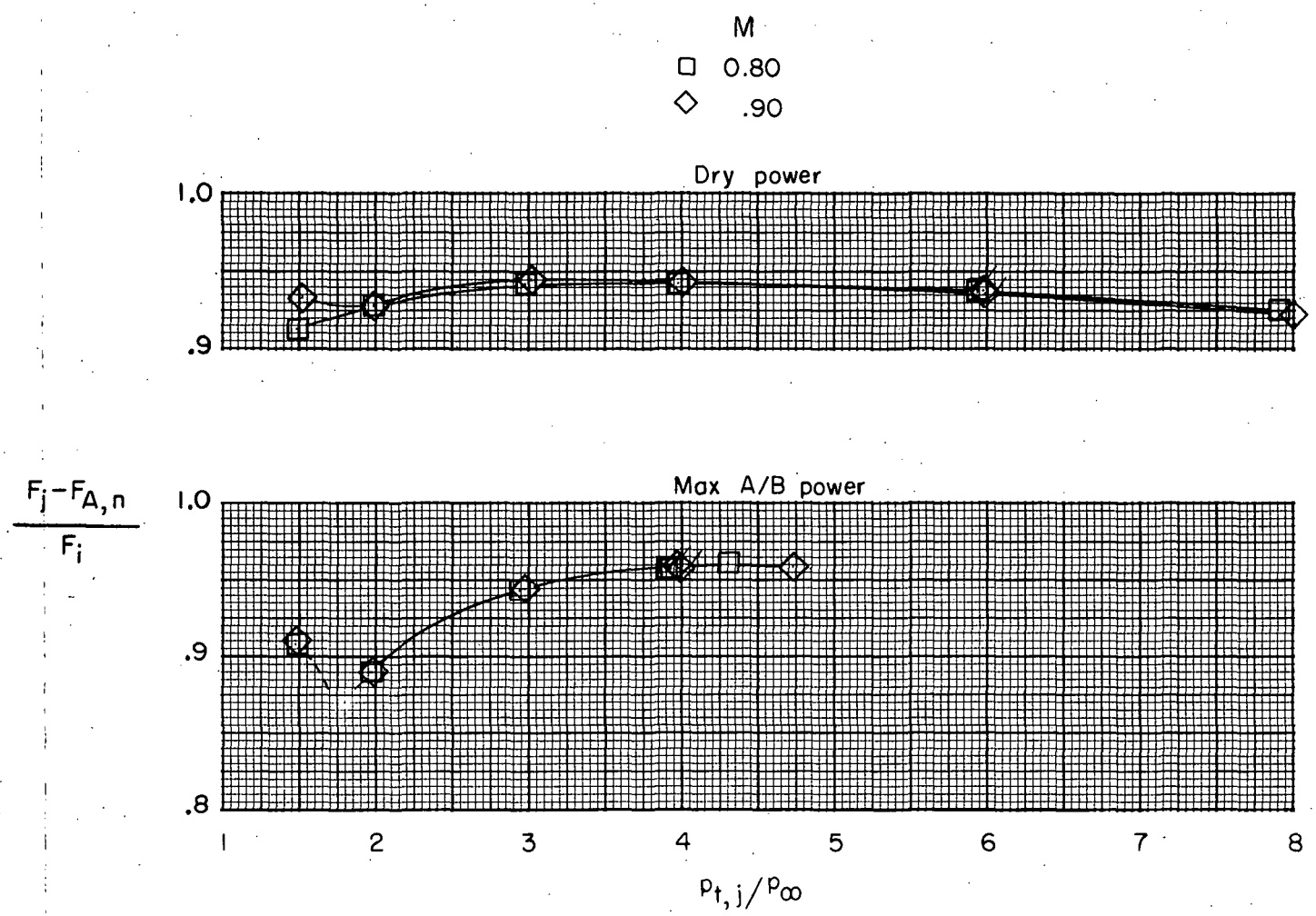


(f) Wide-spaced afterbody; short alternate 2 interfairing.

Figure 23.- Concluded.

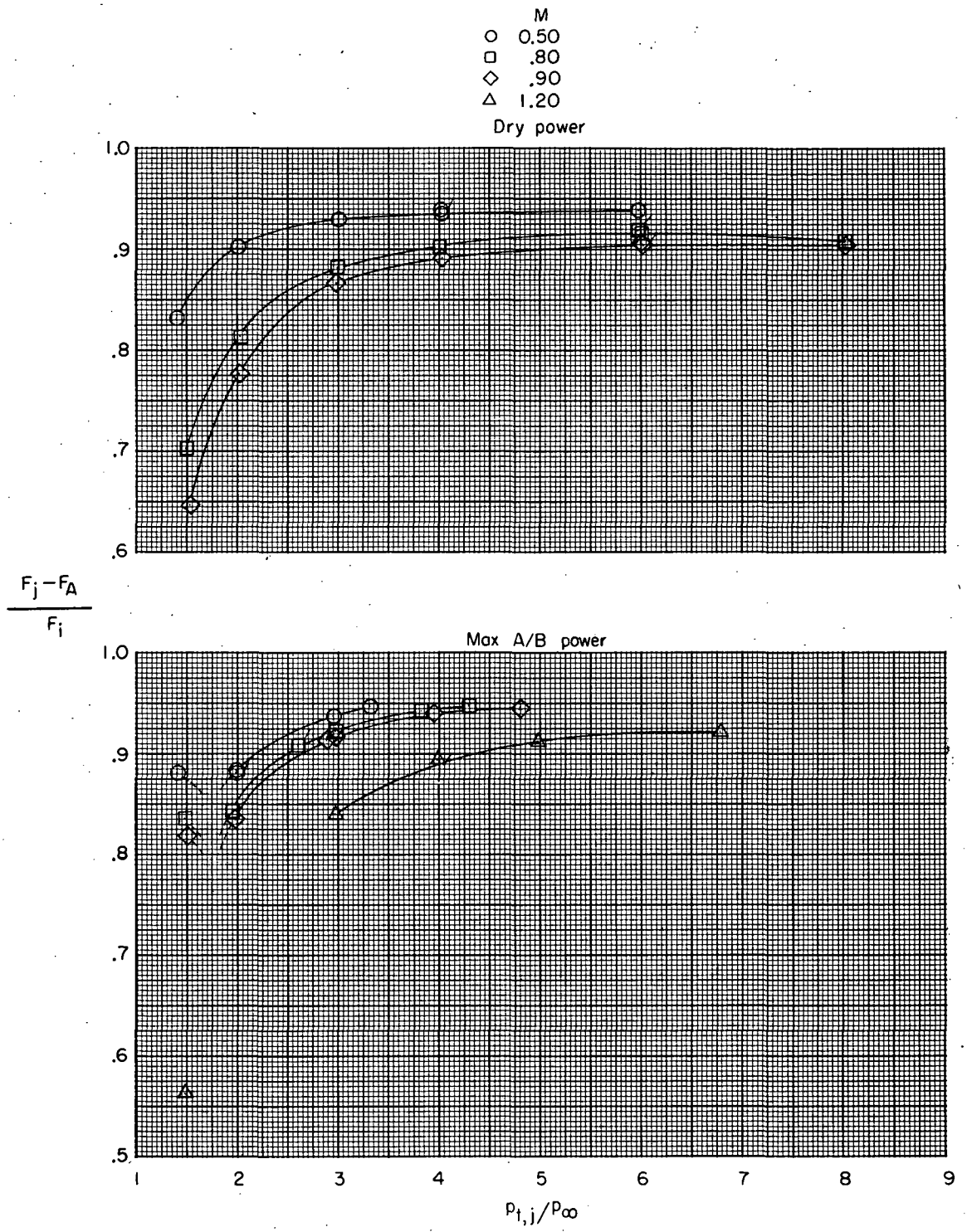


(a) Close-spaced afterbody; basic interfairing.

Figure 24.- Variation of thrust-minus-axial-force ratio with jet total-pressure ratio at two nozzle power settings. Symbols with flags indicate decreasing jet total-pressure ratio; $\alpha = 0^o$.

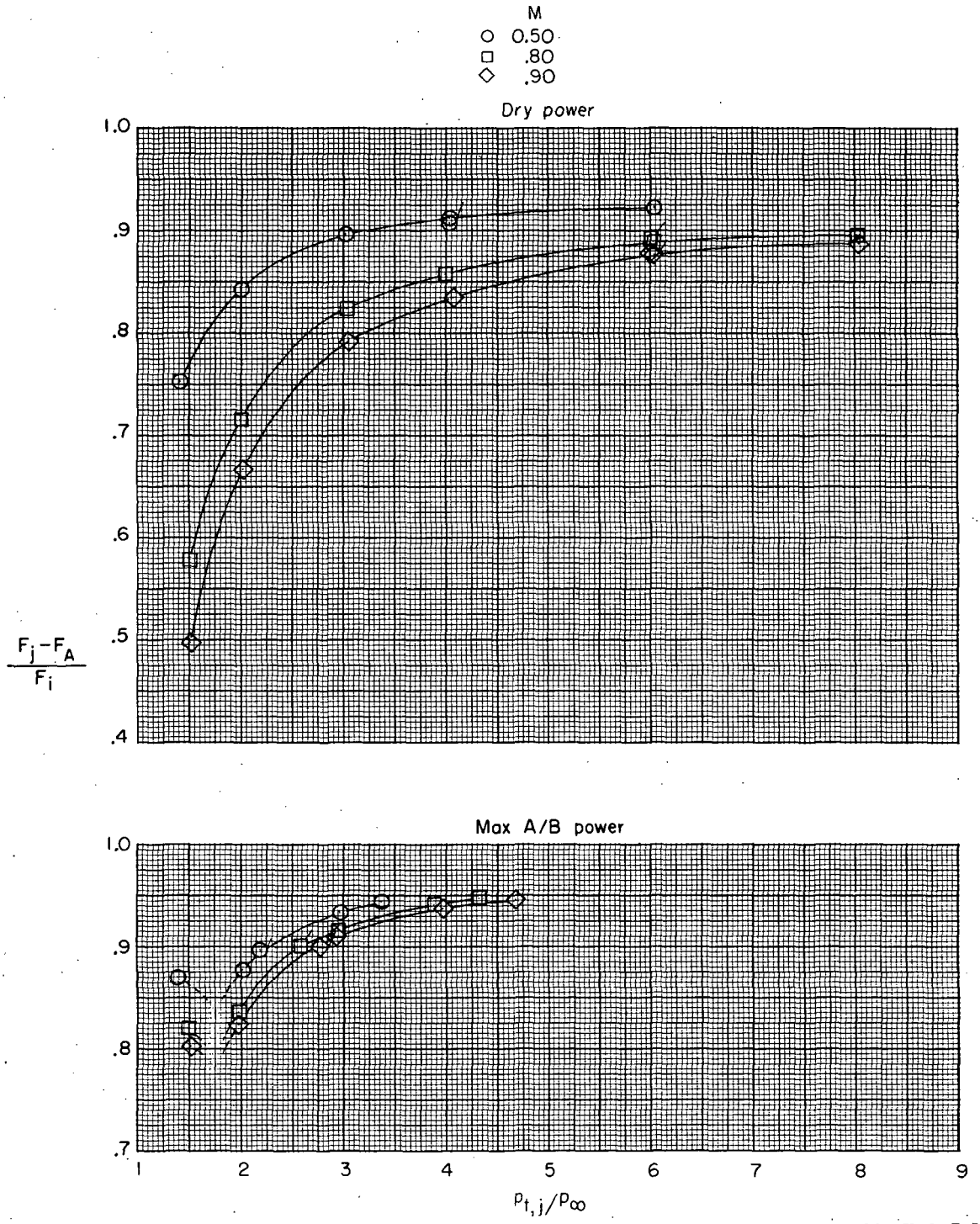


(b) Close-spaced afterbody; alternate 2 interfairing.

Figure 24.- Continued.

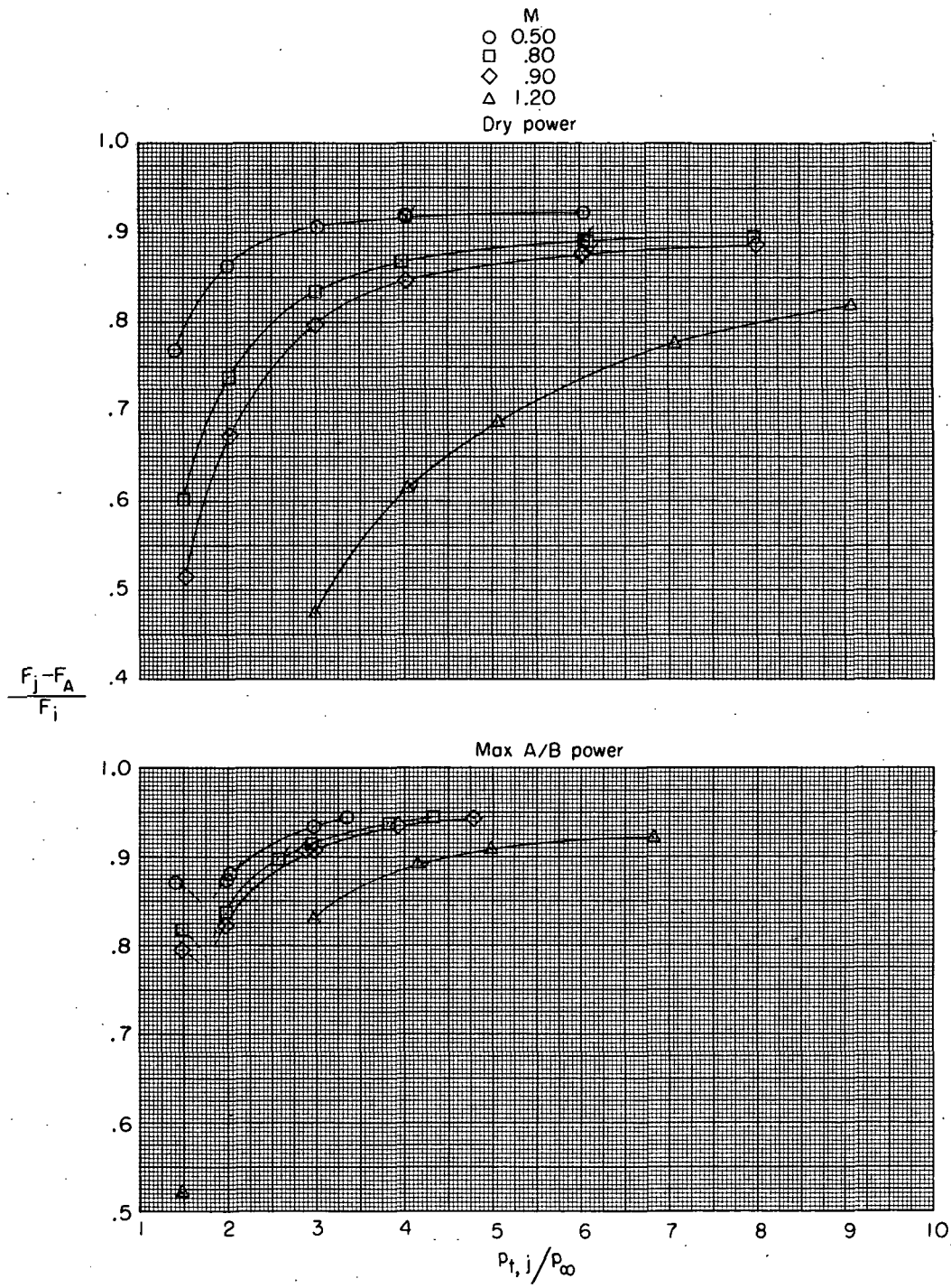


(c) Close-spaced afterbody; short alternate 2 interfairing.

Figure 24.- Continued.

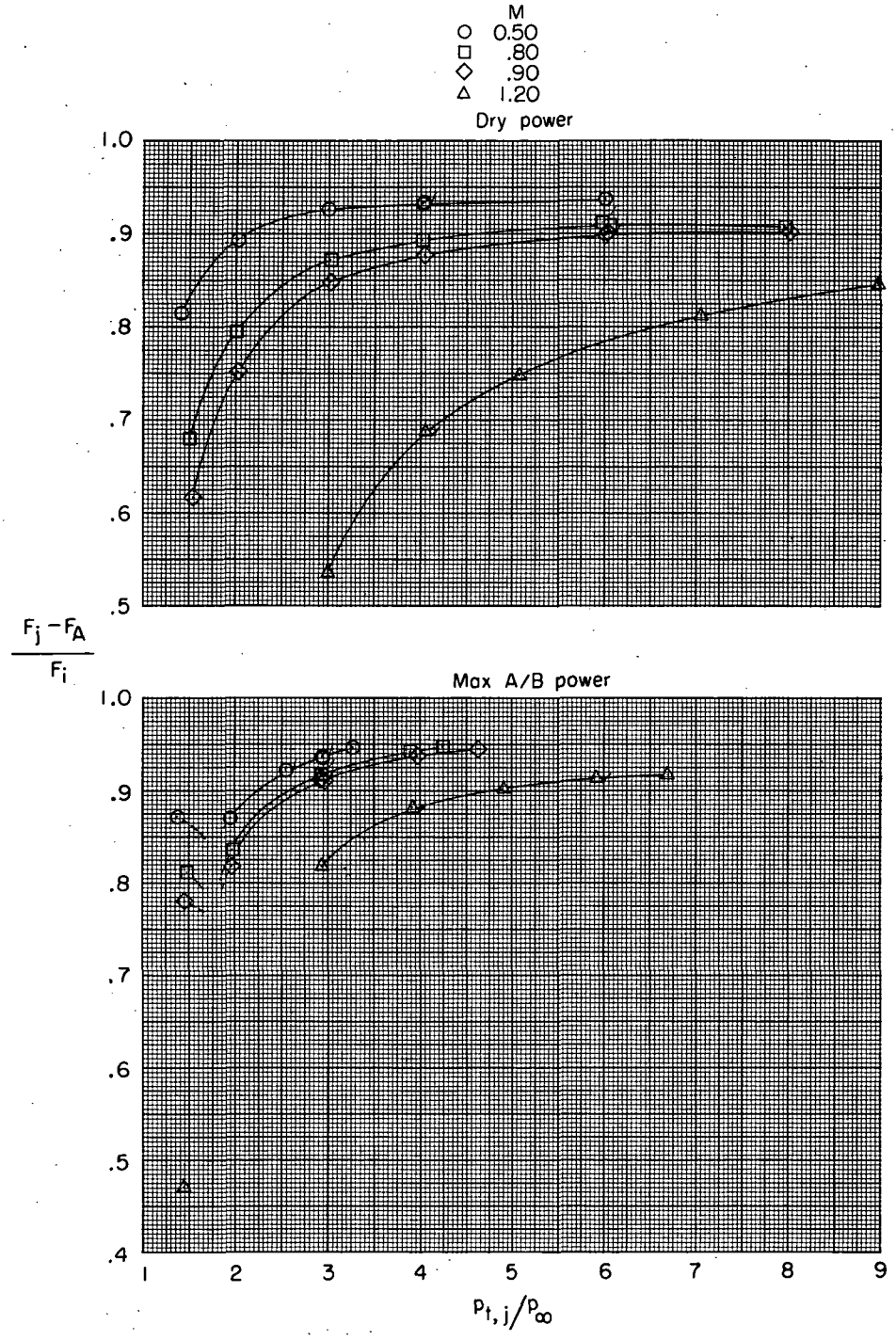


(d) Wide-spaced afterbody; basic interfairing.

Figure 24.- Continued.

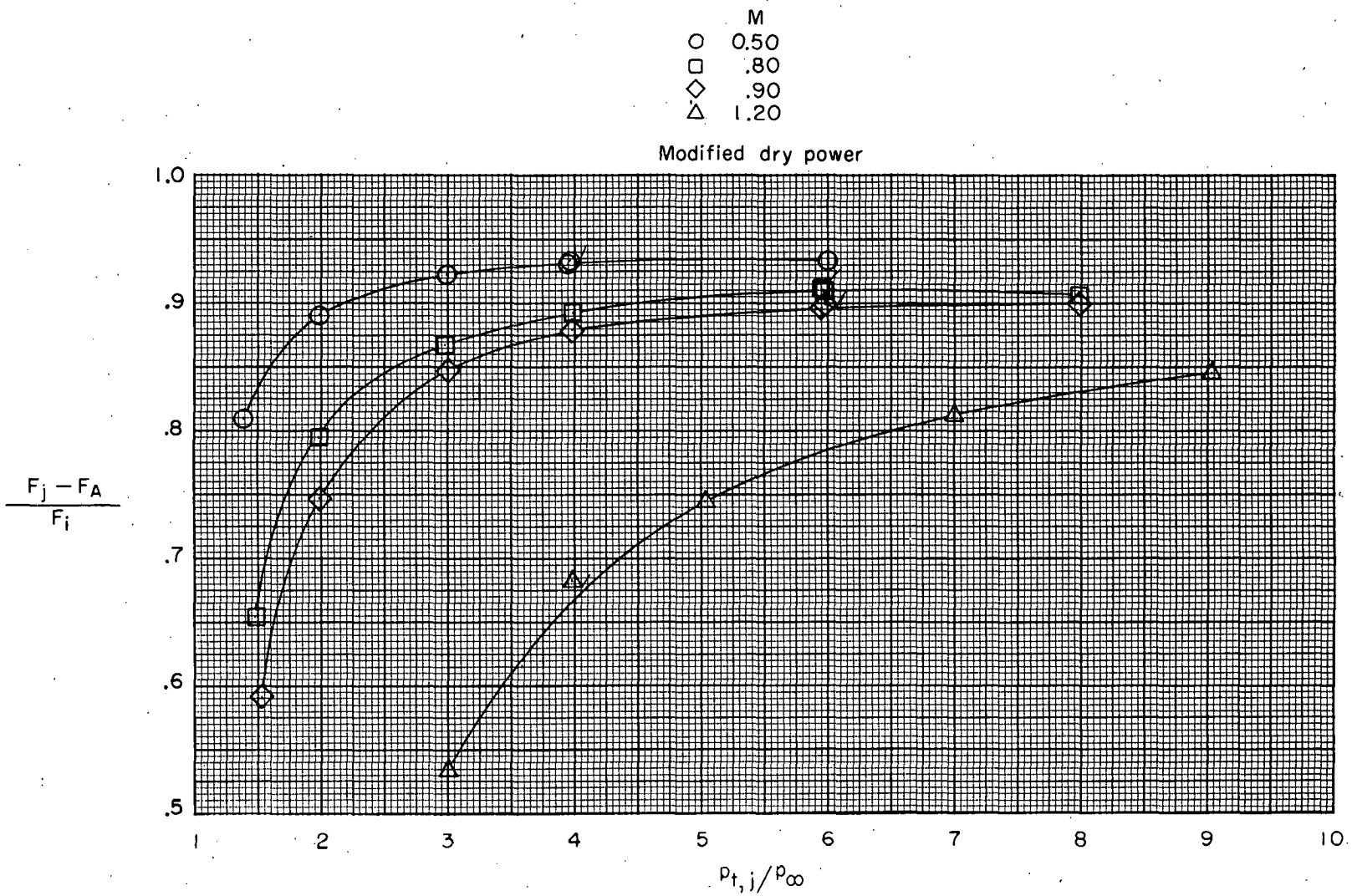


(d) Concluded.

Figure 24.- Continued.

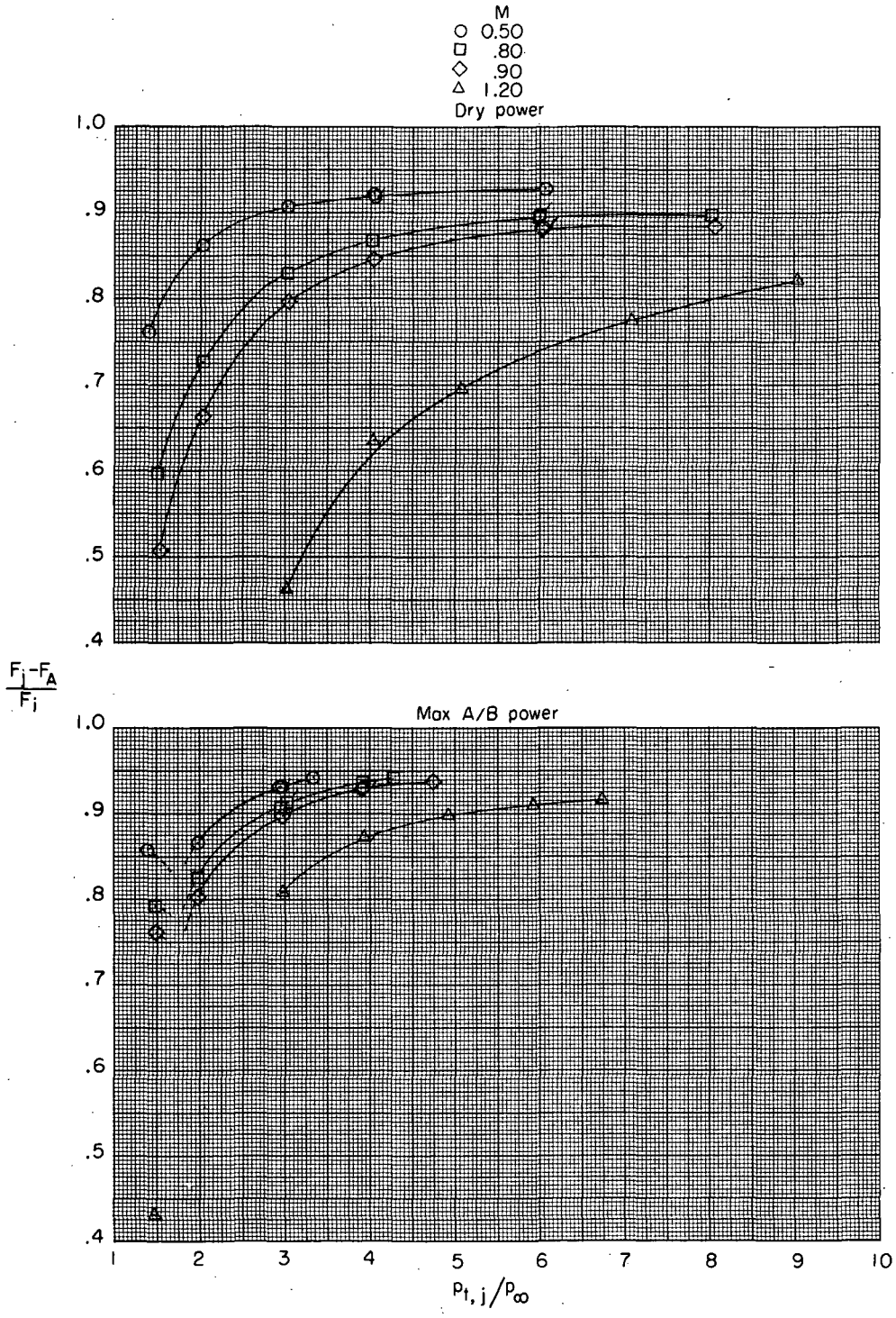


(e) Wide-spaced afterbody; alternate 2 interfairing.

Figure 24.- Continued.

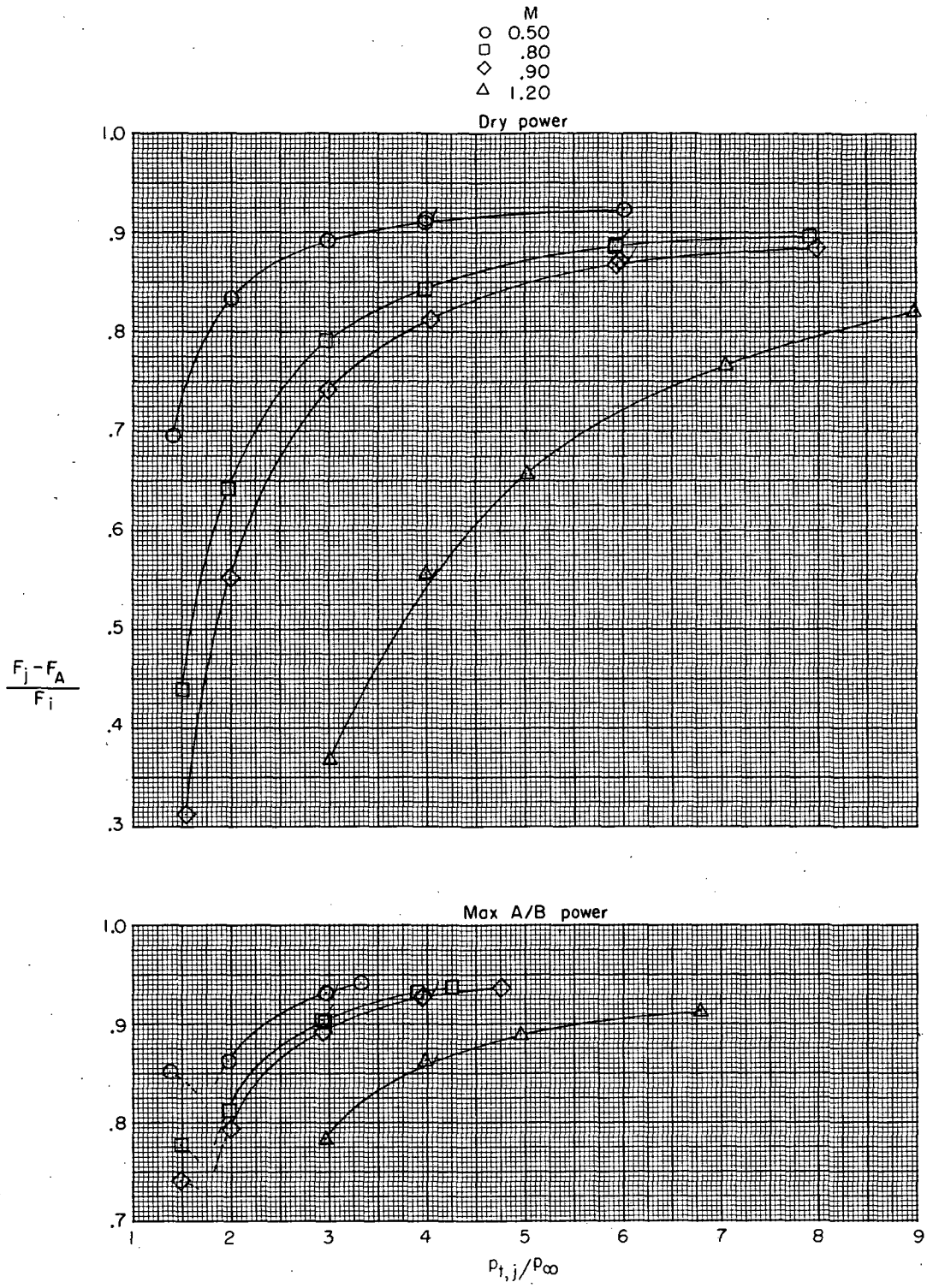


(f) Wide-spaced afterbody; short alternate 2 interfairing.

Figure 24.- Concluded.

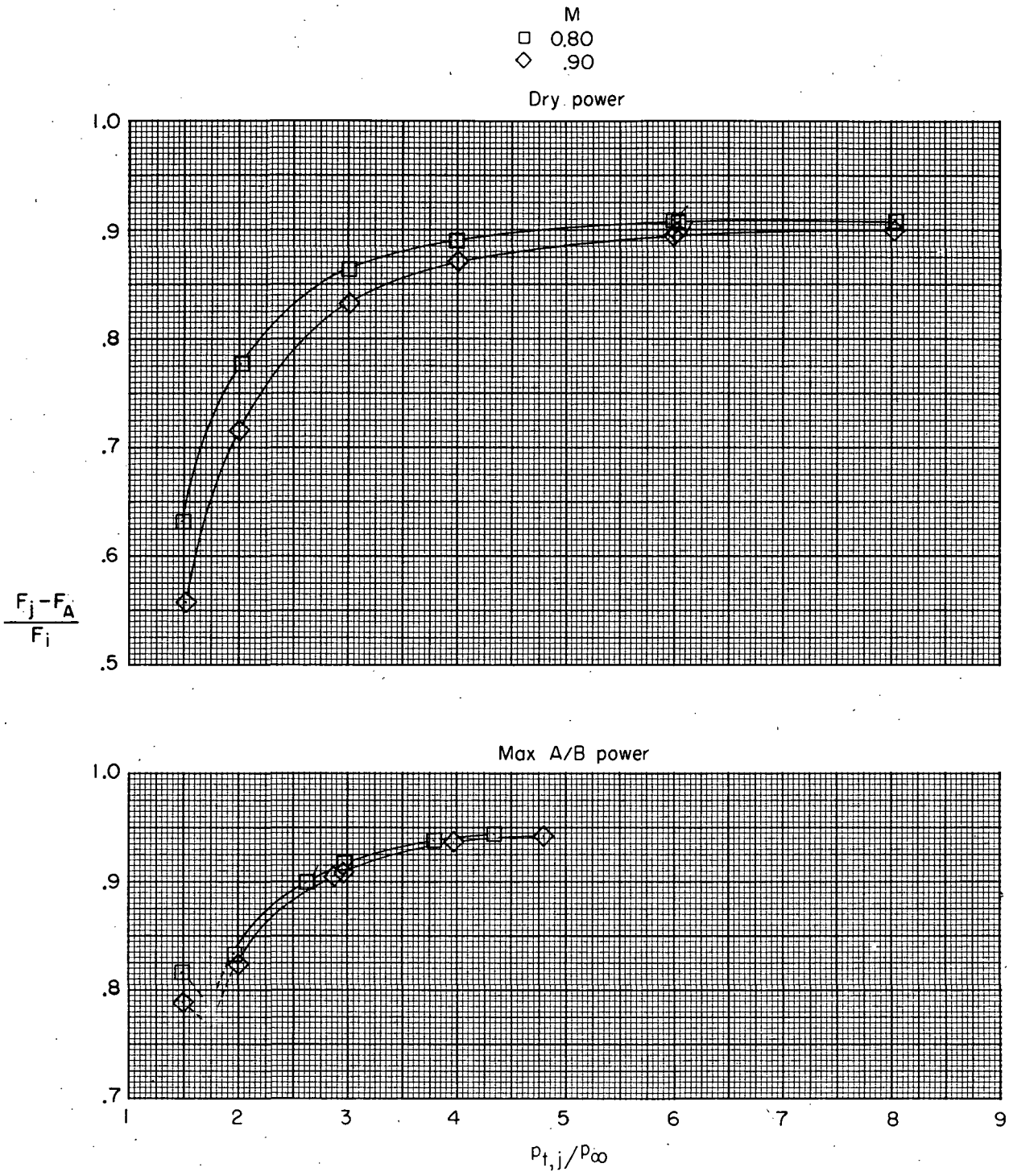


(a) Close-spaced afterbody; basic interfairing.

Figure 25.- Variation of thrust-minus-axial-force ratio with jet total-pressure ratio at two nozzle power settings. Symbols with flags indicate decreasing jet total-pressure ratio; nominal $\alpha = 6^o$.

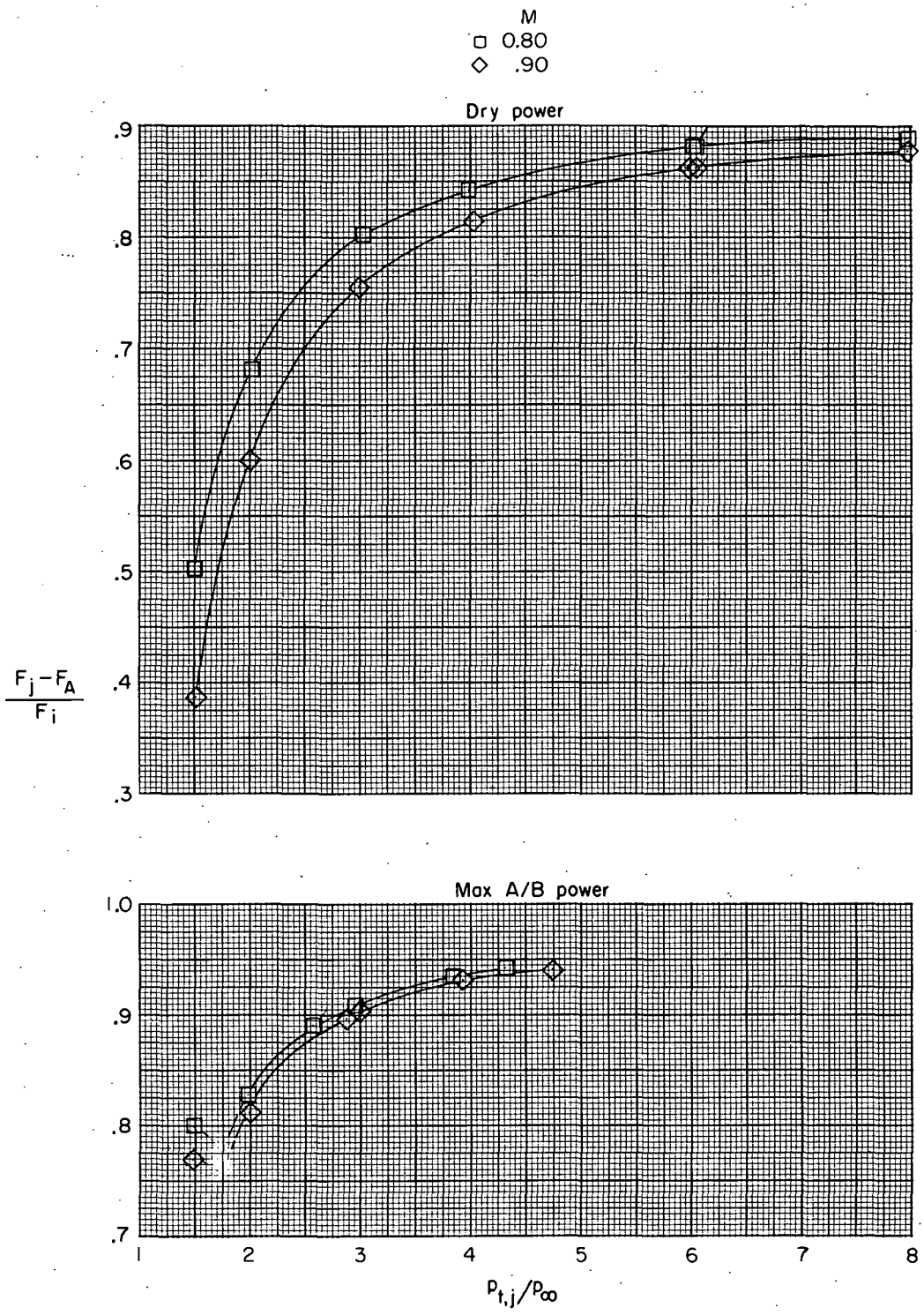


(b) Close-spaced afterbody; alternate 2 interfairing.

Figure 25.- Continued.

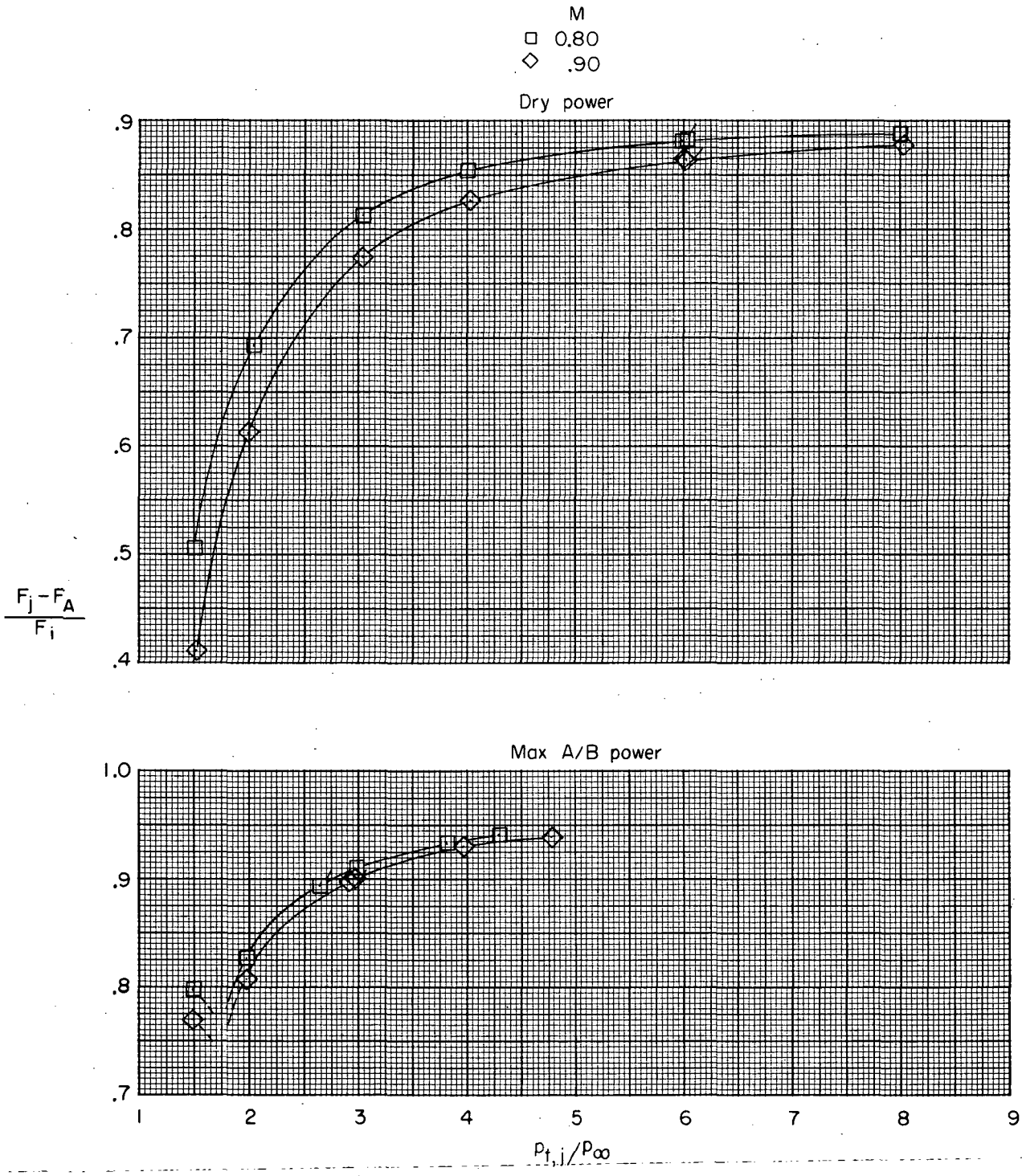


(c) Close-spaced afterbody; short alternate 2 interfairing.

Figure 25.- Continued.

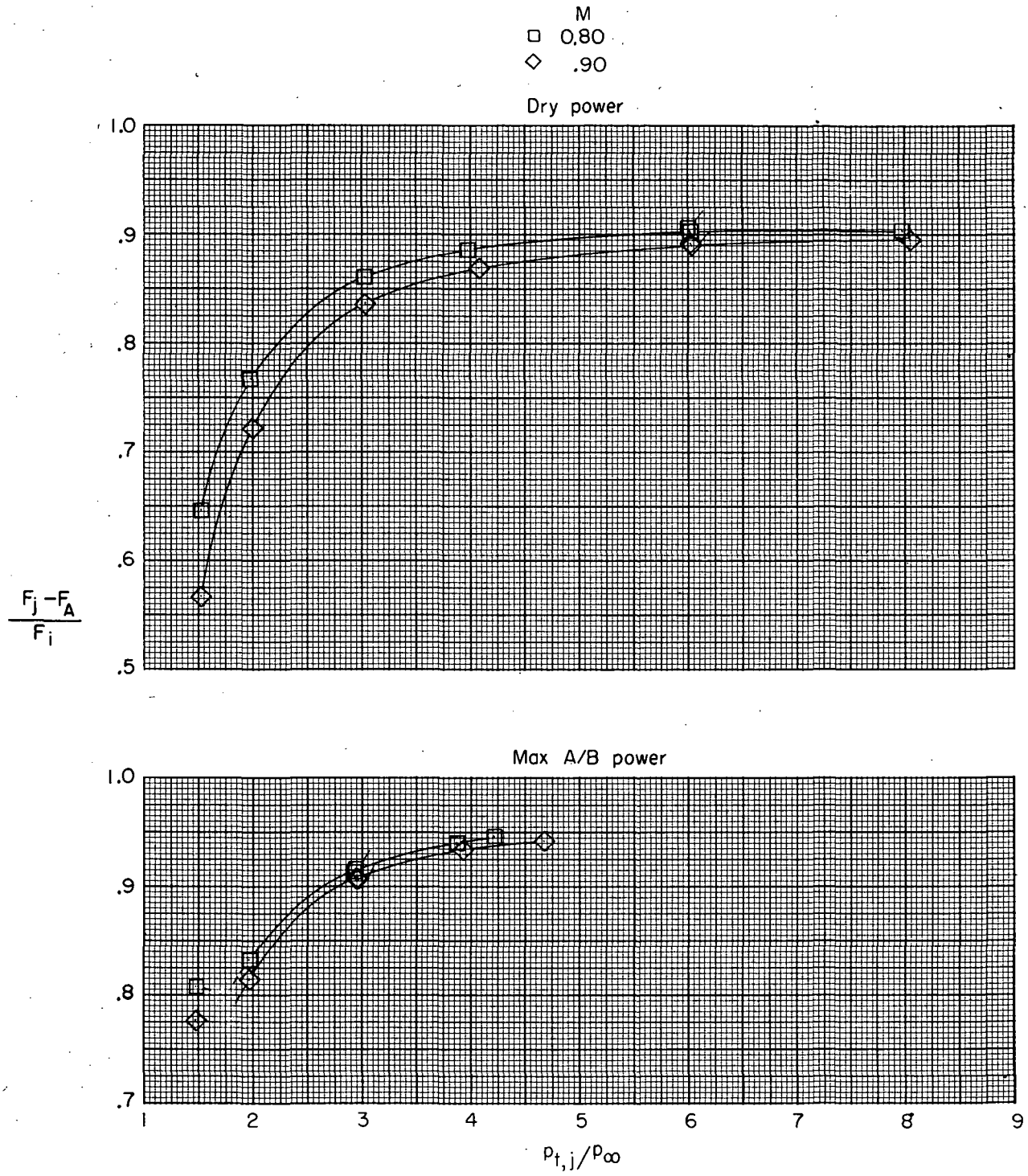


(d) Wide-spaced afterbody; basic interfairing.

Figure 25.- Continued.

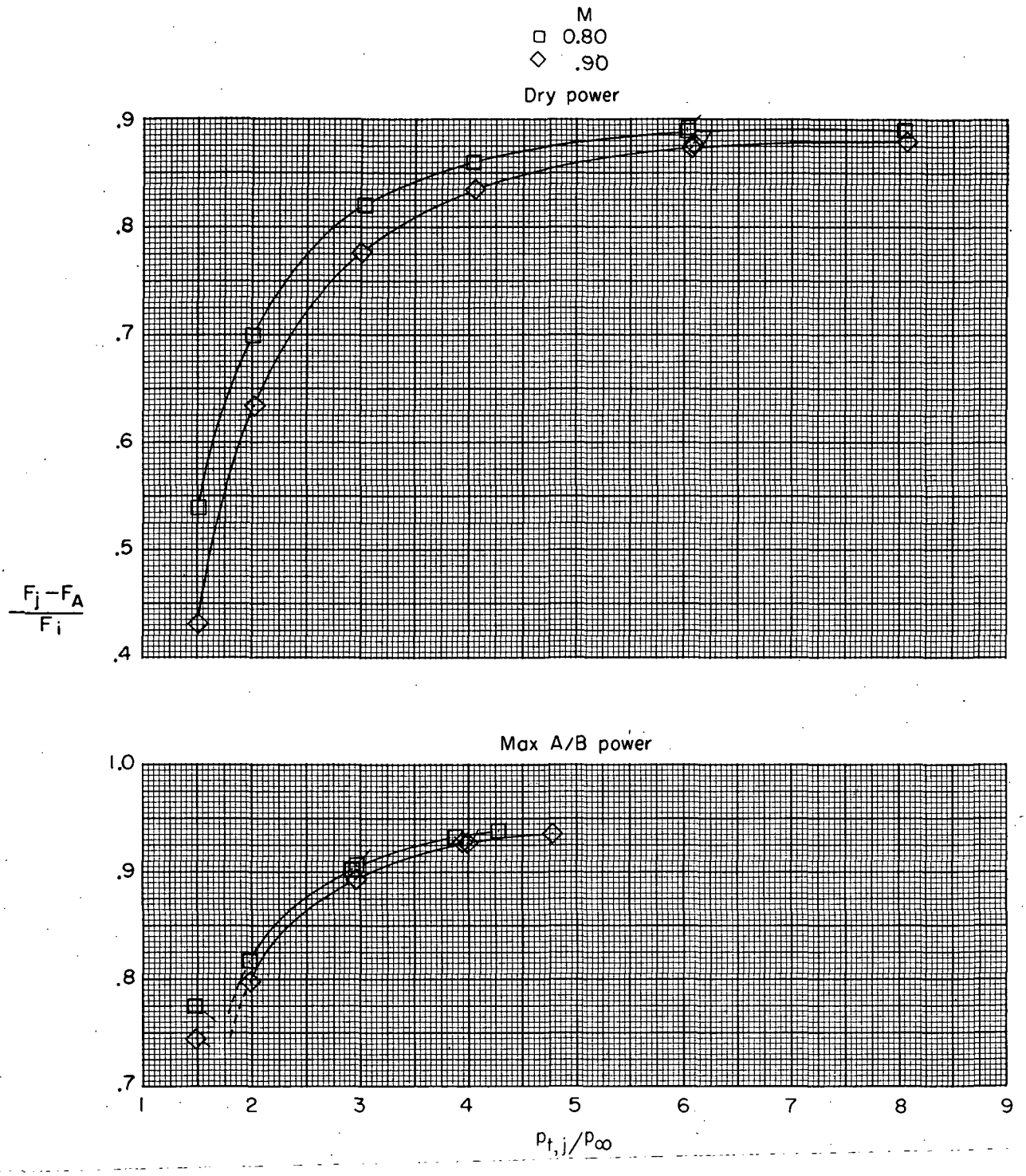


(e) Wide-spaced afterbody; alternate 2 interfairing.

Figure 25.- Continued.

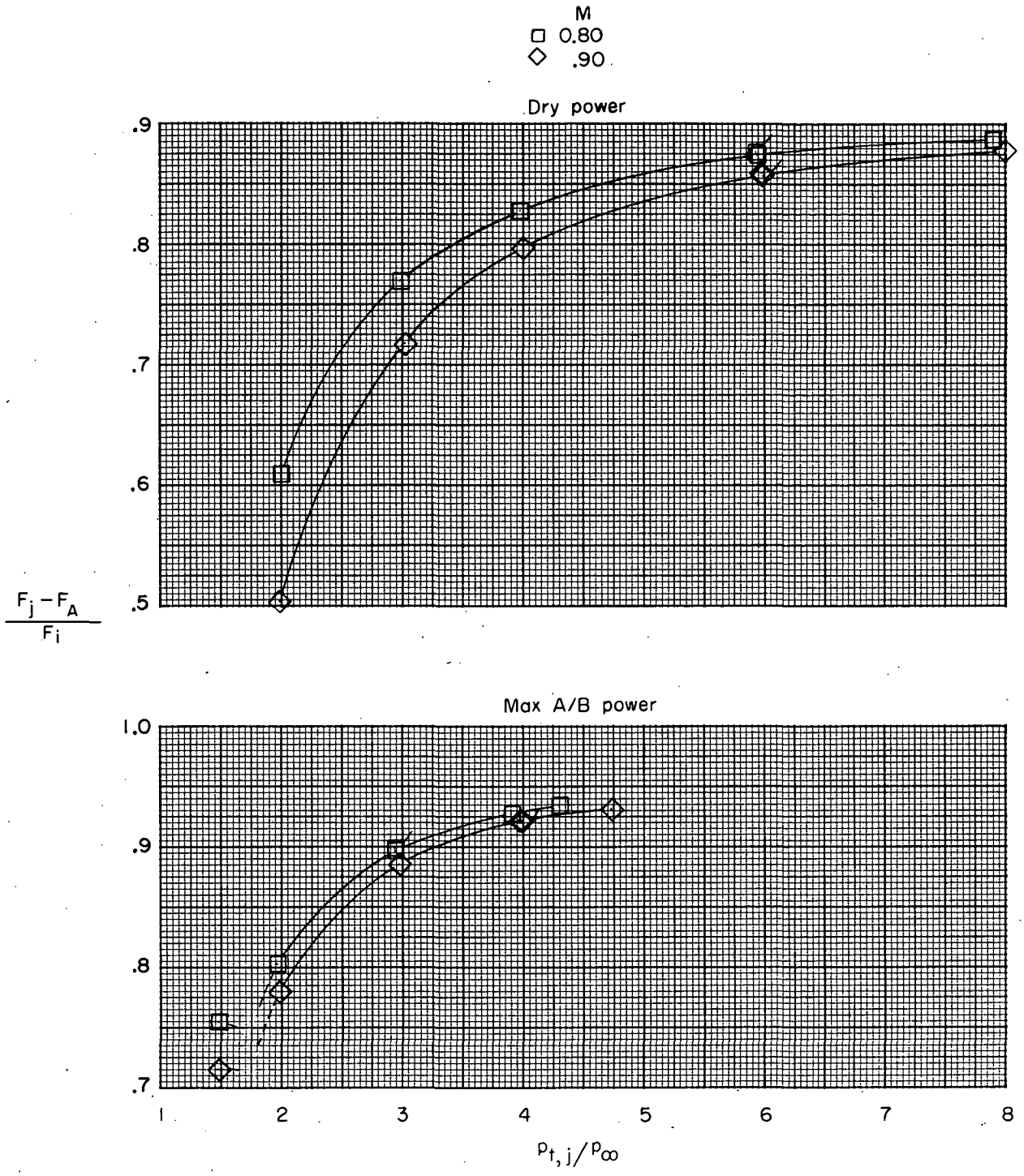


(f) Wide-spaced afterbody; short alternate 2 interfairing.

Figure 25.- Concluded.

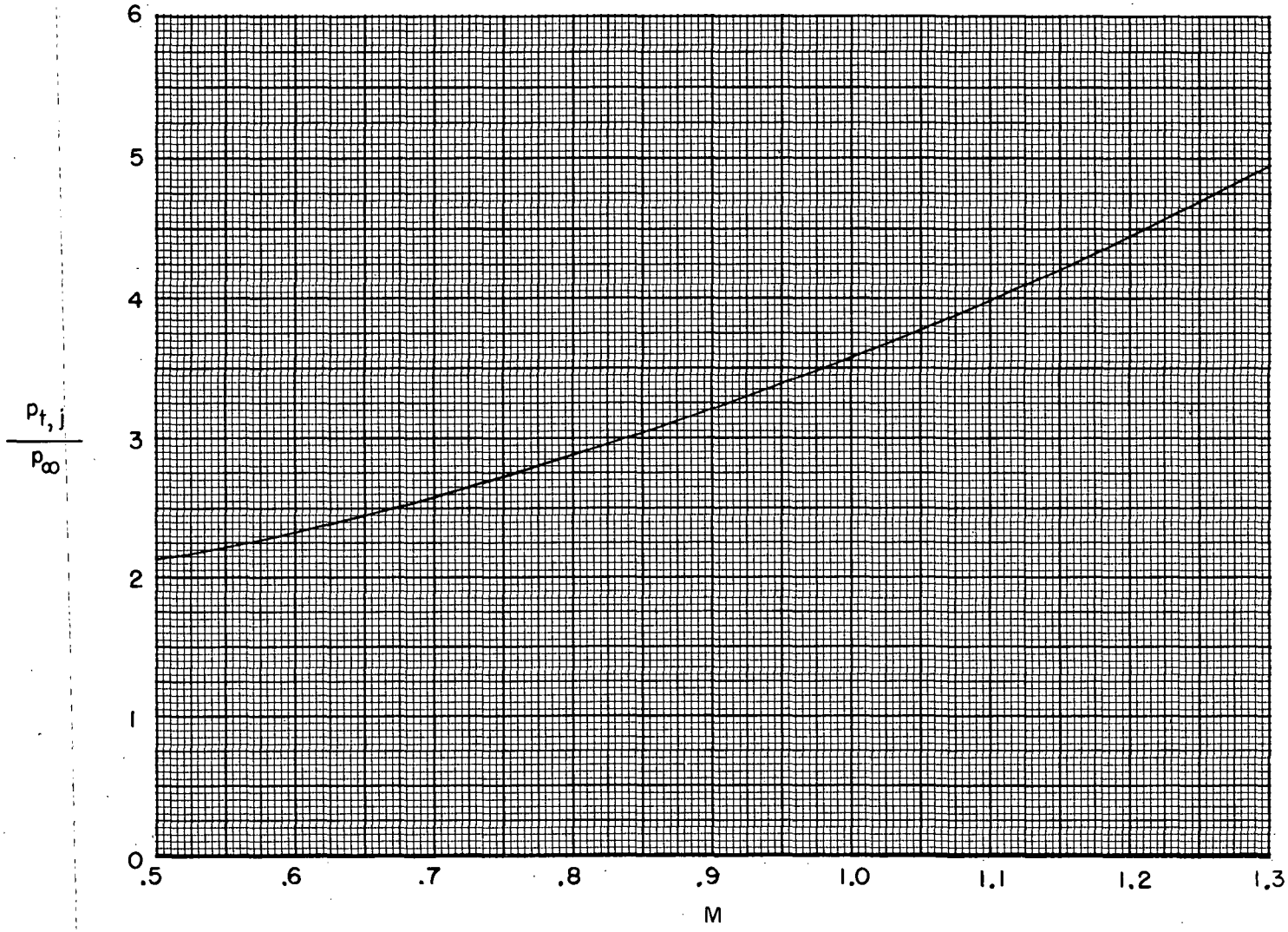


Figure 26.- Typical jet total-pressure-ratio schedule for a turbofan engine (maximum dry power).

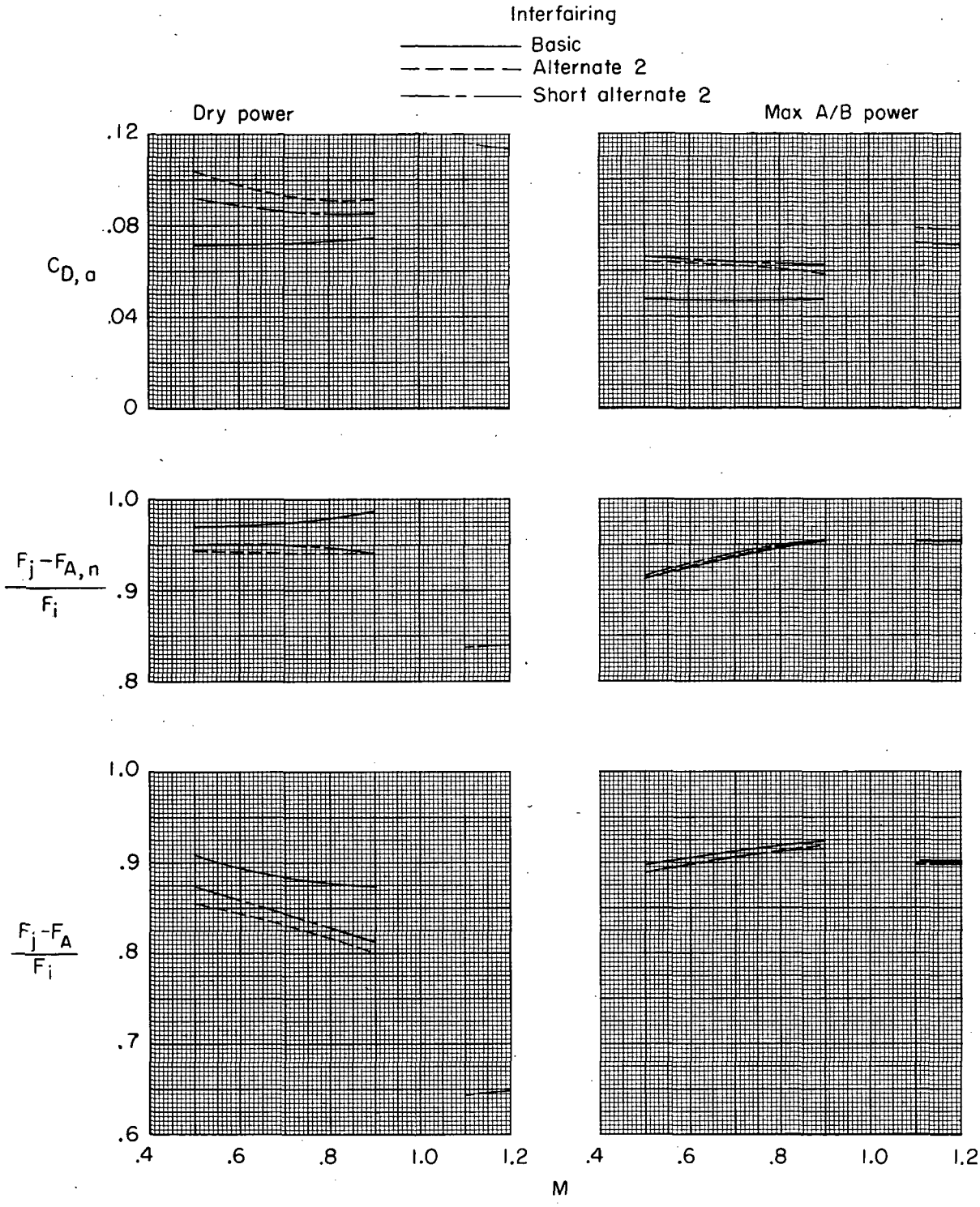


(a) Close-spaced afterbody.

Figure 27.- Variation of afterbody drag coefficient, thrust-minus-nozzle-axial-force ratio, and thrust-minus-total-axial-force ratio with Mach number for scheduled jet total-pressure ratio. Effect of nozzle power setting and interfairing shape. $\alpha = 0^{o}$.

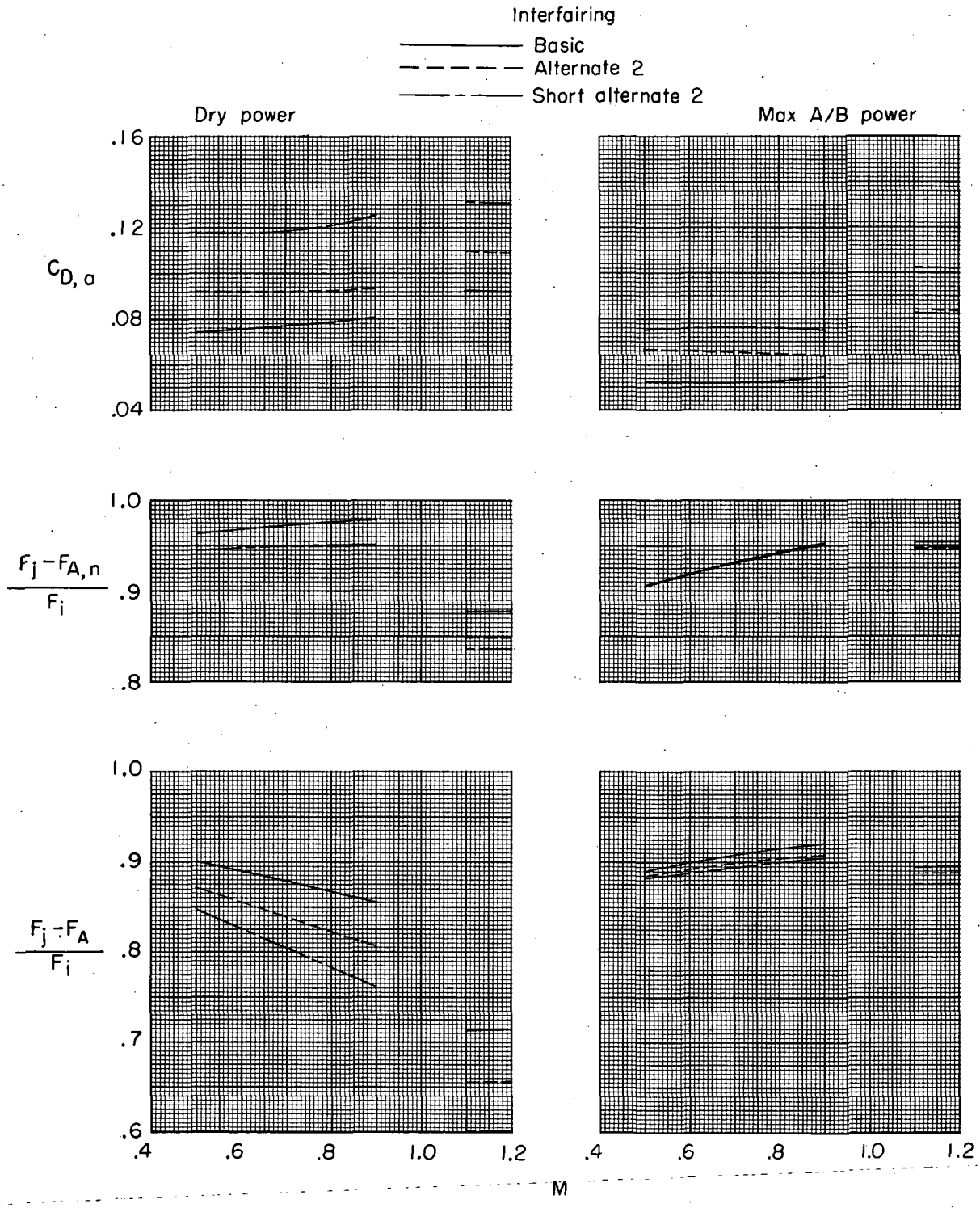


(b) Wide-spaced afterbody.

Figure 27.- Concluded.

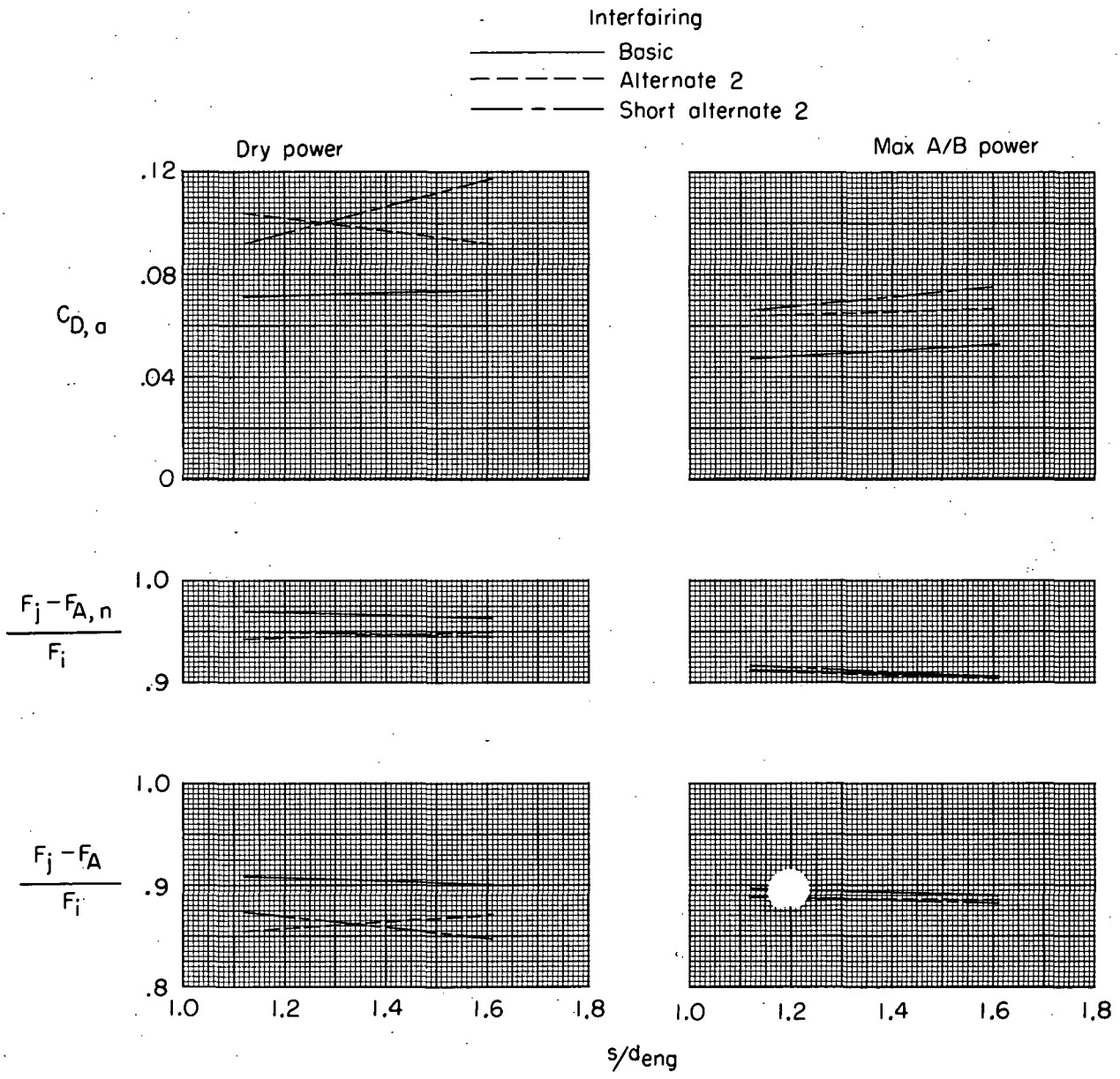


(a) M = 0.50; $\alpha = 0^{o}$.

Figure 28.- Effect of nozzle lateral spacing on afterbody drag coefficient, thrust-minus-nozzle-axial-force ratio, and thrust-minus-total-axial-force ratio.

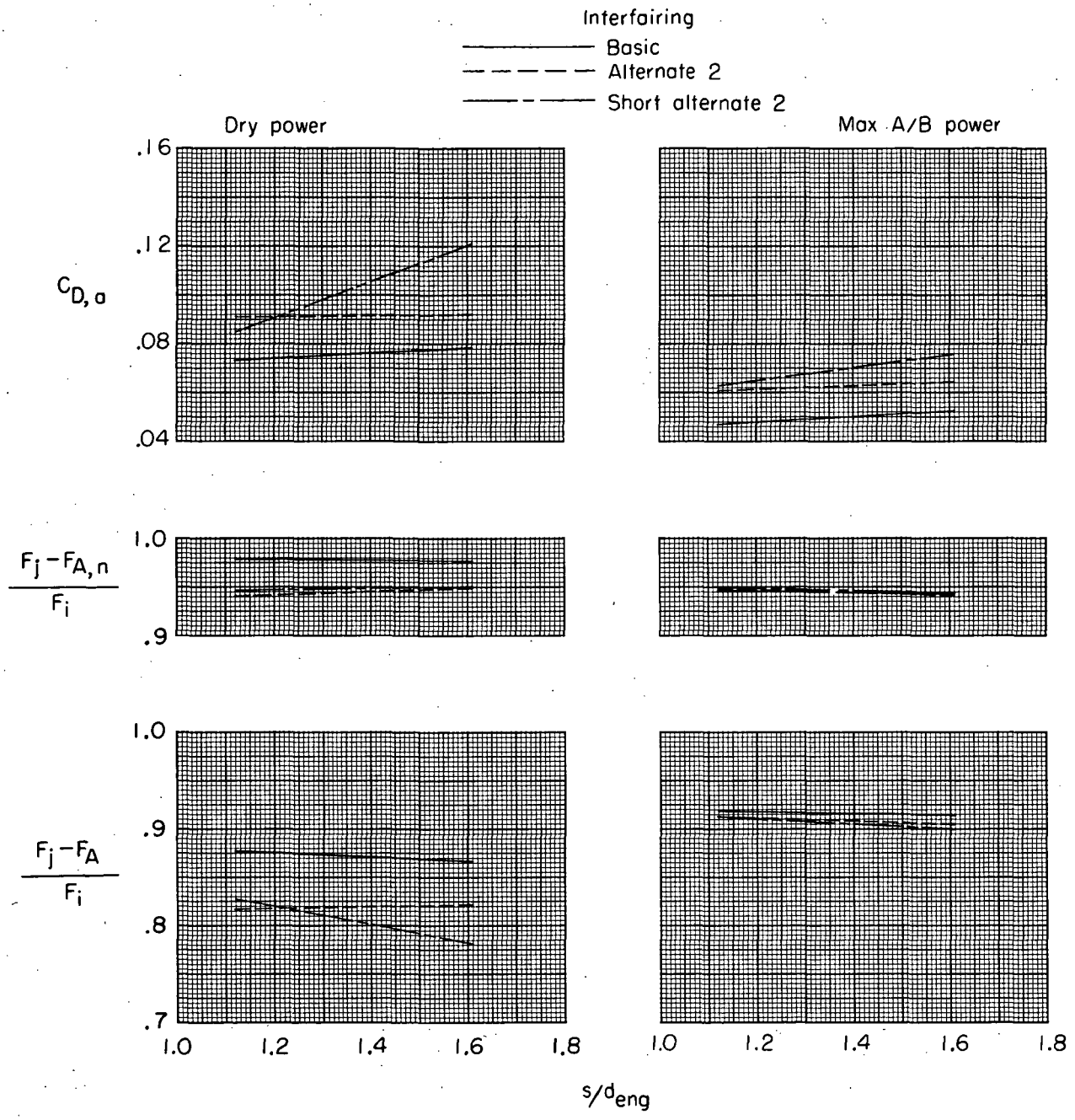


(b) M = 0.80; $\alpha = 0^{o}$.

Figure 28.- Continued.

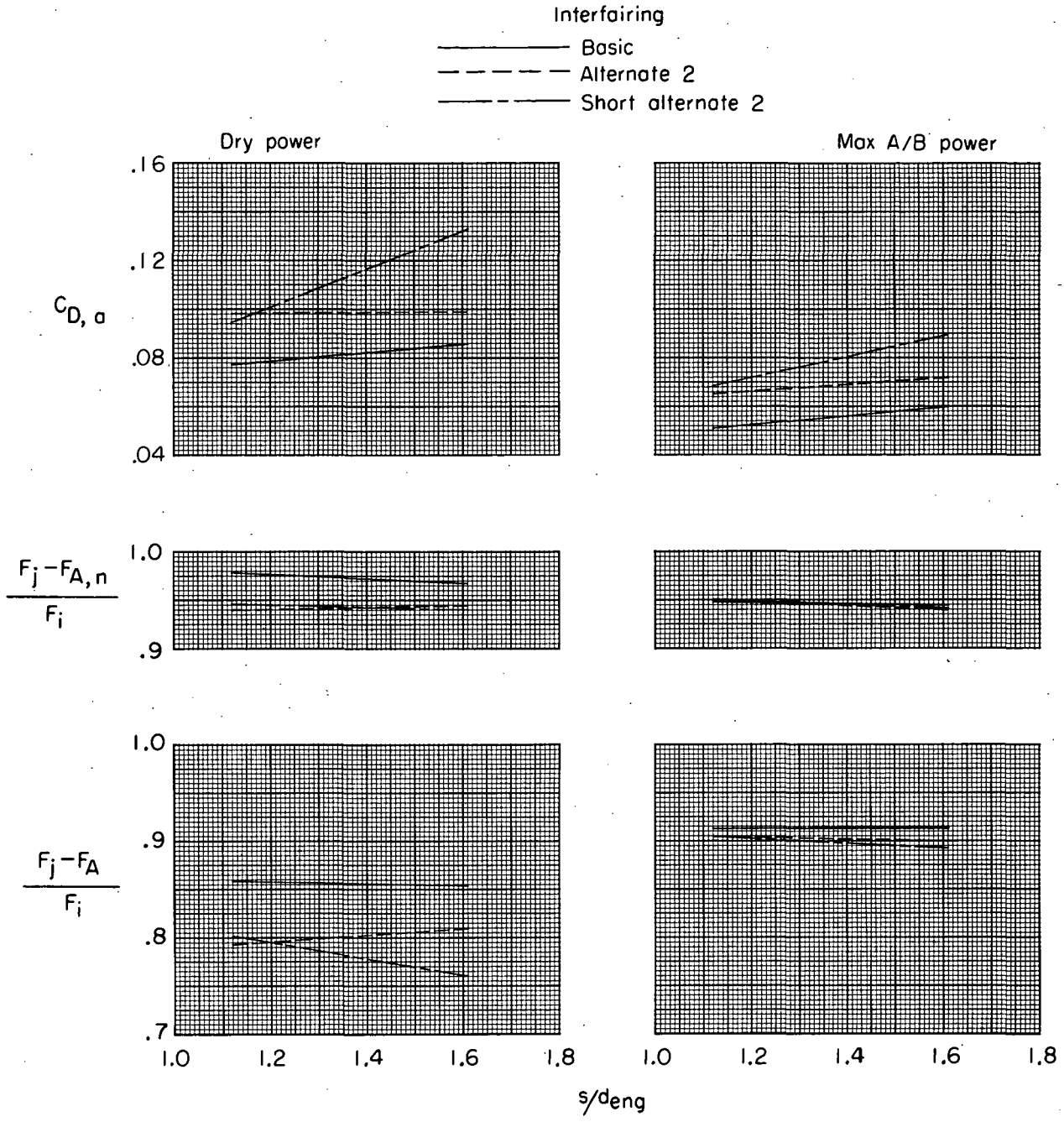


(c) M = 0.80; $\alpha = 6^{o}$.

Figure 28.- Continued.

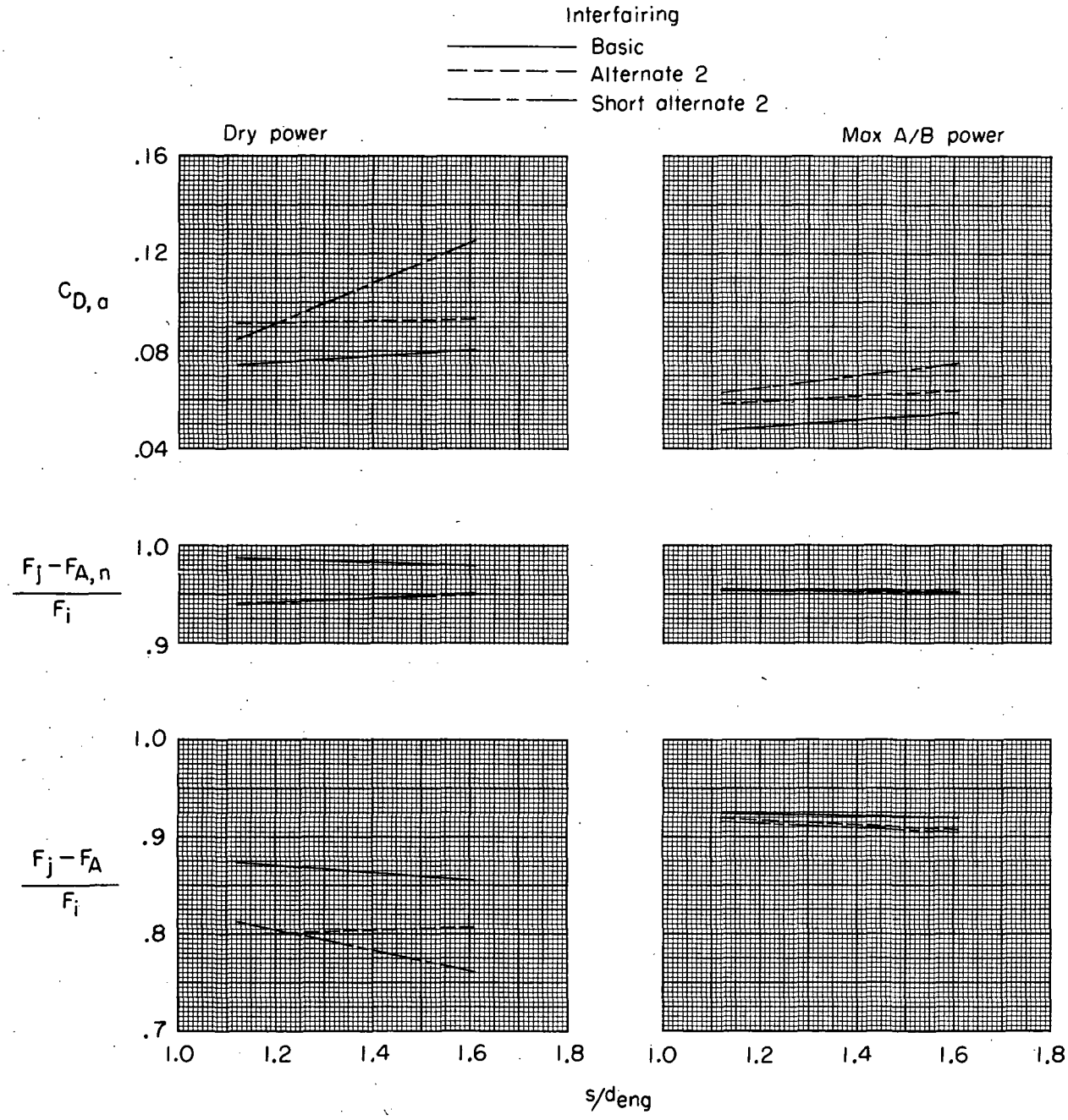


(d) M = 0.90; $\alpha = 0^{o}$.

Figure 28.- Continued.

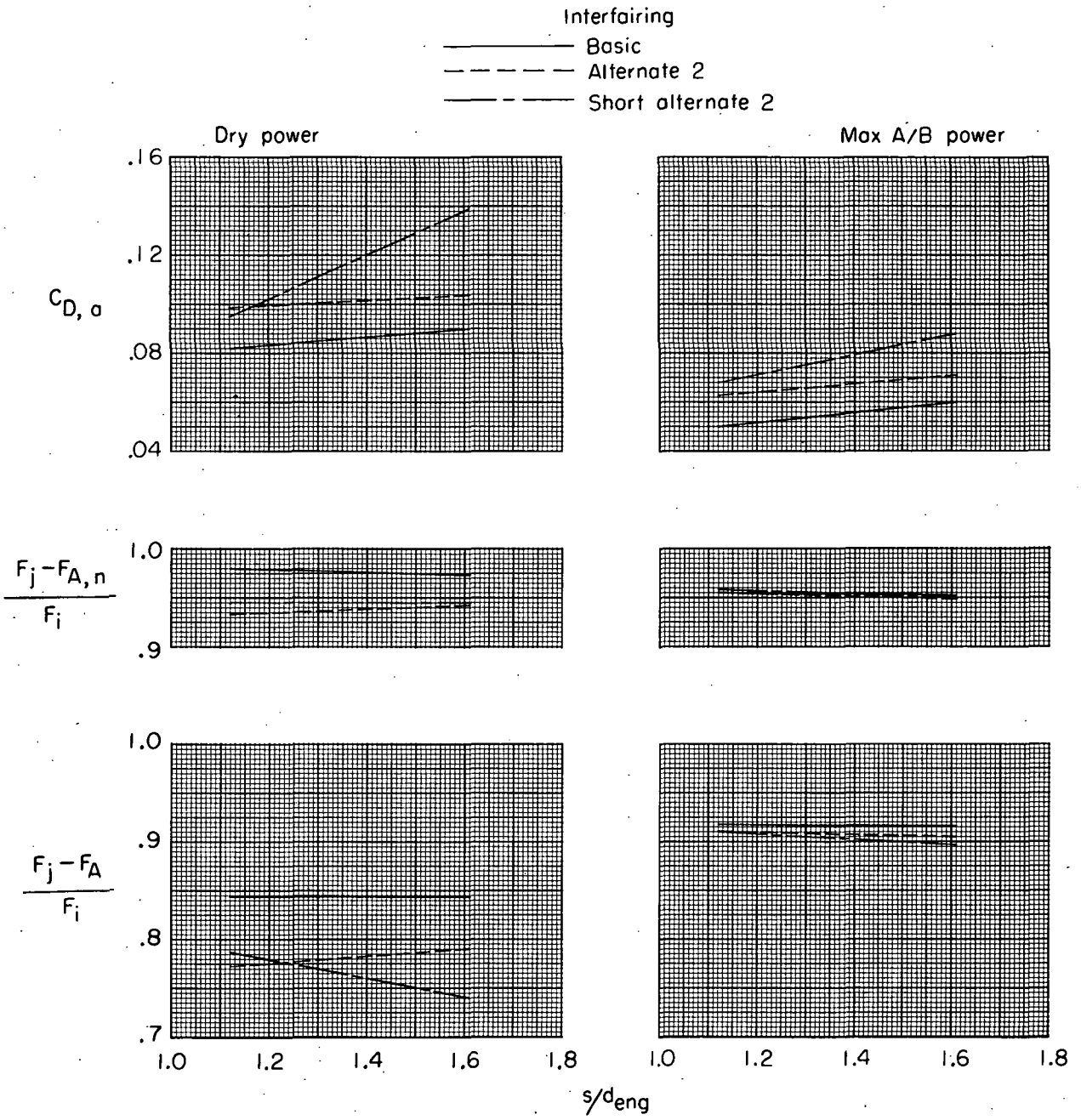


(e) M = 0.90; $\alpha = 6^{o}$.

Figure 28.- Continued.

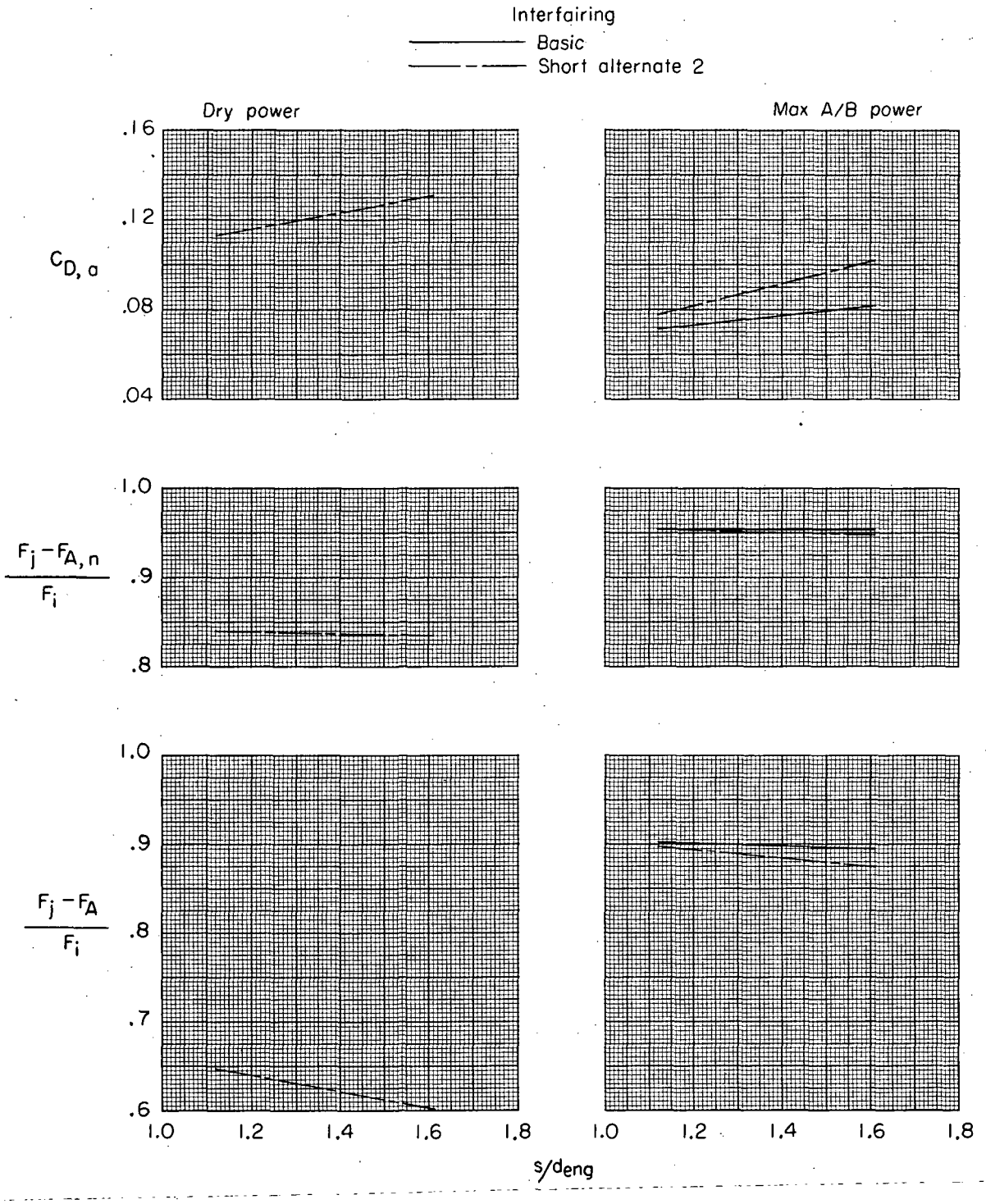


(f) M = 1.20; $\alpha = 0^{\circ}$.

Figure 28.- Concluded.

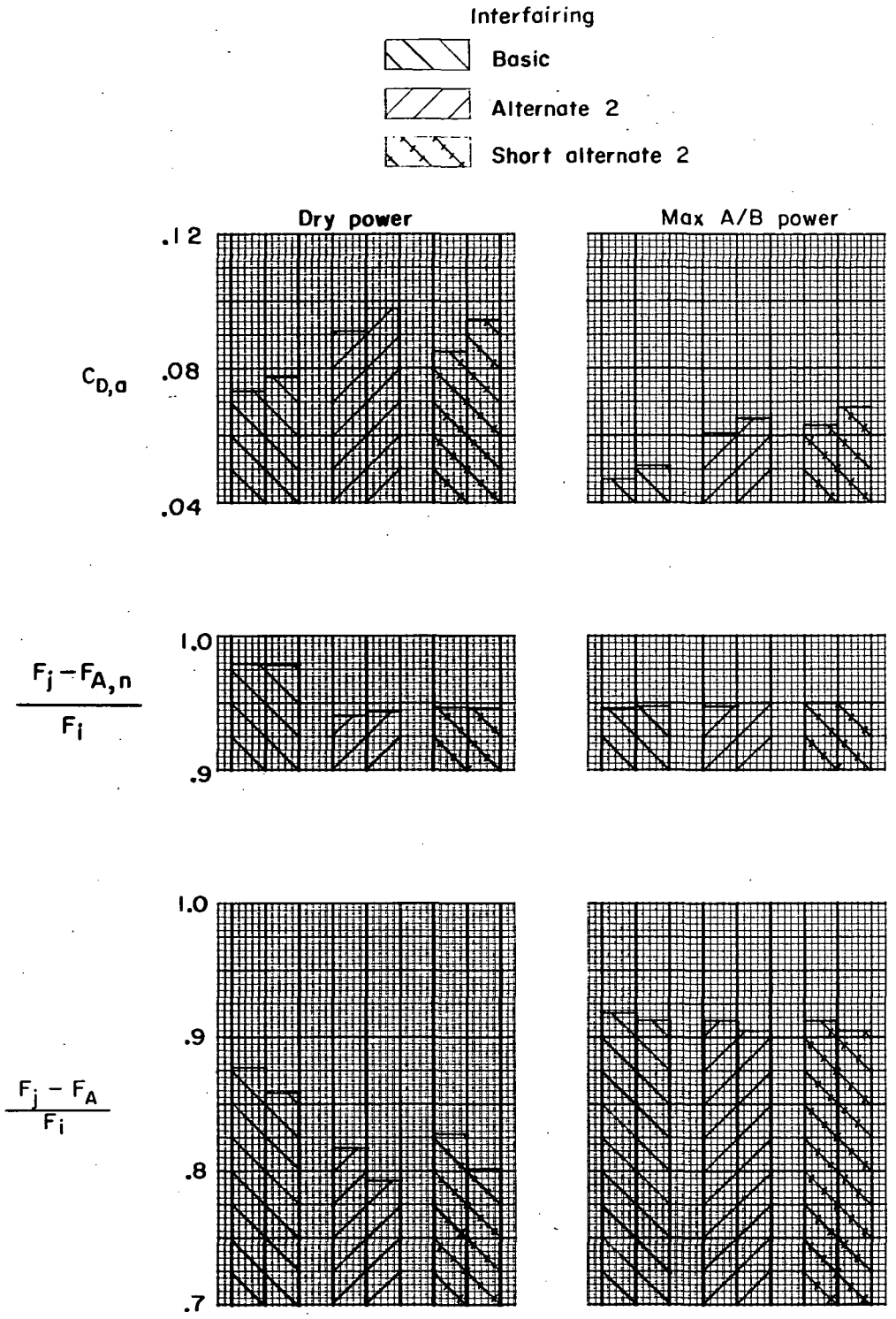


(a) Close-spaced afterbody; M = 0.80.

Figure 29.- Effect of angle of attack on afterbody drag coefficient, thrust minus nozzle axial force, and thrust minus total axial force. First bar in each interfairing set indicates $\alpha = 0^{\circ}$; second bar indicates $\alpha = 6^{\circ}$.

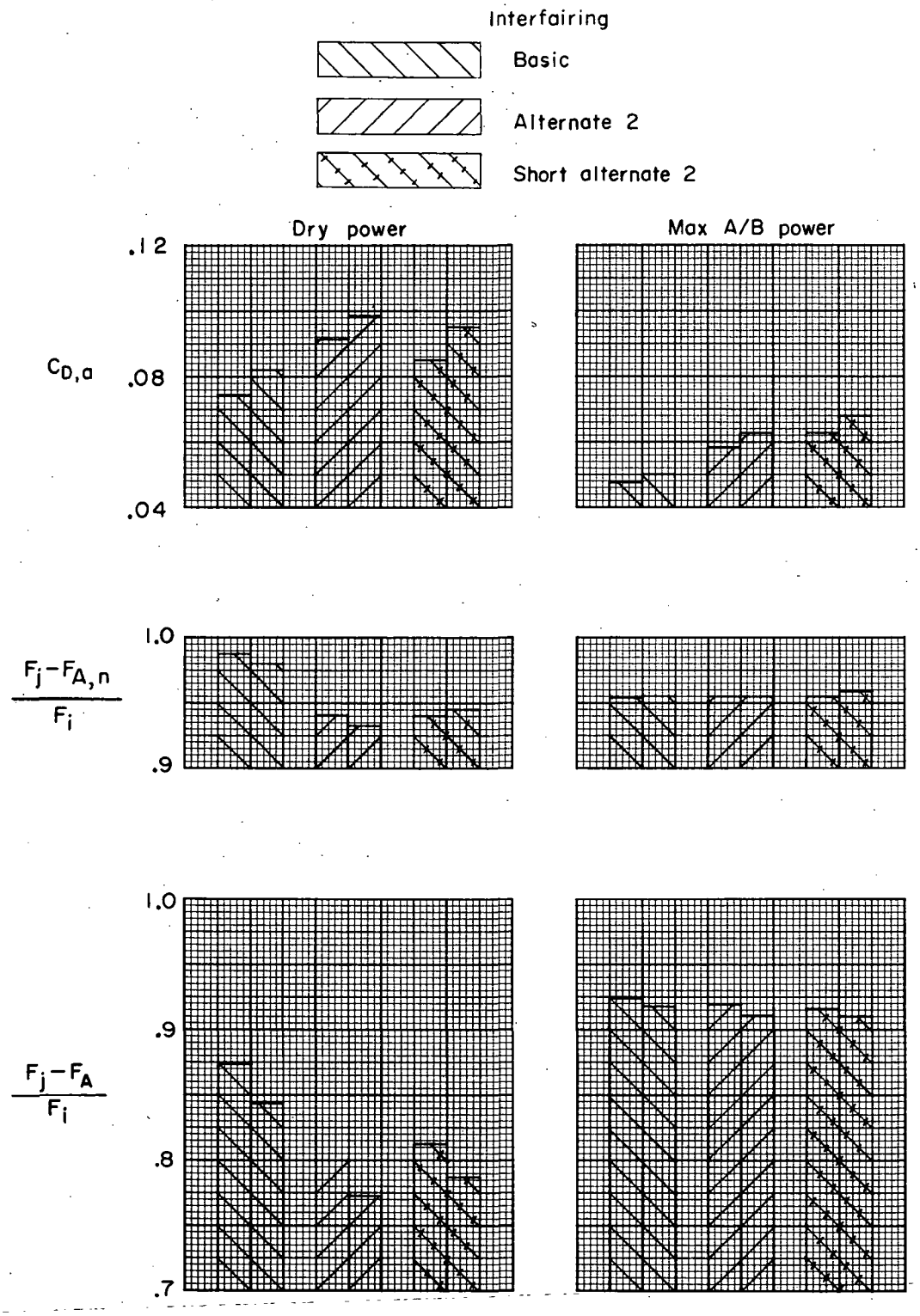


(b) Close-spaced afterbody; M = 0.90.

Figure 29.- Continued.

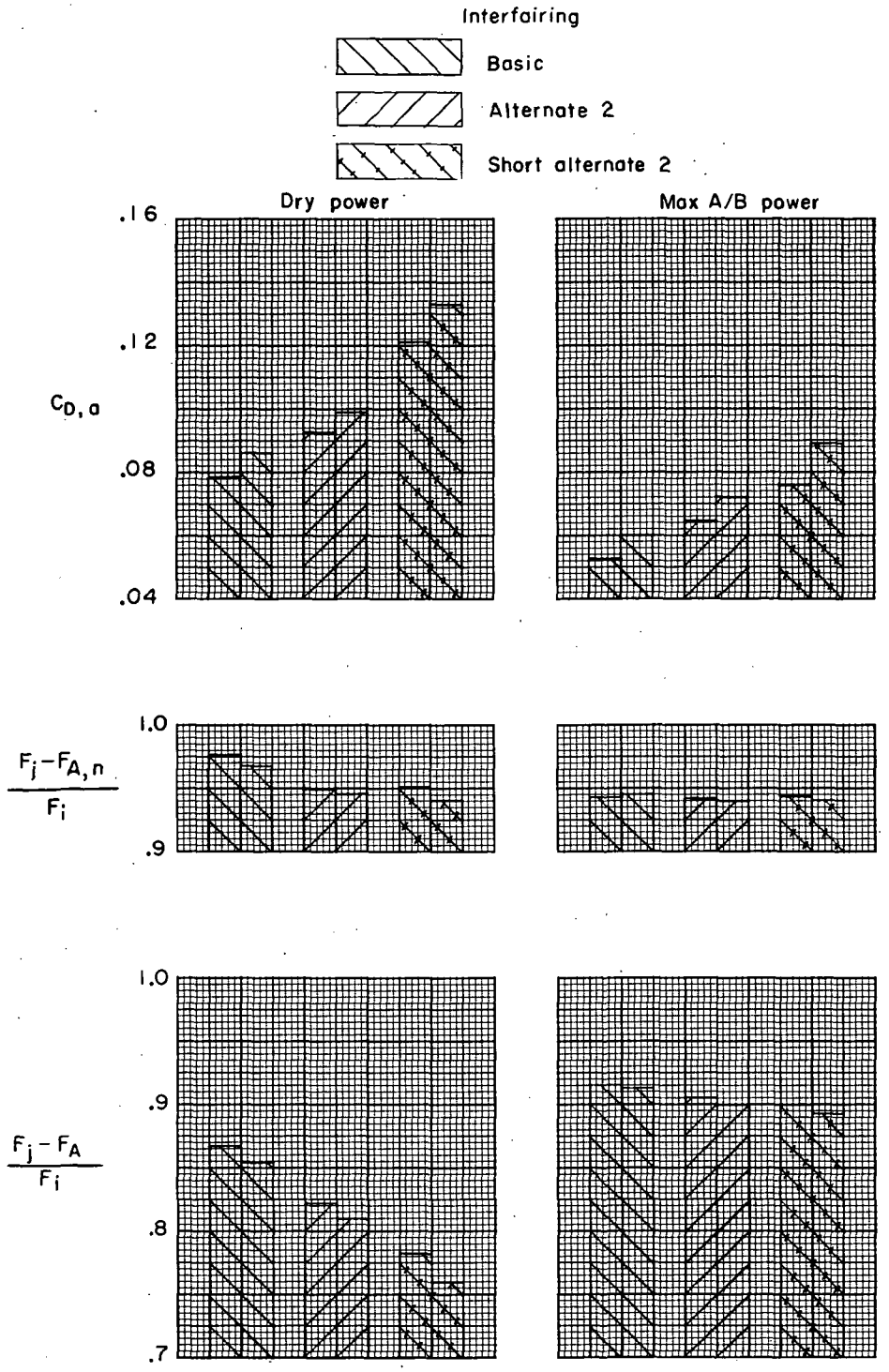


(c) Wide-spaced afterbody; M = 0.80.

Figure 29.- Continued.

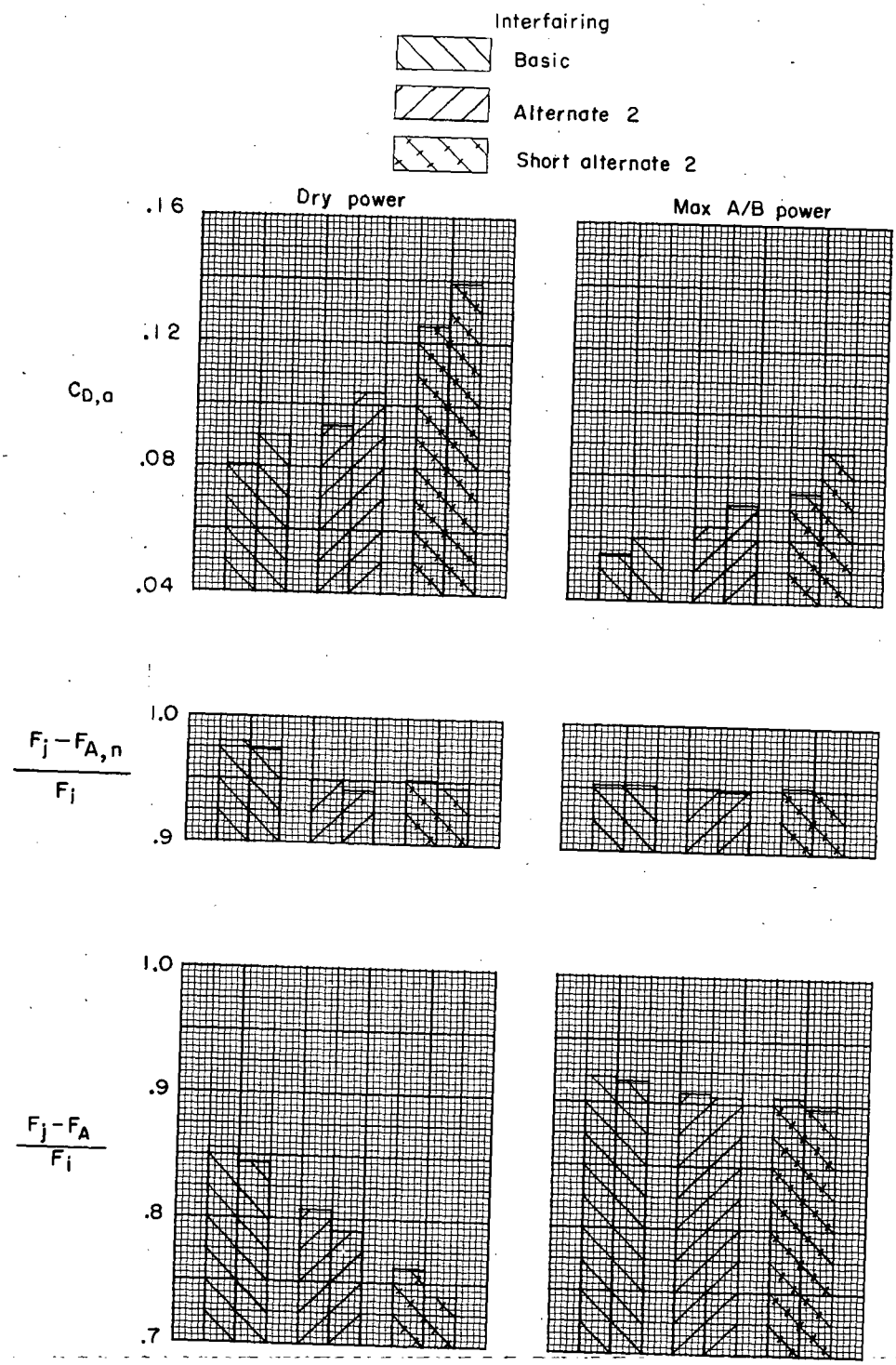


(d) Wide-spaced afterbody; M = 0.90.

Figure 29.- Concluded.

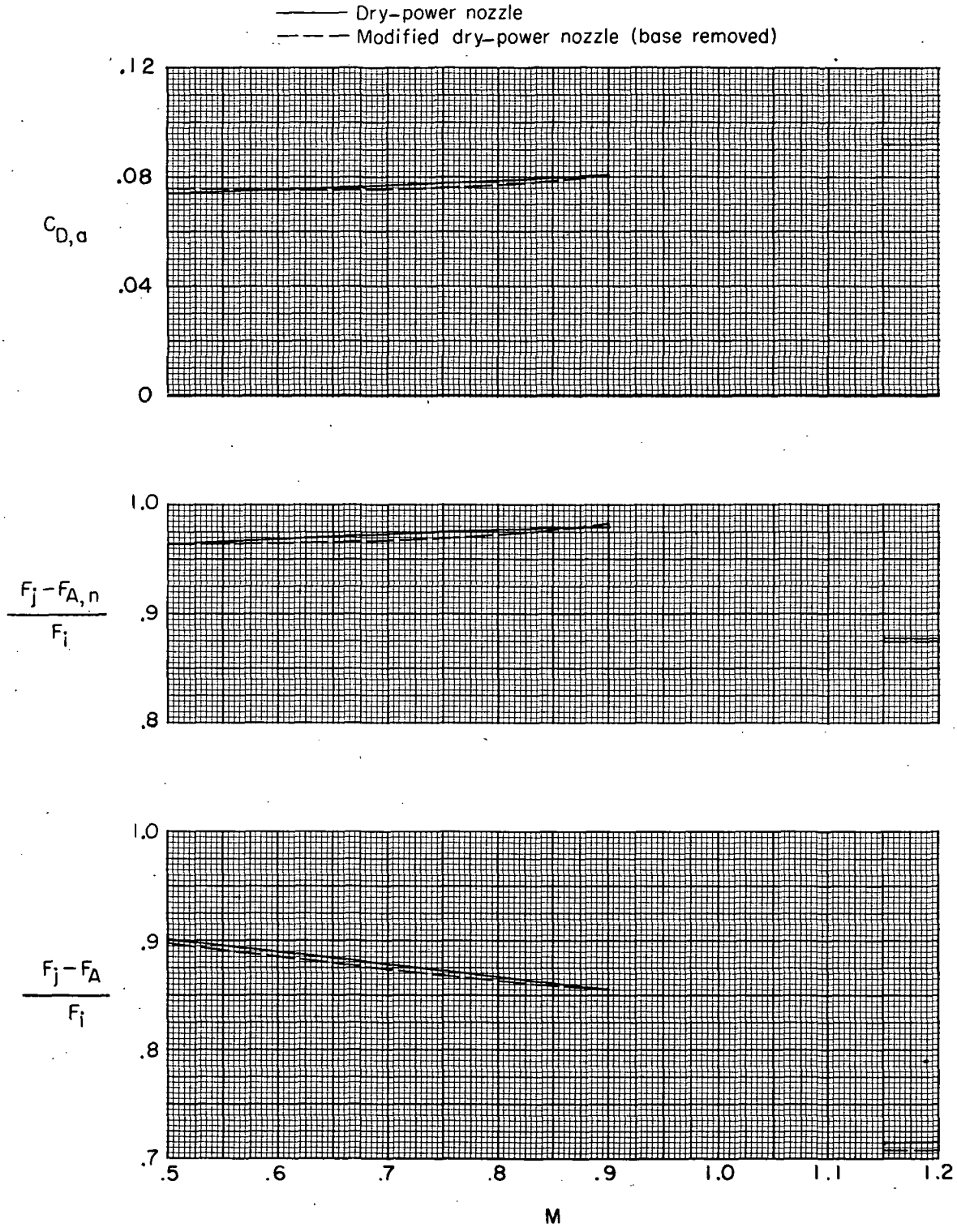


Figure 30.- Effect of nozzle-shroud base area on afterbody drag coefficient, thrust-minus-nozzle-axial-force ratio, and thrust-minus-total-axial-force ratio at scheduled values of $p_{t,j}/p_\infty$. Wide-spaced afterbody; basic interfairing; $\alpha = 0^o$.

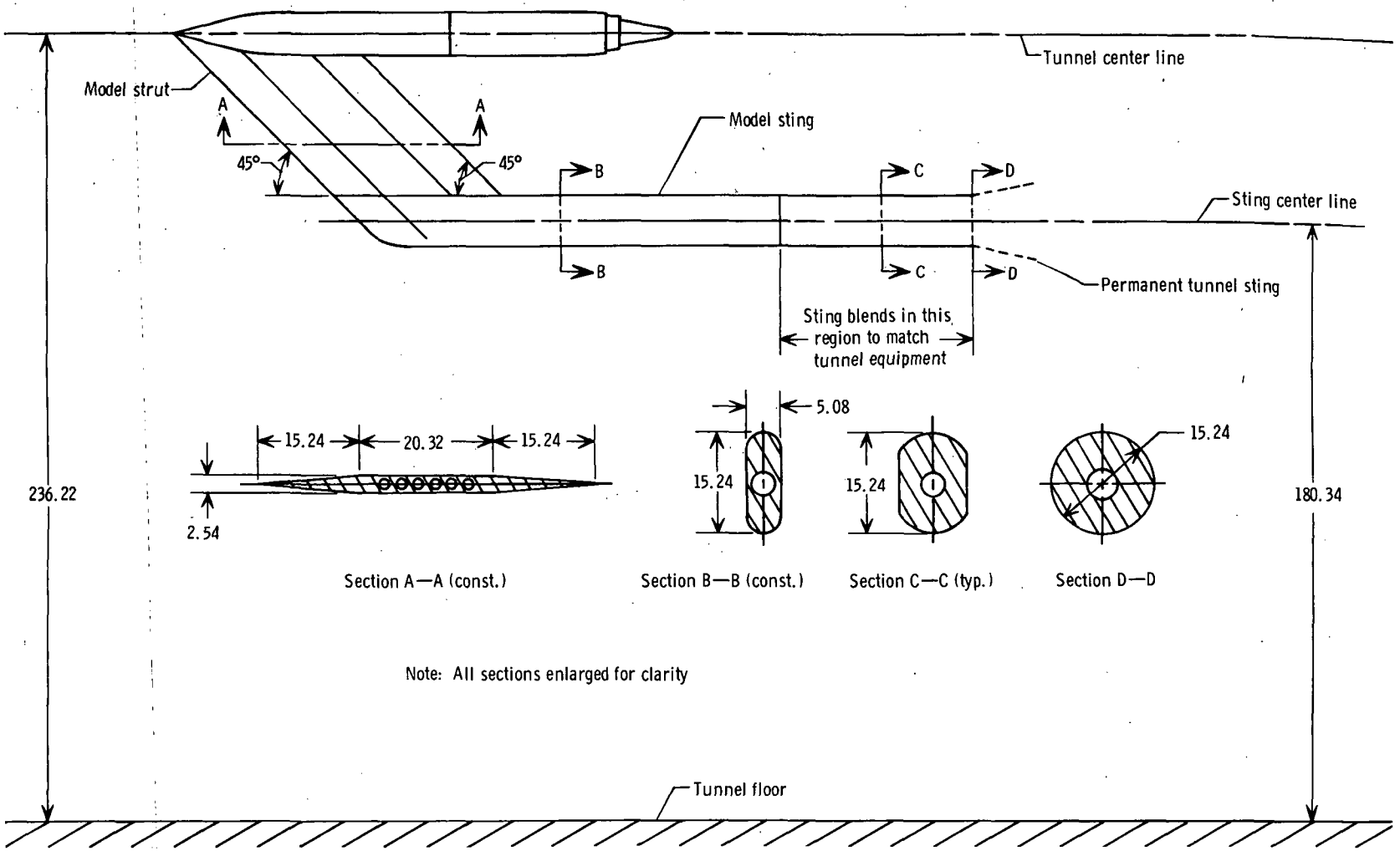


(a) Sting-mounted-strut support system.

Figure 31.- Sketch of model support systems showing important dimensions. All dimensions are in centimeters.

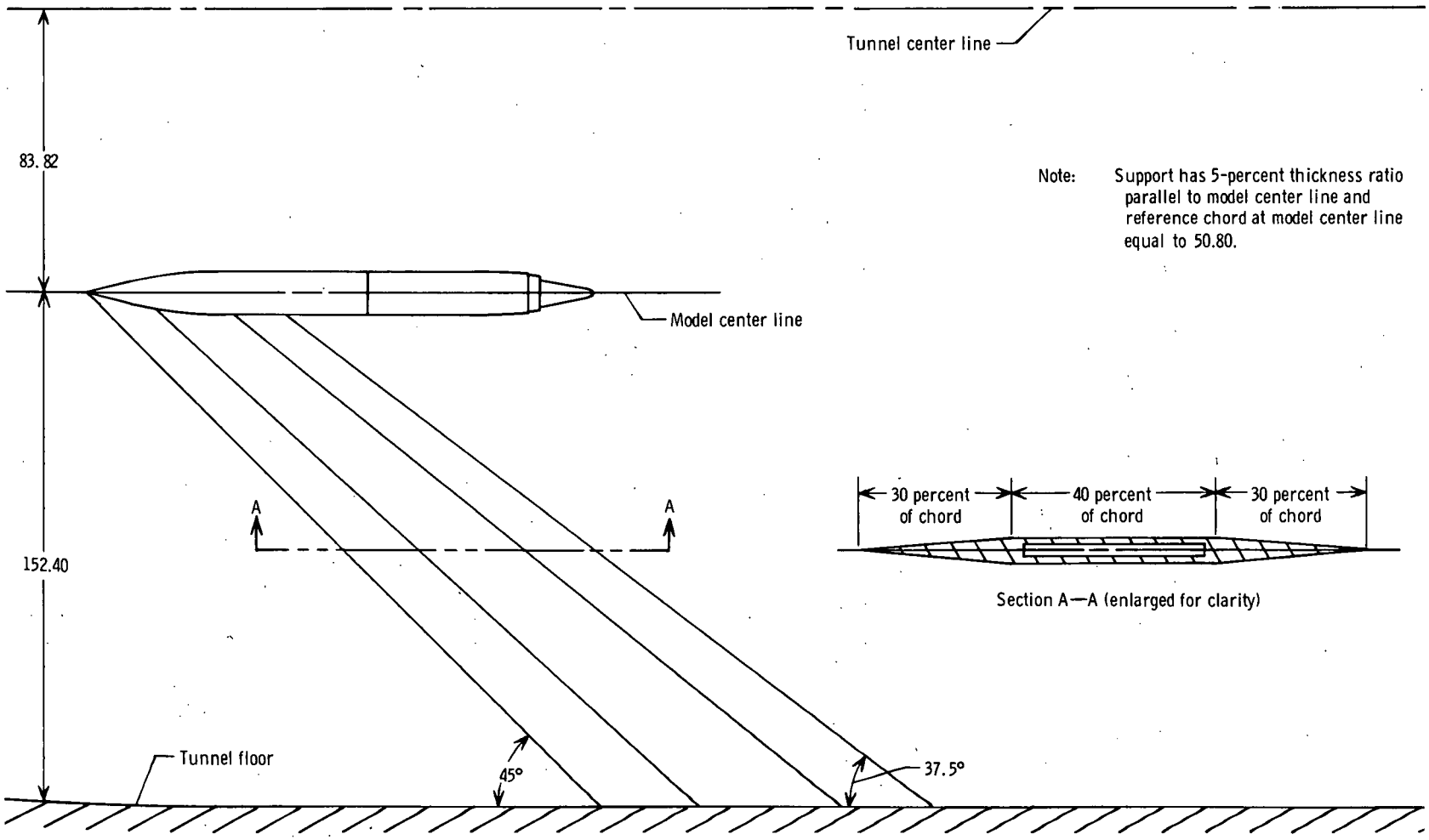


(b) Fixed ($\alpha = 0^{o}$) floor-mounted-strut support system.

Figure 31.- Concluded.

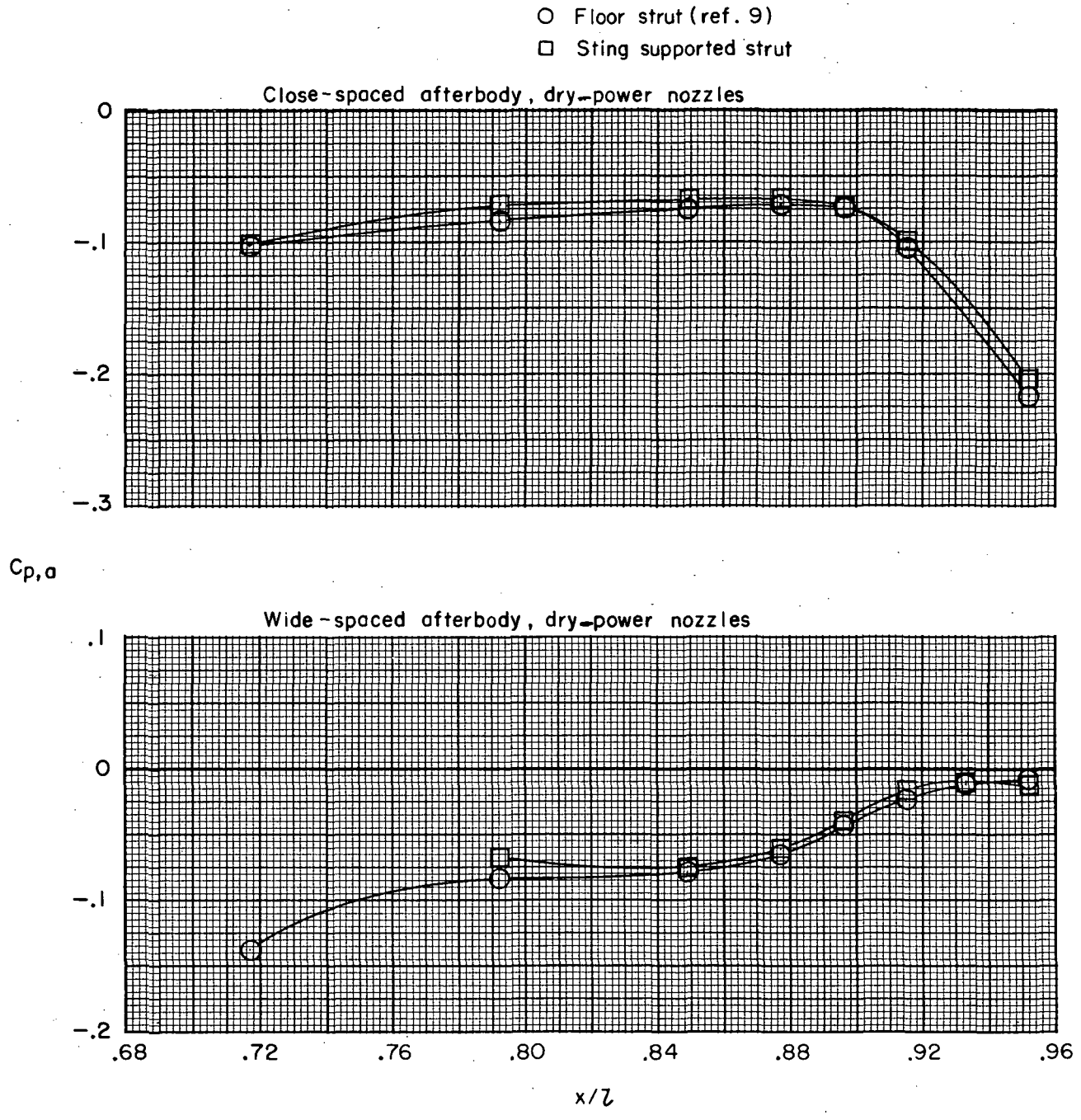


(a) M = 0.80; $p_{t,j}/p_\infty = 3.00$.

Figure 32.- Effect of support system on the afterbody top center-line static pressure distribution for several different configurations. Basic interfairing; $\alpha = 0^o$.

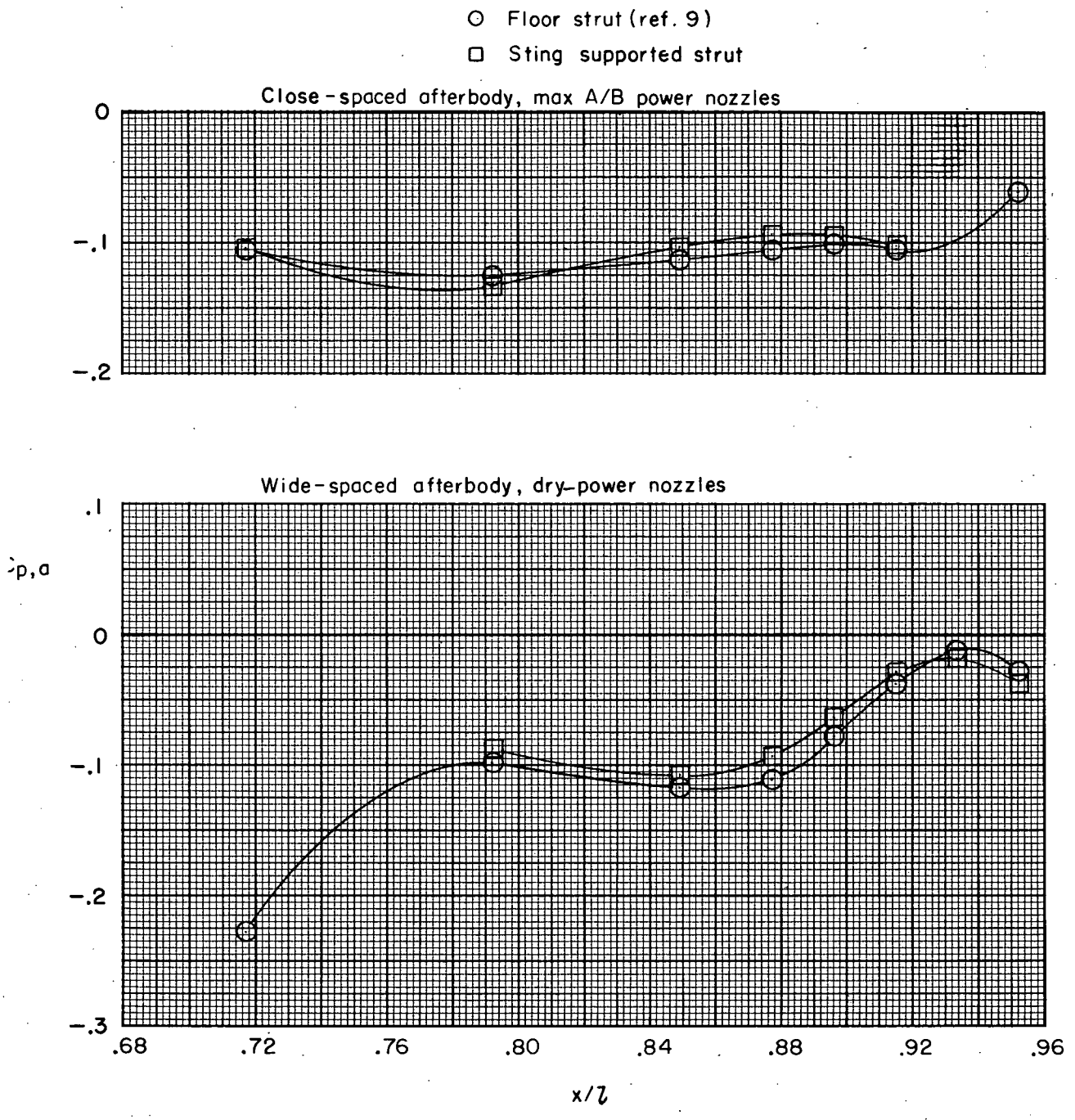


(b) $M = 1.20$; $p_{t,j}/p_\infty = 5.03$.

Figure 32.- Concluded.

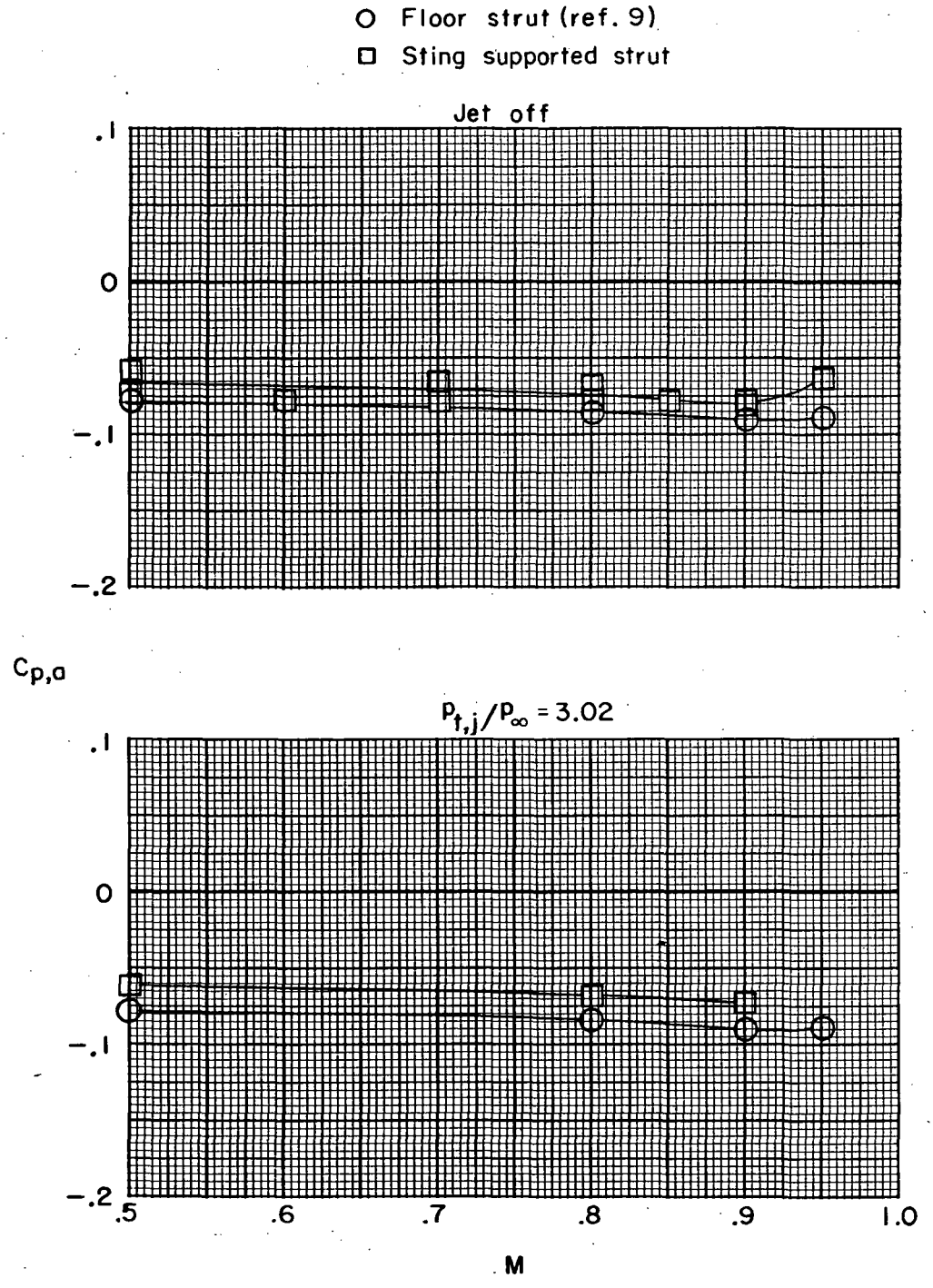


(a) $x/l = 0.717$.

Figure 33.- Variation of bottom center-line afterbody pressure coefficient with Mach number for two different support systems. Close-spaced afterbody; dry-power nozzles; basic interfairing.

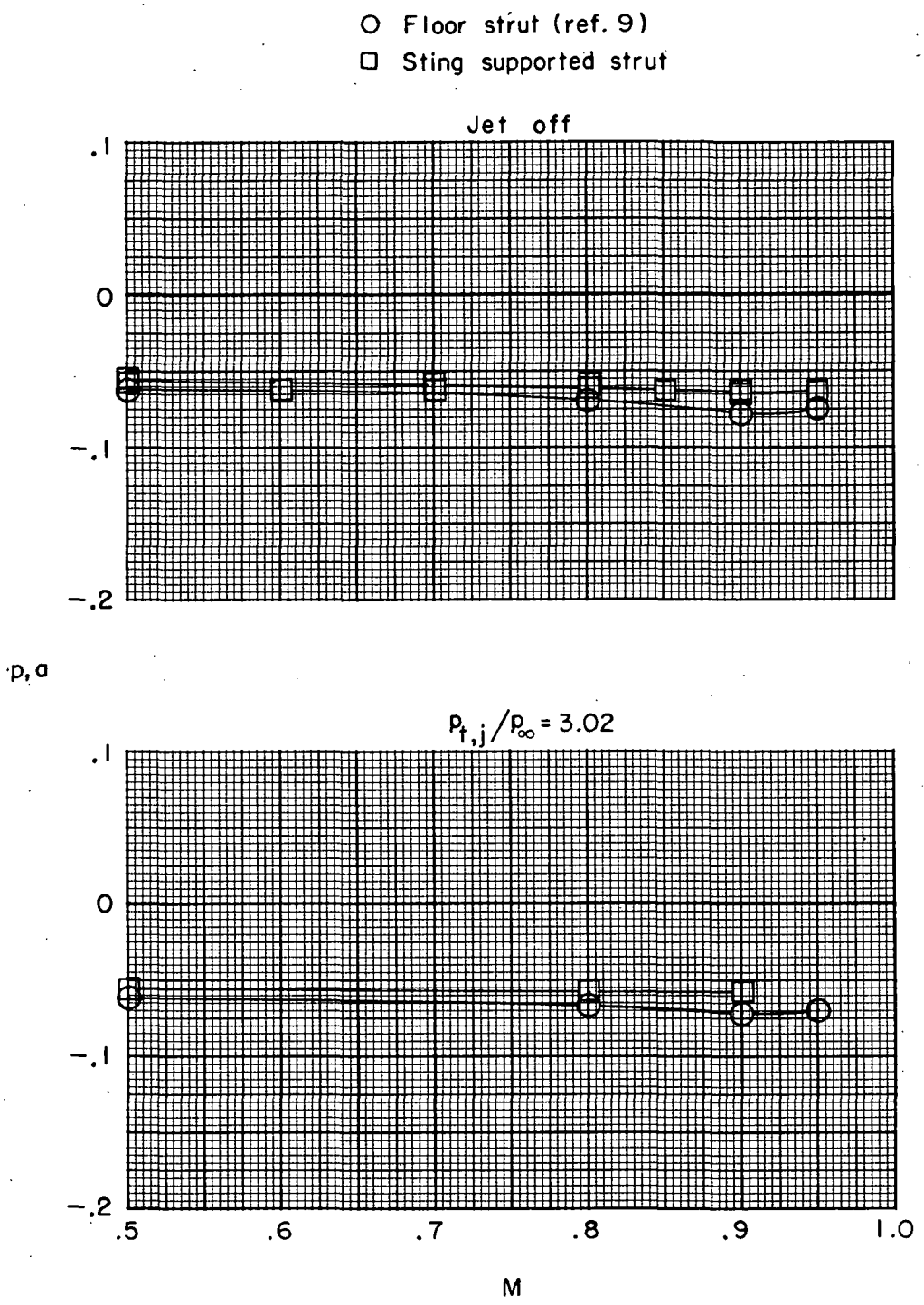


(b) $x/l = 0.849$.

Figure 33.- Concluded.

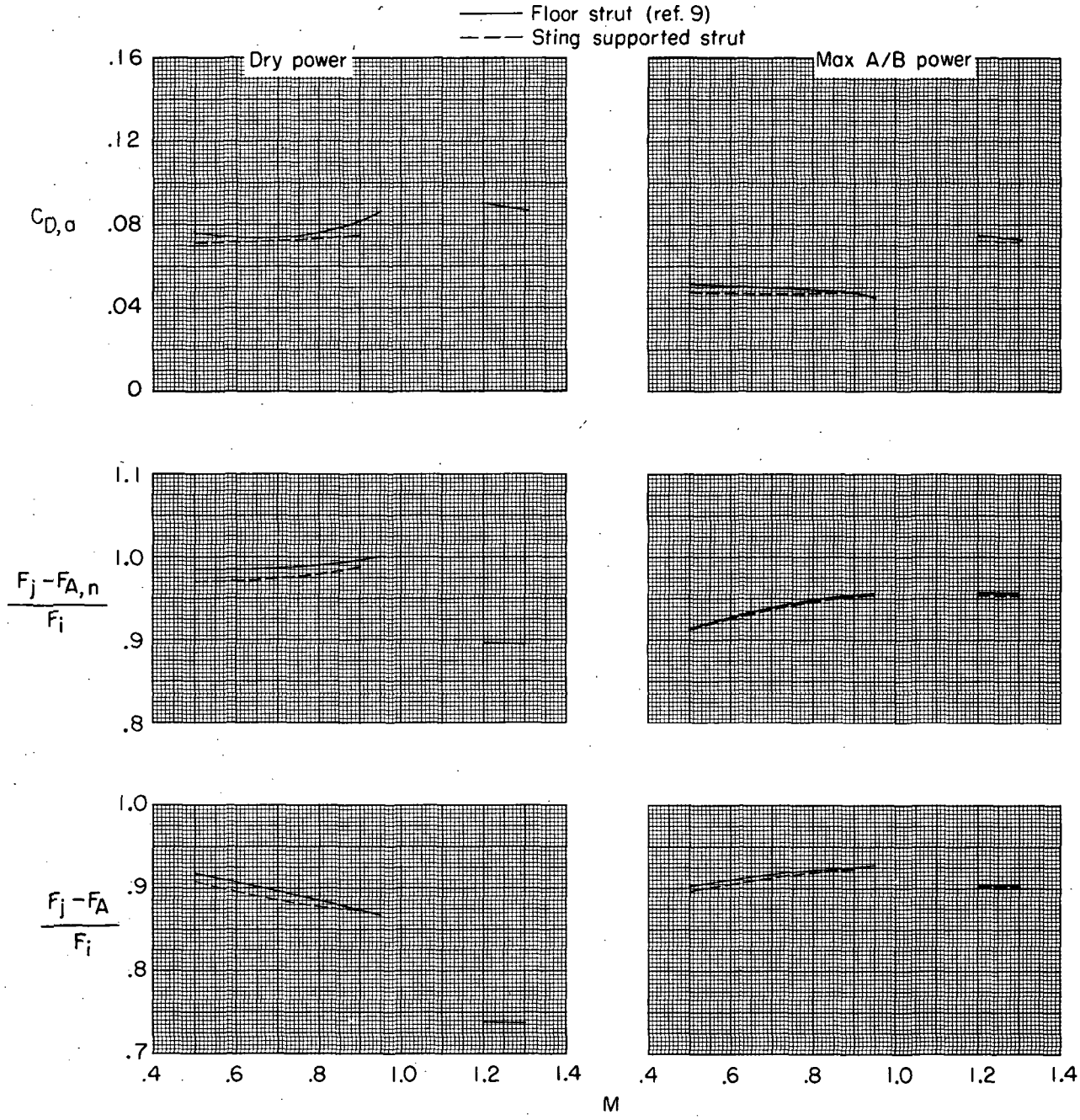


(a) Close-spaced afterbody; basic interfairing.

Figure 34.- Variation of afterbody drag coefficient, thrust-minus-nozzle-axial-force ratio, and thrust-minus-total-axial-force ratio with Mach number for scheduled values of $p_{t,j}/p_\infty$, utilizing two different support systems. $\alpha = 0^o$.

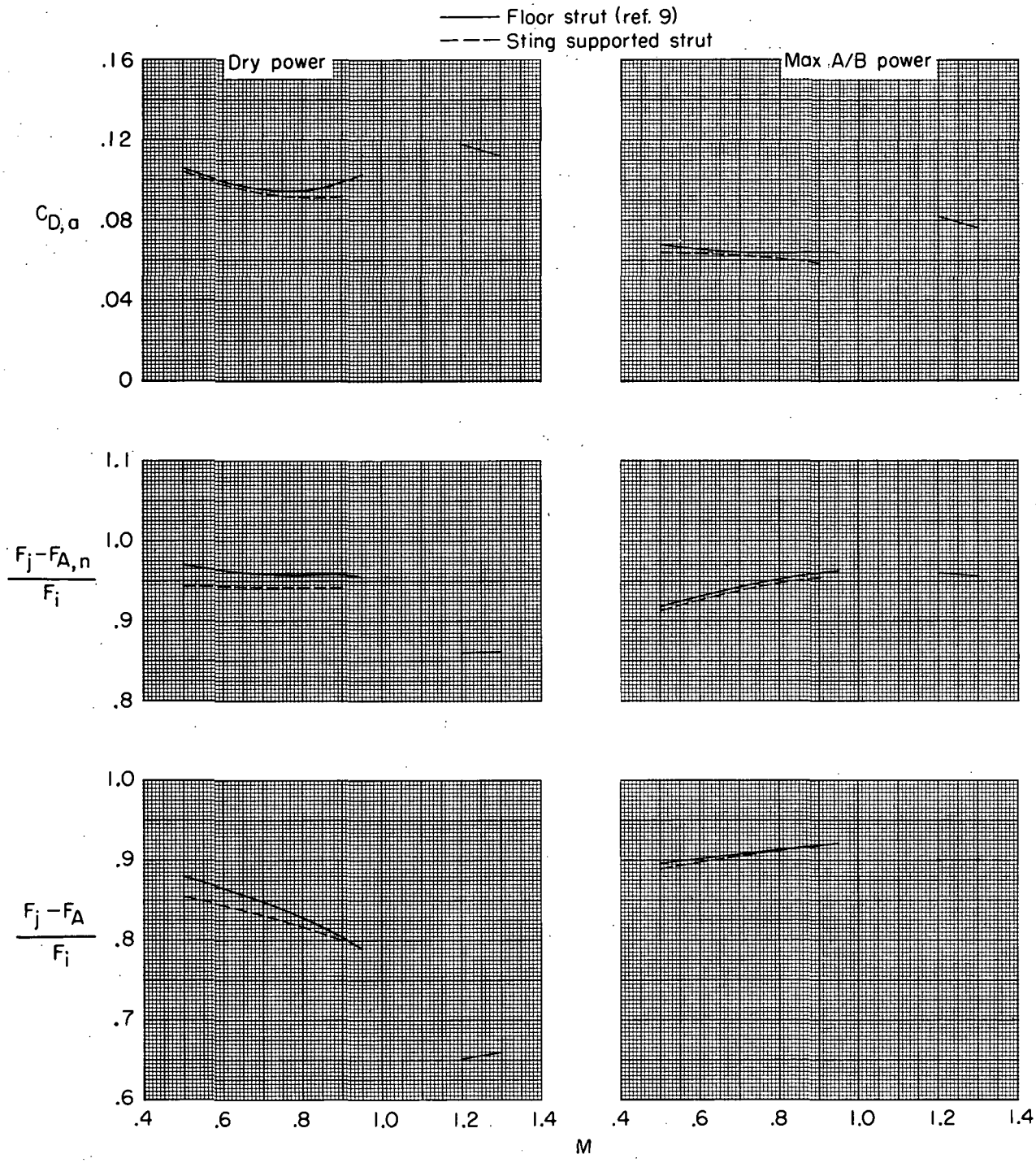


(b) Close-spaced afterbody; alternate 2 interfairing.

Figure 34.- Continued.

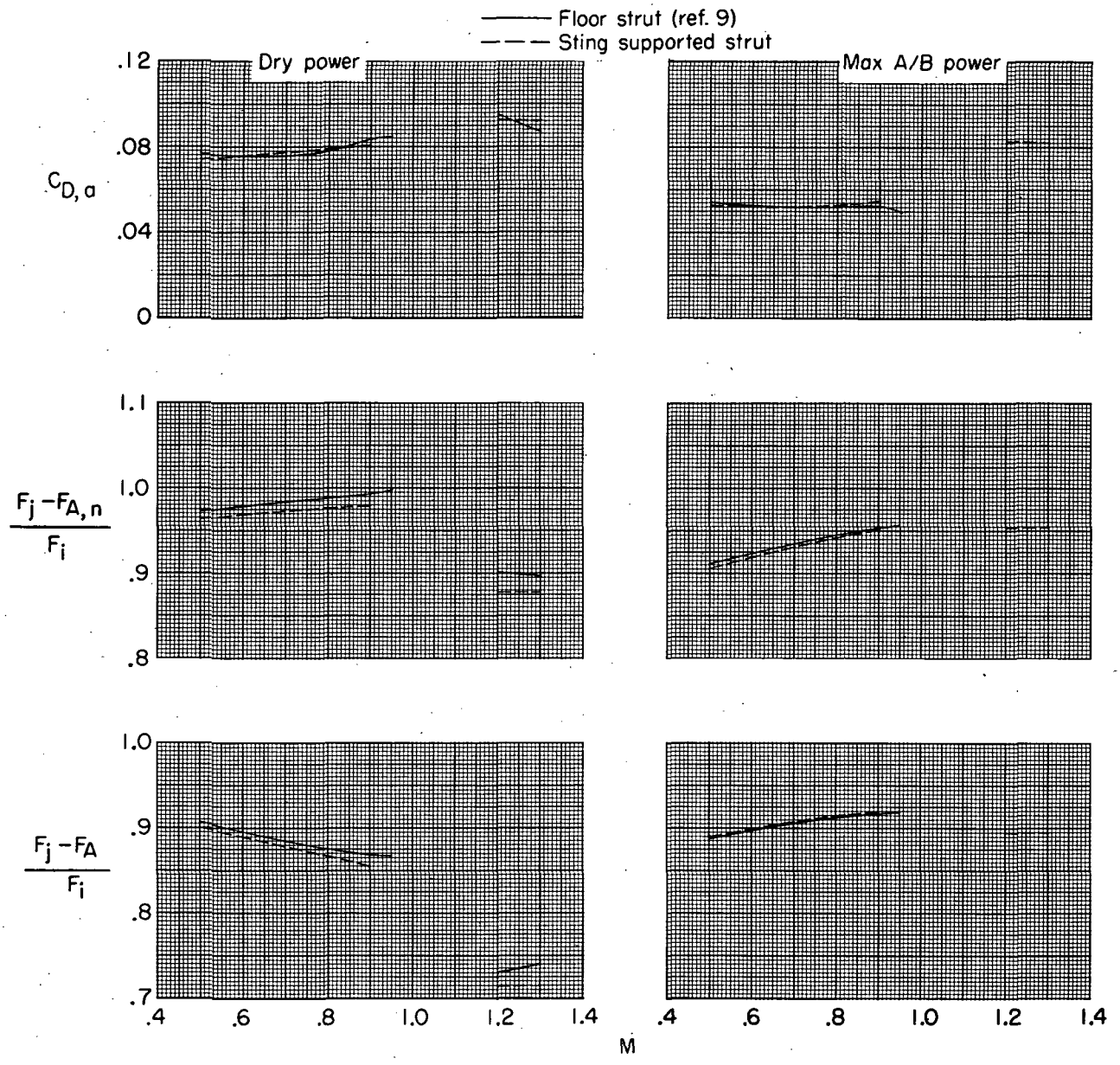


(c) Wide-spaced afterbody; basic interfairing.

Figure 34.- Continued.

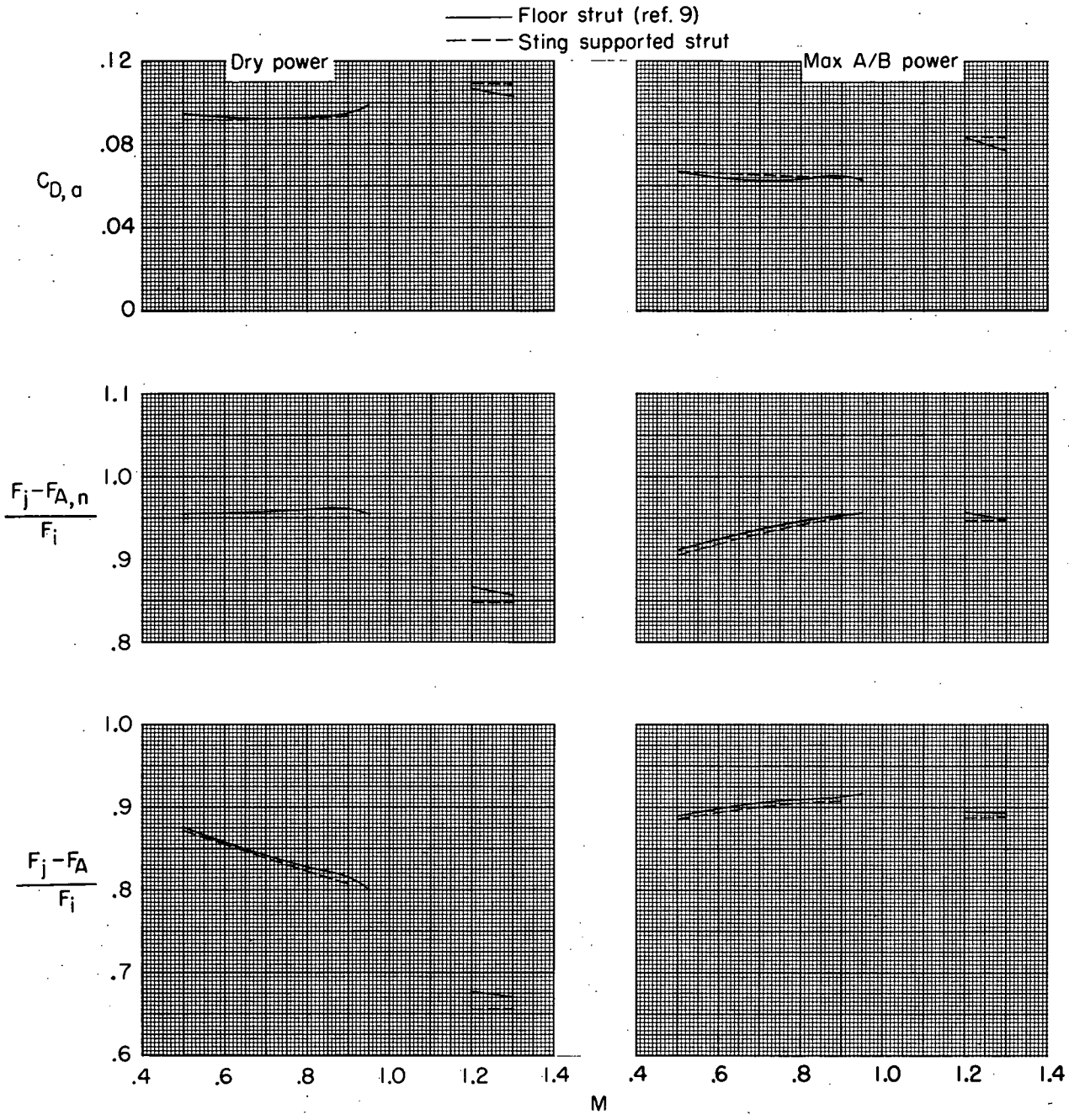


(d) Wide-spaced afterbody; alternate 2 interfairing.

Figure 34.- Concluded.

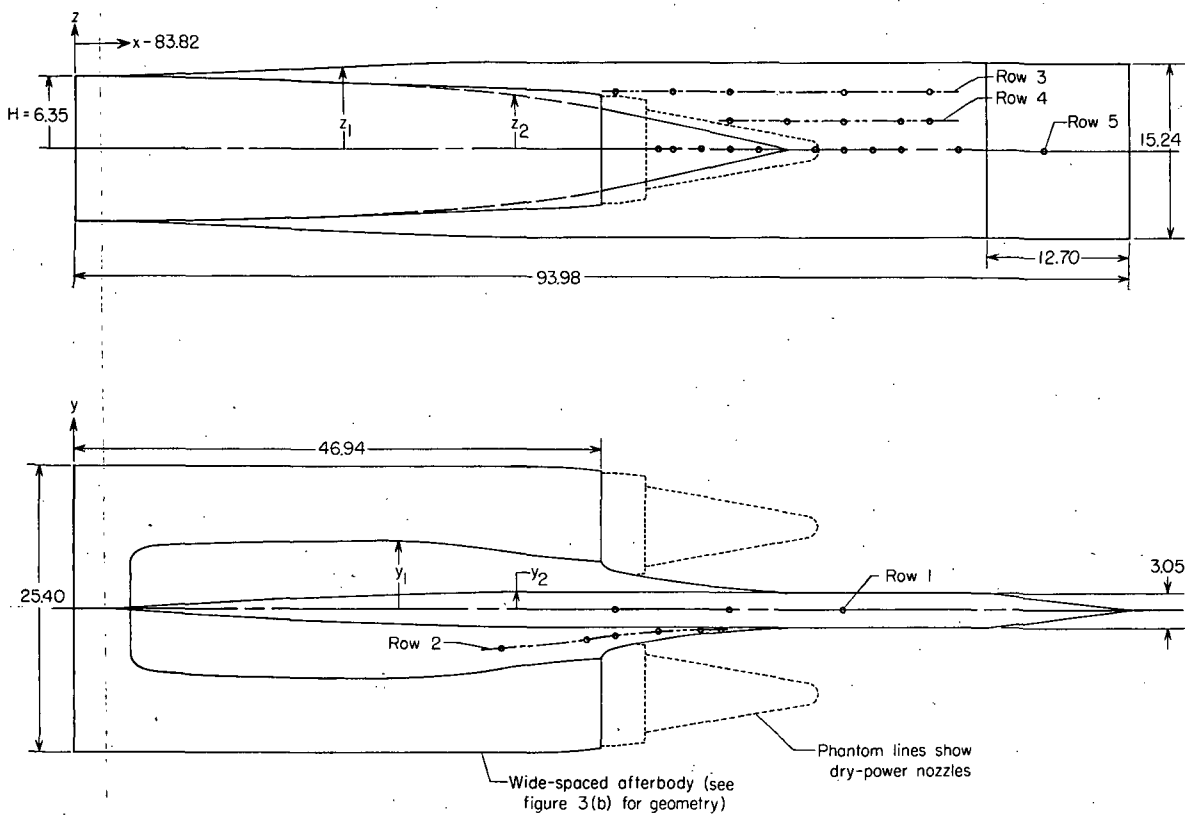


| Simulated fuselage geometry | | | | |
|---|---|---|---|---|
| $\frac{x}{l}$ | $z_1/H$ | $z_2/H$ | $y_1/H$ | $y_2/H$ |
| 0.651 | 0.988 | —— | —— | 0 |
| .679 | 1.020 | 0.988 | 0.888 | .040 |
| .717 | 1.052 | .972 | .932 | .084 |
| .754 | 1.088 | .952 | .948 | .148 |
| .792 | 1.120 | .916 | .960 | .168 |
| .830 | 1.160 | .888 | .960 | .200 |
| .867 | 1.188 | .852 | .932 | .220 |
| .905 | 1.200 | .768 | .816 | .240 |
| .943 | 1.200 | .664 | .728 | .240 |
| .971 | 1.200 | . | .680 | .240 |
| .980 | 1.200 | .520 | .548 | .240 |
| .999 | 1.200 | | .468 | .240 |
| 1.018 | 1.200 | .352 | .400 | .240 |
| 1.056 | 1.200 | .176 | .300 | .240 |
| 1.094 | 1.200 | 0 | .240 | .240 |
| 1.320 | 1.200 | —— | —— | 0 |

| Orifice locations | | | | | |
|---|---|---|---|---|---|
| $\frac{x}{l}$ | Row | | | | |
| | 1 | 2 | 3 | 4 | 5 |
| 0.905 | | X | | | |
| .962 | | X | | | |
| .980 | X | X | X | | |
| 1.009 | | X | | | X |
| 1.018 | | | X | | X |
| 1.037 | | X | | | X |
| 1.046 | | X | | | |
| 1.056 | X | | X | X | X |
| 1.075 | | | | | X |
| 1.094 | | | | X | |
| 1.112 | | | | | X |
| 1.131 | X | | X | X | X |
| 1.150 | | | | | X |
| 1.169 | | | | X | X |
| 1.188 | | | X | X | |
| 1.207 | | | | | X |
| 1.263 | | | | | X |

Note: y and z locations for rows 1, 3, 4, and 5 can be determined from sketch; y and z locations for row 2 are given in table below.

| $x/l$ | $y/l$ | $z/l$ |
|---|---|---|
| 0.905 | −0.026 | 0.036 |
| .962 | −0.019 | .028 |
| .980 | −0.017 | .025 |
| 1.009 | −0.015 | .019 |
| 1.037 | −0.013 | .013 |
| 1.046 | −0.012 | .011 |

Figure 35.- Sketch of simulated fuselage fairing installed on wide-spaced afterbody showing important dimensions and orifice locations. All dimensions are in centimeters.

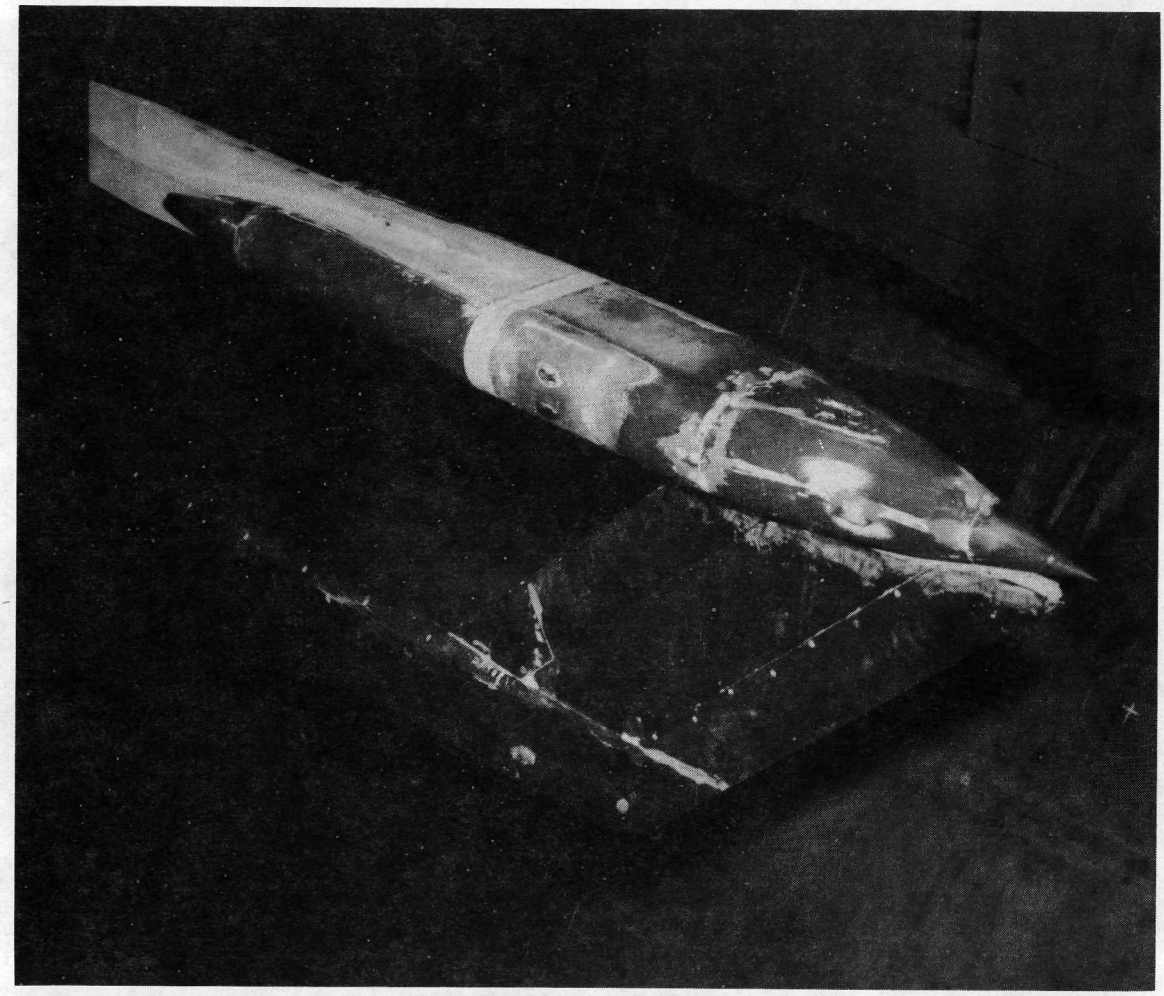

L-72-4338

(a) Front three-quarter view.

Figure 36.- Photographs of simulated fuselage installed on wide-spaced afterbody with dry-power nozzles.

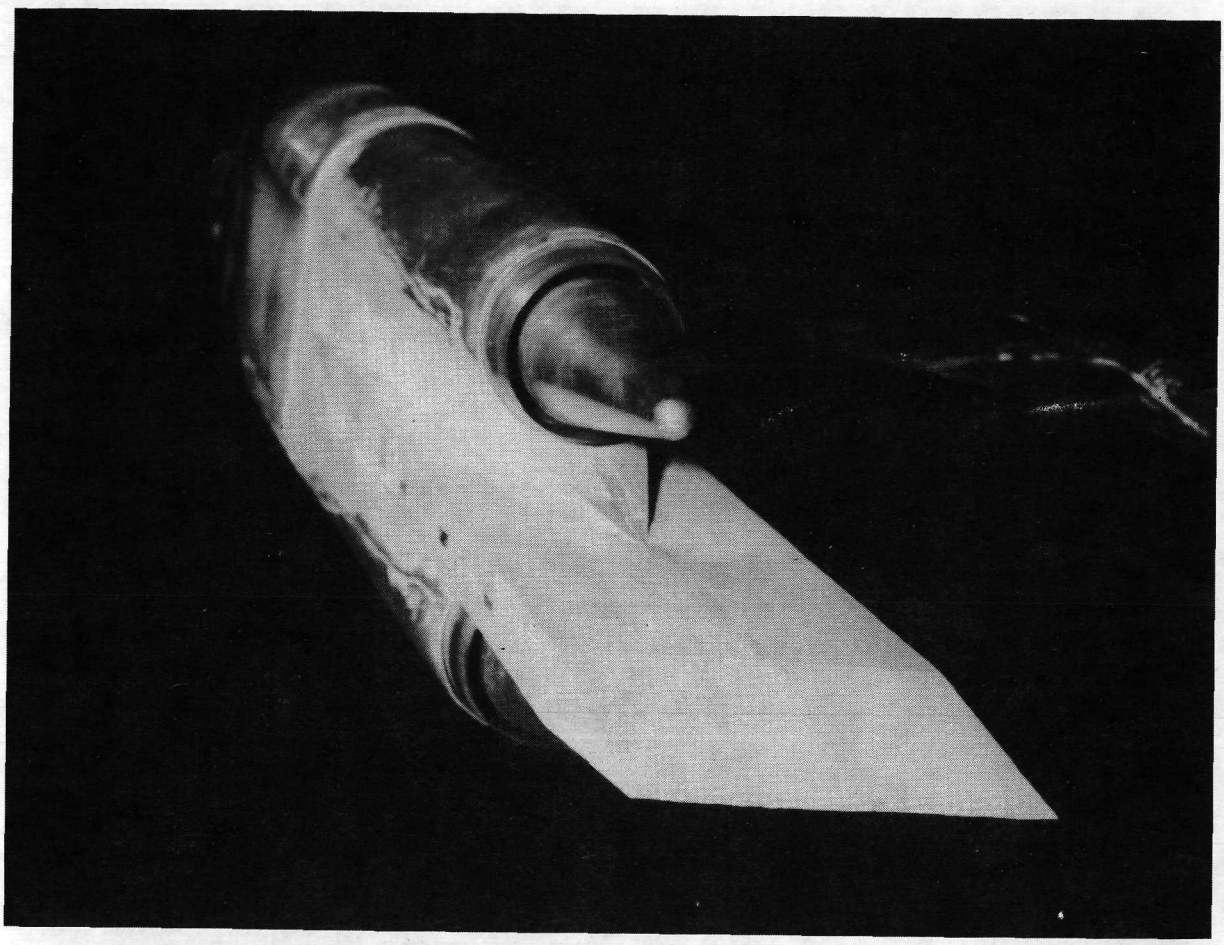

L-72-4341

(b) Rear three-quarter view.

Figure 36.- Concluded.

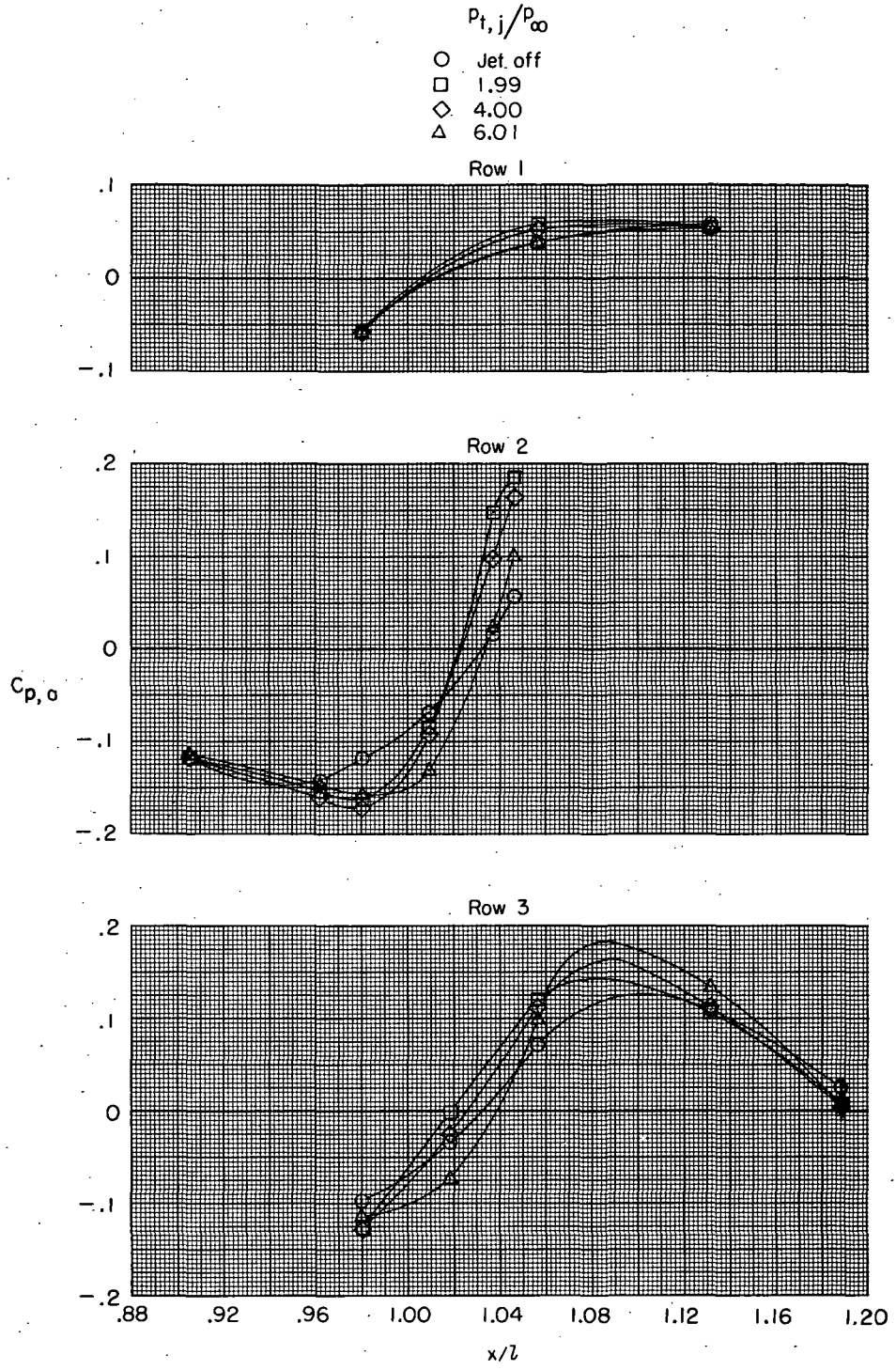


(a) M = 0.50; rows 1, 2, and 3.

Figure 37.- Longitudinal static-pressure distributions on a simulated fuselage adjacent to dry-power cone plug nozzles at several values of $p_{t,j}/p_\infty$.

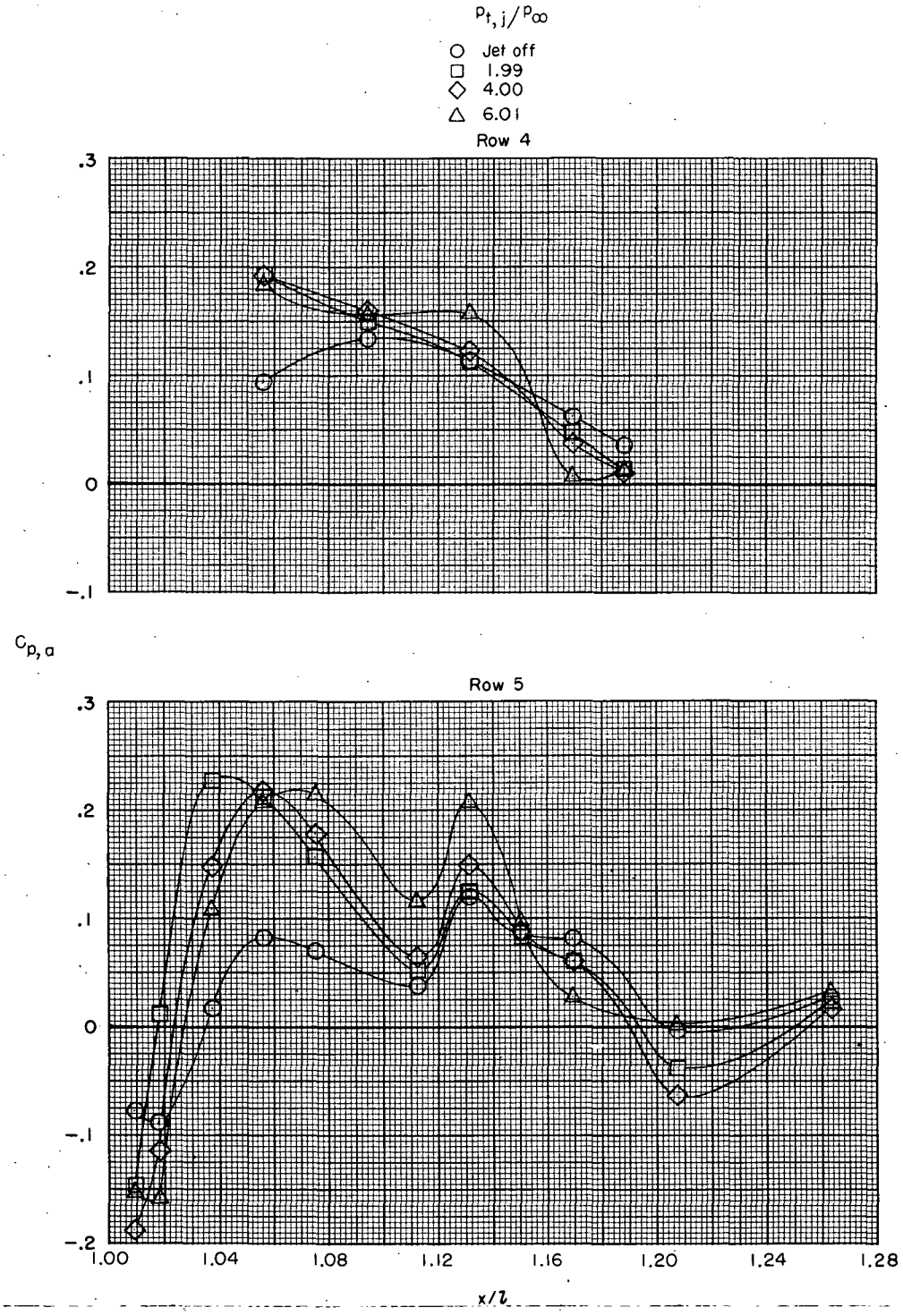


(b) M = 0.50; rows 4 and 5.

Figure 37.- Continued.

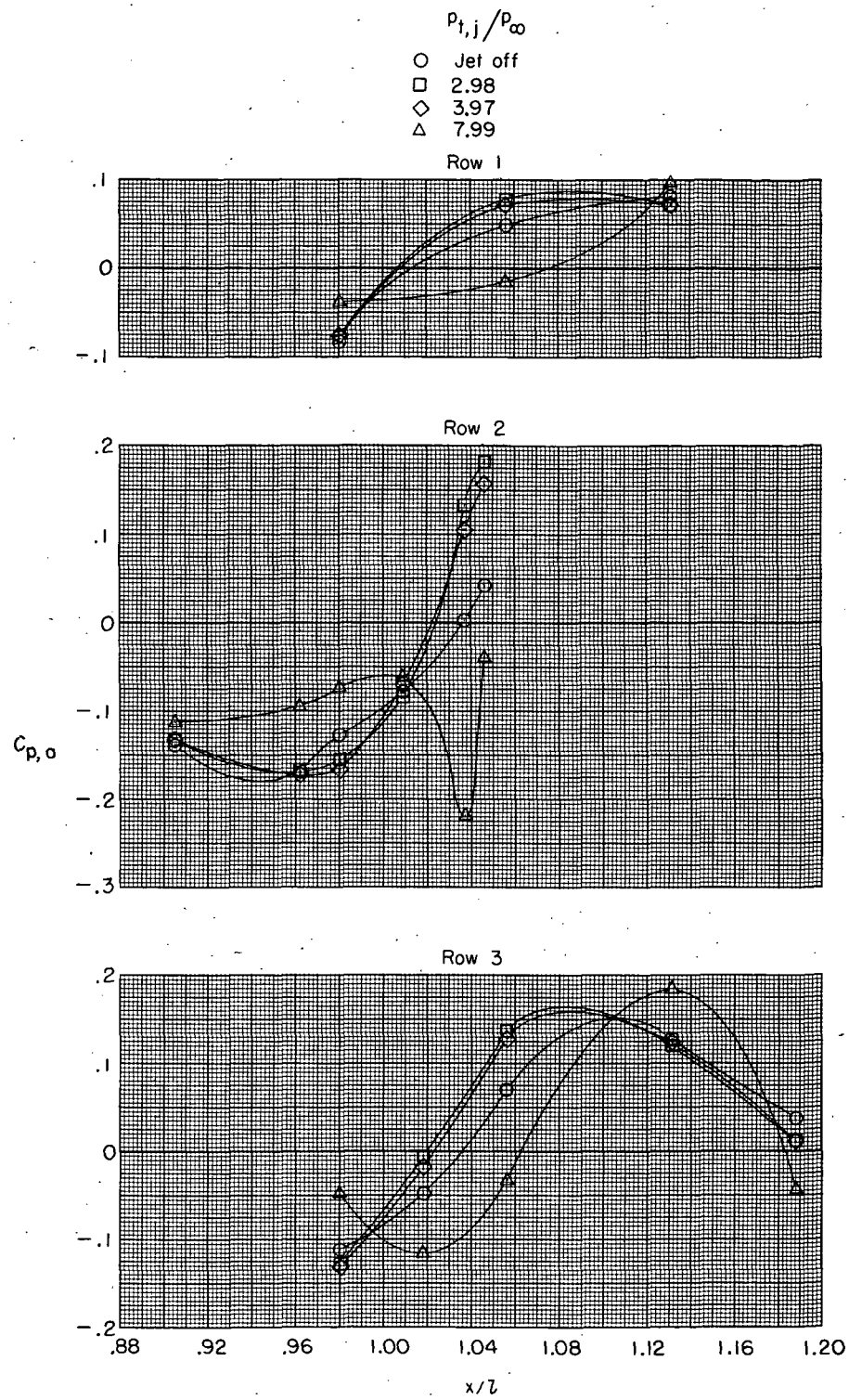


(c) M = 0.80; rows 1, 2, and 3.

Figure 37.- Continued.

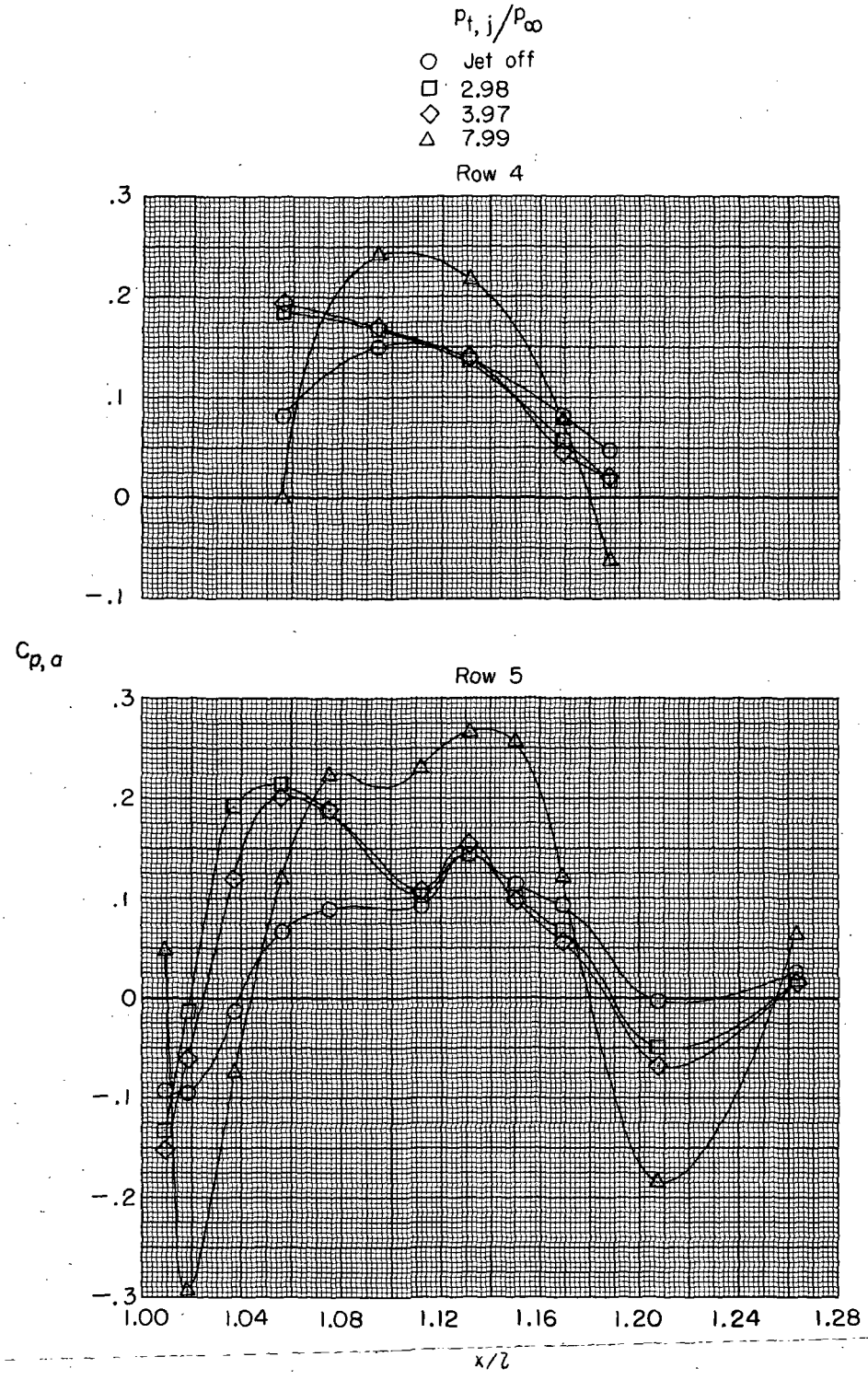


(d) M = 0.80; rows 4 and 5.

Figure 37.- Continued.

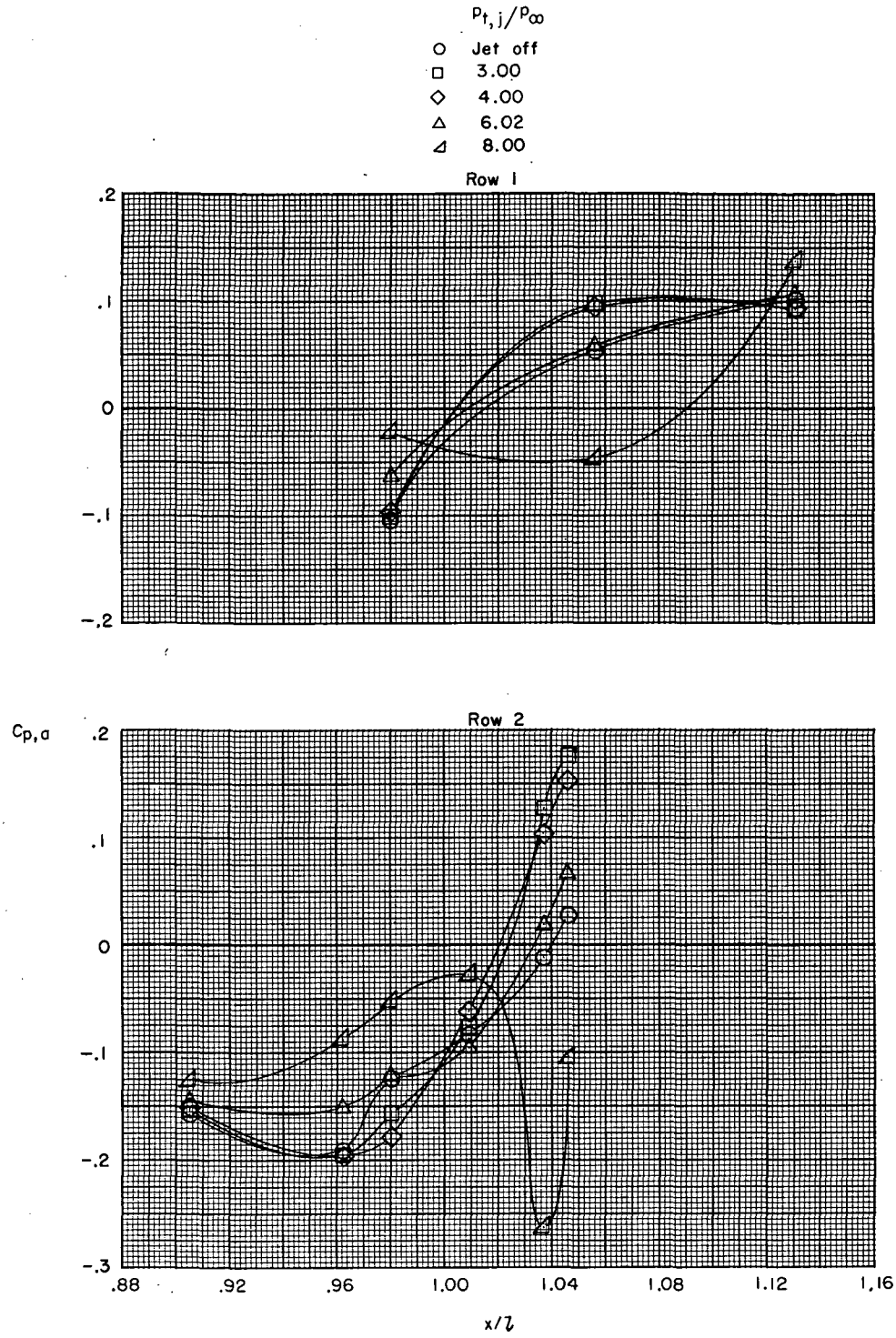


(e) M = 0.90; rows 1 and 2.

Figure 37.- Continued.

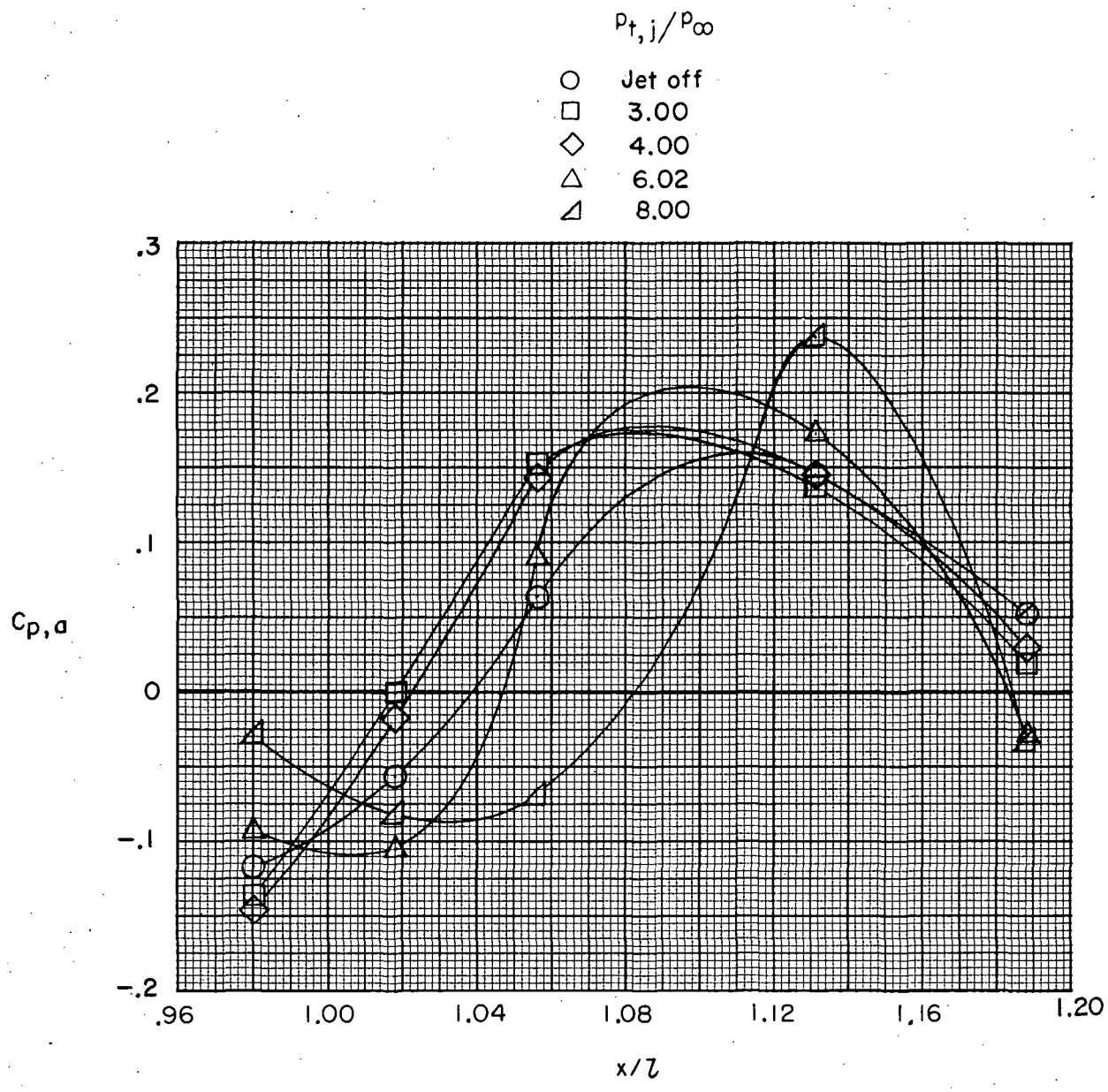


(f) M = 0.90; row 3.

Figure 37.- Continued.

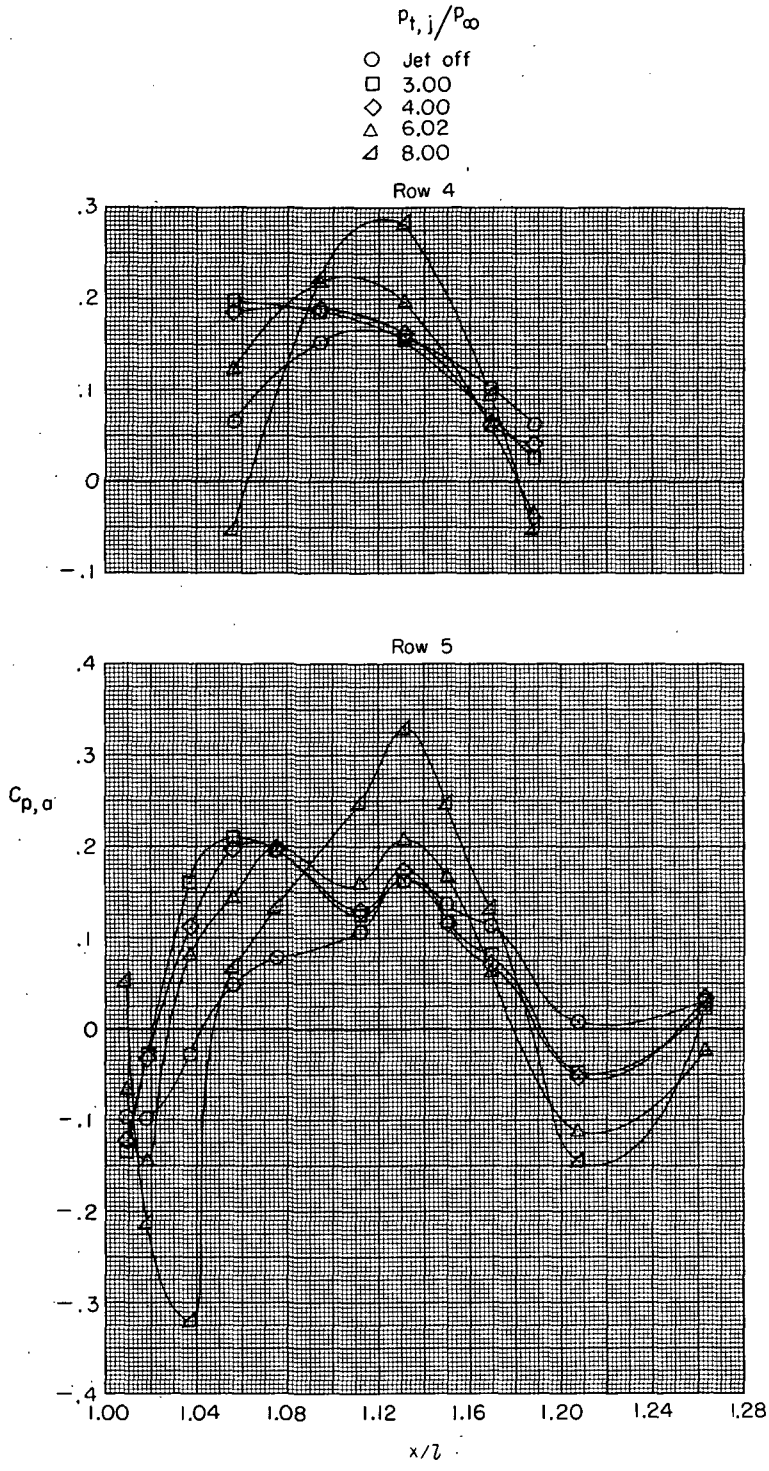


(g) M = 0.90; rows 4 and 5.

Figure 37.- Continued.

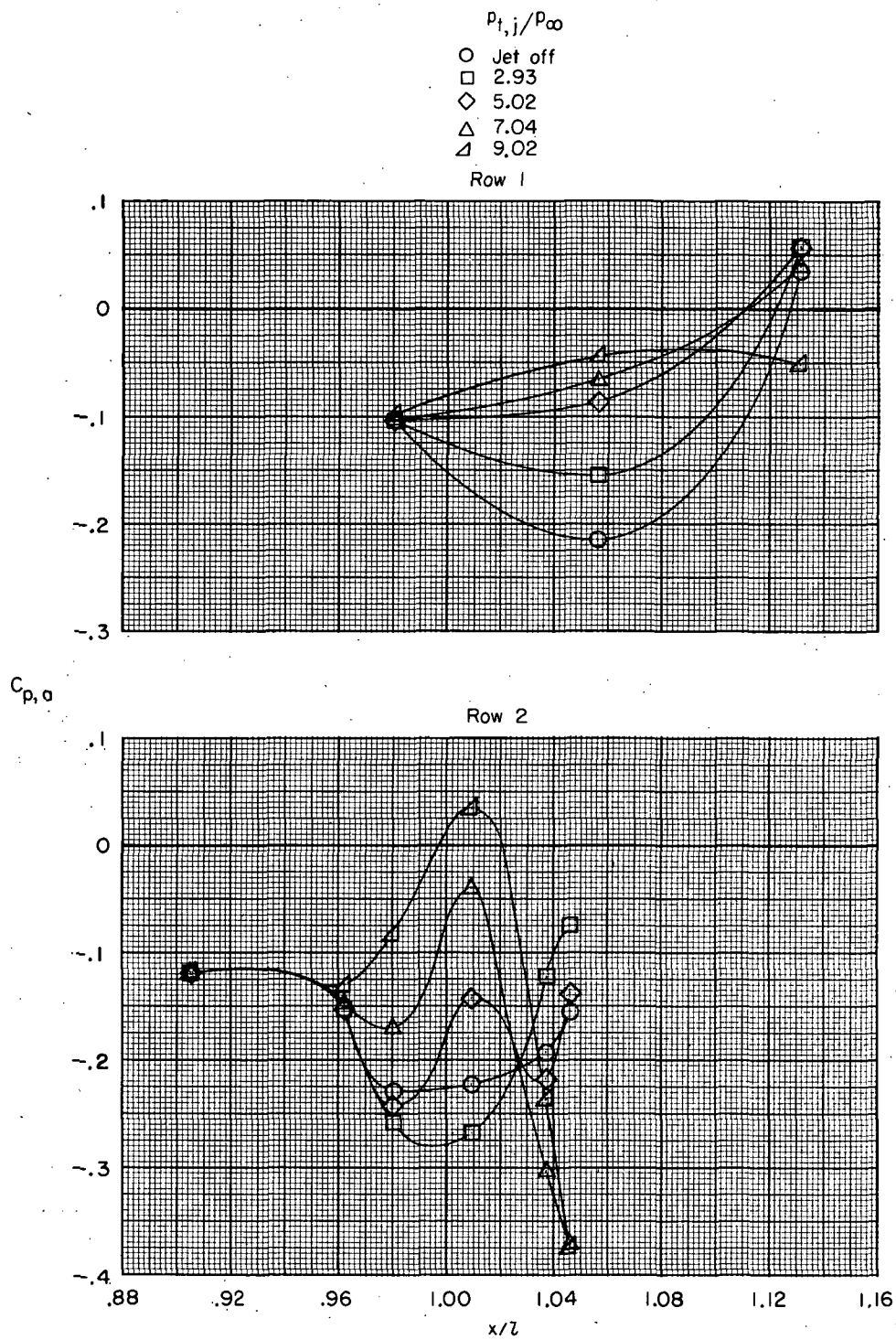


(h) M = 1.20; rows 1 and 2.

Figure 37.- Continued.

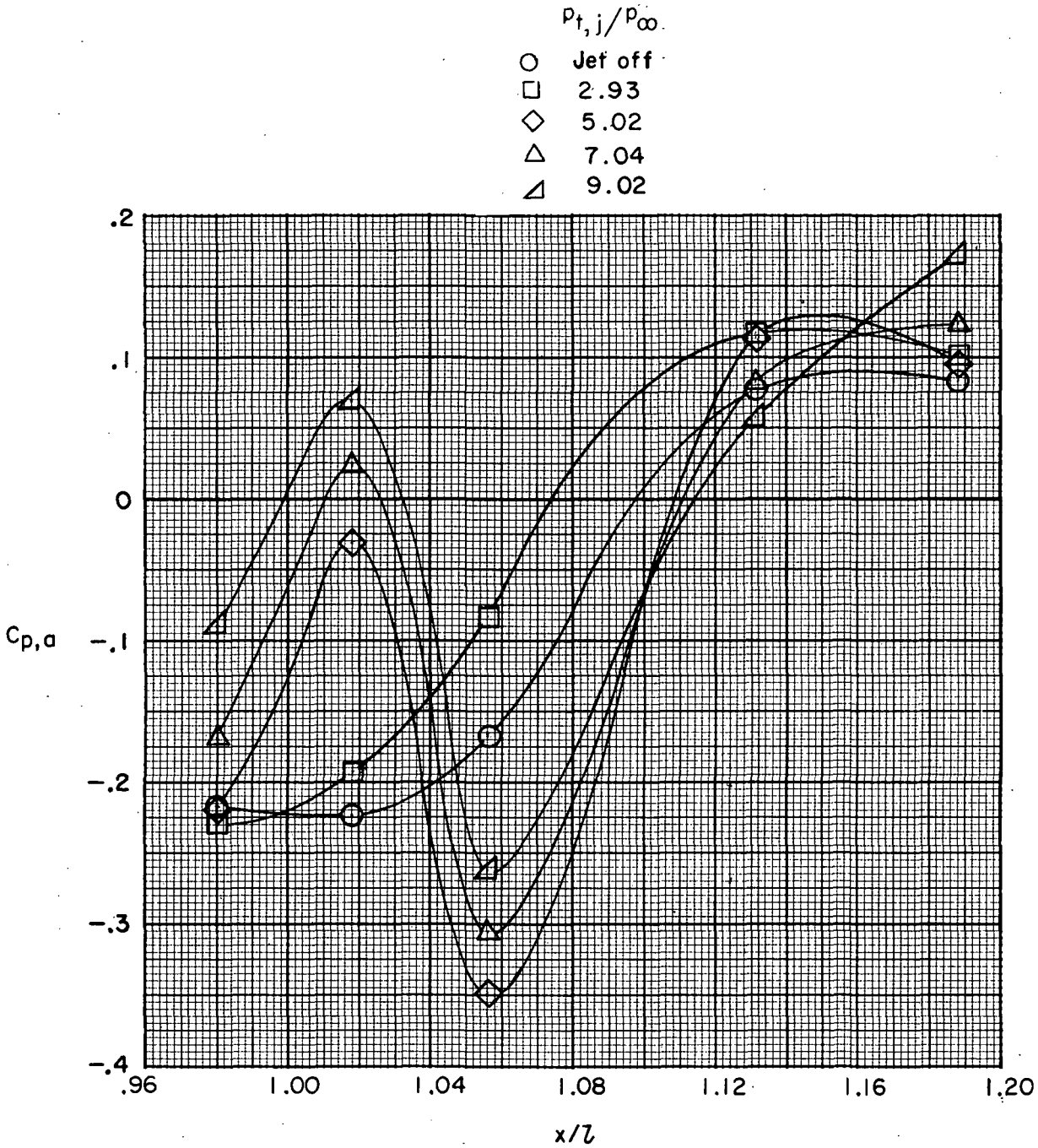


(i) M = 1.20; row 3.

Figure 37.- Continued.

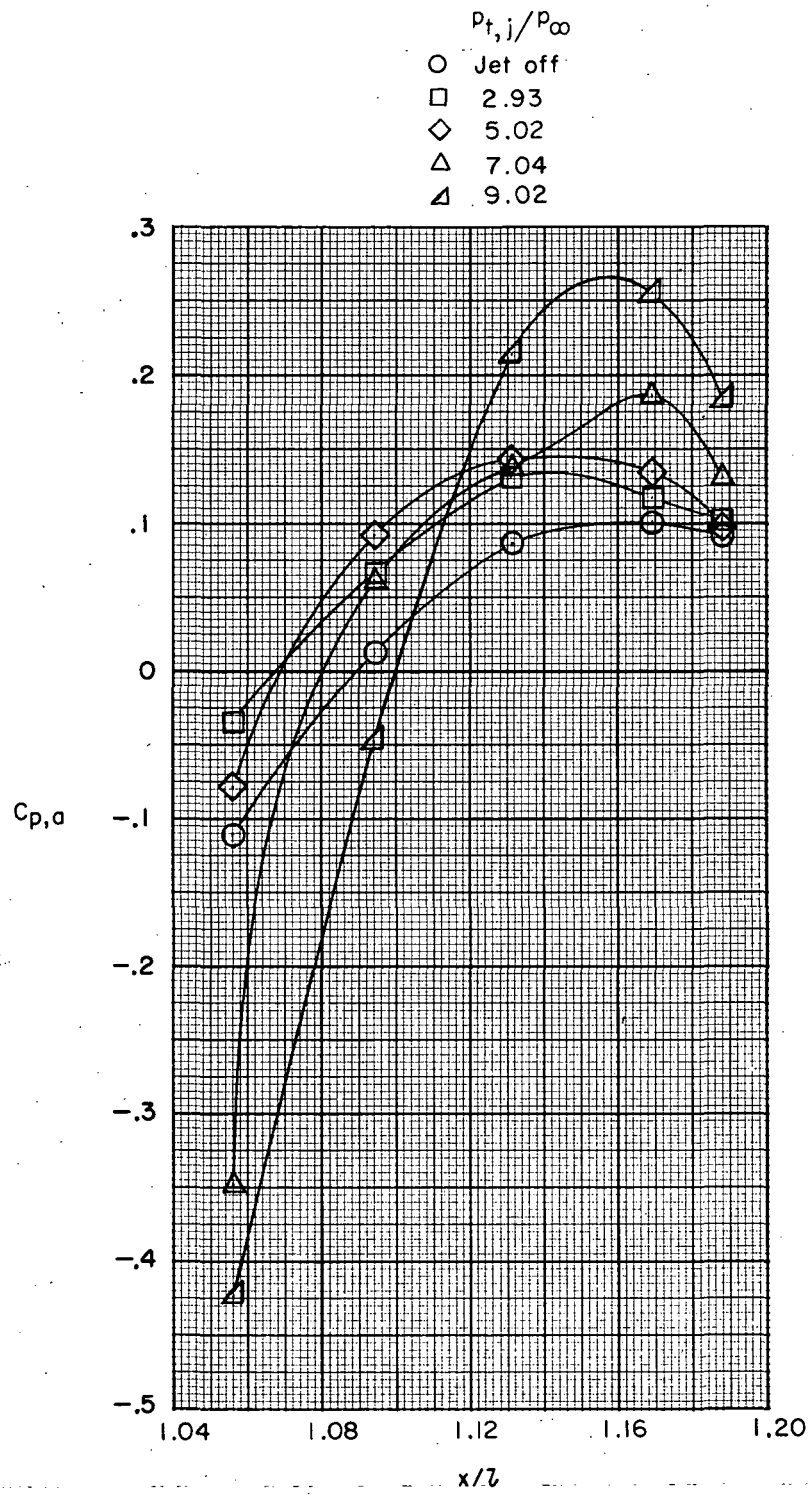


(j) M = 1.20; row 4.

Figure 37.- Continued.

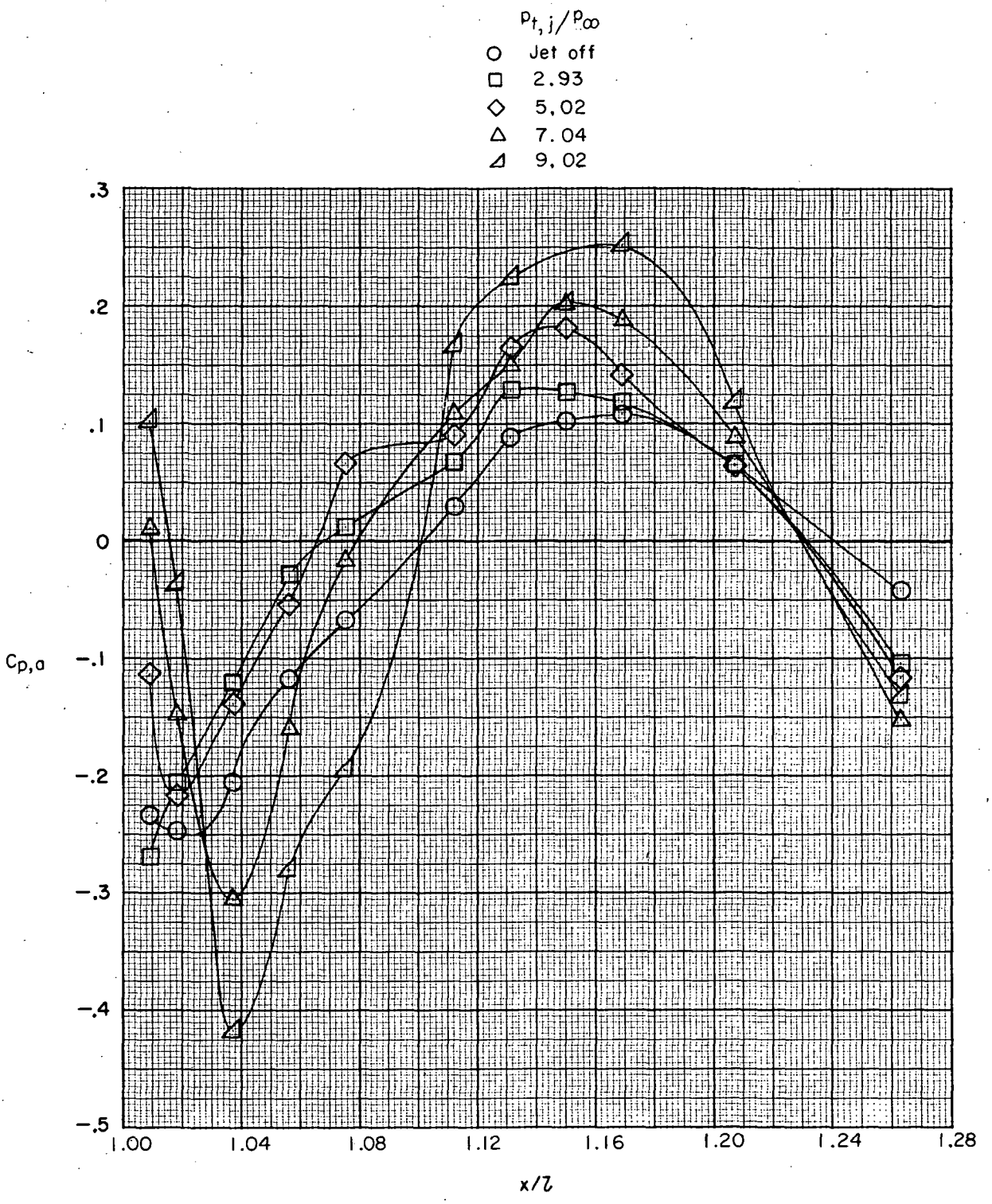


(k) M = 1.20; row 5.

Figure 37.- Concluded.

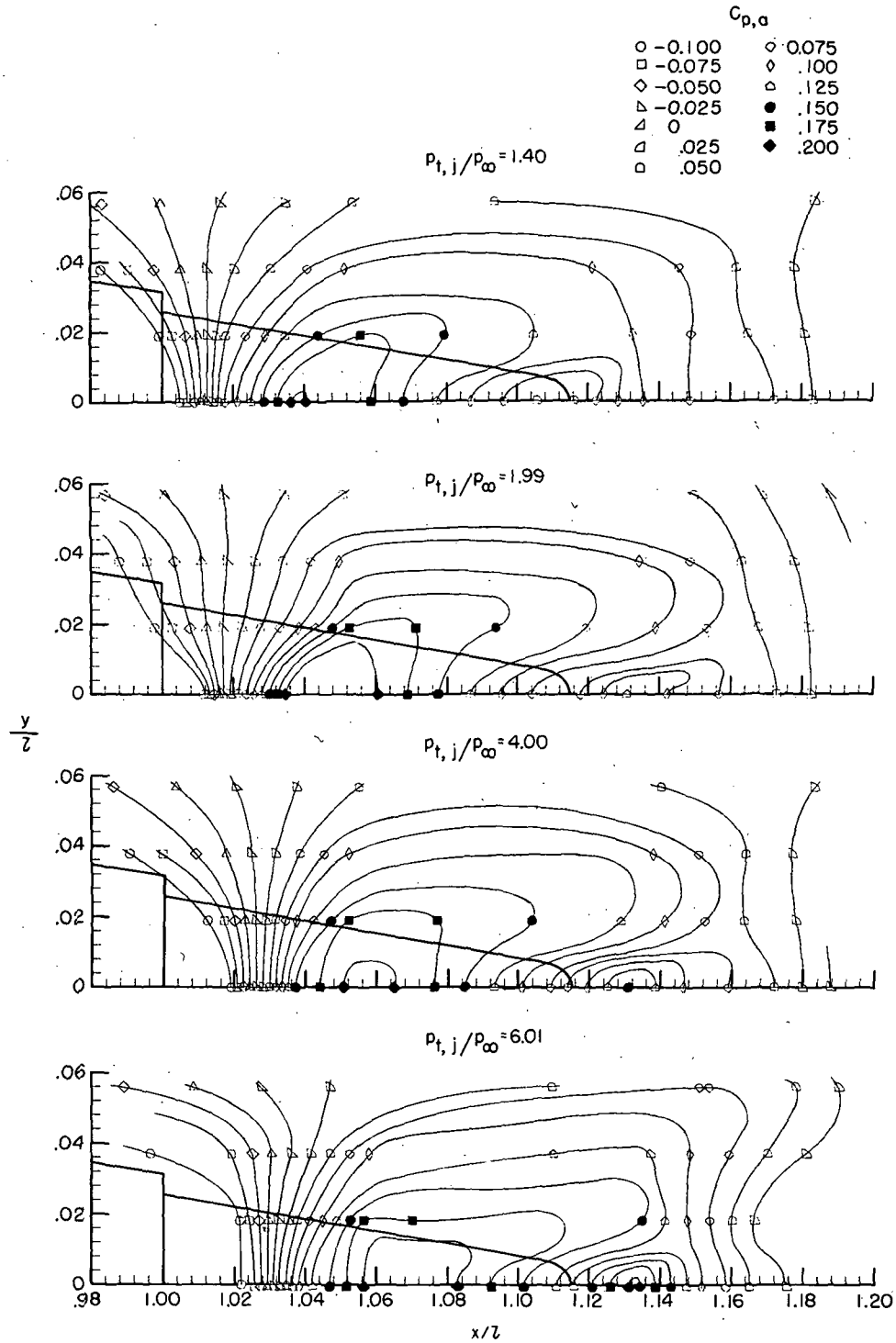


(a) M = 0.50.

Figure 38.- Isobaric contours on simulated fuselage side at several jet total-pressure ratios; upper half shown.

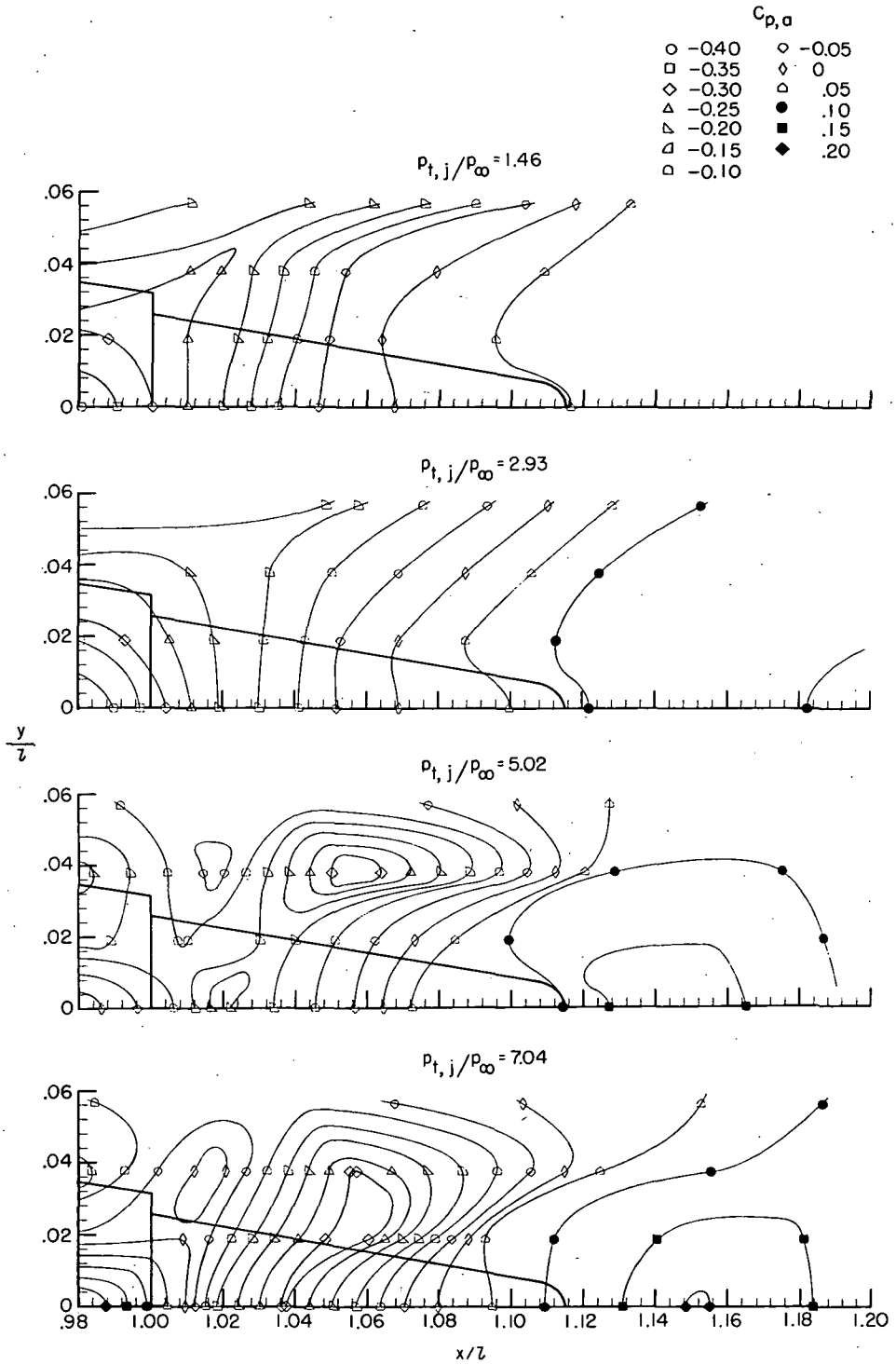


(b) M = 1.20.

Figure 38.- Concluded.

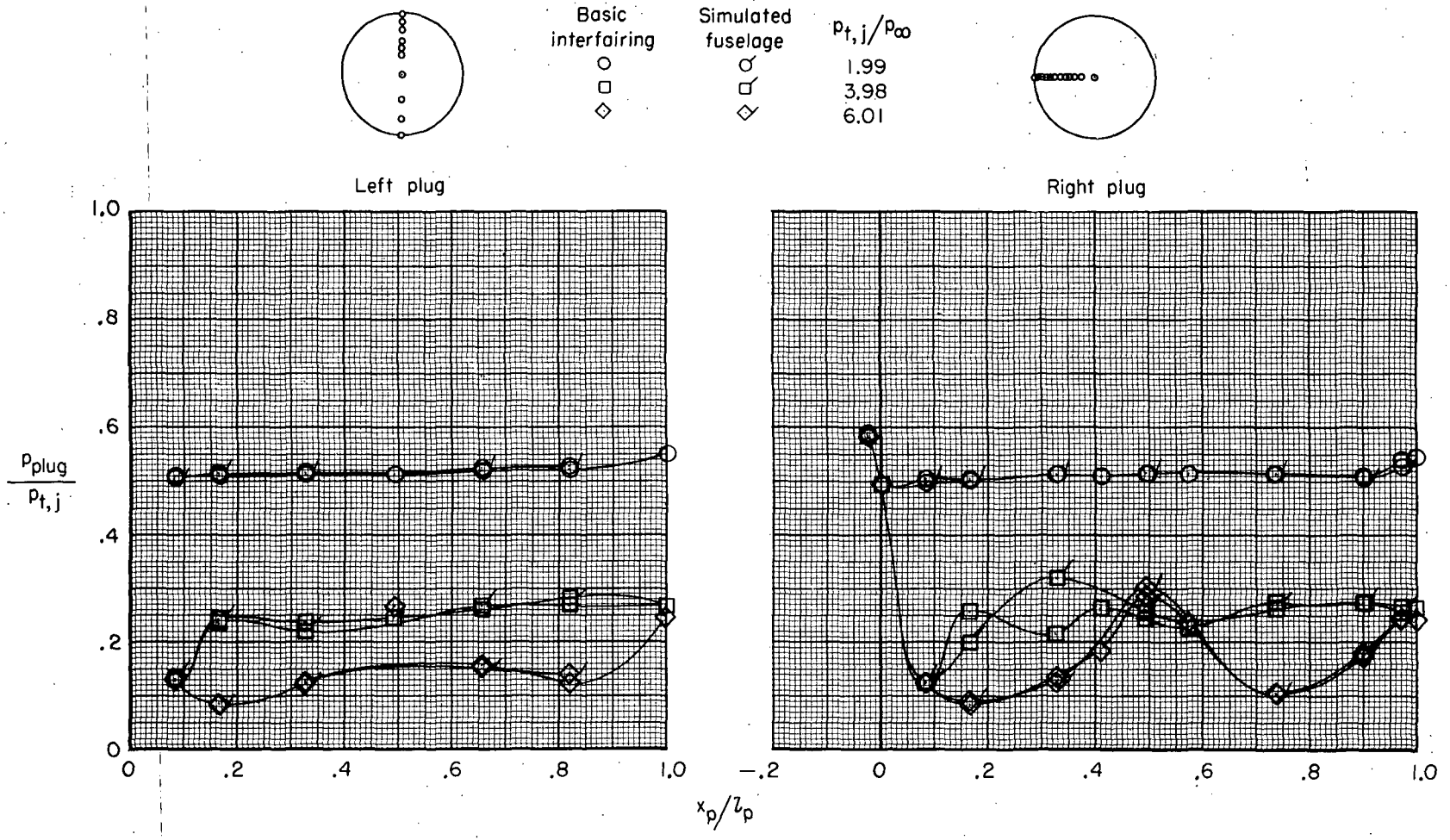


(a) M = 0.50.

Figure 39.- Effect of simulated fuselage on dry-power (shroud base removed) nozzle-plug static-pressure distributions. Wide-spaced afterbody.

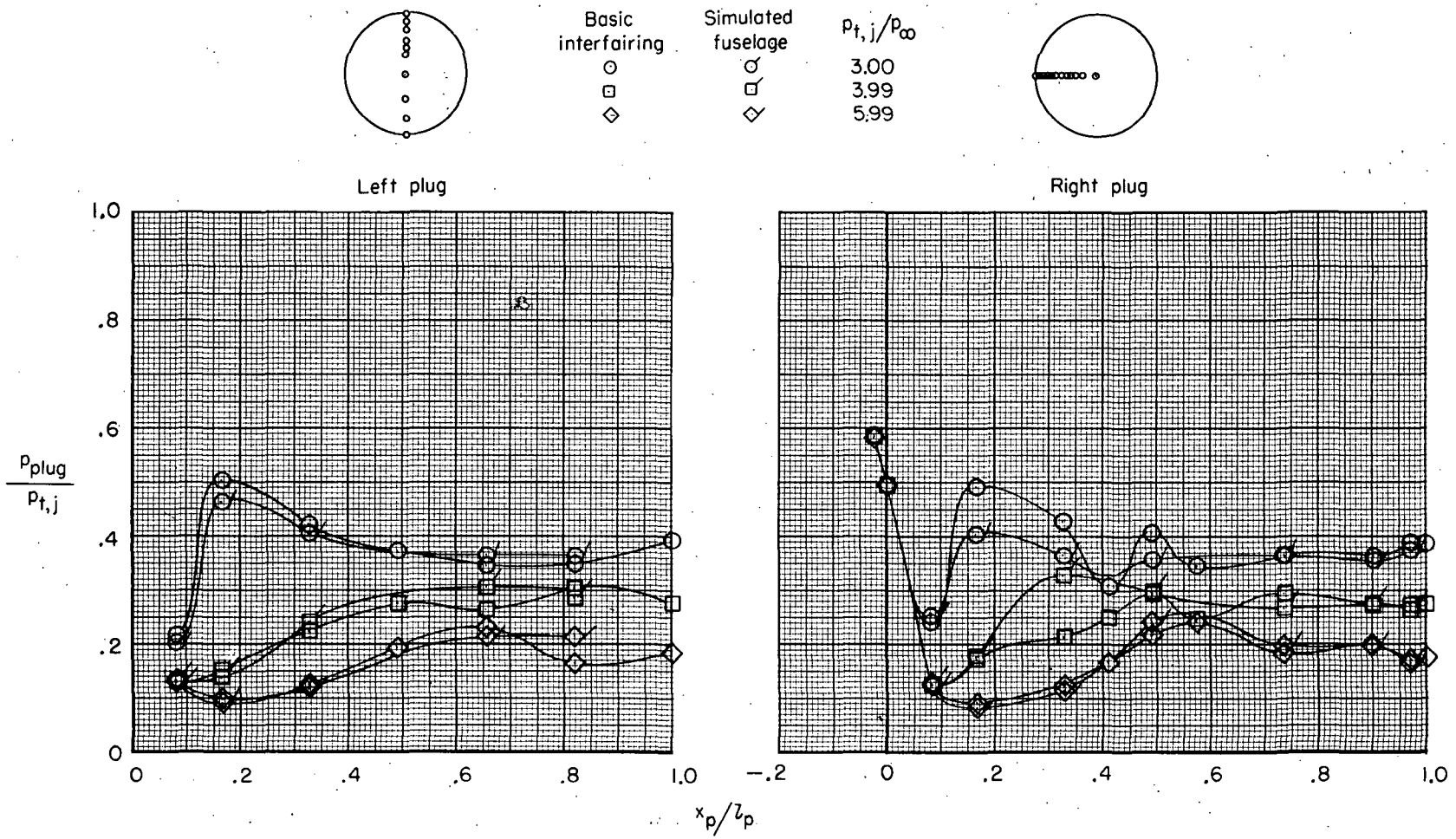


(b) M = 0.90.

Figure 39.- Continued.

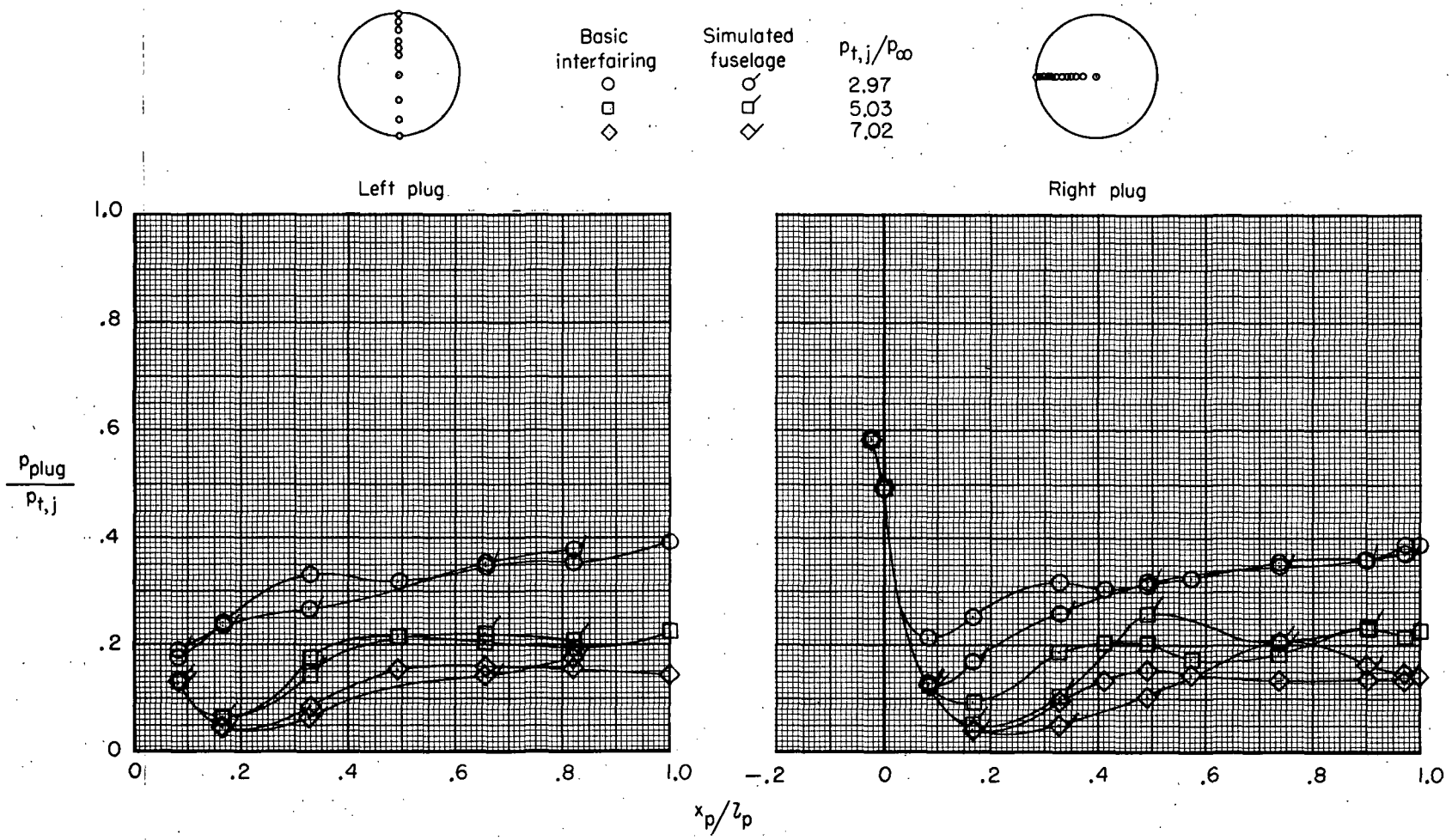


(c) M = 1.20.

Figure 39.- Concluded.

*U.S. GOVERNMENT PRINTING OFFICE: 1973-739-151/6

NATIONAL AERONAUTICS AND SPACE ADMINISTRATION
WASHINGTON, D.C. 20546

OFFICIAL BUSINESS
PENALTY FOR PRIVATE USE $300

SPECIAL FOURTH-CLASS RATE BOOK

POSTAGE AND FEES PAID
NATIONAL AERONAUTICS AND SPACE ADMINISTRATION
451

U.S. MAIL

POSTMASTER: If Undeliverable (Section 158 Postal Manual) Do Not Return

*"The aeronautical and space activities of the United States shall be conducted so as to contribute . . . to the expansion of human knowledge of phenomena in the atmosphere and space. The Administration shall provide for the widest practicable and appropriate dissemination of information concerning its activities and the results thereof."*

—NATIONAL AERONAUTICS AND SPACE ACT OF 1958

# NASA SCIENTIFIC AND TECHNICAL PUBLICATIONS

TECHNICAL REPORTS: Scientific and technical information considered important, complete, and a lasting contribution to existing knowledge.

TECHNICAL NOTES: Information less broad in scope but nevertheless of importance as a contribution to existing knowledge.

TECHNICAL MEMORANDUMS: Information receiving limited distribution because of preliminary data, security classification, or other reasons. Also includes conference proceedings with either limited or unlimited distribution.

CONTRACTOR REPORTS: Scientific and technical information generated under a NASA contract or grant and considered an important contribution to existing knowledge.

TECHNICAL TRANSLATIONS: Information published in a foreign language considered to merit NASA distribution in English.

SPECIAL PUBLICATIONS: Information derived from or of value to NASA activities. Publications include final reports of major projects, monographs, data compilations, handbooks, sourcebooks, and special bibliographies.

TECHNOLOGY UTILIZATION PUBLICATIONS: Information on technology used by NASA that may be of particular interest in commercial and other non-aerospace applications. Publications include Tech Briefs, Technology Utilization Reports and Technology Surveys.

***Details on the availability of these publications may be obtained from:***

**SCIENTIFIC AND TECHNICAL INFORMATION OFFICE**

**NATIONAL AERONAUTICS AND SPACE ADMINISTRATION**

**Washington, D.C. 20546**